Study of the plasma/wall interaction and erosion on a plasma thruster of low power.

Antoine Tavant

université PARIS-SACLAY

NNT : 2019SACLX085

Thèse de doctorat

Plasma-wall interaction and electron transport in Hall Effect Thrusters

Thèse de doctorat de l'Université Paris-Saclay
préparée à l'École polytechnique

Ecole doctorale n°572 Ondes et Matière (EDOM)
Spécialité de doctorat: Physique des Plasmas

Thèse présentée et soutenue à Palaiseau, le 18 décembre 2019, par

Antoine Tavant

Composition du Jury :

Prof. Pere Roca i Cabarrocas Dir. de recherche, LPICM / CNRS	Président
Prof. Achim von Keudell Professeur, Ruhr-Universitäte Bochum	Rapporteur
Dr. Gwenael Fubiani Ch. de recherche, LAPLACE / CNRS	Rapporteur
Dr. Sedina Tsikata Ch. de recherche, ICARE / CNRS	Examinateur
Dr. Anne Bourdon Dir. de recherche, LPP / CNRS	Directeur de thèse
Prof. Pascal Chabert Dir. de recherche, LPP / CNRS	Co-directeur de thèse
Dr. Stephan Zurbach Ing. expert senior, Safran Aircraft Engines	Invité

Acknowledgment

The results presented here are a part of three years of somewhat difficult work, which would have not been possible without a lot of persons.

Foremost, I would like to thank my advisors, Anne Bourdon and Pascal Chabert, for being such wonderful guides. You were always cheerful, and provided me with invaluable help. I would also like to thank Vivien Croes, for motivating me to candidate to this project and for his help and friendship. I would also like to acknowledge Stephan Zurbach for his trust.

This journey was accompanied by three dear fellow travelers, Florian Marmuse, Romain Lucken, and Thomas Charoy, whom I cannot thank enough. I know you will have a strong impact, wherever you go and whatever you do.

I also want to acknowledge all those involved in this work. Trevor Lafleur, for his amazing knowledge both in physics and simulation. Alexis Jeandet and Nicolas Aunai, for all there expertise they shared without counting the time and the cost. All the engineers that administrate the numerous computers I used : Zoidberg, thanks to Nicolas Marsac, but also Hopper, Occigen (CINES), and Nemo (CERFACS).

Furthermore, I used numerous Free and OpenSource software : all the operating system uses Linux, under several distrions ; the simulation code was compiled with the Gnu compilers ; the figures were made using Python and the wonderfull matplotlib package, and Inkspace was used for the illustrations ; the manuscrit, reports and presentations were created using LaTex ; Atom is my text editor of predilection ; and so many more tools that I cannot thank enough.

Lastly, I would like to thank my dear wife Audrey, for supporting me through all the ups, but mostly for the downs that accompanied this experience. Her contribution was the most important for the success of this adventure.

Résumé

Les moteurs électriques pour satellites, qui accélèrent les ions d'un plasma, sont primordiaux pour le succès des missions spatiales, qui sont de plus en plus essentielles dans nos vies (GPS, météo, communication, etc.). En effet, ils utilisent plus efficacement la masse du carburant que les moteurs chimiques plus conventionnels. Le moteur à effet Hall fait partie des technologies les plus performantes et utilisées. Cependant, sa conception et son optimisation sont longs et coûteux, car des processus physiques clefs, qui impactent son fonctionnement, sont encore mal compris. En particulier le transport des électrons à travers les lignes de champs magnétique, et l'interaction entre le plasma et les parois du canal du moteur.

Ces deux phénomènes sont basés sur des mécanismes cinétiques, et donc ne peuvent pas être étudier précisément avec des modèles fluides. Le transport des électrons est fortement impacté par une instabilité de dérive électronique qui croie dans la direction azimutale. L'interaction plasma-surface, elle, se déroule dans la direction radial du moteur. Ainsi, afin d'étudier ces deux phénomènes, nous utilisons une simulation cinétique bidimensionnelle qui modélise les direction radial et azimuthal du moteur. Le code de simulation, *L*PPic, a été développé dans ce but précis par Vivien Croes. Massivement parallélisé, il permet de simuler en un temps respectable le moteur a effet hall dans des conditions réalistes.

Grace aux résultats de simulations, nous avons mis en évidence que les électrons sont non-locaux, car ils sont absorbés plus vite aux parois qu'ils ne sont thermalisés par les collisions. Cette observation est primordiale pour la modélisation de l'interaction plasma-surface, car elle remet en question l'hypothèse des électrons isothermes. En conséquence, nous avons développé un modèle de gaine avec une loi d'état polytropique pour les électrons, qui décrit plus précisément l'interaction plasma-surface. Une très bonne correspondance a été observé entre les simulations bidimensionnelles cinétiques et le modèle de gaine fluid unidirectionnel. Ce modèle peut être utilisé en présence, ou non, d'émission électronique secondaire. Lorsque l'émission secondaire est présente, le modèle de gaine présente jusqu'à trois solutions, ce qui explique les oscillations de gaines observées précédemment dans les simulations. De plus, ce résultats est en accords avec des observations expérimentales, ce qui conforte ça validité.

Ce modèle est une première étape important pour mieux modéliser les moteurs à effet Hall. Cependant, certains aspects, comme la courbure du canal et le gradient de champs magnétiques, ont été négligé. Ces autres aspects de l'interaction plasma surface devront être pris en compte afin d'obtenir une modélisation précise des moteurs à effet Hall.

Concernant le transport des électrons dans la direction axial du moteur, l'instabilité azimutale observée, responsable du transport, est comparée aux relations de dispersions de l'instabilité acoustique ionique et l'instabilité cyclotronique de dérive électronique. Nous montrons que la phase de croissance linéaire est bien comprise, mais que l'état stationnaire dépend de l'interaction onde-particule et de phénomènes non-linéaires qui ne sont pas pris en compte dans les relations de dispersion. Ces phénomènes non-linéaire et cinétique doivent être mieux compris afin de déterminer l'état stationnaire de l'instabilité de dérive électronique, et donc la mobilité des électrons.

Summary

Electric propulsion systems that accelerate plasma ions are important for the success of spatial missions, which are more and more needed in our daily lives (GPS, weather forecast, communication, etc.). Indeed, they uses more efficiently the propellant mass compared to the more conventional chemical thrusters. The Hall effect thruster is one of the most used and efficient technology. However, its conception and optimization is slow and costly, as key processes are still poorly understood. In particular the electron transport across the magnetic field lines, and the interaction between the plasma and the ceramic walls of the channel.

Both phenomena are governed by kinetic mechanisms, and so they cannot be studied precisely with fluid models. Th electron transport is governed by the electron drift instability, which rises in the azimuthal direction. On the other hand, the plasma-wall interaction happens in the radial direction. Consequently, in order to study both phenomena we use a bi-dimensional kinetic simulation. The simulation code, *L*PPic, was developed in the objective by Vivien Croes. Highly parallelized, it allows us to simulate under a reasonable time the Hall effect thruster under realistic conditions.

We showed with 2D PIC simulation results that electrons are non-local, as they are absorbed more quickly at the wall compared to the collision frequency. This observation is essential, as it questions a usually made hypotheses concerning the isothermal electrons. Consequently, we derived a non-isothermal sheath model using a polytropic state law for the electrons that describes more accurately the plasma-wall interaction. A very good agreement was found between the bi-dimensional kinetic simulations and the uni-dimensional sheath model. The model can be used with and without secondary electron emission. With electron emission, the sheath model can present up to three solutions, explaining the oscillations observed in the simulations. Lastly, these results are in agreement with experimental measurements on the maximum , assuring its validity.

This plasma-wall interaction model is an important first step in order to better model Hall effect thrusters. however, some aspects of the thruster, such as the channel curvature and the magnetic field gradient, were neglected. These phenomena would need to be taken into account in order to model more precisely the thruster.

Concerning the electron transport across the magnetic field lines, the azimuthal instability observed, responsible for the transport, is compared to the dispersion relation of the ion acoustic wave and the electron cyclotron drift instability. We show that, while the first linear stage of the instability is well understood, the saturated quasi-steady-state is affected by particle-wave interactions and non-linear mechanisms that are not included in the dispersion relation. These non-linear and kinetic phenomena must be better understood in order to determine the stationary state of the instability, and so the electron mobility.

Table of Content

List of Figures

List of Tables

Acronyms

1D	1 dimension
2D	2 dimensions
3D	3 dimensions
3V	3 dimension for the velocity
BC	Boundary Conditions
BN	Boron Nitride
BNSiO2	Boron Nitride-Silicon Dioxide. A ceramic composed of a mix of Boron Nitride and Silicon Dioxide.
CNES	Centre National d'Etude Spatial. The French space agency
DFT	Discrete Fourier Transform
DK	Direct Kinetic
DR	Dispersion Relation . Relation between the wave number and complex frequency for waves in plasmas.
ECDI	Electron Cyclotron Drift Instability. Another name of the EDI present in HET.
EDI	$E \times B$ Electron Drift Instability. Another name of the ECDI present in HET.
EEDF	Electron Energy Distribution Function
EEPF	Electron Energy Probability Function
EP	Electric Propulsion. Propulsion engines using the electric energy, instead of the chemical energy.
EVDF	Electron Velocity Distribution Function
FT	Fourier Transform
FFT	Fast Fourier Transform
GEO	GEostationary Orbit Corresponds to the Orbit that follows the Earth rotation. Used mainly for telecommunication (Like the French Canal (former Canalsat)), it lies at 36000km from the Earth.
HET	Hall Effect Thruster
IAW	Ion Acoustic Wave
Kr	Krypton
LEO	Low Earth Orbit The LEO corresponds to orbits of altitude lower than 2000 km. Mostly used for Earth observation, and the ISS.
LHS	Left Hand Side
LPP	Laboratoire de Physique des Plasmas A laboratory from Ecole polytechnique, Palaiseau, France .
MCC	Monte Carlo Collision

ML	Laboratory Model
MTSI	Modified Two Stream Instability
NWC	Near-Wall Conductivity. Increased cross-field transport due to electron-wall collision and electron emissions from the wall.
PIC	Particle In Cell
RF	Radio Frequency
RMS	Root Mean Square
RSO	Relaxation Sheath Oscillation Oscillations between the SCL and the usual sheath regimes
SCL	Space Charge Limited
SEE	Secondary Electron Emission. Electron emission from a wall due to an energetic impact of a primary electron.
Xe	xenon

Chapitre 1

Concepts and preliminaries

The Earth is the cradle of humanity, but mankind cannot stay in the cradle forever.

Konstantin Tsiolkovsky, *pioneer of the astronautic theory*

Contents

1.1 Propulsion system for spacecrafts

In order to move in space, satellites, scientific probes, and spacecrafts in general rely on a propulsion system. The cost to go from one location to another can be expressed as Δv, a measure of impulse needed to maneuver. Figure 1.1 illustrates the Δv required to evolve in the solar system. We can see that reaching Low Earth Orbit (LEO) needs a Δv of 9400 m/s while the GEostationary Orbit (GEO) is 3910 m/s further. Landing on the Moon from the Earth ground requires a total of 15 km/s, while landing on Neptune requires $\Delta v = 43.7\,\text{km/s}$. For a spacecraft

of instantaneous mass $M(t)$, with a propulsion system generating a thrust $T(t)$, the Δv between t_1 and t_2 is

$$\Delta v = \int_{t_1}^{t_2} \frac{|T(t)|}{M(t)} dt. \tag{1.1}$$

As expected, we see from Eq. (1.1) that for a more massive spacecraft, a more intense, or a longer thrust is needed in order to obtain the same Δv.

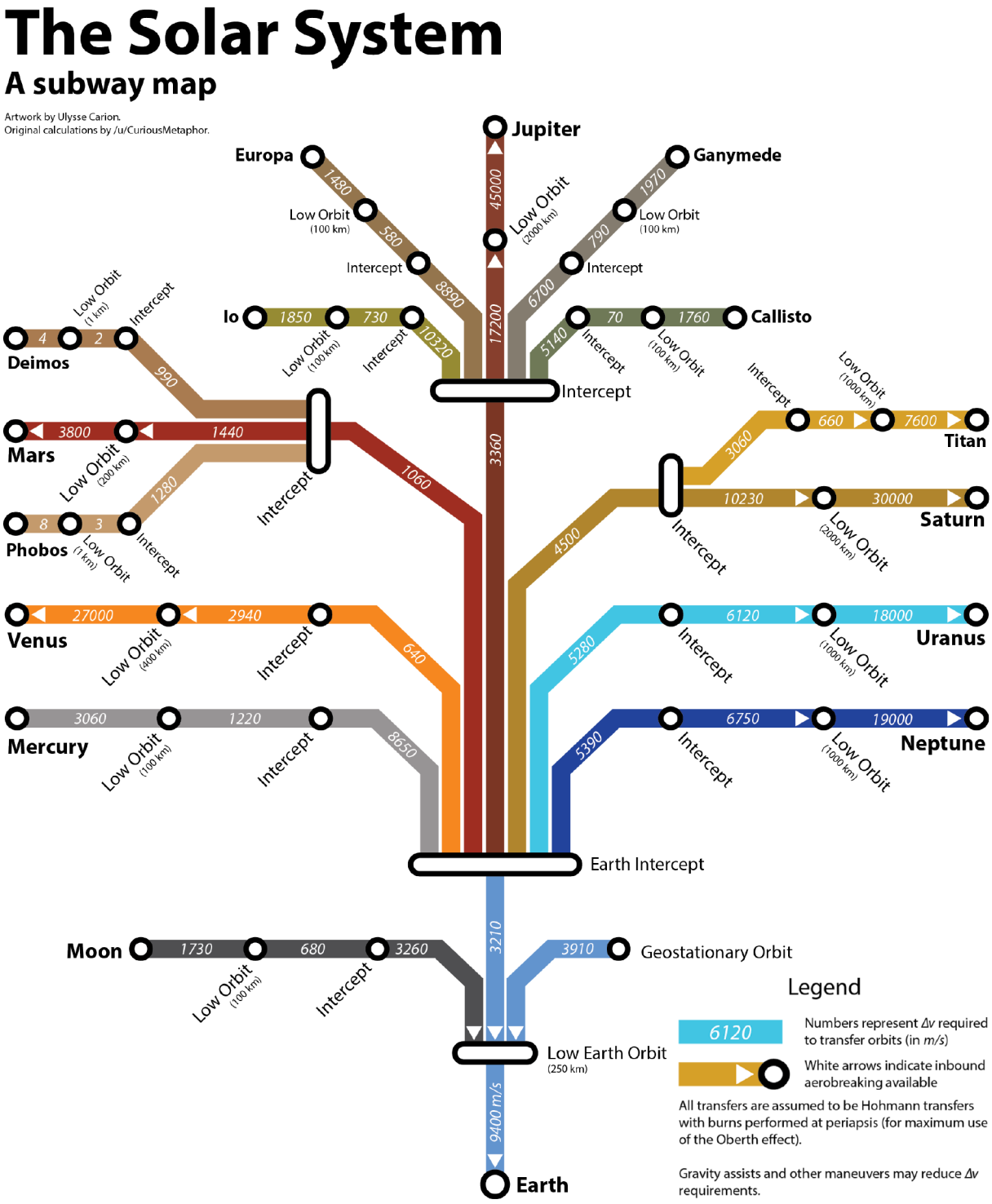

FIGURE 1.1 – Representation of the different Δv needed to go around the solar system, from u/ucarion [1]

1.1.1 The rocket equation

The thrust T generated by ejecting mass at high velocity is

$$T = v_{\text{ex}}\dot{M} \tag{1.2}$$

with v_{ex} the exhaust velocity of the propellant, and $\dot{M}$ the propellant mass flow rate through the thruster. Hence,

$$\Delta v = \int_{t_1}^{t_2} v_{\text{ex}} \frac{|\dot{M}|}{M(t)} dt = v_{\text{ex}} \ln\left(\frac{M_0}{M_1}\right) \tag{1.3}$$

with $M_0 = M(t_0)$ and $M_1 = M(t_1)$, and supposing that v_{ex} is constant. We see from Eq. (1.3) that for a spacecraft of dry mass M_1 to have a given Δv, the exhaust velocity is directly linked to the initial *wet* mass $M_0 = M_1 + M_{\text{prop}}$, with M_{prop} the propellant mass. Equation (1.3) is known as the rocket equation, or Tsiolkovsky's equation. Usually, instead of the exhaust velocity v_{ex}, the specific impulse $\mathrm{I_{sp}} = g_0 v_{\text{ex}}$, with g_0 the standard gravity, is used.

1.1.2 Chemical propulsion systems

The usual rocket thruster uses a chemical reaction to generate the thrust. For instance, the Vulcain (the thruster engine of the main stage of the European Ariane 5 and 6, developed by ArianeGroup, ex. Safran) uses the oxygen-hydrogen combustion, the most efficient chemical reaction for chemical thrusters [12]

$$2\mathrm{H_2} + \mathrm{O_2} = 2\mathrm{H_2O} + 572\ \mathrm{kJ},$$

with the energy of 572 kJ of heat generated by 1 mol of oxygen. This means that burning 1 kg of hydrogen-oxygen mixture generates a total energy of 13 MJ. Supposing that the entire energy is converted into the exhaust of the water produced, its velocity would be of 5.1 km/s. In reality, the exhaust velocity of the Vulcain is of 4.2 km/s, corresponding to $\mathrm{I_{sp}} = 431$ s. The efficiency of the Vulcain is close to 80%, which is a very high efficiency, and it would be difficult to increase it significantly.

In chemical propulsion systems, the fact that the energy released is related to the propellant mass gives an upper limit of exhaust velocity for a given combustion. Electric propulsion engines, on the other hand, decouple the mass ejected (the propellant) from the energy source. This decoupling allows a theoretical unlimited exhaust velocity. Another advantage is the absence of reactive species, which lowers the security requirements impacting the spacecrafts. Unfortunately, electric propulsion engines only work in vacuum and do not deliver sufficient thrust to compensate the earth gravity. Hence, while electric propulsion can be used on spacecrafts, chemical propulsion is the only solution for rockets.

1.1.3 Electric propulsion systems

Electric Propulsion (EP) systems mostly rely on plasmas [13, 14]. They have been successfully used since the 1960s by governments, but their complexity, the limited electric power available, and the inherent risk aversion of the space industry kept the EP technologies hidden from the commercial applications [15]. The breakthrough came in the '90s when the former Soviet Union's companies licensed the technology to Western propulsion companies. However, many commercial satellite manufacturers were skeptical, until the first decade of the 21st century, which brought strong evidence of the competitiveness of EP. The landmark of commercial use of EP is the selling of four all-electric satellites for GEO by Boeing in 2012, the first two of which were launched in March 2015.

The two leading EP technologies used are

— the Hall Effect Thruster (HET), also known as Stationary Plasma Thruster (SPT) in Russia

— the Gridded Ion Thruster (GIT), usually referred simply as Ion Thruster

The Gridded Ion Thruster is a plasma chamber closed at one end by two or more grids. The plasma source can be an emitting cathode, generating energetic electrons that ionize the propellant (usually Xenon), or a Radio Frequency (RF) source. The potential difference between the grids accelerates the ions. Another cathode is used to neutralize the ion beam. Compared to HETs, it produces an ion beam with less divergence and a higher I_{sp} of the order of 3000 to 4000 s. Figure 1.2 shows a picture of the ion thruster used for the BepiColombo mission toward Mercury. We see the neutralizing cathode, the accelerating grid, and the ion beam.

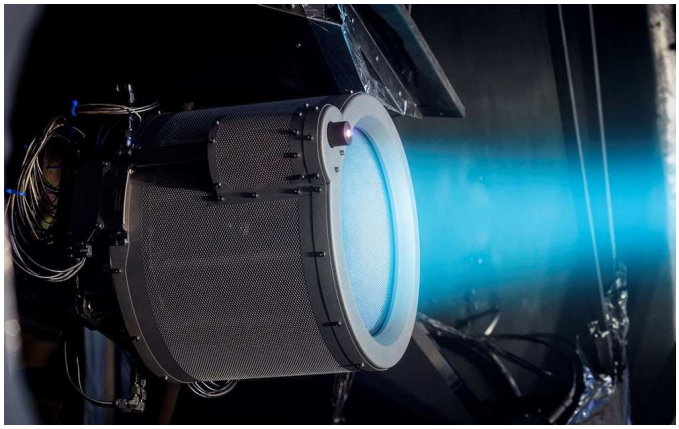

FIGURE 1.2 – The T6 ion thruster will help send BepiColombo to Mercury. The neutralizing cathode is in the upper left quadrant of the thruster. (Credit: QinetiQ)

Hall Effect thrusters use a magnetic barrier to both increase the ionization of the propellant and create the accelerating electric field. A detailed description of the HET is presented in the next section. One cathode is used to start the discharge and neutralize the ion beam. Compared to GITs, HETs need less power, hence reaching better thrust per power ratio and a smaller (therefore lighter) Power Processing Unit. Recently, the first satellites of two mega-constellations (OneWeb, 648 satellites planned, from which six were launched on February, 26th 2019, and Starlink, 12 000 satellites planned, from which 62 were launched on May, 23rd 2019) were sent to Low Earth orbit, both using HETs. Their typical I_{sp} is of the order of 1500 s. Figure 1.3 shows a high power prototype firing. We see the emitting cathode, in this design at the center, and the ion beam.

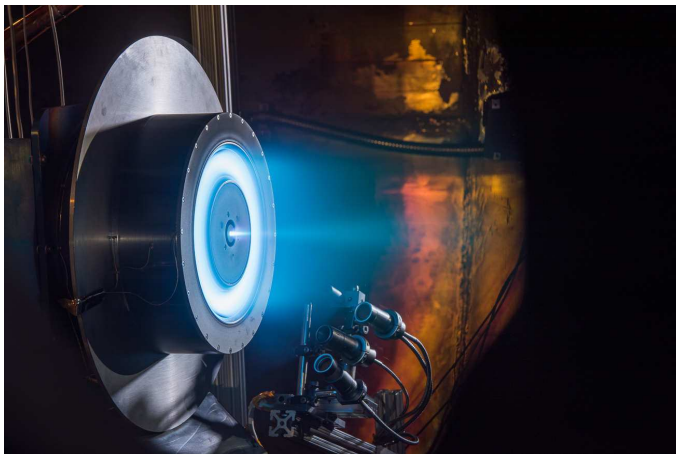

FIGURE 1.3 – A 13 kilowatt HET prototype on a testing bench in a vacuum chamber (Credit: NASA).

1.1.4 Electric propulsion environment in France

France is a leader country in the aerospace industry in both Europe and the world, with companies such as Airbus, Thales, Safran, and ArianeGroup (join-venture of Safran and Airbus). As a consequence, the French ecosystem of electric propulsion is vibrant. The main thrusters produced in France are the PPS series by Safran, with the PPS®1350 (version G at 1.5 kW nominal power, and the version E at 2.7 kW), and the PPS®5000, a high power HET at 5 kW, the first models of which have been delivered to Boeing in May 2019. A low-power version (between 500W and 1kW) of the PPS® is currently developed[11]. A list for the PPS® series elements and their respective characteristics can be seen in Table 1.1.

TABLE 1.1 – Members of the PPS® series developed by Safran Aircraft Engines [9, 10, 11]. The nominal operating condition of the PPS®X00 is not fixed yet.

Name	Power	Thrust	I_{sp}
PPS®1350-G	1.5 kW	89 mN	1650 s
PPS®1350-E	2.7 kW	140 mN	1800 s
PPS®5000	$3-5$ kW	$150-300$ mN	$1850-1700$ s
PPS®X00	$\sim$ 650W	$\sim$40 mN	$\sim$ 1450 s

Several initiatives concerning the small-sat sector are also undertaken, such as the start-ups Exotrail (micro HET) and Thrust Me (radio frequency Ion Thruster), or the Electron Cyclotron Resonance Thruster at ONERA. Since 1996, numerous research projects have been carried out in France on HET with the Centre National d'Etude Spatial (CNES), SAFRAN and several research laboratories : ICARE, LAPLACE, CPHT, LPP, etc. [9]. These numerous actors, combined with the support of the French and European space agencies, compose a stimulating environment that contributes both to the most mature technologies and the promising EP concepts that could disrupt the propulsion sector.

1.2 Electric propulsion challenges

Several challenges are currently tackled in the EP industry. The most prominent are listed by Samukawa et al. [16]:

1. Performance improvement: efficiency, lifetime, and cost-effectiveness. Lifetime is an important issue and is limited by electrode or wall erosion. The lifetime of an electric thruster must be larger than 10 000 h of (reliable) operation.
2. Design of more versatile thrusters, i.e. able to operate at different combinations of thrust and propellant velocity.
3. Extension of the domain of operation to lower power (μN to 10 mN thrust range) for microsatellites or accurate attitude control.
4. Extension to higher power for orbit raising of telecommunication satellites (several tens of kW) and interplanetary missions (100 kW and more).
5. Extension of EP to low-altitude spacecraft: there is an increasing interest in civilian and military satellites flying at altitudes around 100 km where the drag is significant and must be continuously compensated.

HET technology has the potential to answer many of these challenges. For instance, the lifetime issue can be addressed with wall-less and magnetically shielded configurations. Versatility is tackled with dual-mode HET configuration [9], low power thruster is attained with μ-thrusters [17], and so forth. However, the development of HETs is slow and expensive. A better physical

understanding of the processes governing HETs is needed in order to reduce the cost and development times. This is the objective of the current collaboration between Safran Aircraft Engines and Laboratoire de Physique des Plasmas (LPP).

1.3 Hall Effect Thruster research and development

Safran Aircraft Engines has been collaborating with LPP since 2014, starting with the Ph.D. thesis of Viven Croes [5]. During these first three years, a 2 dimensions (2D) Particle In Cell (PIC) code has been developed simulating the radial and azimuthal directions of a HET. Azimuthal instabilities have been observed in Croes et al. [18], and the effects of alternative propellants have been investigated in Croes et al. [19].

From this fruitful collaboration, an ANR (Agence National de la Recherche) industrial chair POSEIDON for "future Plasma thrusters for lOw earth orbit SatEllIte propulsiON systems", Grant No. ANR-16-CHIN-0003-01, has been created. Its objective is to develop novel methods to reduce the development time and cost of the next EP systems. Both experiments and simulations are being worked on to unlock the barriers of HET development. The POSEIDON chair is linked to the current development of a low power HET at Safran, the PPS®X00, which nominal operating point is of the order of 600W. The scientific part of the chair is led by LPP, while an unstructured 3D simulation code is developed by the CERFACS, in Toulouse. Safran leads the technical development and experimental investigation.

At the beginning of my thesis, I participated in the development of a Laboratory Model (ML) of the PPS®X00. The objectives of the PPS®X00-ML is to represent the physics of the PPS®X00 while allowing parametric studies of the main parameters of a HET, such as the geometry, the magnetic field topology, or the wall material. The PPS®X00-ML has successfully shown its usefulness, as the first tests allow to obtain state of the art performances [11]. My work at Safran showed us that the development of HET is still currently driven by experiments because numerical tools are not yet predictive. Simulations can be helpful to engineers to obtain some insights on the thruster behavior, but cannot be used with confidence for development. On the other hand, experiments are costly and time-consuming. They also are prone to delays in the conception schedule, and reduce innovation as designers take fewer risks.

The lack of numerical tools comes from some physical phenomena that need to be better understood, even though HET has been studied and used for more than 40 years. These critical phenomena are [16, 20]

— the electron transport,
— the plasma-surface interaction,
— the wall erosion,
— the nature of the propellant.

The objective of my thesis in the context of the POSEIDON chair was to study the two first points – the plasma wall interaction and the electron mobility – and how they can influence each other. I also studied the wall erosion, but this work is classified, and will not be disclosed in this manuscript.

The propellant's nature impacts mainly two things: the ion mass and the ionization energy. Because of its high mass and low ionization energy, xenon has been used since the beginning of HET. However, it is very costly, as it is mostly extracted from air with cryogenic distillation. The atmosphere is composed on average of $9{\times}10^{-6}\%$ of xenon [21]. The cheaper, but less effective, propellant of choice is krypton, which has recently started to be used. Iodine could also be interesting, as it can be stored at room temperature in a solid state. However, iodine is not a noble gas so it presents a more complex plasma chemistry, with for instance the presence of negative ions. The impact of the propellant mass and chemistry is not yet clear and slows down the use of alternative propellants on already designed systems. Preliminary works concerning the impact of the propellant nature on the accelerating region have been conducted during my

Ph.D. [19], but it is not the subject of this thesis.

1.4 Presentation of the Hall Effect Thruster

The HET is an electrostatic electrical propulsion system accelerating ions by the mean of an imposed voltage difference. Figure 1.4 shows a picture of the front view of an HET switched on and off. We can see the plasma in the annular plasma chamber.

FIGURE 1.4 – Front view of an HET, the BHT-1500 from Busek, USA, switched on (left) and off (right). The cathode is located at the center.

We can summarize the HET design into four parts:

1. The annular chamber.
2. The injecting anode
3. The cathode
4. The magnetic circuit

Figure 1.5 presents a schematic cut of the HET along its axial and radial directions.

The chamber has an annular shape. It is closed at the anode side and kept open at the other side. The axial length of the chamber is between 1 and 3 cm ; the radial width of the chamber is between 1 and 2 cm, and its mean radius is of the order of 5 cm. The walls are usually made out of ceramic, such as the Boron Nitride-Silicon Dioxide (BNSiO2). The material needs to be resistant to erosion by ion impact sputtering. But changing the material is also known to affect the behavior of the discharge. The usually supposed phenomenon for this impact is the secondary electron emission yield that is a function of the material nature. For materials used in HET, this yield may be higher than one.

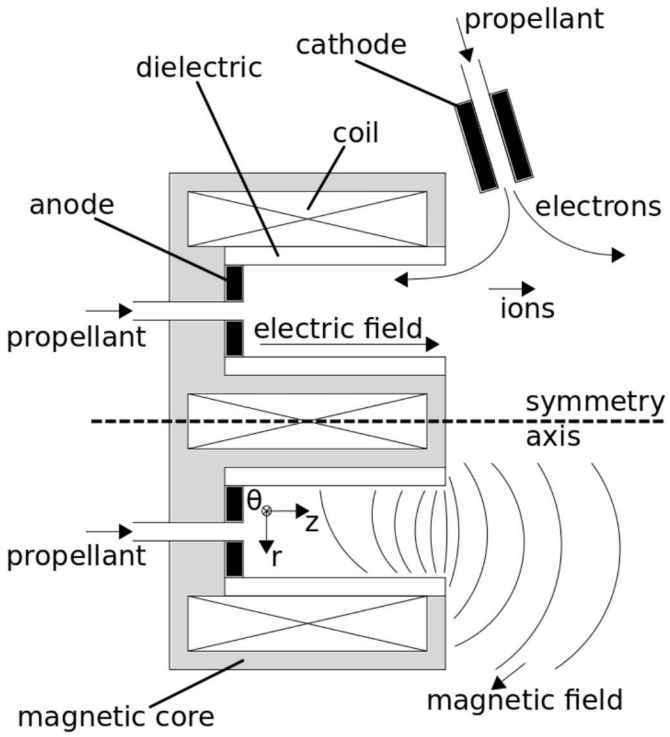

FIGURE 1.5 – Schematic cut of an HET, illustrating its different parts.

The anode is at the bottom of the chamber. The anode voltage is imposed to a few hundred volts. Usually, the neutral gas is injected through the anode itself, or close to the anode. The mass flow rate is of the order of a few mg/s.

The cathode is outside of the chamber. It is grounded, and injects electrons for two reasons:
- most of the electrons ($\sim 90\%$) are used to neutralize the ion flux, for both allowing the ions to leave the thruster and avoiding charging of the spacecraft,
- the others are attracted by the anode, hence entering the chamber. They enable the plasma discharge to switch and remain on.

The magnetic circuit is composed of electromagnets and a magnetic circuit made of different ferromagnetic pieces. It creates a constant radial magnetic field in the annular chamber. The maximum value of the radial magnetic field is located close to the exit plane of the chamber. Its amplitude is of the order of 200 Gauss (2×10^{-2} T). Figure 1.6 illustrates the axial profile of the magnitude of the radial magnetic field.

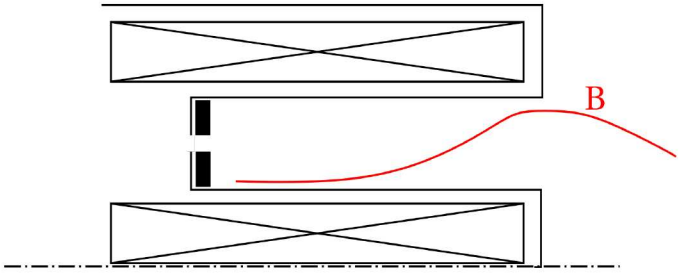

FIGURE 1.6 – Usual shape of the axial profile of the radial magnetic field on the centerline of the channel.

1.4.1 Hall Effect Thruster operating principle

The operation principle of a HET is rather simple. The objective is to ionize the propellant and impose an axial electric field to accelerate the ions.

Ionization

The propellant, usually xenon, is ionized by electron-impact. The ionization energy needed is $\mathcal{E}_{\mathrm{Xe,iz}} = 12.13\,\mathrm{V}$, which corresponds to an electron velocity of 2000 km/s. Due to the low pressure (around $1{\times}10^{-4}$ Pa), the mean free path of the electrons is larger than the chamber size. In consequence, a magnetic field is imposed in order to trap the electrons in a cyclotron motion. It increases the residence time of the electrons, thus promotes ionization. On average in a well designed HET, 90% of the propellant is ionized.

Acceleration

The potential difference between the anode and the cathode is used to accelerate the ions outside of the chamber and create the thrust. Because the magnetic field slows the electrons down, the plasma resistivity increases in the region where the magnetic field amplitude is large. Hence, the axial profile of the magnitude of the axial electric field presents a maximum close to the maximum of the magnetic field. While the typical voltage difference is $U_d = 300\,\mathrm{V}$, the maximum electric field can be of the order of 30 kV/m [22].

Ionization and Acceleration regions overlap

Figure 1.7 shows an illustration of the usual axial profiles of the ionization and the electric and magnetic fields. As the magnetic field governs both the ionization and the acceleration regions, it is challenging to obtain a clear separation between the two regions. However, if ionization happens in the acceleration region, the newly created ions will not be accelerated at their maximum velocity, hence resulting in a loss compared to the maximum theoretical thrust. The theoretical maximum speed is, by conservation of the total energy of the ion

$$v_{\mathrm{ex,max}} = \sqrt{\frac{2eU_d}{m_i}} \sim 31\,\mathrm{km/s} \tag{1.4}$$

with $m_i = 131\,\mathrm{u}$ for xenon and $U_d = 300\,\mathrm{V}$.

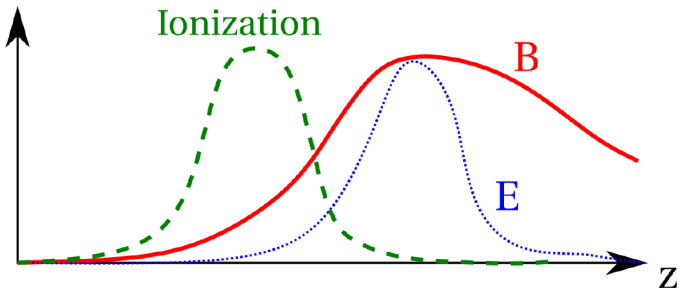

FIGURE 1.7 – Illustration of the usual axial profiles of the ionization and axial electric field amplitudes compared to the radial magnetic field amplitude.

The thruster efficiency, in the usual configuration, is governed by its magnetic field topology. Hence, it can be tough to find the best topology that will optimize the ionization and the location of the ionization and acceleration regions. Some concepts of double stage HET have been proposed to decouple the two phenomena to control them independently and are still under study [23].

1.4.2 Instabilities present in the Hall Effect Thruster

The HETs are subject to numerous plasma oscillations, over a broad range of frequencies [24, 25]. The most important ones are:

1. Low frequency (10-20 kHz) ionization oscillations, usually referred to as breathing mode,
2. Azimuthal low frequency rotating spokes, also in the kHz range,
3. Axial ion transit time oscillations, of the order of 100-500 kHz,
4. Azimuthal fast oscillations, with frequencies of the order of the ion plasma frequency.

1. Breathing mode

The breathing mode is relatively understood [26, 27, 28]. Indeed, a simple predator-prey model of two equations is enough to obtain the observed behavior qualitatively. It is related to the idea that when the ionization is important, the neutral atom density decreases, reducing the ionization. Hence, the plasma density decreases, allowing the neutral density to rise again until the ionization grows up again.

2. Rotating spokes

Experimental measurements with segmented anode [29, 30] seem to indicate that rotating spokes are present in the anode region. Their physical origins are less understood, as they were first attributed to ionization [31] but were later related to Simon-Hoh instability, and they were observed in PIC simulations even with neglecting ionization [32]. However, in recent experiments, the presence of spokes did not seem to affect the HET performances [24].

3. Transit time instability

Transit time instability has been predicted and observed in analytical and numerical models, respectively [33, 8]. Experimental studies of these instabilities are rather scarce, and it is only recently that time-resolved Laser-Induced Fluorescence measurements of the local ion velocity distribution function have confirmed the presence of this instability in a Hall thruster [34]. This oscillation could reduce the performance of the thruster by increasing the overlap between the acceleration and ionization regions [8].

4. High-frequency azimuthal oscillations

These oscillations were first observed in PIC simulations [35, 36, 37, 38] before being witnessed by electron Thomson scattering [39, 40, 41]. They are essential, as they enhance the electron transport in the axial direction [35, 4]. They are further described in the next section.

1.5 Scientific challenges of the Hall Effect Thruster

The scientific challenges are the critical phenomena that are currently not understood enough and prevent the industrial development of HETs. As introduced before, in this Ph.D. manuscript, we focus on two of them : the electron transport and the plasma-wall interaction.

1.5.1 Electron drift and azimuthal instability in the Hall Effect Thruster

The axial electric field E_z and the radial magnetic field B_r induces an azimuthal $E \times B$ drift of the electrons. The drift velocity $v_{\mathrm{d,ExB}}$ is

$$v_{\mathrm{d,ExB}} = \left| \frac{\mathbf{E} \times \mathbf{B}}{B^2} \right| = \frac{E_z}{B_r} \sim 1.5{\times}10^6\,\mathrm{m/s} \tag{1.5}$$

Because of their large mass, the ions are not significantly affected by the magnetic field. Hence they do not drift azimuthally. As a consequence, there is a significant difference between the movement of electrons and ions in the azimuthal direction.

This drift of electrons relative to the ions leads to instability in the azimuthal directions, so some authors refer to this instability as $E \times B$ Electron Drift Instability (EDI). However, as the drift is perpendicular to the magnetic field, it is subject to the cyclotron resonances. Therefore, in this thesis we use the more accurate name of Electron Cyclotron Drift Instability (ECDI). But it should be noted that both terms refer to the same physical phenomena.

The nature of the ECDI remains unclear[8], as the ECDI characteristics are very close to usual Ion Acoustic Wave (IAW), and that experimental measurements are challenging to conduct in the range of parameter of interest. Hence, the community is still arguing about the actual nature of the observed wave. A part of the work undertaken during my thesis focuses on the study and characterization of the instabilities observed in the kinetic simulations. These instabilities are treated in Chapter 3.

1.5.2 Cross-field transport of the electrons

As a first approximation, electrons are usually assumed to be frozen by the magnetic field and rotate only in the azimuthal direction due to the drift $E \times B$. But in fact, they present a so-called cross-field transport toward the anode in the axial direction. For instance because of collisions, the electrons can jump from one magnetic line to another. This leads to a transport in the direction of the electric field. This transport can be expressed considering the electron momentum conservation equation [4]:

$$\begin{aligned} \partial_t(m_e n_e \mathbf{v}_{de}) + \nabla \cdot (m_e n_e \mathbf{v}_{de}\mathbf{v}_{de}) = & q_e n_e(\mathbf{E} + \mathbf{v}_{de} \times \mathbf{B}) && \text{(Lorentz force)} \\ & - \nabla \cdot \mathbf{\Pi}_e && \text{(pressure gradient)} \\ & - m_e \nu_m n_e \mathbf{v}_{de}, && \text{(collisions)} \end{aligned}$$

where m_e, q_e, n_e, $\mathbf{v}_{de}$, and $\mathbf{\Pi}_e$ are the electron mass, charge, density, drift velocity and pressure tensor, and ν_m is the electron-neutral momentum transfer collision frequency. Ignoring the electron inertia and the pressure term, and with $\mathbf{B} = B_0 \mathbf{e}_r$, we can write the conservation equation projected on the axial and azimuthal direction

$$\begin{cases} 0 = n_e E_z - n_e v_{de\theta} B_r - \frac{m_e}{q_e} \nu_m n_e v_{dez} \\ 0 = n_e E_\theta - n_e v_{dez} B_r - \frac{m_e}{q_e} \nu_m n_e v_{de\theta} \end{cases} \tag{1.6}$$

Assuming that there is no electric field in the azimuthal direction because of the azimuthal periodicity ($E_\theta = 0$), we can combine the two equations of Eq. (1.6) to obtain the mobility [42, 43]

$$\mu_{\mathrm{classical}} \equiv \frac{n_e v_{dez}}{n_e E_z} = \frac{\frac{|q|}{m\nu_m}}{1 + \frac{\omega_{ce}^2}{\nu_m^2}} \tag{1.7}$$

with $\omega_{ce} = \frac{|q|B_0}{m}$ the cyclotron frequency. At the exit plane, the classical mobility predicts a mobility of the order of $\mu_{\mathrm{classical}} = 0.001 - 0.01\,\mathrm{m^2(Vs)^{-1}}$ [37]. However, it has been observed in experiments by Meezan et al. [43] that the electron cross-field transport in the axial direction of

the HET is higher than $\mu_{\text{classical}}$. Two phenomena are supposed to be mainly responsible for this enhanced *anomalous* mobility [5]: the azimuthal instability and the near-wall mobility due to electron emission. A significant part of the work of this Ph.D. thesis focuses on the quantitative comparison of the relative importance of the two phenomena.

The mobility induced by the azimuthal instability has first been observed in PIC simulations by Adam et al. [35], since then, it has been reproduced several times [37, 38, 4, 5, 8, 44]. The kinetic approach allowed Lafleur et al. [4] to propose a modified mobility due to the oscillations of the electron density and the azimuthal electric field of the ECDI. This effective mobility obtained is

$$\mu_{\text{eff}} = \mu_{\text{classical}} \left(1 - \frac{\omega_{ce}}{\nu_m} \frac{< \delta n_e \delta E_\theta >_\theta}{n_0 E_z}\right) \tag{1.8}$$

with δn_e and δE_θ the fluctuations in the azimuthal directions of the electron density and azimuthal electric field, respectively, the operator $< . >_\theta$ is the average in the azimuthal direction, and n_0 is the average plasma density. In the case where $\nu_m << \omega_{ce}$, Eq. (1.8) can be simplified to

$$\begin{aligned} \mu_{\text{eff}} &= \frac{\frac{e}{m_e}\nu_m}{\omega_{ce}^2} \left(1 - \frac{\omega_{ce}}{\nu_m} \frac{< \delta n_e \delta E_\theta >_\theta}{n_0 E_z}\right) \\ &= \frac{< \delta n_e \delta E_\theta >_\theta}{n_0 E_z} \frac{1}{B_r} \end{aligned} \tag{1.9}$$

which shows that the instability enhances the electron axial mobility in a way similar to an $E \times B$ drift. The electric field E_θ oscillates and has a zero mean value, but the average effect on the electron transport is not zero if the correlation between δE_θ and δn_e is not zero.

The amplitude of the instability at steady-state depends on the saturation mechanisms and the convection of the wave. Studies have been undertaken very recently but more work is still needed to derive expressions of the effective cross-field mobility that could be used in fluid models [24]. Another approach has been recently proposed by Jorns [45]. The author compared the experimental measurements of four different HET with a radial-axial fluid code, Hall2De. Following a data-driven approach, the author proposes five models of enhanced mobility. These models uses local plasma characteristics, such as the ion sound speed c_s, the ion velocity u_i, the electron velocity u_e, and the Debye length λ_{De}. Unfortunately, the experimental dataset is sparse, hence the domain of validity of this model is difficult to estimate. More precisely, the four HET used operate between 1 and 6 kW, thus the model may not be usable for smaller thruster.

The other mechanism enhancing the electron mobility is the secondary electron emission, responsible for a near-wall conductivity [46, 47, 6]. The coupling between the instability and the electron emission has first been studied in Héron and Adam [38], but the mechanism is still not clearly understood. Consequently, a better understanding of the electron cross-field mobility, the azimuthal instability, and the secondary electron emission is required before being able to model realistically the HET.

1.5.3 Plasma-wall interaction and secondary electron emission

Ceramic walls close the chamber in the radial directions. It has been observed in experiments that the nature of the wall can significantly affect the discharge behavior [48]. The primary phenomenon held responsible for this observation is the electron emission. As usually observed in bounded plasmas, a floating sheath forms between the plasma and the dielectric wall. The sheath confines the electrons in the plasma and accelerates the ions toward the walls. This allows to obtain a flux of electrons equal to the flux of ions, resulting in charge conservation in the plasma, and a neutral flux, also named zero-net current, to the surfaces.

Due to the relatively high electron energy, the impact of a primary electron can lead to the emission of secondary electrons [6, 49]. The probability of Secondary Electron Emission (SEE) depends on the electron impact characteristics (energy, angle) but also of the material: some materials are emitting more than others [48]. Ion induced secondary electron emission is much less

likely to happen at the range of energy impact [50], thus it is neglected compared to the electron induced SEE. In addition to the near-wall conductivity discussed previously, these secondary electrons are accelerated toward the plasma by the sheath. Thus they modify the plasma and the sheath properties. Their impact on the electron temperature also affects the ionization rate, which is directly linked to the thruster efficiency.

Raitses et al. [51] have observed that the current models of plasma-wall interactions with secondary electron emission cannot reproduce the electron temperature measured experimentally. Kinetic effects have been proposed by Sydorenko et al. [52] to explain this discrepancy between the models and the experiments. This could explain the differences between the kinetic simulations results and the global models in Croes [5].

In addition to SEE, the ion impact energy is large enough to erode the walls by sputtering. This erosion is sufficient to be the main limitation of the lifetime of the HETs. While most aspects of the erosion are well understood, we observe the apparition of patterns with a typical scale of the order of the millimeter on the eroded surfaces. The origin and the possible implications of these erosion striations remain open questions.

1.5.4 Three-dimensional physics of the Hall Effect Thruster

The physics governing the HET is three dimensional:

1. The plasma is accelerated in the axial direction by the electric field, and it is observed experimentally that the axial profile of the magnetic field is responsible for the performance of the thruster.
2. The chamber walls close the radial dimension. The walls are responsible for most of the plasma losses, both on the particle and energy balances.
3. The electrons drift in the azimuthal direction, leading to strong instabilities that affect the axial transport.

Consequently, when modeling or simulating a HET, if one of the direction is not included, some of the physics will be missing:

— No axial direction: the ionization or the acceleration, as well as the plasma transport, are missing,
— No radial direction: the wall losses and interactions are missing,
— No azimuthal direction: the instability is missing. Hence the electron cross-field transport is not well represented.

While 3D-simulations have recently been proposed, they use scaling laws to simulate the system in a reasonable amount of time[53]. For instance, a reduced geometry is used in Taccogna and Minelli [54], or a reduced density is used in Fubiani et al. [55]. A 3D simulation at real scale is not yet accessible. Hence, we need to be able to rely on 1D or 2D simulations. Consequently, we have to take into account the missing physics or include a model of its effects on the system.

1.6 Introduction to plasma models and simulations

1.6.1 Describing the plasma

Depending on the pressure, energy, and time scale, different models are more suitable to describe the plasma. There are mainly two distinct models. The first is the *kinetic* description of the species of the plasma, via the Boltzmann equation. The second uses a *fluid* description of the species, by means of moments.

Boltzmann equation

The Boltzmann equation in Eq. (1.10) describes the evolution of the particles (atoms, ions, and electrons) in the phase space. The phase space is the set of each possible position $\mathbf{x}$ and velocity $\mathbf{v}$ that can be attained by a particle. The evolutions in the phase space are due to forces, diffusion, and collisions.

$$\frac{\partial f}{\partial t} + \mathbf{v} \cdot \nabla_{\mathbf{x}} f + \mathbf{F} \cdot \nabla_{\mathbf{v}} f = \left.\frac{\partial f}{\partial t}\right|_{\text{coll}} \tag{1.10}$$

where f is the distribution function of the particle at $\mathbf{x}, \mathbf{v}$, and $\frac{\partial f}{\partial t}|_{\text{coll}}$ denotes the effects of the collisions, ∇ is the gradient in both the positions (subscript $\mathbf{x}$) and the velocities (subscript $\mathbf{v}$) and $\mathbf{F}$ is the force applied to the particle. In the general electromagnetic case,

$$\mathbf{F} = q\mathbf{E} + q\mathbf{v} \times \mathbf{B}$$

with q the particle charge, $\mathbf{E}$ the electric field, and $\mathbf{B}$ the magnetic field. The solution function of the stationary Boltzmann equation without collision, also known as the stationary Vlasov equation, is

$$f(\mathbf{v}) = N(\frac{m}{2\pi k_B T})^{3/2} \exp\left(-\frac{q\phi + mv^2/2}{k_B T}\right), \tag{1.11}$$

with k_B the Boltzmann constant, T is the temperature of the particle population, and ϕ is the electric potential, defined as $\mathbf{E} = -\nabla\phi$, and N is the density at the position where $\phi = 0$. Eq. (1.11) is the Maxwell-Boltzmann distribution function in velocity. The unit of the temperature T is the Kelvin, but in plasma physics, it is usual to use T, defined as

$$e\mathrm{T} = k_B T. \tag{1.12}$$

The unit of T is therefore the Volt. The equivalence is $1\,\mathrm{V} \simeq 10^4\,\mathrm{K}$. [1] We can write Eq. (1.11) with the particle kinetic energy $\epsilon = \frac{1}{2}mv^2$ to define the energy distribution function

$$f_\epsilon(\epsilon) = N\frac{2\sqrt{\epsilon}}{k_B T^{3/2}\sqrt{\pi}} \exp\left(-\frac{q\phi + \epsilon}{k_B T}\right). \tag{1.13}$$

The factor $\sqrt{\epsilon}$ in Eq. (1.13) appears because of the integration of the velocity distribution function f over the three directions. Thus, it is convenient to use the energy probability function

$$f_P(\epsilon) = \frac{f_\epsilon}{\sqrt{\epsilon}}. \tag{1.14}$$

We name the Maxwellian distribution function the distribution

$$f_{\mathrm{M}}(\mathbf{v}) = n\left(\frac{m}{2\pi k_B T}\right)^{3/2} \exp\left(-\frac{mv^2/2}{k_B T}\right), \tag{1.15}$$

with n the density. One can show that the Maxwellian distribution function is the solution of the Boltzmann equation with only elastic collisions [56]. In one dimension, the Maxwellian distribution function becomes

$$f_{\mathrm{M,1D}}(v) = n\left(\frac{m}{2\pi k_B T}\right)^{1/2} \exp\left(-\frac{mv^2/2}{k_B T}\right), \tag{1.16}$$

1. It is usual to find in the literature the temperature T expressed in electron-Volt (eV). This is not coherent with the definition Eq. (1.12), but it highlights the fact that the temperature is related to an energy via k_B. Therefore, the reader needs not to be confused by the equivalence between the electron-Volt and the Volt.

Fluid equations

The description of the plasma in 7 dimensions (3 of space, 3 of velocity, and one of time) can make the resolution of the Boltzmann equation complicated. If the accurate description of f is not needed, we can instead use the first moments of Eq. (1.10) on the velocity to obtain a set of simpler equations.

The first equation is obtained by integrating Eq. (1.10) over the velocity space, which gives

$$\begin{aligned} &\iiint_{\mathbf{v}} \frac{\partial f}{\partial t} d^3v \quad + \quad \iiint_{\mathbf{v}} \mathbf{v} \cdot \nabla_{\mathbf{x}} f d^3v \quad + \quad \iiint_{\mathbf{v}} \mathbf{F} \cdot \nabla_{\mathbf{v}} f d^3v \quad = \quad \iiint_{\mathbf{v}} \frac{\partial f}{\partial t}\Big|_{\text{coll}} \\ \iff &\frac{\partial n}{\partial t} \quad + \quad \nabla_{\mathbf{x}} \cdot (\mathbf{u}n) \quad + \quad 0 \quad = \quad S_{\text{iz}} \end{aligned} \tag{1.17}$$

where $n = \iiint f d^3v$ is the density, $\mathbf{u} = \frac{1}{n} \iiint \mathbf{v} f d^3v$ is the mean velocity, and S_{iz} is the source term of particle due to ionization. Equation (1.17) is the continuity equation for a given species. In a similar way, integrating the Boltzmann equation times the velocity or the kinetic energy gives the momentum conservation equation or the energy conservation equation, respectively. This set of equations is simpler, although it relies on additional hypotheses.

One of them is the closure of the system. Indeed, the continuity equation describes the evolution of the density n but needs the mean velocity $\mathbf{u}$. However, the velocity is described by the momentum conservation equation that needs the temperature T, and so on. To close the system, one has to make a hypothesis on the higher moment of the distribution function. A usual closure is the isothermal hypothesis, that fixes the temperature. Hence, the energy conservation equation is not needed. Other possible closures are the adiabatic hypothesis (no heat flux, the 3$^{\text{rd}}$ moment of f), the polytropic law linking the evolution of n with T, or the Fourier law for heat diffusion.

It is important to note that the set of fluid equations can be written without making any assumption on the distribution function f, except for the collisions. In this work, the temperature is defined by the second moment of the distribution function

$$e\mathrm{T} = k_B T = \frac{m}{3n} \iiint (\mathbf{v} - \mathbf{u})^2 f(\mathbf{v}) d^3v. \tag{1.18}$$

It happens that in the case of the Maxwell-Boltzmann distribution, the quantity defined by Eq. (1.18) is the denominator of the argument of the exponential in Eq. (1.11). The integral in Eq. (1.18) can be decomposed over the three directions x, y, and z as

$$e\mathrm{T} = k_B T = \frac{m}{3n} \sum_{i=x,y,z} \iiint (v_i - u_i)^2 f(\mathbf{v}) d^3v = k_B \frac{T_x + T_y + T_z}{3}, \tag{1.19}$$

which defines the directed temperatures. A distribution is said anisotropic if the three temperatures differ.

1.6.2 Plasma simulation models

As there are two different models to describe the plasma, there are two different simulation approaches: the fluid simulations and the kinetic simulations. The fluid simulations solve the moments of the distribution function (the density, mean velocity, and usually the temperature of the species), and the electromagnetic fields. Depending on the conditions, the system of equations can be simplified before resolution. For instance, under the electrodynamic conditions, mainly for space plasmas and fusion, the Maxwell equations are coupled to the fluid equations leading to magnetohydrodynamics (MHD). In the case of electrostatic conditions, as it is usual for Low-Temperature (LT) plasmas, the Poisson equation is coupled to the fluid equations. In most of LT plasmas the plasma is quasi-neutral except in a limited near-wall region called the plasma sheath. It is also common to neglect inertia terms and assume a steady-state in the momentum equations, leading to the drift-diffusion approximation. The fluid equations can be solved in 3

dimensions (3D), 2D, or 1 dimension (1D) for space. In a low dimension model, the effects of the missing dimensions are usually included, for instance, in the source terms as done by Barral et al. [6].

However, some phenomena can only be described via the knowledge of the distribution function. An example of such phenomena is the particle-wave interaction, such as the Landau Damping [57, 58], or the plasma-beam instability [59], for which the gradient of the distribution function in the velocity space is important. In contrast to the fluid descriptions, *kinetic* simulations solve the distribution function f for both position and velocities. Two approaches are usually used for kinetic simulations:

— The Direct Kinetic (DK) model, that discretizes Eq. (1.10) in the full phase space.
— The Particle In Cell (PIC) model, which uses an ensemble of particles to discretize the distribution function.

While the DK simulations use a Eulerian description of the distribution function, we can see the PIC simulations as a Lagrangian approach. The DK simulations can theoretically better describe the plasma, mostly because there is less numerical noise and we can model binary collisions more easily, especially Coulomb collisions. On the other hand, PIC simulations are much simpler to develop both on a mathematical and a computational perspective. For instance, the kinetic effects of electron emission have been recently studied using DK simulation by Cagas et al. [60], while it has been done since the last century in PIC simulations [61].

1.7 Problem statement and outline of the thesis

My thesis takes part of the collaboration between Safran Aircraft Engines and the Laboratory of Plasma Physics, whose objective is to study the fundamental physics governing the HET, in the prospect of accelerating the developments of the next generations of thrusters. I mainly focused on the electron transport and the plasma-wall interaction, both aspects requiring the use of kinetic tools.

Indeed, the electron transport is affected by instabilities that can only be described by kinetic models [37, 4]. Furthermore, the plasma-wall interaction is also affected by kinetic effects, both regarding the electron emission induced by electron impact [6, 62, 63] and the wall erosion by ion impact sputtering. Relatively few highly parallelized simulation codes have been developed, that could allow parametric studies. But the ever-increasing computational power available allows larger simulations to be conducted. Thus, a significant part of my work involves the development of a highly efficient PIC simulation code, with all of the technical difficulties related to it. The simulation code is then used to proceed to several parametric studies, that I used to derive reliable low-dimensional models that could be used to derive new engineering development tools.

In Chapter 2, we introduce *LPPic* , the primary simulation model used in this work, with an emphasis on the axial convection of the particles and the plasma-wall interaction. Chapter 3 focus on the azimuthal instability observed in the simulation and compares it to the dispersion relation. Chapter 4 presents the results of a parametric study investigating the wall effect. In Chapters 5 and 6, we modify the sheath model in order to reproduce the PIC simulation results. Chapter 5 focuses on a simplified 1D simulation to study the electron state law, while Chapter 6 continues the same model by including the secondary electron emission. While the majority of the work studied the 2D radial and azimuthal simulation, we end by studying the radial direction in a 2D axial and azimuthal simulation in Chapter 7.

Chapter 2

Particle-In-Cell simulations of HETs

This first chapter presents the basics of the Particle In Cell (PIC) - Monte Carlo Collision (MCC) simulations, and the simulation code *LPPic* that is developed at Laboratoire de Physique des Plasmas (LPP). Then the domain simulated is described, focusing on the wall and the axial convection of particle models implemented. The essential theories and laws of the plasma-wall interaction and electron cross-field transport are also given, preparing the discussion of the simulation results in the next chapters.

Contents

2.1 Elements of the 2D PIC-MCC simulations

2.1.1 The PIC simulations

The PIC simulation models particles moving freely on a grid. The grid is used to compute the electric field, in the electrostatic approximation by solving the Poisson equation

$$\Delta\phi = -\frac{\rho}{\epsilon_0} \tag{2.1}$$

where ϕ is the electric potential, ρ is the charge density, and ϵ_0 the vacuum permittivity. If the electrostatic approximation is not correct, one needs to solve the Maxwell equations.

The particles move following the Lorentz forces

$$m\frac{\partial \mathbf{v}}{\partial t} = q\mathbf{E} + q\mathbf{v} \times \mathbf{B} \tag{2.2}$$

with m and q, the particle mass and electric charge, respectively. The numerical particles followed in the simulations correspond to q_f physical particles, with

$$q_f = \frac{nV}{N_{\text{pc}}} \tag{2.3}$$

with n the particle density, V the volume of a cell, and N_{pc} the number of numerical particles in a cell. A large enough number of particles is needed in order to obtain physical results. Indeed, an insufficient number of particles leads to numerical heating [64]. Usually, a minimum of 100 particles per cell is used, but recent results seem to encourage to use more particles [65].

2.1.2 The Monte Carlo collisions

In PIC simulations, collisions between charged and neutral particles can be modeled by binary collision, but this approach is computationally costly. Instead, a Monte-Carlo algorithm can be used [66]. This approach is very efficient and allows scattering, momentum transfer, and ionization to be consistently modeled. The propellant used in Hall Effect Thruster (HET) is xenon (Xe). The cross-sections used for modeling Xe or other gases collisions are taken from the LXCat database project [67, 68]. Unless otherwise stated, the elastic, inelastic scattering and ionization reactions listed in Table 2.1 are used. The cross-section values are summarized in Fig. 2.1.

In the context of this thesis, and except precised otherwise, the 'PIC simulation' refers to the 'PIC-MCC simulation'. In the case where no collision is modeled, we also call it 'collisionless simulation'.

TABLE 2.1 – Reactions for xenon used in the PIC simulations

Reaction	Threshold	Reference
Elastic scattering		
$e + Xe = e + Xe$	–	[2, 3]
Excitation		
$e + Xe = e + Xe^*$	8.315eV	[2, 3]
$e + Xe = e + Xe^*$	9.447eV	[2, 3]
$e + Xe = e + Xe^*$	9.917eV	[2, 3]
$e + Xe = e + Xe^*$	11.7eV	[2, 3]
Ionization		
$e + Xe = e + Xe^+$	12.13eV	[2, 3]

2.2 Numerical implementation of the Particle in cell simulation

LPPic is an explicit electrostatic PIC-MCC simulation code. Every time-step, the simulation loop presented in Fig. 2.2 is computed. The different steps constituting the PIC-loop are described in the next subsections.

2.2.1 Numerical characteristics

In PIC simulations, there are two kinds of data used:
— Particles (electrons and ions ; neutrals can be followed as well but not in the version of *LPPic* I have used for my Ph.D.),
— Mesh, also named fields (densities, electric and magnetic fields, and so on).

Particles

For each particle, its position $\mathbf{x}$ and its velocity $\mathbf{v}$ are known. In most PIC-MCC simulations, the three directions of the velocity vector are followed in order to take into account scattering. It is abbreviated as 3V. The particle positions and velocity are not discretized, except to the numerical floating-point precision.

One numerical particle represents a large number of physical particles. Therefore they can be called *superparticle* or *macroparticle* in the literature. We will simply call them particle, unless the context requires clarification.

Fields

The fields are defined at the center of each cell of the mesh. The charge density ρ is computed by depositing the particle on the mesh, using the Cloud-in-cell model [69]. The electric field at the position of the particle is also obtained by bilinear interpolation. The mesh dimension defines the dimension of the simulation. It is usual to find 1D3V or 2D3V PIC simulations, for particles with 3 directions on the velocity but one or two dimension(s) in space, respectively.

Early studies on the stability of the PIC simulations gave conditions for the cell size and the time step as functions of the physical parameters [69, 70]

$$\Delta t \omega_{pe} \leq 0.2, \tag{2.4}$$

$$\Delta x \leq 0.5 \lambda_{De}, \tag{2.5}$$

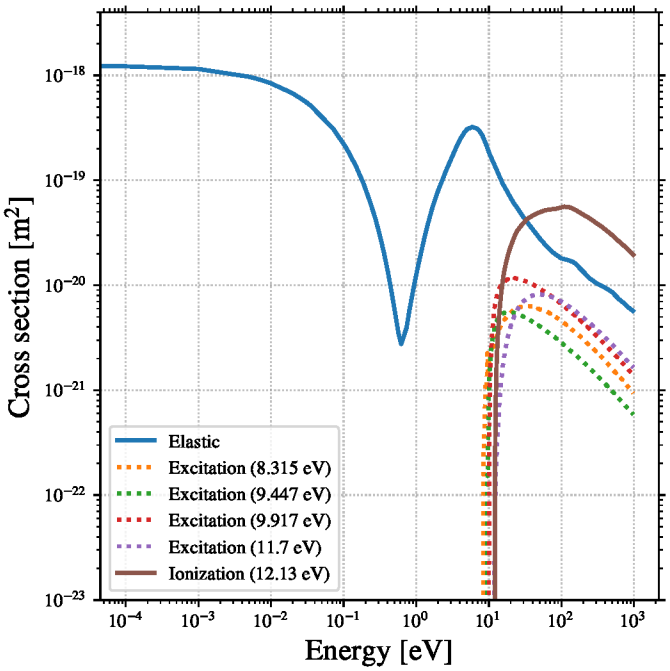

FIGURE 2.1 – Cross section values used in the Monte Carlo procedure [2, 3].

where

$$\omega_{pe} = \sqrt{\frac{e^2 n_e}{\epsilon_0 m_e}} \tag{2.6}$$

is the electron plasma frequency, and

$$\lambda_{De} = \sqrt{\frac{\epsilon_0 e \mathrm{T_e}}{e^2 n_e}} \tag{2.7}$$

is the Debye length. We recall the relation $e\mathrm{T_e} = k_B T_e$, with T_e in Kelvin and $\mathrm{T_e}$ in volt.[1] The conditions 2.4 and 2.5 can be combined to produce

$$\frac{\Delta t}{\Delta x}\sqrt{\frac{e\mathrm{T_e}}{m_e}} \leq 0.4, \tag{2.8}$$

which can be seen as a constraint on the thermal electron velocity that must be much less than one cell per time step. Hence, condition 2.8 is usually referred as the CFL condition.

As presented before in Section 2.1.1, a third condition applies on the ratio between the superparticle density and the physical particle density. No universal rule exists, as a wide range of values may be appropriate to different contexts [71, 70]. A general consensus in low temperature plasma agrees on using approximately 100 numerical particles per cell but a careful convergence study has to be carried out to demonstrate that it is enough for the studied conditions.

1. The Debye length usually refers to the spatial scale over with a charge is screened by the other charged particles.

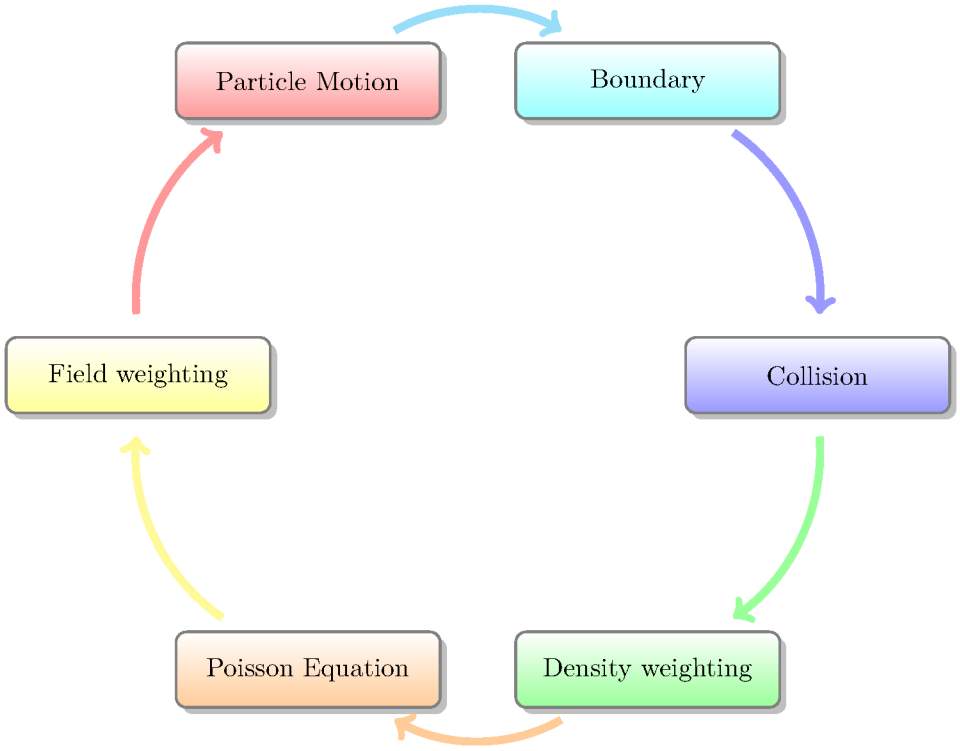

FIGURE 2.2 – PIC-MCC loop executed every time step.

2.2.2 The large memory requirement

Because of the particle discretization, the memory requirement for PIC simulation can be tremendous. For instance, we estimate here the numerical parameters of a 2D HET simulation. With a density $n_e = 3{\times}10^{17}\,/\mathrm{m}^3$, and an electron temperature $\mathrm{T_e} = 20\,\mathrm{V}$, the Debye length is $\lambda_{De} = 6{\times}10^{-5}\,\mathrm{m}$. The simulation of a square domain of 2 cm side needs a mesh of approximately 650 cells in each direction, hence more than $4{\times}10^5$ cells in total. With 100 electrons and 100 ions per cell, it is 85 million particles that are simulated.

For every particle, we need to store at least the two values of position and the three values of velocity, thus five real numbers. Using the double-precision floating-point format, it corresponds to approximately 400 bits per particles. In total, around 33 billion bits, or 4 Go (gigaoctet) are needed to store the particles ! To give a reference to the reader, a modern laptop has a RAM of 8 Go. Adding a third dimension of size 2 cm increases the number of cells to 300 millions, and the memory requirement for the particles to 2.5 Terabytes of memory.

2.2.3 Solving the particles motion

The interaction of the motion equation Eq. (2.2) is different for magnetized and non-magnetized particles. For non-magnetized particles, we use the leapfrog scheme [69]

$$\mathbf{v}^t = \mathbf{v}^{t-1} + \frac{q}{m}\mathbf{E}\Delta t, \tag{2.9}$$

$$\mathbf{x}^t = \mathbf{x}^{t-1} + \mathbf{v}^t\Delta t, \tag{2.10}$$

with the superscript t designing the time step, q and m the particle electric charge and mass, $\mathbf{E}$ the electric field at the particle position, and Δt the time step duration.

Magnetized particles For magnetized particles, we use a modification of the leapfrog algorithm proposed by Boris [72]. It corresponds to an operator splitting between the electrostatic acceleration and the magnetic rotation. This splitting is described below:

1. accelerate the particle during $\frac{\Delta t}{2}$: $\mathbf{v}^{t-\frac{\Delta t}{2}} = \mathbf{v}^{t-1} + \frac{q}{m}\mathbf{E}\frac{\Delta t}{2}$
2. rotate the particle velocity with the magnetic field
3. accelerate the particle during $\frac{\Delta t}{2}$: $\mathbf{v}^{t} = \mathbf{v}^{t-\frac{\Delta t}{2}} + \frac{q}{m}\mathbf{E}\frac{\Delta t}{2}$

It is important to note that the leapfrog and the Boris schemes induce a shift of $\frac{\Delta t}{2}$ between the position and the velocity[69], as illustrated in Fig. 2.3. This shift can lead to erroneous diagnostics when computing moments of the particles distribution. For instance, the mean velocity of a set of N particles at time t is computed as:

$$\bar{\mathbf{v}}^t = \frac{1}{N}\sum_i^N \left({\mathbf{v}_i}^t + \frac{q}{m}\mathbf{E}_i\frac{\Delta t}{2} \right). \tag{2.11}$$

Other moments like the mean energy or heat flux follow the same correction. We can see that the error between $\bar{\mathbf{v}}$ defined above and

$$\tilde{\mathbf{v}} = \frac{1}{N}\sum_i^N {\mathbf{v}_i}^t$$

is

$$\bar{\mathbf{v}} - \tilde{\mathbf{v}} = \frac{q\Delta t}{2m}\frac{1}{N}\sum_i^N \mathbf{E}_i.$$

Hence, the error in the diagnostic is larger in the region of large electric field (as in the sheaths).

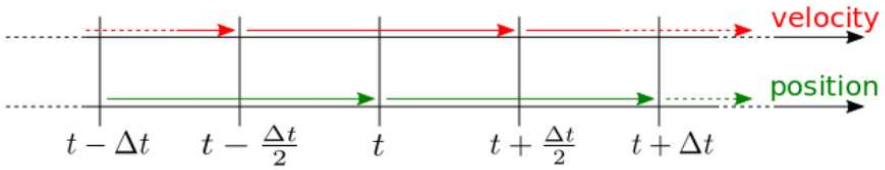

FIGURE 2.3 – Illustration of the shift between the particle velocity and position due to the leapfrog scheme Eqs. (2.9) and (2.10).

2.2.4 Poisson equation solver

In order to compute the electric field due to the particle charge density, the Poisson equation Eq. (2.1) needs to be discretized over the mesh. We can directly discretize the differential operator by using the finite volume approach over a cell of the mesh. The formal discretization is developed in Section 2.4, for the particular case of taking into account the presence of dielectric boundaries.

In 1 dimension (1D), the obtained linear system is tridiagonal. It can be solved directly using THOMAS' algorithm, which stores the Gauss elimination's coefficient. In 2 dimensions (2D), the linear system is pentadiagonal. A direct solver, like the *LU* decomposition, would require a large amount of memory to store the factorization matrices. On the other hand, as the time step is usually small in PIC simulation, we expect the plasma potential ϕ not to change rapidly. Hence, an iterative solver using the previous solution as an initial guess seems more reasonable from both the memory storage and the computational time. The choice of the Poisson solver is discussed later in Section 2.10.

2.3 Bidimensional simulation of an HET

We are interested in studying the azimuthal instabilities and the induced electron transport in the axial direction. In addition, we want to study the plasma-wall interactions. As realistic 3 dimensions (3D) simulations are not yet achievable, we choose to simulate the radial-azimuthal plane. The axial location where the electron drift is the highest is close to the exit plane, where the axial electric field is the highest. Hence, we choose this location to be simulated. In this section, we describe the characteristics of the radial-azimuthal simulation.

2.3.1 Neglecting curvature

The Electron Cyclotron Drift Instability (ECDI) features oscillations of short wavelength of the order of the mm. Hence, neglecting the curvature of the channel is expected not to change the ECDI characteristics while improving the simulation performances.

In Héron and Adam [38], the authors have performed a 2D PIC simulation including the channel curvature. They have observed a small difference between the inner and the outer walls. In Domínguez-Vázquez et al. [73], the authors studied the effect of the curvature using a 1D radial model. They have shown asymmetries due to the combination of the geometric expansion, the magnetic mirror effect, and the centrifugal force. However, the global behavior of the discharge is not affected compared to simulations without the curvature model. Hence, in order to simplify the analogy, we choose to neglect the curvature.

Consequently, we can use a Cartesian mesh (also called a rectangular mesh). In spite of this Cartesion domain, we will continue to use the words 'azimuthal' to characterize the y direction, and 'radial' for the x direction. The z component corresponds to the axial direction, normal to the simulation domain.

2.3.2 Radial-azimuthal domain description

The azimuthal direction is closed using a periodic boundary condition for both the particles and the fields. Consequently, when a particle crosses the azimuthal boundary, it is moved to the other side of the domain. The plasma potential and the azimuthal electric field are continuous in the azimuthal direction. The radial direction is closed by the walls. They can be grounded metallic, or a dielectric boundary can be modeled. The physics related to the boundary conditions of the walls are described and discussed in Section 2.4.

A constant and uniform magnetic field B_0 is imposed in the radial direction. This does not take into account the magnetic mirror effect, that has been shown to be important [74, 75, 73]. However, it cannot be modeled in the 2D Cartesian radial-azimuthal domain while conserving a divergent-free magnetic field topology. A constant and uniform axial electric field E_0 is imposed. Figure 2.4 shows a schematic representation of the simulated domain, overlaid with the computed azimuthal electric field E_y.

2.3.3 Particle balance

As the axial position simulated is the exit plane, the ionization is too low to balance the particle losses to the wall (see Fig. 1.6 and 1.7). Instead, the ionization takes place upstream, and the particles are convected downstream. In these conditions, two models can be used concerning the particle losses at the walls:

— having a simulation that dies off, as done in Janhunen et al. [65],

— forcing an arbitrary ionization to occur in order to compensate the radial losses [73].

The second option is no self-consistent, but allows to obtain a steady-state and is supposed not to affect the simulation significantly. Hence, we use this model to achieve a constant mean plasma

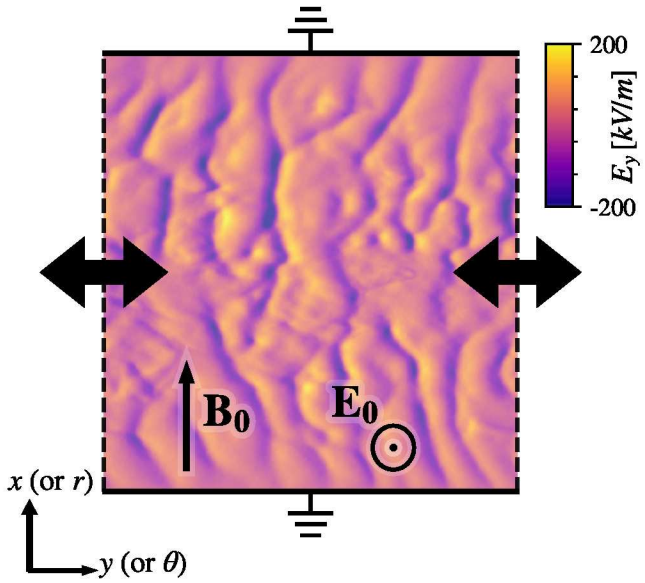

FIGURE 2.4 – Schematic representation of the radial-azimuthal simulation domain. Overlaid is the computed azimuthal electric field given as an example. The radial length is 2 cm, and the azimuthal length is 1 cm. The magnetic field is $B_0 = 0.02\,\mathrm{T}$, the axial electric field is $E_0 = 2{\times}10^4\,\mathrm{V/m}$, and the walls are grounded. More parameters are given in Table 4.1.

density during the simulation. The forced ionization rate is computed in order to compensate the losses of the ions at each time step. The spatial ionization profile is uniform.

2.3.4 Axial convection

Due to the imposed axial electric field, ions and electrons gain energy. In the HET, the axial convection of the particles balances the energy gain. However, in a purely 2D simulation, the convection is missing, resulting in an ever-rising particle energy. This prevents the possibility to reach a steady-state regime, as observed in Héron and Adam [38], Janhunen et al. [65].

We implemented a model of convection initially proposed for a 1D simulation by Lafleur et al. [4], and adapted in 2D by Croes et al. [18]. The model uses a finite axial length L_z. When a particle reaches the boundary $z = 0$ or $z = L_z$, it is removed from the simulation. In order to conserve the particle (and charge) balance, a particle is created at $z = 0$ for the ions (that are accelerated toward $z > 0$) or at $z = L_z$ for the electrons. It has been observed that using a radial position chosen uniformly at random for the newly injected particle would affect the sheath [18]. Hence, the radial position of the new particle is the same as the removed particle.

Concerning the azimuthal particle position, it is more difficult to choose between a random position or the same position as the removed particle. In Lafleur et al. [4], Croes et al. [18], a random azimuthal position was chosen. However, as will be discussed in Section 2.5, this induces a numerical noise that can be harmful in some cases.

2.4 Dielectrics boundary condition

Figure 2.4 shows the simulation of the radial-azimuthal domain with metallic grounded walls. Figure 2.5 illustrates the configuration in the radial-azimuthal plane highlighting the more realistic radial boundary conditions. The plasma is bounded in the radial direction by dielectric layers isolating the magnetic circuit. The magnetic circuit can be considered electrically grounded.

The particles are absorbed when touching the dielectric wall, and we neglect the diffusion of the charge in the dielectric. Hence, we obtain a surface charge σ at a time t with

$$\sigma(t) = e \int_0^t (J_i - J_e) dt \tag{2.12}$$

with J_i and J_e the ion and electron flux respectively, e is the elementary charge, and assuming that there is no surface charge at the interface at the beginning.

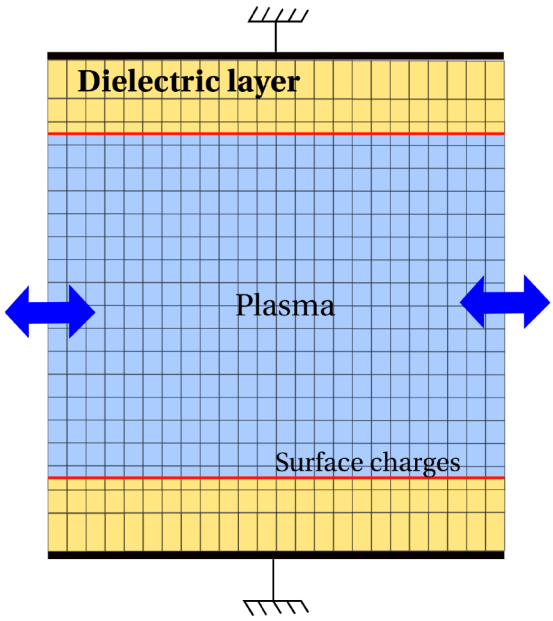

FIGURE 2.5 – Schematic representation of the dielectric layers between the plasma in the 2D radial-azimuthal plane. Are present the dielectric in yellow, the plasma in blue, the surface charges in red, and the grounded magnetic circuit in black.

A common approach is to assume that the electric field inside the dielectric is zero [44]. Therefore, the dielectric layer does not need to be included in the simulation domain. Using Gauss theorem, we obtain a Neumann boundary condition at the plasma-wall interface for the potential

$$|\partial_r \phi| = \frac{|\sigma|}{\epsilon_0} \tag{2.13}$$

with σ the surface charge and ϵ_0 the vacuum permittivity. However, the electric field in a dielectric material is not zero but depends on the global system and the material permittivity. Hence, in order to model the dielectric wall of the HET correctly, we choose to include the whole dielectric layers inside of the simulation domain.

In this section, we derive the discretization of the Poisson equation with a non-uniform permittivity in the 2D radial azimuthal plane using the finite volume approach.

2.4.1 Non-uniform mesh

In the dielectric layers, there is no particle nor charge. Hence, the numerical constraints on the cell size are not applicable, and the cell size can be increased. In order to reduce the cell size difference between two neighboring cells, we use an exponential growth of the cell size in the radial direction. The cell size in the azimuthal direction Δy is kept constant. The resulting non-uniform mesh can be seen in Fig. 2.5.

2.4.2 Poisson equation discretization

The dielectric permittivity is $\epsilon = \epsilon_R \epsilon_0$ with ϵ_R the relative permittivity of the dielectric. The Poisson equation with a not-constant permittivity is

$$-\nabla \cdot \epsilon \nabla \phi = \rho \tag{2.14}$$

with ρ the charge density. We note $\mathbf{D} = \epsilon \mathbf{E} = \epsilon \nabla \phi$ the electric flux. Figure 2.6 shows the Cartesian decomposition of the 2D domain. The cell (i, j) has four direct neighbors:

— the east E in $(i+1, j)$
— the west W in $(i-1, j)$
— the north N in $(i, j+1)$
— the south S in $(i, j-1)$

The cell dimensions are $\Delta x_{i,j}$ and $\Delta y_{i,j}$, and $\Omega_{i,j} = \Delta x_{i,j} \Delta y_{i,j}$ is the cell volume. As the mesh is Cartesian, we have for a given j $\Delta x_{i,j} = cst$ for all i. Hence, we note $\Delta x_{i,j} = d_i$ and $\Delta y_{i,j} = d_j$

The boundaries are noted $S^s_{i,j}$ with $s = E, W, N$ or S. We can see that $S^W_{i,j} = S^E_{i-1,j}$, and the same goes for the other borders. We note $C_{i,j} = S^E_{i,j} \cup S^W_{i,j} \cup S^N_{i,j} \cup S^S_{i,j}$ the cell surface boundary. The center of the cell is located at (i, j) and the borders are located at $i \pm 1/2$ in the East-West direction and $j \pm 1/2$ in the North-South direction.

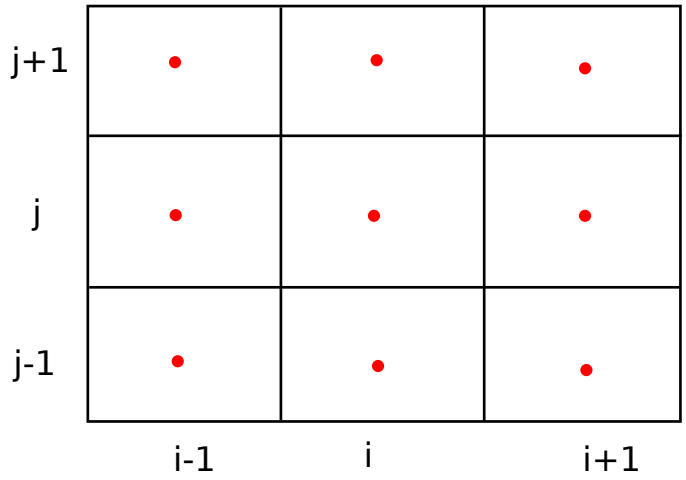

FIGURE 2.6 – Illustration of the Cartesian decomposition of the 2D domain

We start the discretization by positioning the plasma-dielectric interface on the surface between two cells. This means that the permittivity $\epsilon = \epsilon_0 \epsilon_R$ is constant over a cell. In order to discretize the Poisson equation, we integrate Eq. (2.14) over the cell volume

$$\int_{\Omega_{i,j}} -\nabla \cdot (\epsilon \nabla \phi) dv = \int_{\Omega_{i,j}} \rho dv. \tag{2.15}$$

Using Gauss (also known as Green-Ostrogradsky) theorem, we obtain

$$\oint_{C_{i,j}} (-\epsilon \nabla \phi) \cdot \mathbf{n} dS = Q_{tot} = \Omega_{i,j} \bar{\rho}, \tag{2.16}$$

with $\mathbf{n}$ the normal vector directed outward, Q_{tot} is the total charge of the cell and $\bar{\rho}$ is the mean value of ρ in the cell. We can decompose the integration over the cell boundary with the four surfaces $S^s_{i,j}$ as

$$\oint_{C_{i,j}} (-\epsilon \nabla \phi) \cdot \mathbf{n} dS = \sum_{k\in(E,W,N,S)} S^k_{i,j} \mathbf{D}^k_{i,j} \cdot \mathbf{n} \tag{2.17}$$

with $\mathbf{D}^k_{i,j}$ the flux through the surface k of the cell (i,j).

Electric flux

Let us define the electric flux through the East border $\mathbf{D}^E_{i,j}$. We assume there is no surface charge on S^E. We can hence write the electric flux as

$$\mathbf{D}^E_{i,j} \cdot \mathbf{n} = \epsilon_{i,j} E^-_{x,i+1/2,j} \tag{2.18}$$

$$= -\epsilon_{i,j} \frac{\phi_{i+1/2,j} - \phi_{i,j}}{d_i/2}, \tag{2.19}$$

with $E^-_{x,i+1/2,j}$ the electric field at the left of the border (respectively $E^+_{x,i+1/2,j}$ the electric field on the right of the border. In Eq. (2.19), we used an off-center discretization of the electric field $E^-_{x,i+1/2,j}$. Using Gauss law, we have the jump relation between the electric fields on the left on the right of the border

$$\epsilon_{i,j} E^-_{x,i+1/2,j} - \epsilon_{i+1,j} E^+_{x,i+1/2,j} = 0, \tag{2.20}$$

we have

$$\epsilon_{i,j} \frac{\phi_{i+1/2,j} - \phi_{i,j}}{d_i/2} = \epsilon_{i+1,j} \frac{\phi_{i+1,j} - \phi_{i+1/2,j}}{d_{i+1}/2}. \tag{2.21}$$

Hence

$$\phi_{i+1/2,j} = \frac{\epsilon_{i,j} d_{i+1} \phi_{i,j} + \epsilon_{i+1,j} d_i \phi_{i+1,j}}{\epsilon_{i,j} d_{i+1} + \epsilon_{i+1,j} d_i}, \tag{2.22}$$

which corresponds to the usual discretization [5] when ϵ and d_i are both constant. Using Eq. (2.22) in Eq. (2.18) we obtain

$$\mathbf{D}^E_{i,j} \cdot \mathbf{n} = \quad 2\frac{\epsilon_{i,j}\epsilon_{i+1,j}}{\epsilon_{i,j} d_{i+1} + \epsilon_{i+1,j} d_i}(\phi_{i,j} - \phi_{i+1,j}) = \quad 2\epsilon_0 \frac{\epsilon_{Ri,j}\epsilon_{Ri+1,j}}{\epsilon_{Ri,j} d_{i+1} + \epsilon_{Ri+1,j} d_i}(\phi_{i,j} - \phi_{i+1,j}) \tag{2.23}$$

We note $Q^E_{i,j} \equiv 2\frac{\epsilon_{i,j}\epsilon_{i+1,j}}{\epsilon_{i,j} d_{i+1} + \epsilon_{i+1,j} d_i}$. Reproducing the same decomposition on the other borders, we obtain

$$S^E_{i,j} Q^E_{i,j} \phi_{i+1,j} + S^W_{i,j} Q^W_{i,j} \phi_{i-1,j} + S^N_{i,j} Q^N_{i,j} \phi_{i,j+1} + S^S_{i,j} Q^S_{i,j} \phi_{i,j-1} - Q^C_{i,j} \phi_{i,j} = -\Omega_{i,j} \bar{\rho_{i,j}} \tag{2.24}$$

with

$$\begin{cases} Q^E_{i,j} & = 2\dfrac{\epsilon_{i,j}\epsilon_{i+1,j}}{\epsilon_{i,j} d_{i+1} + \epsilon_{i+1,j} d_i} \\ Q^W_{i,j} & = Q^E_{i-1,j} \\ Q^N_{i,j} & = 2\dfrac{\epsilon_{i,j}\epsilon_{i,j+1}}{\epsilon_{i,j} d_{j+1} + \epsilon_{i,j+1} d_j} \\ Q^S_{i,j} & = Q^N_{i-1,j} \\ Q^C_{i,j} & = Q^E_{i,j} S^E_{i,j} + Q^W_{i,j} S^W_{i,j} + Q^N_{i,j} S^N_{i,j} + Q^S_{i,j} S^S_{i,j} \end{cases}$$

as well as $S^E_{i,j} = S^W_{i,j} = d_i d_z$, $S^N_{i,j} = S^S_{i,j} = d_j d_z$ et $\Omega_{i,j} = d_j d_i d_z$. We observe that the evolution of the relative permittivity and the cell size affects the coefficients to be used, but the system remains symmetric as we have $Q^S_{i,j} = Q^N_{i-1,j}$ and $Q^W_{i,j} = Q^E_{i-1,j}$.

A symmetric system is a linear system of equation $A \cdot X = B$ which matrix A is equal to its transpose: $A = A^T$. It allows reducing by a factor of two the memory needed to store the matrix. It also allows to use algorithms exploiting this property. For instance, the eigenvalues are real-valued, and the matrix factorization only need to store one factor using Cholesky decomposition, which gives $A = LL^T$ with L a lower-triangular matrix.

2.4.3 Including surfaces charges

Let us now consider the presence of surface charges on the surface $S^E_{i,j}$. Gauss's law now reads

$$-\epsilon_{i,j}E^-_{x,i+1/2,j} + \epsilon_{i+1,j}E^+_{x,i+1/2,j} = \sigma^E, \tag{2.25}$$

with σ^E the surface charge on the surface. The surface charge is not taken into account when computing the total charge in a cell. Using the same discretization as before, we obtain

$$\epsilon_{i,j}\frac{\phi_{i+1/2,j} - \phi_{i,j}}{d_i/2} - \epsilon_{i+1,j}\frac{\phi_{i+1,j} - \phi_{i+1/2,j}}{d_{i+1}/2} = \sigma^E \tag{2.26}$$

so that

$$\phi_{i+1/2,j} = \frac{\epsilon_{i,j}d_{i+1}\phi_{i,j} + \epsilon_{i+1,j}d_i\phi_{i+1,j}}{\epsilon_{i,j}d_{i+1} + \epsilon_{i+1,j}d_i} + \frac{1}{2}\sigma^E\frac{d_i d_{i+1}}{\epsilon_{i,j}d_{i+1} + \epsilon_{i+1,j}d_i} \tag{2.27}$$

hence

$$\mathbf{D}^E_{i,j} \cdot \mathbf{n} = 2\frac{\epsilon_{i,j}\epsilon_{i+1,j}}{\epsilon_{i,j}d_{i+1} + \epsilon_{i+1,j}d_i}(\phi_{i,j} - \phi_{i+1,j}) - \sigma^E\frac{\epsilon_{i,j}d_{i+1}}{\epsilon_{i,j}d_{i+1} + \epsilon_{i+1,j}d_i}$$

We obtain the same relation as Eq. (2.23) updated by $-\sigma^E\frac{\epsilon_{i,j}d_{i+1}}{\epsilon_{i,j}d_{i+1}+\epsilon_{i+1,j}d_i}$

Hence, we finally obtain

$$S^E_{i,j}Q^E_{i,j}\phi_{i+1,j}+S^W_{i,j}Q^W_{i,j}\phi_{i-1,j}+S^N_{i,j}Q^N_{i,j}\phi_{i,j+1}+S^S_{i,j}Q^S_{i,j}\phi_{i,j-1}-Q^C_{i,j}\phi_{i,j} = -\Omega_{i,j}\rho^-_{i,j}+Q^W_\sigma\sigma^W \tag{2.28}$$

with $Q^W_\sigma = S^W_{i,j}\frac{\epsilon_{i,j}d_{i-1}}{\epsilon_{i,j}d_{i-1}+\epsilon_{i-1,j}d_i}$.

2.4.4 Verification of the Poisson solver

We verify the discretization by modeling a 1D capacitor. The length of system is $L = 1\,\text{m}$. The relative permittivity of the dielectric inside the capacitor (from $x = 0.475$ to $0.525\,\text{m}$) is set to $\epsilon_R = 8$, and a surface charge of $\sigma = 8\ \text{nC.cm}^{-2}$ is imposed on one side, and $-8\ \text{nC.cm}^{-2}$ on the other side. The expected electric field in the capacitor using the infinite plane approximation is $E = \sigma/(\epsilon_0\epsilon_R) = 1.15\ \text{kV.mm}^{-1}$.

Figure 2.7 shows the electric field computed using the obtained decomposition We see that we obtain the expected jump for the electric field due to the surface charge ($\Delta E = 1.15\ \text{kV/m}$). The difference with the theoretical value is due to the Dirichlet conditions $\phi = 0$ used in $x = 0$ and $x = 1\,\text{m}$.

2.4.5 Interface at the cell center

In the previous section, we supposed that the plasma-dielectric boundary was at the interface between the cells. However, this means that the electric field close to the interface is unknown, as it is defined at the cell center. Moreover, the Dirichlet condition for the potential is better defined at the cell center, and for the sake of simplicity, changing the boundary conditions should not change the particle domain. Hence, we chose to position the plasma-wall interface at the center of the cell as shown in Figs. 2.5 and 2.8. This means that the permittivity is not constant over a cell.

Because the wall boundaries are only in the radial direction, we consider only an interface in the North-South direction. Figure 2.8 shows the domain decomposition. The decomposition is the same as previously, except for the permittivity that can have two different values: one in the North half-plane $\epsilon^n_{R,i,j}$ and another in the South half plane $\epsilon^s_{R,i,j}$.

The discretization of the Poisson (Equation (2.17)) follows the same path as previously, except that the electric flux in not constant anymore so that Eq. (2.17) becomes

$$\oint_{C_{i,j}}(-\epsilon\,\nabla\,\phi) \cdot \mathbf{n}dS = \sum_{k\in(E,W,N,S)} S^k_{i,j} < \mathbf{D}^k_{i,j} \cdot \mathbf{n} > . \tag{2.29}$$

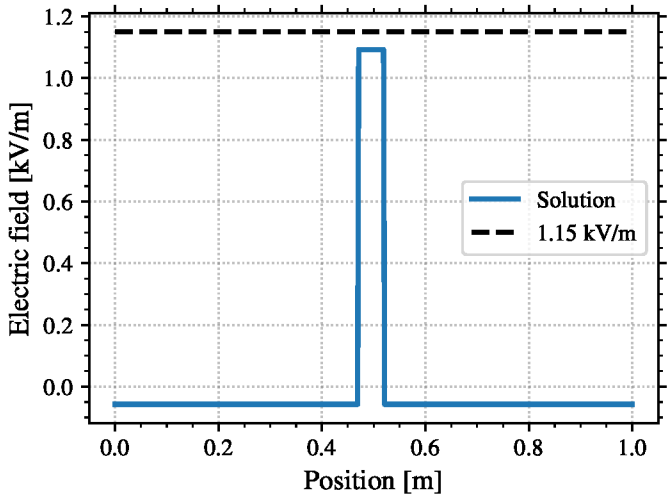

FIGURE 2.7 – Electric field of the capacitor configuration calculated by the Poisson solver in order to validate the discretization and the solver developed.

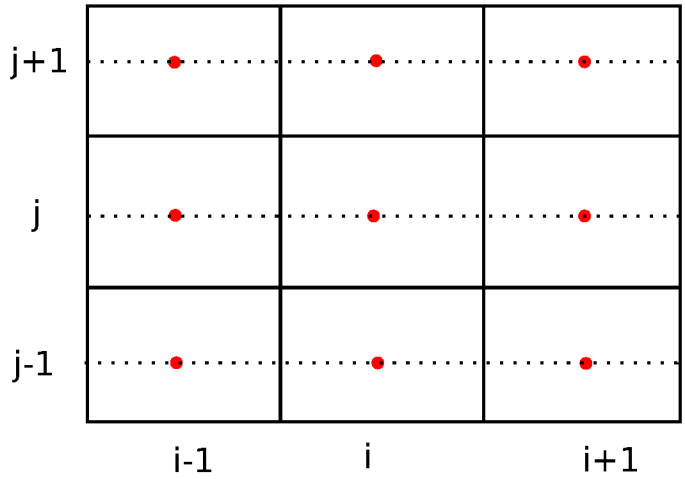

FIGURE 2.8 – Cartesian decomposition of the 2D domain. The dash lines represent discontinuities in the permittivity value.

We can define

$$< \mathbf{D}^E_{i,j} \cdot \mathbf{n} > = \frac{1}{2}\epsilon^N_{i,j} E^-_{x,i+1/2,j} + \frac{1}{2}\epsilon^S_{i,j} E^-_{x,i+1/2,j} \tag{2.30}$$

$$= \frac{-1}{2}(\epsilon^N_{i,j} + \epsilon^S_{i,j}) \frac{\phi_{i+1/2,j} - \phi_{i,j}}{d_i/2} \tag{2.31}$$

so that in the East-West direction, the flux behaves as if the cell permittivity is the average of the North and South half-planes

$$\epsilon_{i,j} = \frac{1}{2}(\epsilon^N_{i,j} + \epsilon^S_{i,j}).$$

Hence, the rest of the computation is similar. For the North and South boundaries, the permittivity is constant, hence there is no modification. Consequently, we obtain the discretization

$$S^E_{i,j} Q^E_{i,j} \phi_{i+1,j} + S^W_{i,j} Q^W_{i,j} \phi_{i-1,j} + S^N_{i,j} Q^N_{i,j} \phi_{i,j+1} + S^S_{i,j} Q^S_{i,j} \phi_{i,j-1} - Q^C_{i,j} \phi_{i,j} = -\Omega_{i,j} \bar{\rho_{i,j}} \tag{2.32}$$

with

$$\begin{cases} Q^E_{i,j} &= 2\dfrac{\epsilon_{i,j}\epsilon_{i+1,j}}{\epsilon_{i,j}d_{i+1}+\epsilon_{i+1,j}d_i} \\ Q^W_{i,j} &= Q^E_{i-1,j} \\ Q^N_{i,j} &= 2\dfrac{\epsilon^N_{i,j}\epsilon^S_{i,j+1}}{\epsilon^N_{i,j}d_{j+1}+\epsilon^S_{i,j+1}d_j} \\ Q^S_{i,j} &= 2\dfrac{\epsilon^S_{i,j}\epsilon^N_{i,j-1}}{\epsilon^S_{i,j}d_{j+1}+\epsilon^N_{i,j-1}d_j} \\ Q^C_{i,j} &= Q^E_{i,j}S^E_{i,j}+Q^W_{i,j}S^W_{i,j}+Q^N_{i,j}S^N_{i,j}+Q^S_{i,j}S^S_{i,j} \end{cases}$$

As well as $S^E_{i,j} = S^W_{i,j} = d_i d_z, S^N_{i,j} = S^S_{i,j} = d_j d_z$ et $\Omega_{i,j} = d_j d_i d_z$. Here, the system is no more symmetric. However, we can assume that the only permittivity jump happens at the cell center, so that $\epsilon^S_{i,j} = \epsilon^N_{i,j-1}$. Hence, $Q^N_{i,j} = 2\frac{\epsilon^N_{i,j}}{d_{j+1}+d_j}$ and the system is symmetric.

2.4.6 Surface charges for centered interface

In the case of centered plasma-wall interface, we have surface charges at the center of the cell. Hence

$$\int_{\Omega_{i,j}} \rho dv = \Omega_{i,j}\bar{\rho} + S^N_{i,j}\sigma_{i,j}. \tag{2.33}$$

The surface charges behave like volume charges. Hence, we obtain

$$S^E_{i,j}Q^E_{i,j}\phi_{i+1,j}+S^W_{i,j}Q^W_{i,j}\phi_{i-1,j}+S^N_{i,j}Q^N_{i,j}\phi_{i,j+1}+S^S_{i,j}Q^S_{i,j}\phi_{i,j-1}-Q^C_{i,j}\phi_{i,j} = -\Omega_{i,j}\bar{\rho_{i,j}}-S^N_{i,j}\sigma_{i,j} \tag{2.34}$$

The discretization obtained for the cell-centered plasma-wall interface is very similar to the one obtained for the interface at the cell interface. However, it conserves the particle domain when the dielectric layer is not modeled, and that Dirichlet conditions are applied, and the electric field at the plasma-wall interface is better defined. Hence, the cell-centered interface will be used.

This decomposition has been validated with the same test than presented in Section 2.4.4. We observed no difference between the two decompositions in term of precision.

2.4.7 Electric field computation

The resolution of the Poisson equation returns the value of the plasma potential ϕ at the cell center. The electric field is computed by taking the first derivative of the potential at the cell interface, as in Eq. (2.18),

$$E^-_{x,i+1/2,j} = -\epsilon_{i,j}\frac{\phi_{i+1/2,j}-\phi_{i,j}}{d_i/2}, \tag{2.35}$$

with $\phi_{i+1/2,j}$ defined with Eq. (2.22). However, in order to have consistent data, the electric field is also computed at the cell center by interpolation

$$E_{x,i,j} = \frac{1}{2}\left(E_{x,i-1/2,j}+E_{x,i+1/2,j}\right) = -\epsilon_{i,j}\frac{\phi_{i+1/2,j}-\phi_{i-i/2,j}}{d_i}. \tag{2.36}$$

In the cells along to the plasma-wall interface, the effect of the surface charge must be taken into account, as previously described.

2.5 Axial convection of the particles

As introduced in the previous section, the 2D radial-azimuthal simulation does not model the axial convection of the particles. This results in an ever increasing particle energy [4, 38]. We present in this section an algorithm to model the convection of the particle. Its drawbacks are discussed, and we propose a way to reduce them.

2.5.1 Lafleur's model of convection

Lafleur et al. [4] proposed a way to model the axial convection of the particles in 1D purely azimuthal simulation. Figure 2.9 shows a schematic illustration of the model. The principle is as follows

- We set a finite axial length, noted L_z in Fig. 2.9.
- We follow the positions of the particle in the axial direction z
- When a particle crosses the boundary, it is removed.
- A new particle is created
  - at $z = 0$ for the ions
  - at $z = L_z$ for the electrons

We create a new particle in order to conserve the charge in the simulation. The new particle has a random velocity following a Maxwellian flux distribution function of a given temperature. The azimuthal position of the particle is chosen uniformly at random.

The Maxwellian flux distribution is the velocity distribution of the particles crossing a surface if the particles follow a Maxwellian distribution function. Thus we have

$$f_{\text{flux}}(\mathbf{v}) = \mathbf{v} \cdot \mathbf{n} f_{\text{M}}(\mathbf{v}), \tag{2.37}$$

with f_{M} the Maxwellian distribution function defined in Eq. (1.11) and $\mathbf{n}$ the vector normal to the surface.

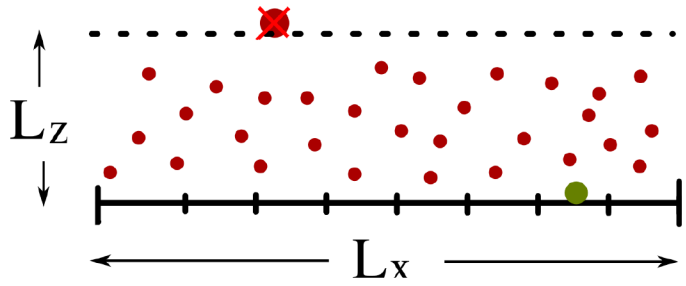

FIGURE 2.9 – Schematic representation of Lafleur's convection model [4]. The red particle is removed of the simulation, and the green particle is created. In this illustration, the particle is an ion, and the reinjection is at $z = 0$. The x direction corresponds to the azimuthal direction.

Lafleur's model of convection has been adopted in 2D by Croes et al. [18]. The principle is exactly similar. The particles are followed in the three directions, and a finite length is used to close the axial direction. It is important to note that even if the particles are followed in the three directions, the meshed domain is only 2D. The simulation is not 3D-3 dimension for the velocity (3V), but only 2D-3V.

In Croes et al. [18], the authors have observed that if the newly created particle has a radial position chosen uniformly at random, it will affect the sheath. Hence, they decided to use the same radial position as the removed particle. Figure 2.10 presents a schematic representation of the convection model in 2D.

Figure 2.11 shows the evolution as a function of time of the electron mean energy in a typical 2D radial-azimuthal simulation, adapted from Croes [5]. We can see that without the convection, the mean energy quickly rises to unphysical values. When the convection is modeled, using an axial length of $L_z = 1$ cm, the energy reaches a steady-state.

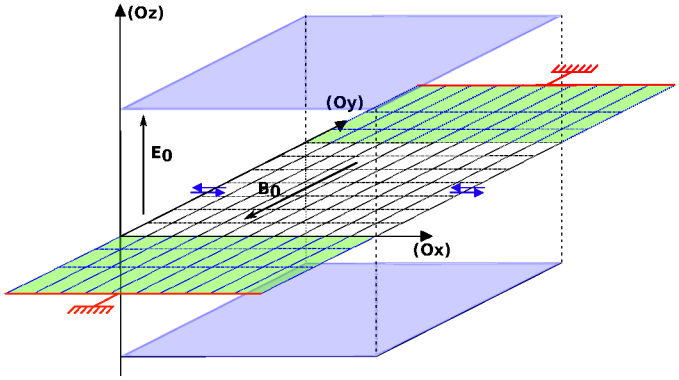

FIGURE 2.10 – Schematic representation of the Lafleur's convection model adapted in 2D. The new particle radial position corresponds to the removed particle, but its azimuthal position is chosen uniformly at random.

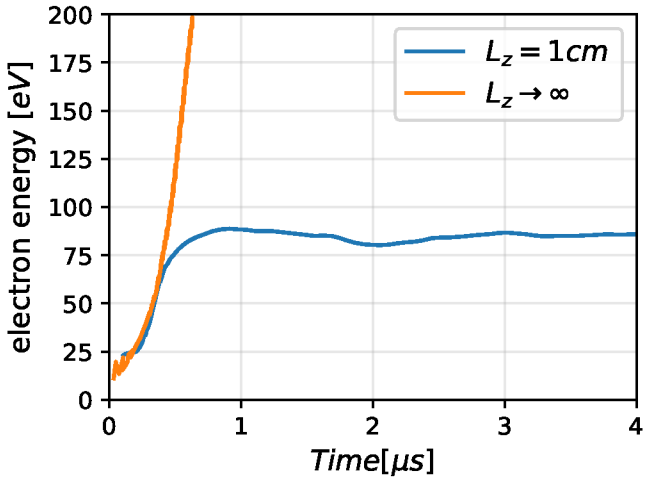

FIGURE 2.11 – Time evolution of the electron mean energy when the convection is not modeled ($L_z \to \infty$) and with Lafleur's convection model used, $L_z = 1$ cm. Adapted from Croes [5].

2.5.2 Numerical artifacts

Lafleur et al. [4] studied the impact of the convection model on the simulation results. The authors observed in particular that changing the azimuthal length of the simulation domain could affect the simulation results.

Figure 2.12 shows the time evolution of the azimuthal electric field E_θ from the 1D simulation [4].

On the first row (Fig. 2.12.**a** and **b**), the length of the periodic azimuthal direction is $L_\theta = 0.5$ cm. Fig. 2.12.**a** corresponds to the case without axial convection. We see that the ECDI rises and does not saturate. The wavelength is short, of the order of $\lambda = 1.5$ mm. Fig. 2.12.**b** corresponds to the same case as Fig. 2.12.**a** but this time with the axial convection modeled. We observe this time a saturation of the oscillation's amplitude, and the wavelength is close to $\lambda \simeq 1.5$ mm.

On the second row (Fig. 2.12.**c** and **d**), the length of the periodic azimuthal direction is $L_\theta = 1$ cm. Fig. 2.12.**c** corresponds to the case without axial convection, and Fig. 2.12.**d** corresponds to the same case but with the axial convection modeled. In Fig. 2.12.**c**, we can see that increasing the azimuthal length compared to Fig. 2.12.**a** did not affect the ECDI, as expected. However, in Fig. 2.12.**d**, the instability is clearly affected. A single oscillation is observed, corresponding to $\lambda = 10$ mm, which seems almost undoubtedly unphysical.

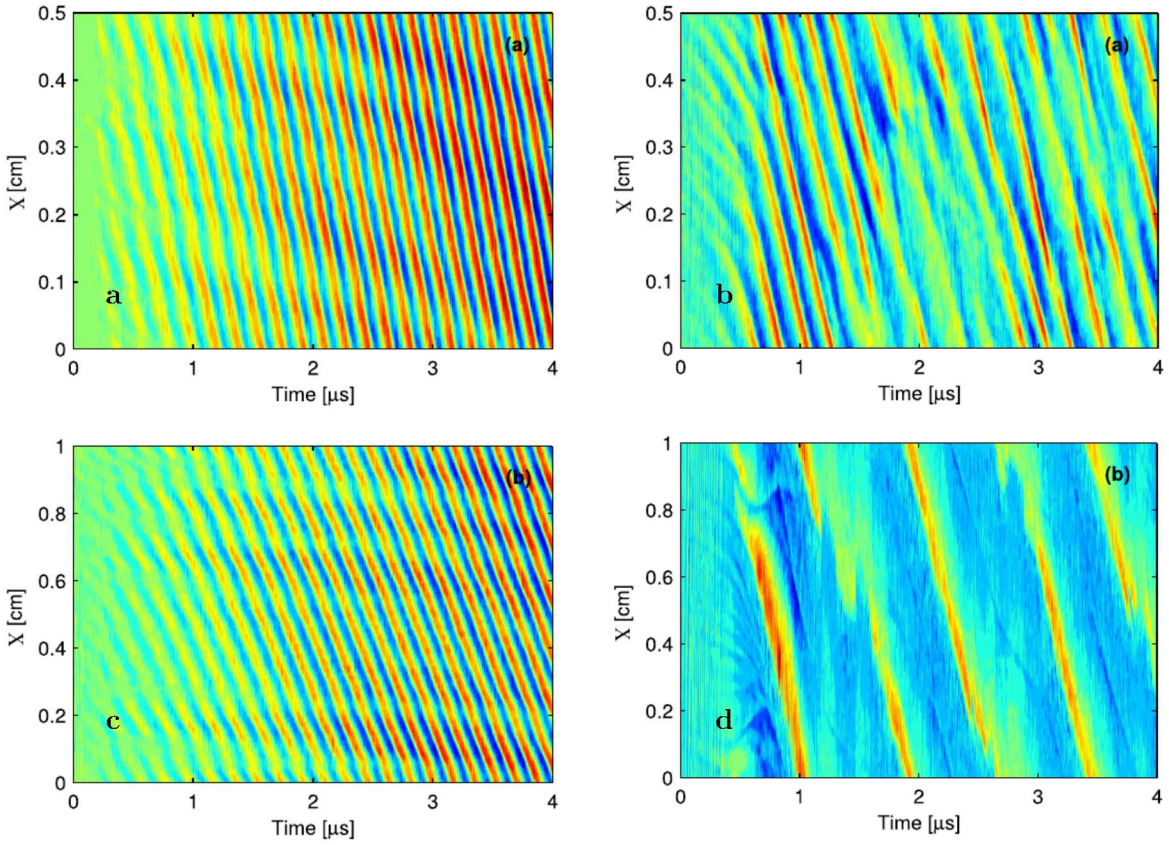

FIGURE 2.12 – Effects of Lafleur's convection model for two different azimuthal lengths on the azimuthal electric field. (**a**) No convection, $L_x = 0.5$ cm, (**b**) convection modeled, $L_x = 0.5$ cm, (**c**) No convection, $L_x = 1$ cm, (**d**) convection modeled, $L_x = 1$ cm. The color of each plot is normalized to the maximum amplitude. Adapted from [4].

Croes [5] observed similar behavior with the bidimensional simulation. The author investigated the values of the azimuthal length, which presented physical and unphysical results for different values of the axial length. Figure 2.13 shows the results obtained (adapted from [5]). We can see that for a given value of the axial length, the azimuthal length must be less than a specific value to present physical results. However, the value of this upper limit depends on the axial length, such that if the axial length decreases, the upper limit of the azimuthal length decreases as well. The dotted gray line is a rough representation of the limit between the physical and unphysical results.

In the next section, we develop a theory that could explain the observation, and a new convection model for the simulation is proposed.

2.5.3 Numerical noise of Lafleur's convection model

Let us consider Lafleur's convection model in 1D on the charge density. When computing the charge density on the mesh vertices, the axial position is not taken into account. Consequently, the convection process illustrated in Fig. 2.9 is similar to moving a particle arbitrarily (read randomly). Seen by the charge density, this is similar to Poisson noise, also named shot noise, on the charge density. [2]

After a certain number of particles removed and created, the Poisson noise is similar to a Gaussian noise, also named thermal noise, following a normal distribution $\mathcal{N}$. Hence, the charge

2. In fact, this noise is the combination of Poisson noise with a uniform noise as we use a cloud in cell method. In addition it is happening twice for every particle convection, once with a positive charge and once with a negative charge. But the result is not affected by this simplification due to the central limit theorem.

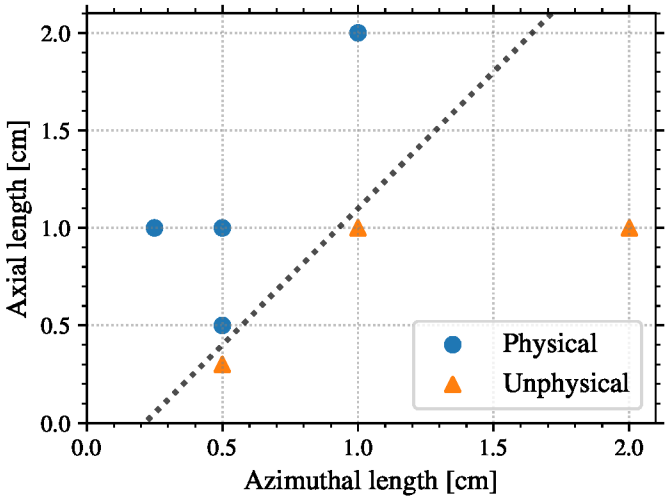

FIGURE 2.13 – For 2D PIC simulations: values of the azimuthal length and the axial length for which the simulation result is physical (similar to Fig. 2.12.**b**) or unphysical (similar to Fig. 2.12.**d**). The dotted gray line is an approximation of the limit between the domains.

density becomes [3]

$$\rho = \rho_0 + \mathcal{N}(0, \sigma_{\text{Reinj}}), \tag{2.38}$$

with ρ the charge density, ρ_0 the charge density without the convection process, and σ_{Reinj} the standard deviation of the distribution of the noise associated with the convection model. Surprisingly, the noise due to the convection model is similar to the numerical noise induced by the decomposition of the plasma into particles $\mathcal{N}(0, \sigma_{\text{stat}})$. However, the amplitude of this statistical noise decreases with the number of particles per cell used

$$\sigma_{\text{stat}} \propto \frac{1}{\sqrt{N_{pc}}}.$$

On the other hand, the amplitude of the noise induced by the convection model depends on the plasma density n, the axis velocity of the particles v_z and the axial length L_z

$$\sigma_{\text{Reinj}} \propto \frac{n}{L_z} v_z. \tag{2.39}$$

We can see in Eq. (2.39) that the amplitude of the convection induced noise on the charge density is proportional to the inverse of the axial length L_z. This could explain the observation of Fig. 2.13 when using a smaller L_z. However, it does not explain the effects of the azimuthal length observed in Figs. 2.12 and 2.13.

2.5.4 Effect of the noise on the electric field

In order to explain the impact of the azimuthal length on the instability, we can study the azimuthal electric field E_θ resulting of the charge density ρ. As the Poisson equation is linear, we have

$$E_\theta(\theta) = C + \frac{1}{\epsilon_0} \int_0^\theta \rho(s) ds \tag{2.40}$$

$$= C + \frac{1}{\epsilon_0} \int_0^\theta (\rho_0(s) + \mathcal{N}(0, \sigma_{\text{Reinj}})) ds \tag{2.41}$$

$$= C + E_{\theta,0} + E_{\theta,1} \tag{2.42}$$

3. One can note that the mean noise is strictly zero (with probability 1), as the charge density is conserved.

with C a constant that ensures that the periodical Boundary Conditions (BC) are respected. The part of the electric field $E_{\theta,0}$ corresponds to the unperturbed charge density ρ_0 and $E_{\theta,1}$ corresponds to the noisy charge density $\mathcal{N}(0, \sigma_{\text{stat}})$. Hence, let us focus now on $E_{\theta,1}$. We can study $E_{\theta,1}$ using two equivalent means: the Fourier Transform (FT) and the Brownian bridge.

Fourier Transform

Applying the FT on the equation

$$E_{\theta,1} = \frac{1}{\epsilon_0} \int_0^{\theta} \mathcal{N}(0, \sigma_{\text{Reinj}}) ds \tag{2.43}$$

gives

$$\mathcal{FFT}\left(E_{\theta,1}\right)(k) = \frac{1}{\epsilon_0} \mathcal{FFT}\left(\int_0^{\theta} \mathcal{N}(0, \sigma_{\text{Reinj}}) ds\right) \tag{2.44}$$

$$= \frac{1}{\epsilon_0} \frac{\mathcal{N}(\mu_{\text{FT}}, \sigma_{\text{FT}})}{k} \tag{2.45}$$

Equation (2.45) shows that $E_{\theta,1}$ also follows a Gaussian distribution, but with a non-zero mean value. It is also inversely proportional to the wave number k. Hence, when we increase the azimuthal length, which means that small wave numbers can exist in the simulation domain, the amplitude of $E_{\theta,1}$ increases as well.

Brownian Bridge

Equation (2.43), combined with the BC, is the definition of the a Brownian bridge.

A Brownian bridge is a particular Brownian motion that reaches at a given distance the same value as the initial value. Hence, we have [76]

$$\mathbb{E}(E_{\theta,1}) = 0,$$
$$\text{var}(E_{\theta,1}) = \sigma^2_{\text{Reinj}} \frac{L^2_{\theta}}{4}$$

Hence, the increase of the azimuthal length increases the amplitude of $E_{\theta,1}$.

We believe that when the amplitude of $E_{\theta,1}$ is too large, it can trigger an unphysical oscillation. The next section uses this conclusion in order to adapt the convection model.

2.5.5 Noiseless convection model

In the previous section, we have shown that the convection model induces a noise in the charge density, that produces an azimuthal electric field which amplitude depends on the azimuthal length.

We propose here a modified version of Lafleur's convection model in order to remove the noise in the charge density. The noiseless convection model follows the same algorithm as before, but the azimuthal position of the particle created is not chosen uniformly as random, but instead the new particle has the same position as the removed particle. Figure 2.14 shows a schematic illustration of the noiseless convection algorithm applied on a particle.

We have implemented this modified convection model in the 2D radial and azimuthal simulation. Figure 2.15 shows the time evolution of the azimuthal electric field at the center of the radial dimension with and without the noiseless convection model. It presents the same conditions as in Fig. 2.12.**a** and **b**. As previously, the convection stabilizes the growth of the instability to a steady-state, but it does not affect the physics.

Figure 2.16 shows the time evolution of the azimuthal electric field at the center of the radial dimension with the convection modeled using Lafleur's model and the noiseless model with a small azimuthal length. We can see that the two models give almost exactly the same results.

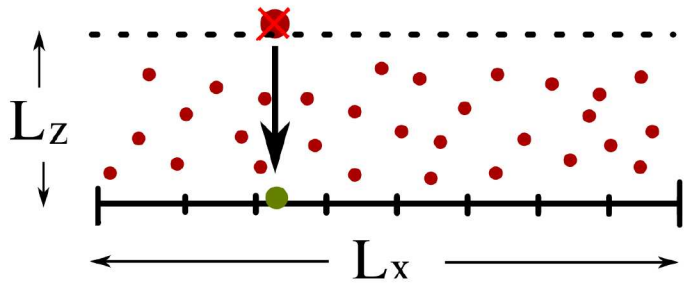

FIGURE 2.14 – Illustration of the noiseless convection model

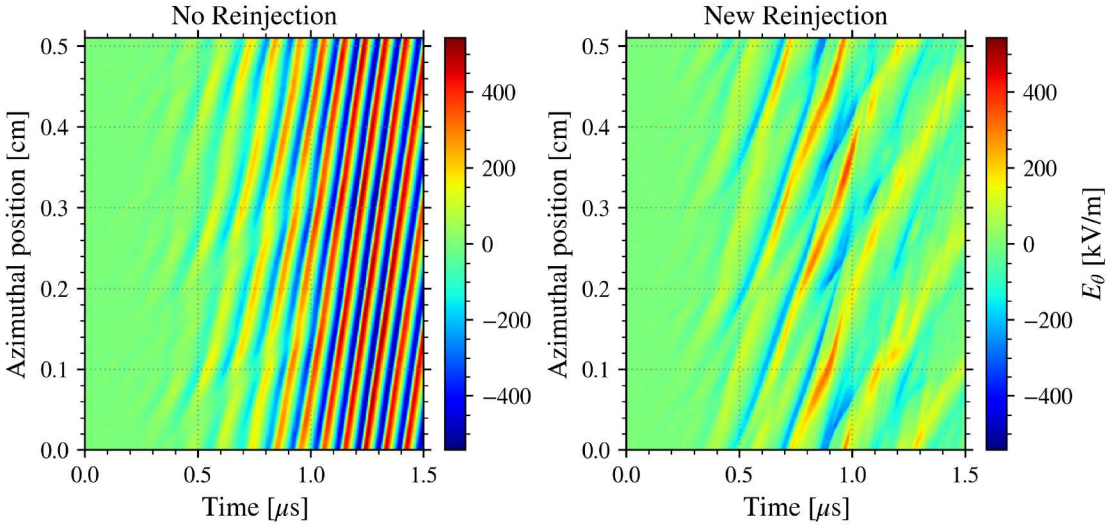

FIGURE 2.15 – Time evolution of the azimuthal electric field at the center of the radial dimension with and without the noiseless convection model.

Figure 2.17 shows the time evolution of the azimuthal electric field at the center of the radial dimension with the convection modeled using Lafleur's model and the noiseless model but using a longer azimuthal length than Fig. 2.16. In this case, we can see that Lafleur's convection model induces oscillations that are not observed with the noiseless model.

These observations have shown that Lafleur's convection model induces a noise on the charge density, that does not affect the simulation when the domain size is small, but can rise numerical artifacts when the domain size is larger. We have seen that minor modifications on the model do not affect the simulation results on a small domain, and allows us to use a larger simulation domain without any numerical artifact.

2.5.6 Effects on a 2D simulation domain

The mathematical development of Section 2.5.4 has been done in 1D. We can legitimately wonder if the results can be extended directly to a 2D domain. A mathematical definition of $E_{\theta,1}$ in 2D is more difficult, as we have, neglecting the dielectric layers,

$$E_{\theta,1} = -\partial_\theta \phi_1 \text{ such that } \nabla \cdot \nabla \phi_1 = -\frac{\mathcal{N}(0, \sigma_{\text{Reinj}})}{\epsilon_0} \text{ following the BC.} \tag{2.46}$$

The BCs are

— periodic BC in the azimuthal direction,

— Dirichlet BC in the radial direction, modeling grounded walls,

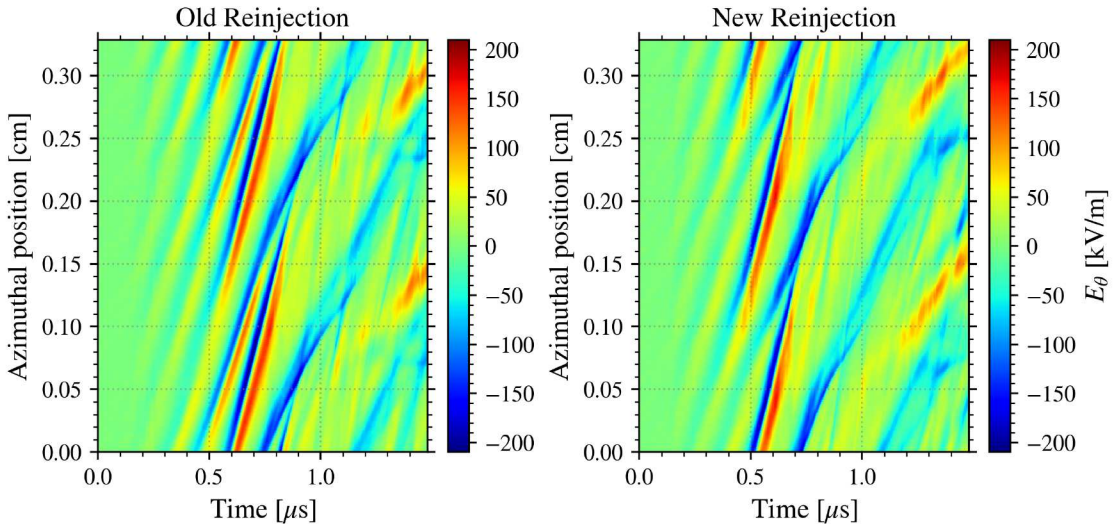

FIGURE 2.16 – Time evolution of the azimuthal electric field at the center of the radial dimension with the convection modeled using (left) Lafleur's model and (right) the noiseless model with a small azimuthal length (0.325cm).

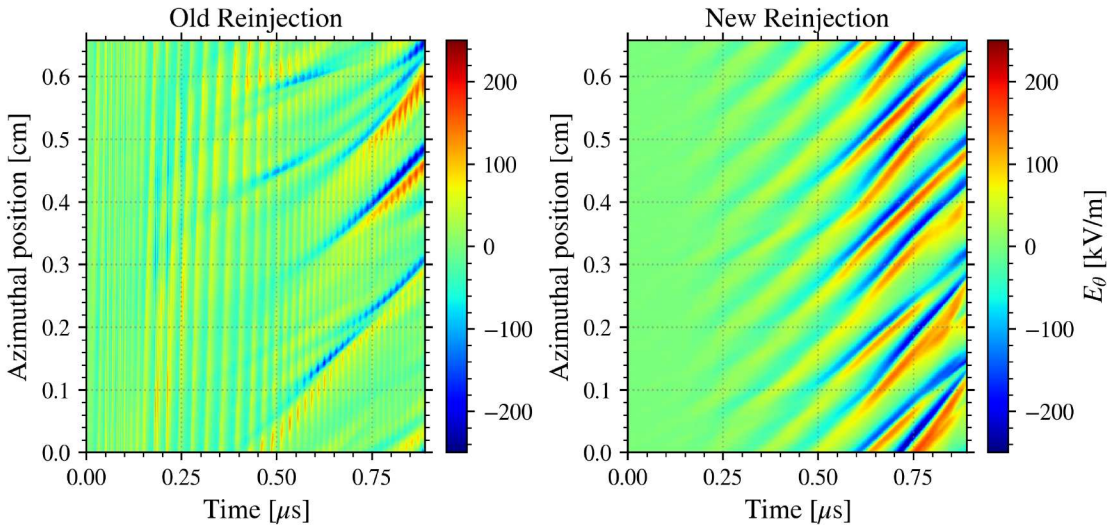

FIGURE 2.17 – Time evolution of the azimuthal electric field at the center of the radial dimension with the convection modeled using (left) Lafleur's model and (right) the noiseless model with a longer azimuthal length (0.65cm).

which translate as

$$\phi = 0 \text{ for } r = 0 \text{ and } r = L_r, \qquad \forall\theta \tag{2.47}$$

$$\phi(\theta = 0) = \phi(\theta = L_\theta), \qquad \forall r \tag{2.48}$$

Solving Eq. (2.46) with the conditions Eqs. (2.47) and (2.48) analytically is much more difficult that the 1D development, because of the Dirichlet BC. However, we can investigate it numerically, by solving Eq. (2.46) for a given random source term. Using a Monte Carlo approach, we average the results 200 times to better observe the mean behavior with respect to the noise (i.e. increasing signal to noise ratio). For each computation, a normalized source term $\rho_1 = \mathcal{N}(0, 1)$ is generated over a 2D domain, then the 2D Poisson equation is solved numerically [4]

4. The SOR algorithm is used in this MC calculation. The iterations are stopped using a relative tolerance of

to obtain ϕ_1, and the azimuthal electric field $E_{\theta,1} = -\partial_\theta \phi_1$ is computed.

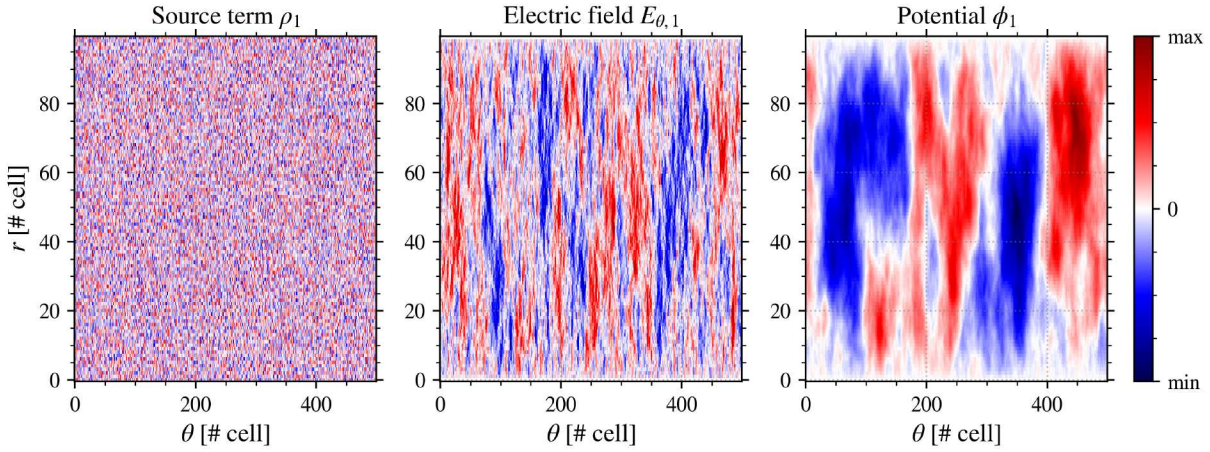

FIGURE 2.18 – Results for one case used in the Monte Carlo calculation with 100 cells in radial direction and 500 cells in the azimuthal direction, with (left) the normalized source term $\rho = \mathcal{N}(0, 1)$, (center) the azimuthal electric field, and (right) the plasma potential.

One typical result is shown in Fig. 2.18. We can see the impact of the radial Dirichlet boundary conditions, Eq. (2.47), on the potential ϕ_1 induced by the noise. The potential mostly oscillates in the azimuthal direction, and its amplitude is larger on the centerline between the walls. A similar behavior is observed for the azimuthal electric field.

Figure 2.19 shows the Discrete Fourier Transform (DFT) of the source term ρ_1, the resulting azimuthal electric field $E_{\theta,1}$ and plasma potential ϕ_1 computed on the centerline of the simulation domain, for three different radial lengths expressed in number of cells in the radial direction N_x. Is also shown the "equivalent" source term ρ_{eq}, which is the source term that would give the frequency spectra of $E_{\theta,1}$ observed in a 1D domain

$$\rho_{\text{eq}} = \epsilon_0 \partial_\theta E_{\theta,1}. \tag{2.49}$$

The results are given for different radial lengths $N_x = 15, 50$ and 200, while the azimuthal length $N_y = 200$ is kept constant. We can see that the plasma potential and the electric field show larger amplitudes for small wave numbers (large wavelength) compared to large wave numbers in the three cases. However, the amplitude of the smallest wave numbers is affected. In the cases of small radial length ($N_x = 15$ and 50), the spectra of the electric field is not monotonic. This can be explained by the Dirichlet BCs that *pins down* the fluctuation of the plasma potential.

To compare the results to the purely azimuthal 1D case, Fig. 2.19 shows the frequency spectra of the equivalent source term ρ_{eq}. We see that ρ_{eq} is always smaller than ρ_1, and is significantly reduced in the small and large wavenumber. However, even though the amplitude is reduced in 2D with small radial direction compared to a 1D model, we still observe large amplitude of small wave number oscillations in both the electric field and the plasma potential. It means that the 2D domain does not change significantly the effect of the numerical noise ρ_1. Hence, the conclusions of Section 2.5.4 derived in 1D can be legitimately used for 2D domains.

2×10^{-6} on the mean square error.

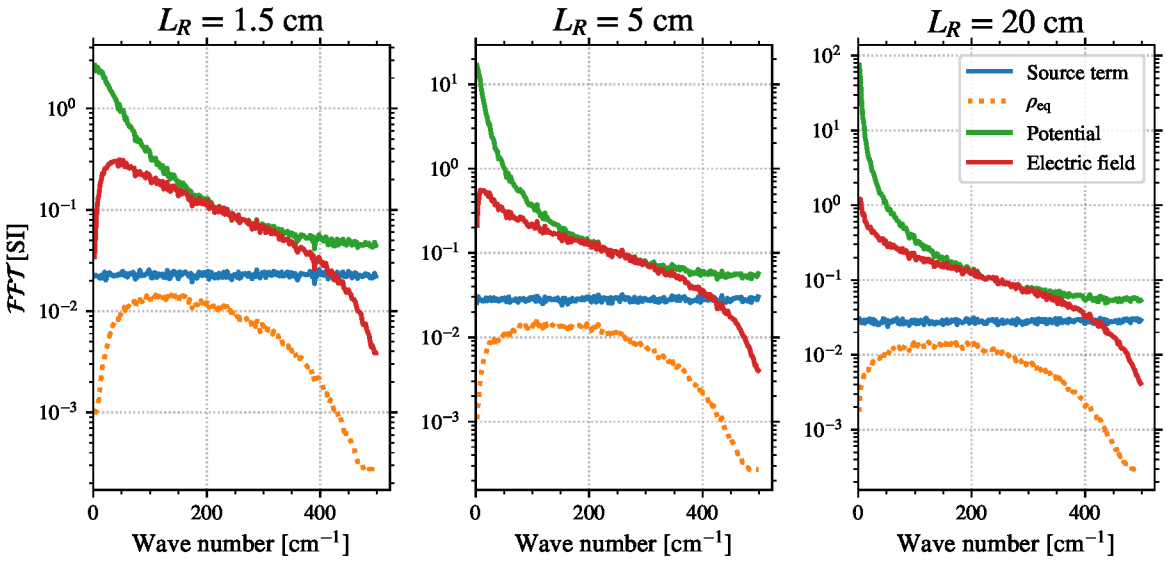

FIGURE 2.19 – DFT of the source term $\rho_1 = \mathcal{N}(0, \sigma_{\text{Reinj}})$, the resulting azimuthal electric field $E_{\theta,1}$ and plasma potential ϕ computed on the centerline of a radial-azimuthal simulation, and the Equivalent 1D source term defined by Eq. (2.49). The azimuthal length is $L_\theta = 50$ cm. The DFT are averaged 200 times

2.6 Electron-induced secondary electron emission

When an incident electron reaches the wall material, several scenarii are possible, as described in Villemant [49]

1. Elastic reflection: the electron encounters only elastic collision with the material, hence its energy is constant. However, its reflection is not necessary specular.
2. Inelastic reflection: the electron looses some of its energy to the material before returning to the plasma.
3. Secondary electron emission: the energy of the primary electron is enough to extract one or more electrons from the material.
4. No emission, the electron is absorbed by the wall.

The probability σ that one event happens instead of another depends predominantly on the particle energy, and weakly on its impact angle. Concerning the mean flux of electron incident and emitted, we use the mean emission rate, or yield, $\bar{\sigma}$

$$\bar{\sigma} = \frac{\Gamma_{e,\text{secondary}}}{\Gamma_{e,\text{primary}}}$$

which can be developed using the distribution function to

$$\bar{\sigma} = \frac{\iiint_\Omega v_x \sigma(\mathbf{v}_e) f(\mathbf{v}_e) d^3v}{\iiint_\Omega v_x f(\mathbf{v}_e) d^3v} \tag{2.50}$$

with Ω the ensemble of $\mathbf{v}_e$ directed towards the wall: $\mathbf{v}_e \cdot \mathbf{n} > 0$, with $\mathbf{n}$ the unit vector normal to and towards the wall.

2.6.1 Models of emission

Several models can be used to describe the electron emission.

Monte Carlo models are the most realistic. They are based on the computation of the trajectory of the electrons through the material, during which the electron can encounter several interactions with the material. Each interaction can modify the electron direction, energy, and generate new electrons. Several models have been proposed, as Furman and Pivi [77], Pierron et al. [78]. These models allow a precise characterization of the processes, but depend on a large number of parameters difficult to obtain due to the lack of experimental data.

Analytical models provide a simplified description of the rate of emission. Their complexity depends on the accuracy desired. The most largely used are the models of Vaughan [79], Barral et al. [6], Sydorenko et al. [80].

In this work, we are interested only in representing qualitatively the electron emission. Moreover, Croes [5] showed that changing the model used does not affect significantly the results. Hence, we will use the model of Barral et al. [6] for its simplicity.

2.6.2 Barral electron emission model

The emission model used follows a linear-saturated law for the probability of emission with three parameters. It describes the total emission corresponding to the sum of the elastic and inelastic backscattering and the secondary electron emission.

$$\sigma(\epsilon) = \begin{cases} \sigma_0 + (1-\sigma_0)\frac{\epsilon}{\epsilon^*} & \text{if } \epsilon < \epsilon_{\max} \\ \sigma_{\max} & \text{if } \epsilon \geq \epsilon_{\max} \end{cases} \tag{2.51}$$

where ϵ is the kinetic energy of the incoming electron, σ_0 is the asymptotic probability of emission at null energy, ϵ^* is the crossover energy above which the probability of emission is higher than one, $\sigma_{\max}$ is the maximum probability and $\epsilon_{\max} = \frac{\sigma_{\max}-\sigma_0}{1-\sigma_0}\epsilon^*$ is the minimum energy for which $\bar{\sigma} = \sigma_{\max}$. Equation (2.51) is illustrated in Figure 2.20.

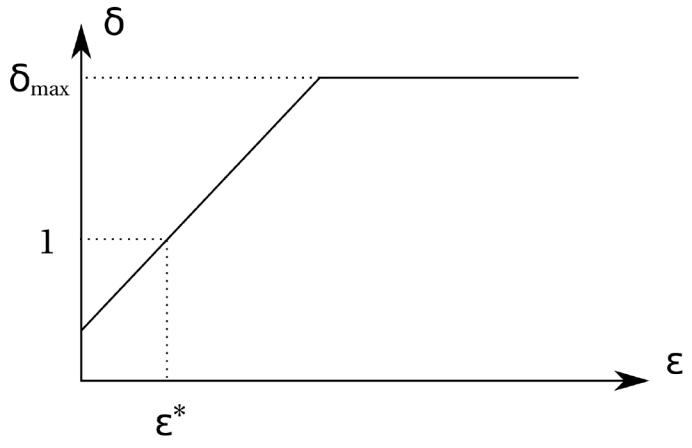

FIGURE 2.20 – Linear-saturated emission model from Barral et al. [6].

We suppose that all the electrons are isotropically emitted following a Maxwellian flux distribution function of temperature T_{SEE}. The parameters σ_0, $\sigma_{\max}$ and ϵ^* can be obtained from experiments. Table 2.2 shows the crossover energy and the probability of emission at energy null for different materials. The value of σ_0 is always close to 0.5, but ϵ^* can vary from 18 to 305 V. Hence, in the following parametric studies, σ_0 will be kept at 0.5 while we vary ϵ^* from low values, corresponding to highly emissive materials, to high values, representing less emissive materials.

TABLE 2.2 – Emission parameters for different materials, from Barral et al. [6].

Material	ϵ^* (V)	σ_0
BN-SiO_2	53	0.45
Al_2O_3	18	0.57
SiC	43	0.69
Graphite	305	0.40

Since the model used describes both the reflected and true secondary electron emission, we will use the general name *electron emission* to refer to the flux of electrons emitted by the walls towards the plasma. In contrast, the electrons reaching the plasma are referred to as the *primary electrons*.

2.7 Sheath model with electron emission

The floating sheath is the plasma response to the presence of an absorbing boundary. The light electrons are quickly absorbed by the material. Hence, in order to balance the particles fluxes, a non-neutral region appears between the plasma and the boundary.

The sheath model featuring SEE processes has been historically studied by Hobbs and Wesson [81], but is still an active research topic nowadays [82]. The sheath is often considered to be collisionless and isothermal, while the plasma is composed of hot Maxwellian electrons and cold ions. A third population of electron-induced secondary electrons is also present in the sheath, and the re-emission rate $\bar{\sigma}$ is assumed to be constant. The sheath must ensure the charge balance, hence

$$\Gamma_i = (1 - \bar{\sigma})\Gamma_e \tag{2.52}$$

with Γ_i and Γ_e the ion and electron particle flux to the wall, respectively. The SEE process modifies the potential drop in the sheath as [81]

$$\Delta\phi_{\text{sheath}} = \mathrm{T_e} \ln\left((1 - \bar{\sigma})\sqrt{\frac{m_i}{2\pi m_e}}\right). \tag{2.53}$$

Adding a pre-sheath drop of $\mathrm{T_e}/2$ [83], the total potential drop to the wall becomes

$$\Delta\phi = \Delta\phi_{\text{sheath}} + \frac{\mathrm{T_e}}{2} = \mathrm{T_e}\left(\frac{1}{2} + \ln\left[(1 - \bar{\sigma})\sqrt{\frac{m_i}{2\pi m_e}}\right]\right) \tag{2.54}$$

We can see that Eq. (2.53) becomes negative for a critical value of the emission rate

$$\bar{\sigma}_{\max} = 1 - \sqrt{\frac{2\pi m_e}{m_i}} \simeq 0.985 \text{ for xenon.} \tag{2.55}$$

However, before that $\bar{\sigma}$ reaches $\bar{\sigma}_{\max}$, the model of Hobbs and Wesson [81] presents another behavior against the hypotheses of Eq. (2.53), as the sheath becomes Space Charge Limited (SCL). In the SCL conditions, the electron emission is so large that the electric field at the wall becomes zero

$$\left.\frac{\partial\phi}{\partial r}\right|_{\text{wall}} = 0 \tag{2.56}$$

In this case, the plasma potential drop to the wall for any ion mass is [81]

$$\Delta\phi_{\text{SCL}} \simeq 1.02\mathrm{T_e} \simeq \mathrm{T_e}, \tag{2.57}$$

and the limit emission rate is

$$\bar{\sigma}_{\mathrm{cr}} \simeq 1 - 8.3\sqrt{\frac{m_e}{m_i}} \tag{2.58}$$

For xenon, Eq. (2.58) gives $\bar{\sigma}_{\mathrm{cr}} = 0.983$ [84]. Figure 2.21 illustrates the sheath model of Hobbs and Wesson [81] by showing the plasma potential profile in the sheath for different values of electron emission rate for a xenon plasma. Fig. 2.21.**a** gives the potential ϕ normalized by $\Delta\phi_{\mathrm{sheath}}$ from Eq. (2.53), and Fig. 2.21.**b** gives ϕ normalized by $\mathrm{T_e}$. We can see in Fig. 2.21 that for $\bar{\sigma} < \bar{\sigma}_{\mathrm{cr}}$, the plasma potential reached $\Delta\phi_{\mathrm{sheath}}$. However, for $\bar{\sigma} > \bar{\sigma}_{\mathrm{cr}}$, the plasma potential does not reach $\Delta\phi_{\mathrm{sheath}}$, resulting in a non-zero current to the wall. Indeed, the sheath is not monotonic in this case, hence the hypotheses needed to develop Eq. (2.53) are not fulfilled. We see in Fig. 2.21.**a** that Eq. (2.53) is correct even for $\bar{\sigma} = 0.984 > \bar{\sigma}_{\mathrm{cr}}$. This is because the value $\bar{\sigma}_{\mathrm{cr}} = 0.983$ is obtained after several approximations, as Eq. (2.56), some of which should not allow to use three significant digits.

In Fig. 2.21.**b**, we can see that at $\bar{\sigma} \simeq \bar{\sigma}_{\mathrm{cr}}$, the plasma potential tends towards $\mathrm{T_e}$, as mentioned by Eq. (2.57).

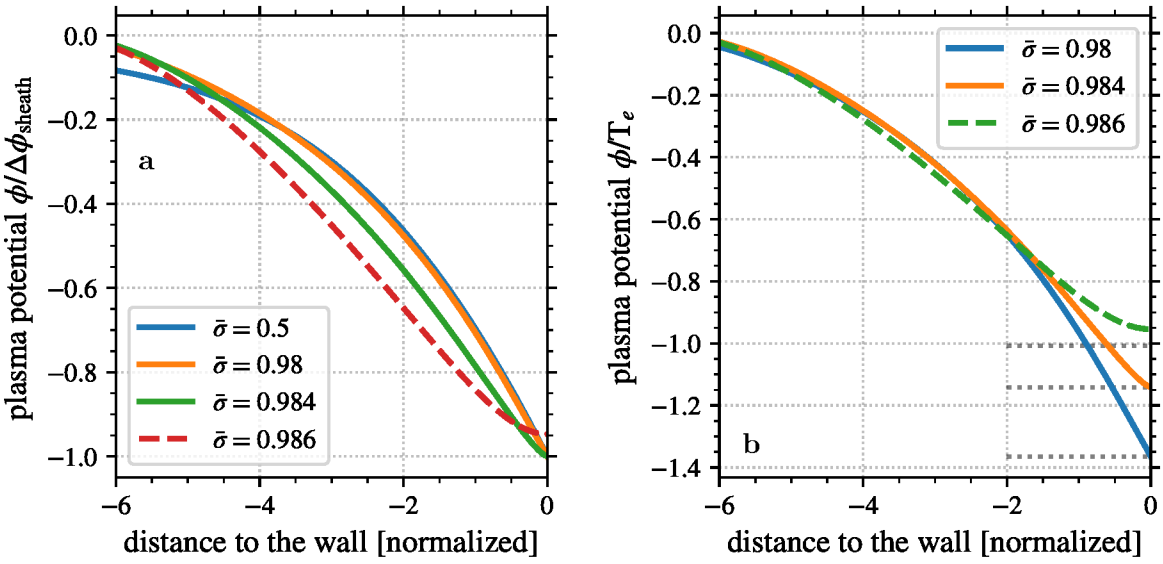

FIGURE 2.21 – Evolution of the plasma potential in the sheath for different values of electron emission rate $\bar{\sigma}$ for a xenon plasma, (**a**) normalized by the total potential drop $\Delta\phi_{\mathrm{sheath}}$ from Eq. (2.53), and (**b**) normalized by the electron temperature, but $\Delta\phi_{\mathrm{sheath}}/\mathrm{T_e}$ is noted with the black dotted line.

2.8 Study of electron cross field transport with a 2D radial-azimuthal PIC simulation

A key topic of my PhD work is to study the impact of surface processes on the plasma discharge and in particular on the electron mobility. The electron mobility in the axial direction μ_{e} is defined as the ratio between the mean velocity u and the electric field

$$\mu_{\mathrm{e}} = \frac{u_{e,z}}{E_z} \tag{2.59}$$

with $u_{e,z} =< v_{e,z} >$ the electron mean velocity. In the PIC simulations, Eq. (2.59) can be used directly to compute μ_{PIC}. As introduced before, in the PIC simulation the velocity is shifted by half a time step compared to the position. Thus, a special care is needed to compute μ_{PIC}.

In the classical drift diffusion theory of the electron mobility transverse to a magnetic field presented in Chapter 1 (Eq. (1.7)), the mobility is due to collisions is

$$\mu_{\text{classical}} = \frac{e}{m_e} \frac{\nu_m}{\nu_m^2 + \omega_{ce}^2} \tag{2.60}$$

with $\omega_{ce} = \frac{eB}{m_e}$ the electron cyclotron frequency and ν_m the electron-neutral momentum transfer collision frequency. In order to evaluate Eq. (2.60), ν_m is calculated in the PIC simulations at every cell. The mobility induced by the instability when neglecting the collisions, as introduced in Chapter 1 (Eq. (1.9)), is

$$\mu_{\text{eff}} = \frac{< \delta n_e \delta E_\theta >_\theta}{n_0 E_z} \frac{1}{B_r} \tag{2.61}$$

The correlation term $< \delta n_e \delta E_\theta >_\theta$ can be computed in the PIC simulation at each radial position. Using its radial profile, we will be able to determine where the instability enhances the most the electron mobility.

In Lafleur et al. [85], the authors present the instability effect as an electron-ion friction force $R_{ei} = -e < \delta n_e \delta E_\theta >_\theta$. Under the assumption that the saturation of the instability is mainly due to ion trapping, the electron-ion friction force can be simplified in the 2D geometry of the simulation to

$$R_{ei}^{sat} = \frac{e|\nabla \cdot (n_e \mathrm{T_e} \mathbf{v}_i)|}{4\sqrt{6} c_s} \simeq \frac{e n_e \mathrm{T_e} v_{i,\text{out}}}{4\sqrt{6} c_s L_z} \tag{2.62}$$

where $\mathbf{v}_i$ is the ion velocity, $c_s = (e\mathrm{T_e}/m_i)^{1/2}$ is the ion sound speed, and the spatial derivative has been approximated across the axial simulation direction, with $v_{i,\text{out}}$ the ion outlet velocity

$$v_{i,\text{out}} = \sqrt{\frac{2eU_z}{m_i}}, \tag{2.63}$$

with $U_z = E_z L_z$ the total potential difference in the axial direction.

Using Eq. (2.62) in Eq. (1.9), we obtain the simplified expression of the effective mobility at saturation

$$\mu_{\text{eff}}^{sat} = \frac{\sqrt{\frac{\mathrm{T_e}}{U_z}}}{4\sqrt{3} B_r}. \tag{2.64}$$

Equation (2.64) shows that for the radial and azimuthal 2D geometry being used here, the enhanced mobility due to ECDI scales as the square-root of the electron temperature $\mathrm{T_e}$ if the simulation parameters are constant. However, it is not the case in general, as the saturation of the instability can be also be due to convection, and there are axial gradients in the electron temperature and plasma density as well.

We can note that $\mu_{\text{PIC}}, \mu_{\text{eff}}$ and $\mu_{\text{classical}}$ are defined at every position of the simulation, but that μ_{eff}^{sat} can only be globally calculated.

2.9 Axial-azimuthal 2D PIC simulation

The radial and azimuthal simulation allows us to study the plasma-wall interaction coupled with the self-consistent azimuthal instability. As previously mentioned, however, axial gradients are missing (magnetic field, densities, temperatures, etc.) as well as the axial convection of the wave and the particles. In order to study those phenomena, the axial and azimuthal simulation domain is used [35, 86, 87, 8]. Figure 2.22 shows a schematic representation of this simulation domain. In this configuration, the anode voltage is set to U_d, and the cathode is grounded.

A radial magnetic field is imposed, whose amplitude follows an axial profile such as in Fig. 1.6. The axial electric field is self-consistently computed by solving the Poisson equation. In this configuration, one needs to inject a flux of electrons $J_{e,c}$ corresponding to the contribution of the cathode to sustain the plasma. While this configuration models the physics of the axial

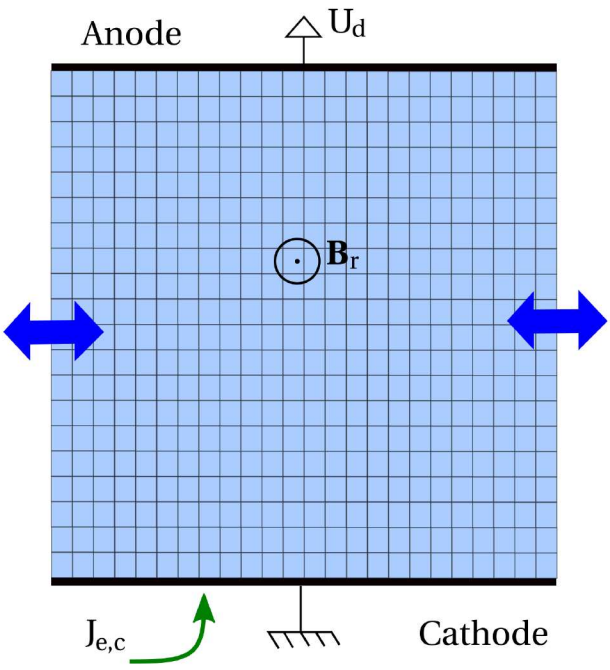

FIGURE 2.22 – Schematic representation of the axial and azimuthal simulation domain. U_d is the voltage imposed at the anode (of the order of 300 V) and $J_{e,c}$ corresponds to the electrons emitted by the grounded cathode, used to initiate and maintain the plasma discharge. Periodic boundary conditions are used in the azimuthal direction. A radial magnetic field B_r is imposed, which amplitude depends on the axial position.

direction, it does not model the plasma-wall interaction. In Chapter 7, we propose an algorithm to model the effects of the walls on the particle and power balance. The main idea is to model the absorption of the particles by the wall in a way similar to the axial convection of particles used in the radial-azimuthal simulation (described in Section 2.5). More information of the axial-azimuthal simulation domain and the radial losses algorithm are given in Chapter 7.

2.10 Characteristics and performances of the LPPic simulation code

LPPic is the electrostatic particle-in-cell simulation code developed at LPP to study principally magnetized plasma thruster, such as the HET. Written in Fortran (2008), it uses the Message Passing Interface (MPI) to parallelize the computational load using a domain decomposition. The principle of the domain decomposition is that each Central Processing Unit (CPU) knows a small chunk of the whole domain. We use HYPRE's multigrid solver to solve Poisson equation in 2D [88].

The main data input/output is done using the HDF5 format, which enables parallel access to a hierarchical file. The output data does not yet use the open standard for particle-mesh data files (openPMD). Thus, the data post processing is done using a python package.

The use of these efficient libraries allows us to obtain a good scalability. Figure 2.23 shows the speed up measured for the Strong Scalability test. The Strong scalability compares the performances of the execution of the task at fixed workload with varying the number of CPUs. The theoretical speedup accessible is given by Amdahl [89] as

$$S = \frac{1}{1 - \alpha + \frac{\alpha}{s}} \tag{2.65}$$

with α the proportion of the task that is parallel, and s the speedup of the parallelized part. A

perfectly parallel code has $\alpha = 1$, hence a speedup $S = s$.

In Fig. 2.23 are shown the speedup for the overall simulation, as well as the main functions of the PIC algorithm (Charge deposition to the mesh, Particle pusher, Monte Carlo Collision and the Poisson solver). The scalability test is realized over two 2D radial-azimuthal cases. The bigger case uses a mesh of 1000×1024 cells with 140 particles per cell, which corresponds to a typical simulation case. Unfortunately, this case cannot be run with less than 240 CPUs because of the maximum memory available per CPU. Hence, we use a case four times smaller to test fewer number of CPU. The simulation is run over 2000 time steps. More information on the scalability is given in Appendix A.

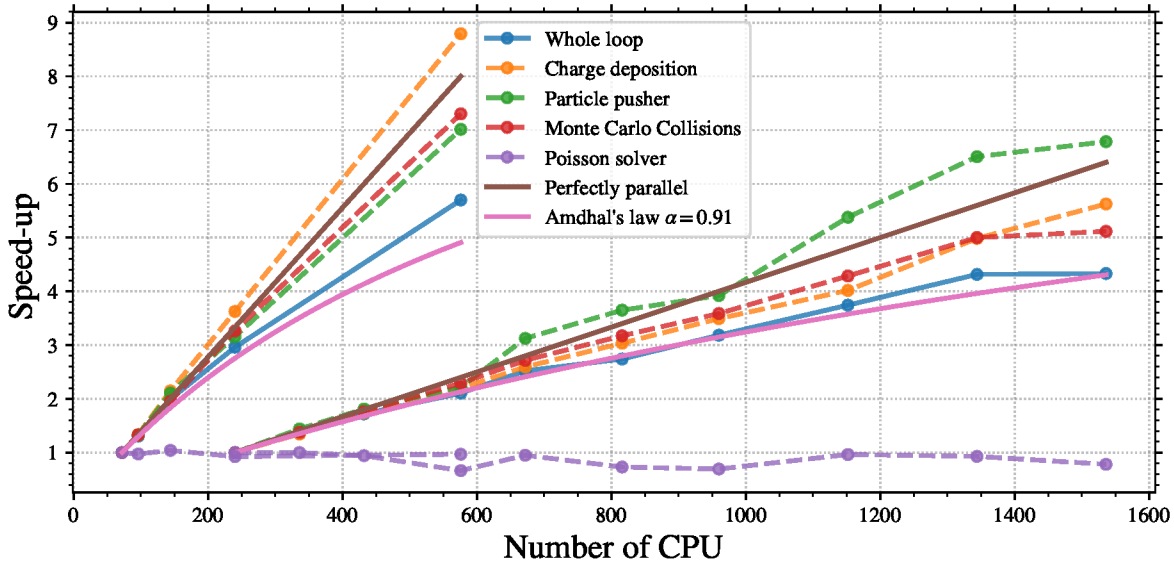

FIGURE 2.23 – Strong scalability profile of *LPPic* with a small and a large job on the Cluster Occigen (CINES). In addition to the overall performance, the profiles of the main sub-functions of the PIC loops are given.

We can see that the overall performance of the code is very good, as it scales as if it is parallelized at 91% from Amdahl's law. Most of the sub-functions have higher speed-ups, but the Poisson solver does not scale at all. It is due to the size of the chunk of domain of each CPU, which is too small. A way to improve the performances of *LPPic* would be to use an hybrid parallelization with the shared memory openMP library. But the current performance is acceptable, as the typical simulation cases presented in this manuscript run in around one week (7 days) on 360 CPUs.

The development of the simulation code *LPPic* started in 2015 by Vivien Croes. I joined the development with Romain Lucken in 2016, and Thomas Charoy started in 2017. Because of the number of contributors, and our different experiences in software development, we quickly set a Continuous Integration (CI) pipeline on a self hosted server using Teamcity. This allows a systematic verification of the modifications by the mean of unit, mezzanine and integration tests [90].

The validation of the code is done using the Benchmark of Turner et al.(2013) 70. While it allows to validate a significant part of the PIC code, it is not magnetized and only in 1D. Unfortunately, this is the only Benchmark available. Hence, the comparison of several codes on a 2D magnetized has been conducted in 2019 by Thomas Charoy in order to create a new Benchmark to validate such simulation codes, in Charoy et al. [91].

Since 2015, *LPPic* has grown to 23000 lines of code, has been used on more than 5 different clusters of various architectures, and has been used to produce several publications [18, 19, 92, 93, 94, 95].

2.11 Conclusion

In order to study the plasma wall interaction in an HET, we developed a bi-dimensional simulation code using PIC-MCC modeling. As the electrons drift azimuthally due to the $E \times B$ configuration, the ECDI rises, enhancing the cross-field transport of the electron towards the anode. The walls closing the chamber in the radial direction are also important for the discharge behavior. Hence, in order to compare the interaction between these phenomena, we simulate the radial-azimuthal domain. In my Ph.D., I have worked on the development of *LPPic* , the 2D-3V PIC-MCC simulation code, concerning in the radial-azimuthal configuration

— the modeling of the axial convection, in order to model the energy losses and so attain a steady-state,

— the modeling of the radial boundary with the dielectric layer included in the simulation domain.

We also adapted *LPPic* to simulation the axial-azimuthal domain, that is presented in more detailed in Chapter 7. The performances of the code are good, with 90% of the calculation parallelized, and an important effort as been made concerning the validation and verification.

Chapter 3

Evolution of the azimuthal instability and generalized dispersion relation (DR)

As briefly mentioned previously, the $E \times B$ configuration of the Hall Effect Thruster (HET) gives rise to azimuthal instabilities. These instabilities are important for the behavior of the HET, as they are responsible for the electron cross-field transport. Even if these instabilities have been the subject of numerous studies, they are still not well understood. Using the Particle In Cell (PIC) simulations, we propose new insights for the understanding of the instability. In particular, we develop a dispersion relation solver that uses the velocity distribution function measured in the simulations. Then, we compare the simulation instability characteristics with the dispersion relations. A special care is taken with the boundary condition and the instability non-linear saturation.

Contents

3.1 Instability in the 2D radial-azimuthal PIC simulations

3.1.1 Introduction and state of the art

The presence of azimuthal instabilities in the Hall effect thrusters has first been shown with numerical simulations by Adam et al. [35]. Then, they have been the subject of numerous studies, especially numerical [36, 85, 4, 5, 19, 65, 44], but also experimental [96, 97, 98]. However, their nature remains unclear [8]. Viven Croes studied the azimuthal instability in a bi-dimensional (2D) radial-azimuthal simulation domain of radial length $L_R = 2\,\mathrm{cm}$ and azimuthal length $L_\theta = 0.5\,\mathrm{cm}$, with the model of particle convection proposed by Lafleur [5, 19]. He showed that the saturation of the oscillations was due to ion-wave trapping. Using a parametric study over the plasma density and the ion mass, he observed that the main oscillation is consistent with the characteristics of the Ion Acoustic Wave (IAW).

During the three years of my Ph.D., other groups presented new simulation results in similar radial-azimuthal geometries. Hara [99] presented kinetic simulation results on a two-dimensional domain, of size similar to the case studied here. However, that work was focused on the electron mobility values, and little information on the instability is given. In Janhunen et al. [65], the authors presented a collisionless highly resolved 2D PIC simulation. No convection and no compensation model for radial losses are used, hence the electron energy quickly rises and the density decreases. On the other hand, the domain is bigger, with a radial length of $L_r = 53.8\,\mathrm{mm}$ for an azimuthal length of $L_\theta = 13.45\,\mathrm{mm}$. Three cells by Debye length are used, while there are on average 800 particles per cell. Under these conditions, the instability rises, but a large radial structure, named Modified Two Stream Instability (MTSI), of radial wavelength twice as big as L_r is observed. The simulation parameters of Taccogna et al. [44] are similar to the results presented here, with $L_r = 15\,\mathrm{mm}$ and $L_\theta = 12.5\,\mathrm{mm}$. The results are qualitatively similar to the others, however the authors also observed radial structures, but this time with a wavelength of a third of L_r.

We can see that the results obtained with similar configurations differ significantly, meaning that some points needs to be clarified. In Section 3.1, we present the oscillations observed in the PIC simulations carried out with *LPPic* . After that, we derive the dispersion relation with no hypothesis concerning the particle distribution functions in Section 3.2, and we present in Section 3.3 a numerical algorithm that solves the dispersion relation using the distribution function measured in the PIC simulations. The oscillations observed in the simulation are compared in Section 3.4 to the results of the dispersion relation. To finish with, the impact of the radial boundary condition is investigated in Section 3.5.

3.1.2 Overview of the 2D simulation

We present in this section the simulation conducted to study the azimuthal instability. The parameters of the simulation are given in Table 3.1. The imposed axial electric field E_z and the radial magnetic field B_r are uniform in space and constant in time. The radial direction is closed with the dielectric boundary condition of dielectric width $L_{diel} = 3\,\mathrm{mm}$. No Secondary Electron Emission (SEE) is modeled, and the convection is modeled with the new noiseless model (see Section 2.5.5). The simulation is initialized with a uniform electron and ion density $n_e = n_i = 3{\times}10^{17}/\mathrm{m}^3$, with an electron temperature $\mathrm{T_e} = 10\,\mathrm{V}$ and an ion temperature $\mathrm{T_i} = 0.025\,\mathrm{V}$. The mean particle density is conserved by imposing an ionization which compensate the particle losses at the wall a each time step.

Figure 3.1 shows the radial profile of the electron and ion densities, as well as the plasma potential, at the end of the simulation, averaged azimuthally and in time between $t = 4$ and $7\,\mu\mathrm{s}$. The results are averaged azimuthally and in time over the 3 last microseconds. We can observe

TABLE 3.1 – Parameters of the 2D PIC simulations

Physical Parameter			
Parameter	Symbol	Value	Unit
Dimensions	$L_r \times L_\theta \times L_z$	$1 \times 0.26 \times 0.5$	cm
Radial magnetic field	B_r	0.02	T
Axial electric field	E_z	$2{\times}10^4$	sV/m
Dielectric layer of width	L_{diel}	3	mm
Mean plasma density	n_0	3×10^{17}	m^{-3}
Initial electron temperature	$\mathrm{T}_{\mathrm{e},0}$	10.0	V
Initial ion temperature	$\mathrm{T}_{\mathrm{i},0}$	0.025	V
Duration of the simulation	T_{simu}	7	µs
Numerical Parameter			
Time step	Δt	4×10^{-12}	s
Cell size	$\Delta x = \Delta y$	2×10^{-5}	m
Number of particles per cell	N/NG	80	part/cell

on the radial profile of both the densities and the plasma potential the sheaths close to the walls (regions of high electric field due to a charge unbalance) and the quasineutral plasma bulk in the center. These profiles are typical of low temperature low pressure bounded plasmas.

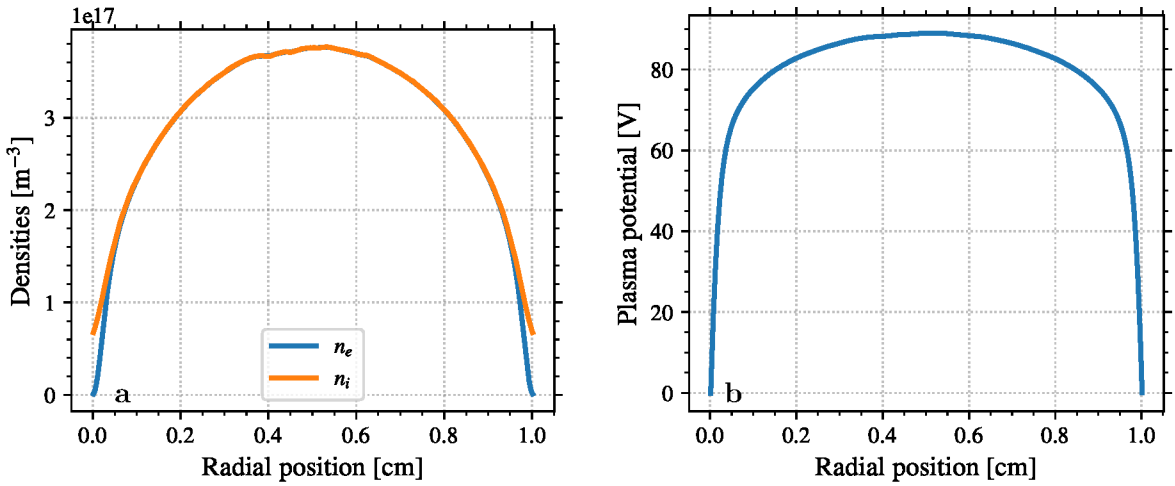

FIGURE 3.1 – Radial profile of (**a**) the ion and electron densities, and (**b**) the plasma potential, averaged azimuthally and in time between $t = 4$ and 7 µs.

Figure 3.2 shows the temporal evolution of the mean kinetic energy $\mathcal{E}_e$ during the simulations. The mean kinetic energy is computed in the simulations by averaging over the whole electron population

$$\mathcal{E}_{ed} = \frac{m_e}{2eN_e} \sum_{j=1}^{N_e} v_{j,d}^2 \tag{3.1}$$

with d the direction (r, θ, or z), N_e is the number of electrons, and $v_{j,d}$ is the velocity in the direction d of the j^{nt} electron. We see that the simulation starts at $\mathcal{E}_e = \mathrm{T}_{\mathrm{e},0}/2$, and that after a few microseconds of transition, the simulations reaches a quasi steady-state with small

fluctuations, that we name the saturated regime. This corresponds to an initial Debye length of $\lambda_{De} = 4.3\times10^{-5}$ m, increasing up to $\lambda_{De} = 7.0\times10^{-5}$ m during the saturated regime.

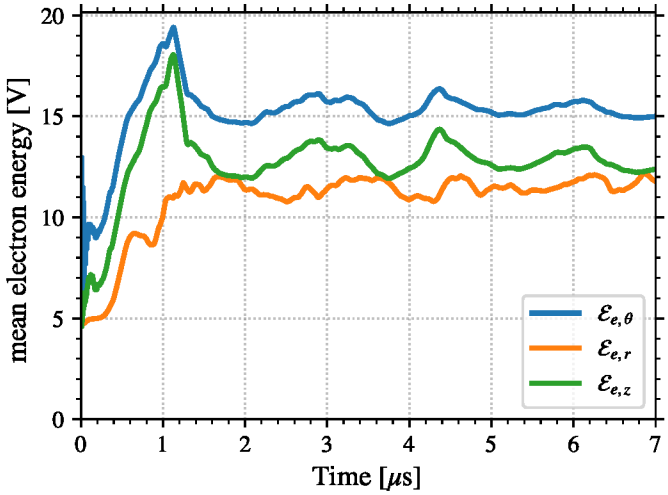

FIGURE 3.2 – Temporal evolution of $\mathcal{E}_e$ the electron mean kinetic energy decomposed over the three directions. The kinetic energy includes the internal energy (temperature) and the kinetic energy of the mean velocity.

3.1.3 General characteristics of the azimuthal instability

In this section, we present the general characteristics of the azimuthal instability observed in the 2 dimensions (2D) PIC simulations. Figure 3.3 shows the radial-azimuthal distribution of the electron density and the plasma potential during the saturated regime. We can see the instability in the azimuthal direction with a wavelength of a third of the azimuthal length. The instability can be seen in all of the plasma quantities (electron and ion densities, potential, electric field). In the radial direction, we can see the presheaths and the sheaths, characterized by the decrease of the plasma density between the center and the walls.

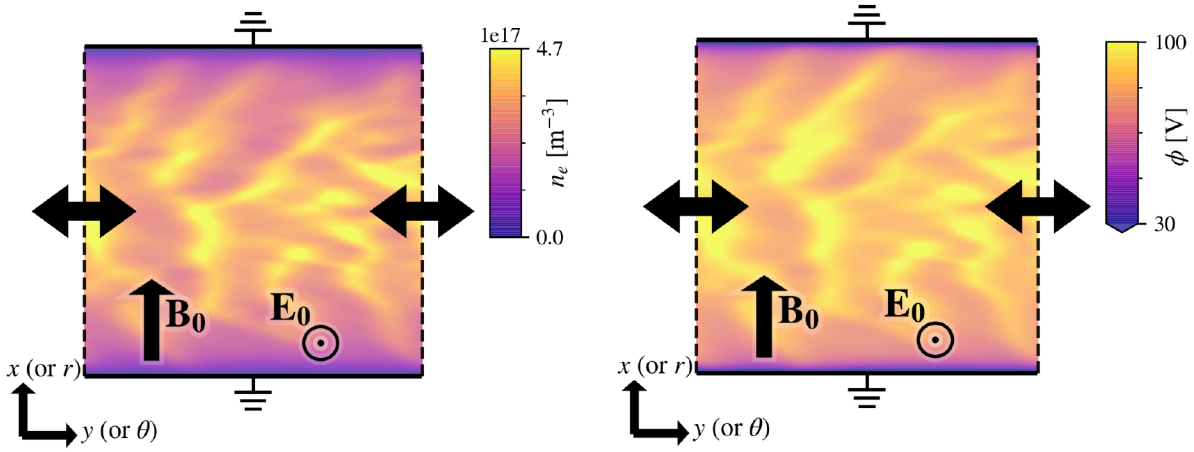

FIGURE 3.3 – Radial and azimuthal distribution of (left) the electron density n_e at $t = 6$ µs (during the saturated regime), and (right) the plasma potential ϕ. The azimuthal instability is clearly seen, as well as the sheaths in the radial direction.

Figure 3.4 shows the temporal evolution of the azimuthal electric field and the electron density as a function of the azimuthal position, measured at the center of the radial direction. We see the instability growing at the beginning, up to the saturation around $t = 1$ µs. Then, we observe,

in addition to the fast oscillation, a slower modulation of the oscillation amplitude, similar to the fluctuations seen in Fig. 3.2.

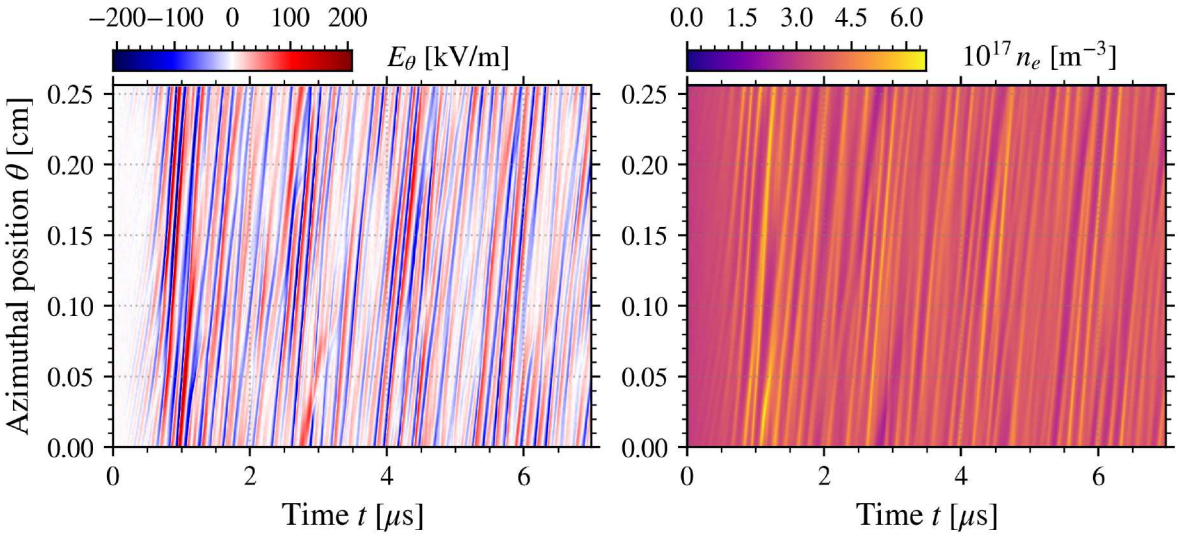

FIGURE 3.4 – Temporal evolution of (left) the azimuthal electric field E_θ, and (right) the electron density n_e as a function of the azimuthal position.

Figure 3.5 shows the frequency spectrum of the azimuthal electric field presented in Fig. 3.4 computed via Fast Fourier Transform (FFT) in the saturated regime between 2 and 7 µs. The spectrum has been averaged in the azimuthal direction, in order to reduce the noise. The theoretical frequency $f_{\text{theo}} = \frac{\omega_{pi}}{\pi\sqrt{6}}$ [19] is shown with a dashed line. We can see a very good agreement between f_{theo} and the maximum of the frequency spectrum. The value of the theoretical frequency f_{theo} corresponds to the most growing frequency of the IAW and is detailed in Section 3.2.

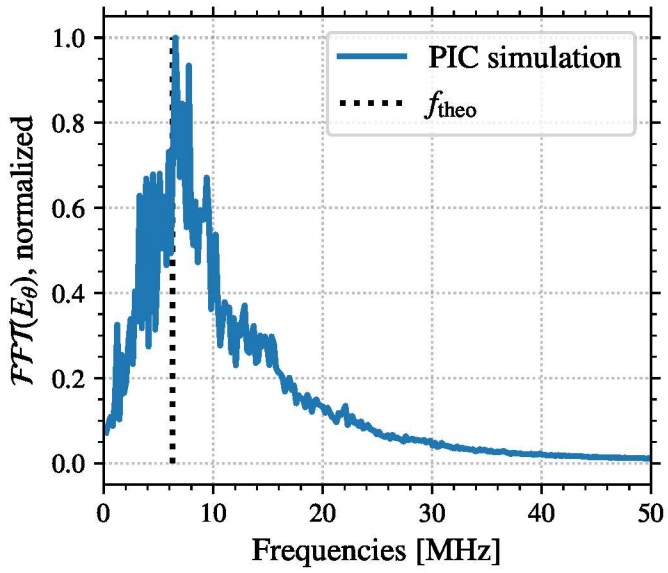

FIGURE 3.5 – Frequency spectrum of the azimuthal electric field computed between 2 and 7 µs, averaged in the azimuthal direction. The black line is the theoretical frequency $f_{\text{theo}} = \frac{\omega_{pi}}{\pi\sqrt{6}}$.

3.1.4 Energy cascade

We can see in Fig. 3.5 a slow decrease of the frequency amplitude from f_{theo} to larger frequencies. This type of cascade may be the signature of turbulence, and can be a source of energy dissipation - hence saturation. Kolmogorov's hypothesis of incompressible fluid leads to a cascade in power law

$$W(f) = |\mathcal{FFT}(E_\theta)(f)|^2 \propto f^{-\alpha},$$

with $\alpha = 5/3$.

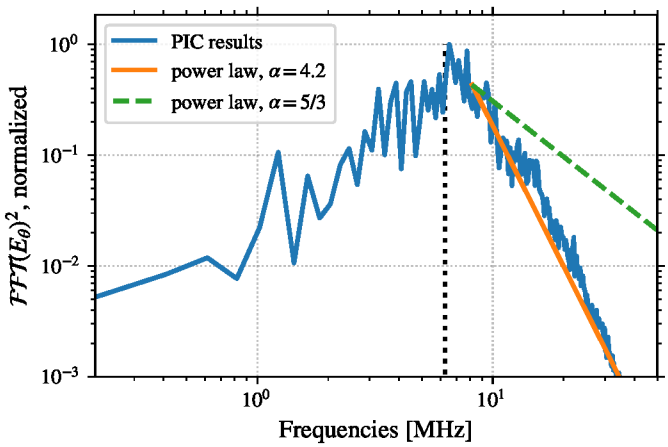

FIGURE 3.6 – Normalized frequency power spectrum in log-log scale computed between 1.5 and 7 µs. The black dotted line shows the theoretical frequency f_{theo}, the orange solid line is a linear fit of coefficient α, and the green dashed line correspond to Kolmogorov's turbulent spectra.

Figure 3.6 shows the frequency power spectrum computed between 2 and 7 µs in log scale. Overlaid is a fit of the cascade, for frequencies above the maximum amplitude. The power law obtained is $\alpha \simeq 4.2$, which is much greater than Kolmogorov's value of 5/3. The oscillations observed present a decrease of the power spectrum much steeper than expected from turbulence. Even if the mechanism of plasma turbulence differs from the fluid turbulence [100], the value of α is significantly larger than expected. Consequently, we expected that there is no significant dissipation or cascade to the small scales.

3.1.5 Temporal evolution of the oscillation amplitude

We have seen in the previous section that after a growing phase, the amplitude of the instability saturates with a low frequency oscillation around a stable value. This section analyses these temporal characteristics.

Figure 3.7 shows the temporal evolution of the characteristics of the electrostatic oscillation. As the oscillation is not monochromatic (i.e. it is the sum of multiple waves), we display both the maximum of the electric field $\max(E_\theta)$, and its standard deviation σ_{E_θ}. In the case of a monochromatic wave, one would have

$$\sigma_{E_\theta} = \frac{\max(E_\theta)}{\sqrt{2}}.$$

We can see in Fig. 3.7 that during the first microsecond, the growth of the wave amplitude is exponential, corresponding to a constant growth rate γ_{PIC} that can be extracted from the simulation. A linear fit in log scale give $\gamma_{PIC} \simeq 0.07\omega_{pi}$ during the linear phase. After $t = 1$ µs, the amplitude of the electric field oscillates around a mean value, with a period of the order of $T_{NL} = 1.5 \pm 0.1$ µs (NL for *non-linear* oscillation). Hence, the azimuthal electric field becomes of the type of

$$E_\theta = E_{\text{LF}}(t) E_{\text{HF}}(t, \theta)$$

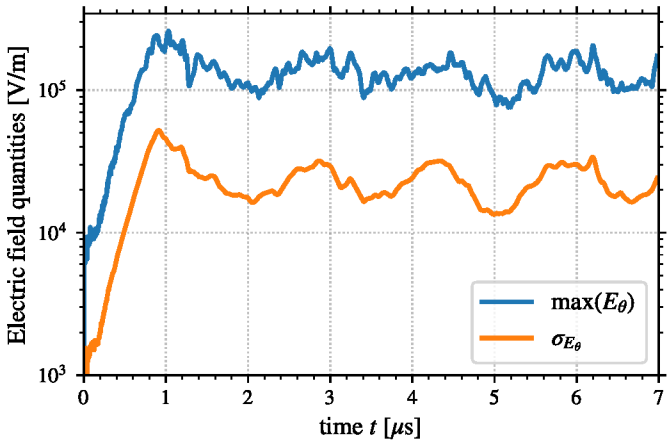

FIGURE 3.7 – Temporal evolution of the maximum and the standard deviation of the azimuthal electric field, in log scale.

with $E_{\mathrm{HF}}(t,\theta)$ the high frequency instability, and $E_{\mathrm{LF}}(t)$ the low frequency modulation of the amplitude, with a low frequency $f_{\mathrm{LF}} \simeq 660 \pm 45\,\mathrm{kHz}$. Several phenomena are candidates to the modulation observed, which are discussed here-after.

Ion transit time

The ions are injected at the anode, and are accelerated by the uniform axial electric field E_z. The transit time of the ions in the axial direction T_t is the time needed for the ions to travel L_z. Neglecting the collisions we have

$$T_t = \sqrt{\frac{2m_i L_z}{eE_z}} \simeq 0.8\mu s. \tag{3.2}$$

The transit time is of the good order of magnitude, but T_{NL} is still twice bigger. In addition, we tried to initialize the simulation with ions distributed in the axial direction, so that their flux is constant in time. Such an initialization did not modify the low frequency oscillations.

Particle trapping and bouncing

A common reason for wave saturation is the ion-wave trapping. The ion-wave trapping is a particle wave interaction that happens for the ions that have a velocity near the phase velocity of the wave. Ions are first accelerated by the wave where the electric field is positive. Hence, their velocity become slightly above the phase velocity of the wave, so that they reach the negative electric field of the wave. Then, their decelerate and reaches the first step of the process.

Ion-wave trapping has been observed in both 1 dimension (1D) simulation by Lafleur et al. [4] and in 2D simulation [18]. Hence, the low frequency modulation could be due to the ions bouncing [101]. However, the bouncing time scale is

$$T_B = 2\pi\sqrt{\frac{m_i}{ek\max(E_\theta)}} \simeq 0.5\,\mu\mathrm{s}, \tag{3.3}$$

which is 3 times smaller than T_{NL}. Using $\sqrt{2}\sigma_{E_\theta}$ instead of $\max(E)$, we find $T_B = 0.9\,\mu\mathrm{s}$. Even though in Belmont et al. [101], the authors say that when the amplitude of the electric field is large (as it is the case here), the bouncing time scale increases due to non-linear phenomenon (the particle trajectory is no longer harmonic), we cannot conclude for now that this is the origin of the low frequency modulation.

Ion-wave trapping oscillation

The wave saturating due to ion-wave trapping has an amplitude of [102, 8]

$$\sigma_{E_\theta} = \frac{\mathrm{T_e}}{12\lambda_{De}}. \tag{3.4}$$

Defining the wave energy density by

$$\epsilon_{\mathrm{wave}} = \frac{\epsilon_0}{2}\sigma^2_{E_\theta} \tag{3.5}$$

and the electron thermal energy density with

$$\epsilon_{\mathrm{th}} = \frac{3}{2} e n_e \mathrm{T_e} \tag{3.6}$$

Using Eq. (3.4) in the definition of the wave energy Eq. (3.5) and the definition of the Debye length λ_{De} Eq. (2.7), we obtain

$$\begin{aligned}\epsilon_{\mathrm{wave}} &= \frac{\epsilon_0}{2}\frac{\mathrm{T_e}^{(2)}}{12^2}\frac{e^2 n_e}{\epsilon_0 e \mathrm{T_e}} \\ &= \frac{e n_e \mathrm{T_e}}{288} = \frac{\epsilon_{\mathrm{th}}}{432}\end{aligned}$$

This gives us a criterion for the ion-wave trapping using the wave and thermal energies

$$432\epsilon_{\mathrm{wave}} = \epsilon_{\mathrm{th}}. \tag{3.7}$$

Figure 3.8 shows the temporal evolution of the electron thermal energy ϵ_{th} and the wave energy density ϵ_{wave}, scaled by the factor 432. We can see that ϵ_{th} is relatively constant. However, ϵ_{wave} oscillates significantly, and passes regularly above and below ϵ_{th}. In order to understand the reason for this behavior, we can look at the evolution of the ion temperature. Indeed, the trapped ions gain energy, which increases the total ion temperature.

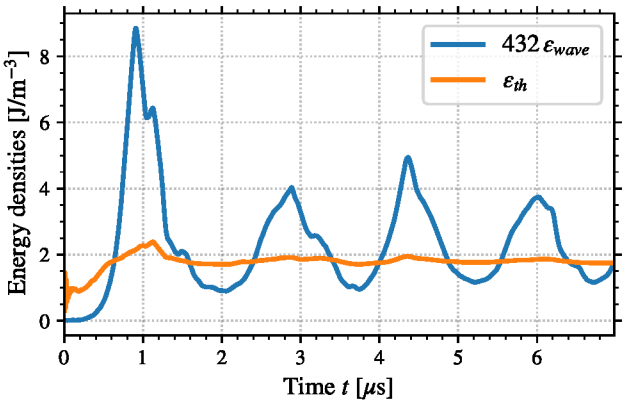

FIGURE 3.8 – Temporal evolution of the wave energy density ϵ_{wave} compared to the thermal energy density ϵ_{th}.

The correlation between the wave amplitude and the ion temperature is shown in Figure 3.9. Fig. 3.9.**a** shows the temporal evolution of the ion temperature $\mathrm{T_i}$ and the standard deviation of the azimuthal electric field $\sigma_{E_{theta}}$, both normalized. We see that the oscillation of the wave amplitude is a quarter of a period before the oscillation of the ion temperature. This means that first the wave increases, then the ion temperature increases. After that, the wave amplitude decreases, which leads to the decreases of the ion temperature.

Fig. 3.9.**b** shows the temporal derivative of the ion temperature $\partial_t \mathrm{T_i}$ and the ion-wave trapping criterion defined as $432\epsilon_{\mathrm{wave}} - \epsilon_{\mathrm{th}}$ from Eq. (3.7), both normalized. When the ion-wave

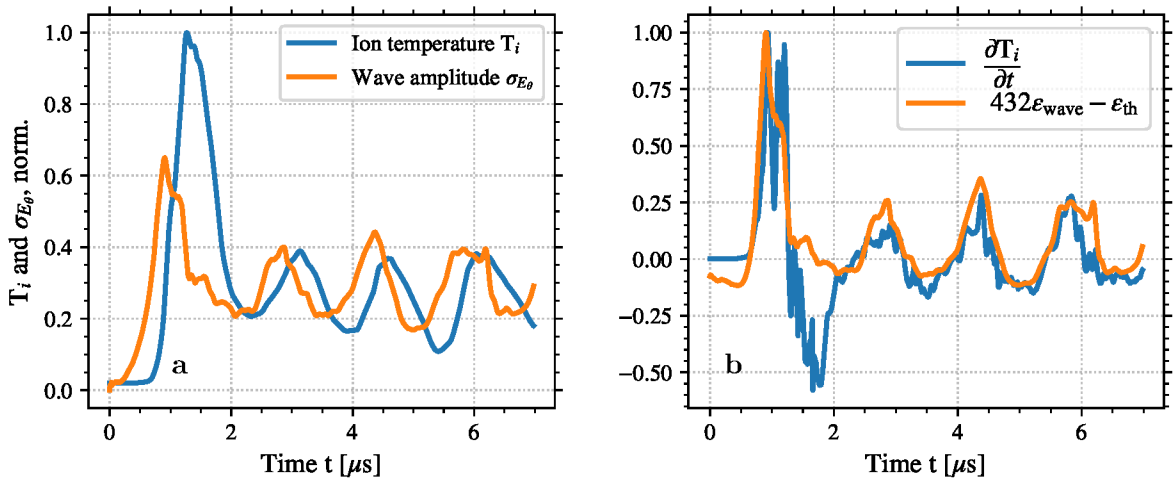

FIGURE 3.9 – Temporal evolution of (**a**) the ion temperature T_i and the standard deviation of the σ_{E_θ}, normalized, and (**b**) the temporal derivative of the ion temperature $\partial T_i/\partial t$ and the ion-wave trapping criterion, normalized.

trapping criterion is negative, it means that the wave amplitude is too small, so that the ions are not trapped. In contrast, if it is positive the ions will be trapped. Again, we see a good correlation between the sign of the ion-wave trapping criteria and the growth, or decrease, of the ion temperature.

In Figs. 3.8 and 3.9, the period of the oscillations of ϵ_{wave} is $T_{NL} \simeq 1.5\,\mu\text{s}$. This period could be related to the response time of the ions, as we have [103]

$$T_{NL}/4 \simeq 0.4\,\mu\text{s} \sim T_B.$$

The hypothesis that the low frequency modulation of the amplitude of the azimuthal wave could be validated by varying the ion mass, and observe if T_{NL} varies in $\sqrt{m_i}$. To summarize, the low frequency modulation of the azimuthal wave amplitude is certainly due to non-linear behavior of wave-particle interaction. Complementary results are presented in Section 3.4.3 by solving the dispersion relations.

3.2 Dispersion relation of the instabilities

The dispersion relations are obtained by coupling the particle dynamics with the electric fields. In the case of the kinetic electrostatic dispersion relation, we couple the Vlasov equation with the Poisson equation. In our 2D geometry, we can neglect all the gradients. A fixed axial electric field $\mathbf{E} = E_0\mathbf{e}_z$ and a fixed radial magnetic field $\mathbf{B} = B_0\mathbf{e}_r$ are imposed. The electrons are drifting in the azimuthal direction due to the $E \times B$ drift, hence

$$\mathbf{u}_e = \frac{\mathbf{E}\times\mathbf{B}}{|\mathbf{B}|^2} = \frac{E_0}{B_0}\mathbf{e}_\theta.$$

The ions are accelerated in the axial direction, $\mathbf{u}_i = u_i\mathbf{e}_z$. Using a perturbations as waves of the form

$$\exp\left(i\mathbf{k}\cdot\mathbf{x} - i\omega t\right),$$

with $\mathbf{x}$ the position vector. The oscillation wave vector $\mathbf{k} = k_r\mathbf{e}_r + k_\theta\mathbf{e}_\theta$ is real but its frequency $\omega = \omega_r + i\gamma$ can be complex, where γ is the growth rate of the oscillations.

The dispersion relation has been studied by Ducrocq et al. [36] in the case of cold ions and Maxwellian electrons in a 2D geometry. A numerical algorithm has been proposed by Cavalier

[97] and compared to experimental measurements. In Lafleur et al. [85], the authors added the ion drift velocity to the dispersion relation.

The Electron Cyclotron Drift Instability (ECDI) dispersion relation obtained presents resonances at the cyclotron frequencies, which broadens when k_r increased. The limit when k_r tends to large values is similar to an IAW. This limit is usually used, even if recently, 2D PIC simulations with a larger domain observed radial structures in the oscillations [65, 99].

Lafleur et al. [87] removed the Maxwellian hypothesis by using directly the distribution functions measured in the PIC simulations in the IAW dispersion relation. The authors showed that the frequency of the oscillation is almost unperturbed, but the growth rate is significantly reduced, even when the ions were still supposed Maxwellian [87, Fig. 8].

Here, we propose to continue the investigation by solving the dispersion relation numerically with the electron and ion distribution function for both the IAW and the ECDI.

3.2.1 General dispersion relation

We follow the development presented in Ducrocq et al. [36], Cavalier [97], Lafleur et al. [85]. The plasma dielectric function is defined as

$$\hat{\epsilon}(\mathbf{k},\omega) = 1 - \sum_s \chi_s(\mathbf{k},\omega) \tag{3.8}$$

where $\chi_s(\mathbf{k},\omega)$ is the susceptibility of the species s. It is obtained by coupling the Poisson equation with the particles description. The dispersion relation is obtained by setting $\hat{\epsilon}(\mathbf{k},\omega) = 0$ and solving for $\mathbf{k},\omega$.

For the unmagnetized ions, supposing a Maxwellian distribution, the susceptibility is

$$\chi_i(\mathbf{k},\omega) = \frac{\omega_{pi}^2}{k^2 v_{th,i}^2} Z'\left(\frac{\omega - \mathbf{k}\cdot\mathbf{u}_i}{k v_{th,i}}\right) \tag{3.9}$$

where ω_{pi} the ion plasma pulsation, $k = |\mathbf{k}|$ and $\mathbf{u}_i$ is the mean velocity of the ions. The function Z' is the derivative of the Fried and Conte function [104]

$$Z(\eta) = \frac{1}{\sqrt{\pi}} \int_{-\infty}^{\infty} \frac{\exp(-t^2)}{t-\eta} dt. \tag{3.10}$$

We use here the Fried and Conte function because of the Maxwellian hypothesis. Xie [105] proposes a numerical algorithm to calculate the susceptibility for a general distribution function

$$Z(\eta, f) = \int_{-\infty}^{\infty} \frac{f(t)}{t-\eta} dt, \tag{3.11}$$

with f the velocity distribution function to consider, normalized to one, centered, and of standard deviation $\sigma = 1/2$. For the sake of brevity, the generalized dispersion function $Z(\eta, f)$ is noted $Z(\eta)$, and the Fried and Conte function is noted $Z_M(\eta)$. The derivative of Z is

$$Z'(\eta) = \int_{-\infty}^{\infty} \frac{\partial f(t)/\partial t}{t-\eta} dt, \tag{3.12}$$

A general expression for the plasma dielectric function can be obtained for magnetized electrons by making use of the method of characteristics and is given by

$$\begin{aligned}\hat{\epsilon}(\mathbf{k},\omega) =& 1 - \\ & \frac{\omega_{pi}^2}{k^2 v_{th,i}^2} Z'\left(\frac{\omega - \mathbf{k}\cdot\mathbf{u}_i}{k v_{th,i}}\right) + \\ & \frac{1}{k^2\lambda_{De}^2}\left[1 + \left(\frac{\omega - \mathbf{k}\cdot\mathbf{u}_e}{k v_{th,e}}\right) \sum_{n=-\infty}^{\infty} e^{-\beta} I_n(\beta) Z\left(\frac{\omega - \mathbf{k}\cdot\mathbf{u}_e - n\omega_{ce}}{k_r v_{th,e}}\right)\right],\end{aligned} \tag{3.13}$$

where I_n are the modified Bessel functions of the first kind, and

$$\beta = \frac{(k_\theta^2 + k_z^2) b_{th,e}^2}{\omega_{ce}^2} \tag{3.14}$$

Equation (3.13) is the dispersion relation for drifting magnetized electrons and unmagnetized ions. It will be used to study the Electron Cyclotron Drift Instability (ECDI).

3.2.2 Modified Ion Acoustic Wave

The dispersion relation of Eq. (3.13) presents sharp resonances due to cyclotron resonances. However, kinetic simulations in Janhunen et al. [65] and Taccogna et al. [44] have shown that after some time (around $t = 0.5\,\mu s$ and $t = 3\,\mu s$ respectively) the resonances are no longer present, with a progressive decrease of the higher harmonics and the first harmonics becoming the most prominent. Without the resonances, the dispersion relation evolves to the nonmagnetic ion-acoustic instability

$$\begin{aligned} \hat{\epsilon}(\mathbf{k}, \omega) =& 1 - \\ & \frac{\omega_{pi}^2}{k^2 v_{th,i}^2} Z'\left(\frac{\omega - \mathbf{k}\cdot\mathbf{u}_i}{k v_{th,i}}\right) + \\ & \frac{1}{k^2 \lambda_{De}^2} Z'\left(\frac{\omega - \mathbf{k}\cdot\mathbf{u}_e}{k v_{th,e}}\right), \end{aligned} \tag{3.15}$$

Lafleur et al. [85] and Janhunen et al. [65] show that after some assumptions – mostly a drifting Maxwellian distribution, cold ions, and a small electron drift velocity compared to thermal speed – Eq. (3.15) can be solved to obtain

$$\omega = \omega_r + i\gamma = \mathbf{k}\cdot\mathbf{u}_i \pm \frac{k c_s}{\sqrt{1 + k^2\lambda_{De}^2}} \pm i\sqrt{\frac{\pi m_e}{8 m_i}} \frac{\mathbf{k}\cdot\mathbf{u}_e}{(1 + k^2\lambda_{De}^2)^{3/2}}. \tag{3.16}$$

The above equation represents the analytic modified ion-acoustic dispersion relation. The wave-number that corresponds to the maximum growth rate is [85]

$$k_{max} = \frac{1}{\sqrt{2}\lambda_{De}} \tag{3.17}$$

which gives, subtituted in Eq. (3.16)

$$\omega_{max} = \mathbf{k}\cdot\mathbf{u}_i \pm \frac{\omega_{pi}}{\sqrt{3}} + i\sqrt{\frac{\pi m_e}{54 m_i}} \frac{u_e}{\lambda_{De}} \tag{3.18}$$

We can see that the growth rate is proportional to the electron drift velocity, and inversely proportional to the Debye length.

However, one should note that there is no consensus on the transition to an IAW. It could be attributed to non-linear resonance broadening, because the electron orbit is distorted, leading to the loss of the phase relation between the electron and the wave [44]. The electron demagnetization leads to a dispersion relation where the ions and the electrons have the same type of contribution. But recently, Janhunen et al. [106] stated that the demagnetization condition due to nonlinear resonance broadening is not fulfilled. Lafleur and Chabert [107] use the fact that in 2D simulations, the finite minimum value for the radial wave vector is responsible for the ion acoustic dispersion relation.

3.3 Solving the kinetic DR for general distribution functions

In order to solve the Dispersion Relation (DR) $\hat{\epsilon}(\mathbf{k}, \omega) = 0$ of Eq. (3.13), we solve for every $\mathbf{k}$ the complex value of ω that is a zero, also named a root, of $\hat{\epsilon}(\mathbf{k}, \omega)$. Hence, we first need to evaluate $\hat{\epsilon}(\mathbf{k}, \omega)$ for any given arguments $\mathbf{k}, \omega$. Then, we can find the root.

3.3.1 Numerical determination of $\hat{\epsilon}$

The calculation of Z, needed to determine $\hat{\epsilon}$, is usually done using the Maxwellian hypothesis [97] (hence using the Fried and Compte function Z_M), the kappa distribution [108], or other analytic expressions. We can also use a linear combination of such simple distribution functions, such as done in the software WHAMP in Rönnmark [109]. Here we propose to solve the dispersion relation $\hat{\epsilon} = 0$ using the distribution function measured in the PIC simulation.

The numerical computation of $|\hat{\epsilon}|$ is done using the method of Xie [105] for computing $\tilde{Z}$ the numerical approximation of Z. It uses the fact that Z is an Hilbert transform of the distribution function, and that the Hilbert transform can be changed to a Fourier Transform, weighted by well chosen basis functions, so the FFT algorithm can be used [110]. An interesting point is that the evaluation of $\tilde{Z}(\eta)$ is done by a polynomial function, which coefficients depend only on the distribution function f. Hence, they need to be determined only once, and evaluating $\tilde{Z}(\eta)$ is relatively fast.

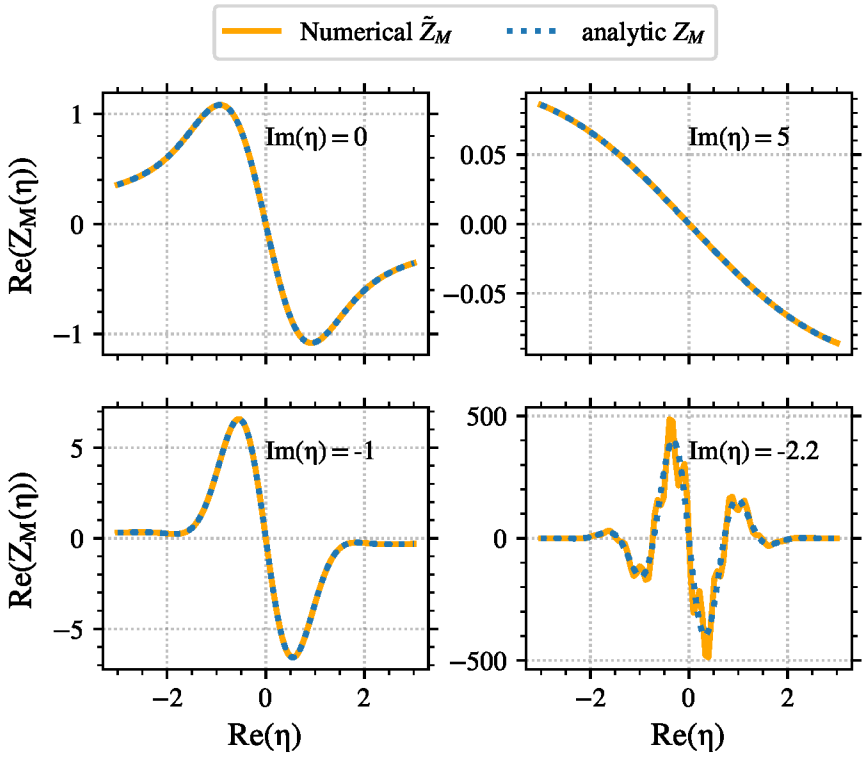

FIGURE 3.10 – Comparison of the numerical evaluation of $\tilde{Z}_M(\eta)$ for a Maxwellian distribution function with the Fried and Conte function (from the `plasmapy` python package) for different values of the imaginary part of η : $5, 0, -1$, and -2.2.

Fig. 3.10 shows the comparison of the numerical evaluation of $\tilde{Z}(\eta)$ for a Maxwellian distribution function with the Fried and Conte function (from the `plasmapy` python package) for different values of the imaginary part of η. We can see that for $\mathrm{Im}(\eta)$ positive, null or slightly negative, the two functions gives exactly the same results. However, for larger negative values of $\mathrm{Im}(\eta)$, the two functions gives different results.

This discrepancy between Z_M and $\tilde{Z}_M$ for large negative imaginary argument is certainly due to the fact that the analytic expansion of Z to the complex plane require the evaluation of the distribution function for complex velocities [105, 110]. However, the discrete velocity distribution function measured in the PIC simulation cannot be properly evaluated for complex velocities. On the other hand, we are only interested in instabilities, with positive growth rate. Hence, the discrepancy observed should not affect the conclusions of the study.

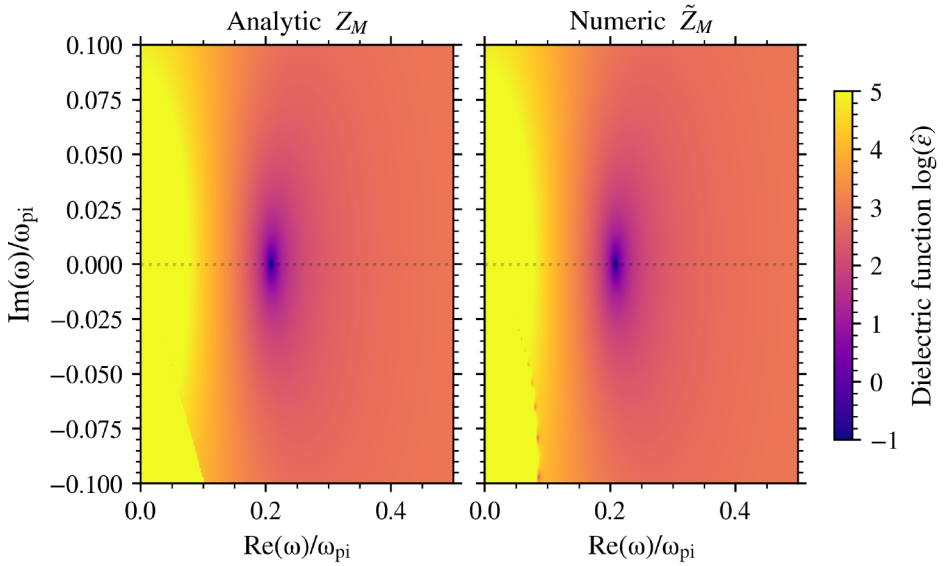

FIGURE 3.11 – Comparison of the numerical evaluation of $\hat{\epsilon}$ from Eq. (3.13) for a Maxwellian distribution function with (left) the Fried and Conte function (from the `plasmapy` python package) and (right) the numerical $\tilde{Z}$, in logarithmic scale.

Figure 3.11 presents the comparison of the calculation of $\hat{\epsilon}$ from Eq. (3.13) for a Maxwellian distribution function with (left) the Fried and Conte function (from the 'plasmapy' python package) and (right) the numerical $\tilde{Z}$. We can see that the root with the greater imaginary part, located close to (0.2, 0), is the same in both cases, but that other roots for large negative imaginary part are not similar. But as said previously, these roots are of no interest for our problem, hence the DR should be well computed using $\tilde{Z}$.

3.3.2 Finding the root of $\hat{\epsilon}$

Now that we can compute $\hat{\epsilon}$, we can solve the dispersion relation. In order to find the root (the zeros) of $\hat{\epsilon}$, two methods have been tested.

Exact root finding algorithm

The first approach has the advantage of finding all of the roots in a given domain. It uses Cauchy's argument principle in order to determine the number of roots in a given domain by integrating over the domain contour

$$N - P = \frac{1}{2i\pi} \int_C \frac{\hat{\epsilon}'(\omega)}{\hat{\epsilon}(\omega)} d\omega \tag{3.19}$$

where N and P denote the number of roots and poles in the contour C. Supposing that there are no poles, we either have

1. $N = 0$, hence no roots are presents in the domain,
2. $N = 1$, exactly one root is present,
3. $N > 1$, there are more than one root present.

Starting from a large rectangular domain, if $N > 1$, we divide the first domain into four sub-domains, and we repeat recursively the algorithm. If $N = 1$, we can once again use an integral on the contour to find the root [111].

This algorithm has been implemented in a python package and successfully tested. However, it takes a significant amount of time to obtain the solutions, as $\hat{\epsilon}$ needs to be evaluated several times during the integration. Moreover, we have observed that the dispersion relations Eqs. (3.13) and (3.16) present only one solution with a positive growth rate. This solution, corresponding to the instability, is isolated from the others as observed in Fig. 3.11. Hence, a simpler algorithm, as the Gradient descent, can be used.

Fast root finding algorithm

A faster root finding algorithm is proposed to solve the dispersion relation by supposing that the wave growing the most is the only root over a domain sufficiently large. In other words, it is not close to other roots. Hence, we can use a standard minimization method for non-linear equation. As the analytic expression of the Hessian or the gradient are unknown, we use the Nelder-Mead method [112]. We also tried the Conjugate gradient method by approximating the gradient using finite differences. However, even if this method converges in fewer steps, the gradient estimation takes a significant amount of time. Powell's method [113] has also been implemented, but the Nelder-Mead method features the best performances.

The first guess of the iterative Nelder-Mead method is either

— the solution obtained for the previous value of $\mathbf{k}$,

— the solution of the analytic ion acoustic wave dispersion relation (Eq. (3.16)).

In addition, we can see in Fig. 3.11 that the interesting root is far from the others in the complex plane. Hence, a poor initial guess should not affect significantly the converged results, as long as the step size is small enough. The results presented hereafter have been obtained using this second faster algorithm.

3.3.3 Use of analytic distribution functions

Before using the electron and ion distribution functions measured in the PIC simulations, we compare the dispersion relation for ECDI and IAW for different analytic distribution functions.

Ion acoustic wave

Figure 3.12 shows the comparison with the dispersion relation Eq. (3.15) for cold ions and drifting Maxwellian electrons of temperature $\mathrm{T_e} = 50\,\mathrm{V}$ and drift velocity $u_e = 2{\times}10^6\,\mathrm{m/s}$ for which the plasma dispersion function Z_M is computed analytically (with the `plasmapy` package) or numerically. The plasma density is $n_e = n_i = 1{\times}10^{17}\,/\mathrm{m}^3$. The frequency and growth rate obtained using the simplified dispersion relation of Eq. (3.16) is also shown.

We can see that the three approaches give almost the same solutions. The growth rates are all overlapping, hence it is difficult to see the differences. For ω_r, the simplified analytic expression returns a slightly different result, but the difference is negligible. The numerical evaluation of $\tilde{Z}_M$ gives the same result as the analytic evaluation.

Figure 3.13 shows the effect of a Druyvesteyn electron distribution compared to a Maxwellian. We recall that a Druyvesteyn distribution follows the expression

$$f_D(v) = v_{th}^{-1} C2 \exp\left(-C1 \frac{|v|^4}{v_{th}^4}\right), \tag{3.20}$$

where $C1 \simeq \Gamma(3/4)^2\Gamma(5/4)^{-2}/4 \simeq 0.457$ and $C2 = \Gamma(3/4)^{1/2}\Gamma(5/4)^{-3/2}2^{-3/2} \simeq 0.453$ are two normalizing constants, so that the density and the thermal velocity v_{th} are consistent with the Maxwellian distribution. The electron density used is $n_e = 1{\times}10^{17}\,\mathrm{m}^{-3}$ and the electron temperature is $\mathrm{T_e} = 50\,\mathrm{V}$, the ion temperature is $\mathrm{T_i} = 0.1\,\mathrm{V}$, and the drift velocity is $u_e =$

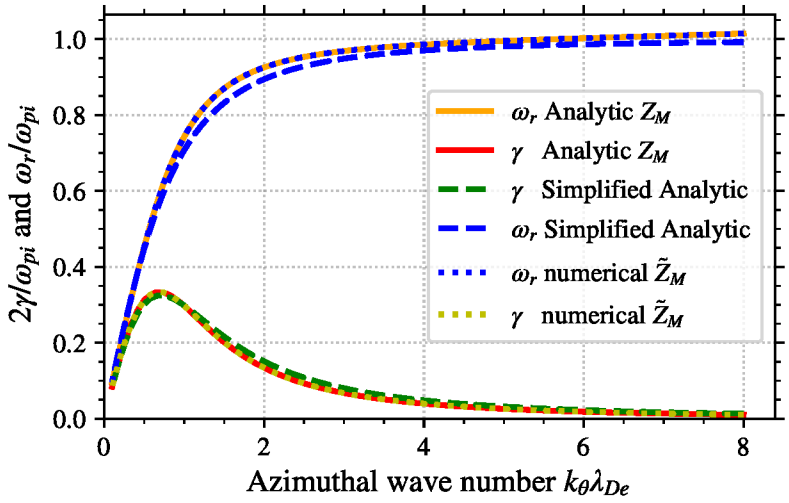

FIGURE 3.12 – IAW frequency ω_r and growth rate γ (scaled by a factor of two) for a Maxwellian distribution function using the Freid and Conte function (labelled Analytic Z_M), the numerical estimation of $\tilde{Z}_M$, and the simplified analytic expressions of Eq. (3.16).

1.8×10^6 m/s $\simeq 300c_s$ with $c_s = \lambda_{De}\omega_{pi} \simeq 6$ km/s. We see in Fig. 3.13 that the impact of the Druyvesteyn Electron Velocity Distribution Function (EVDF) on the IAW dispersion relation is small, except that the maximum growth rate is decreased by 15%.

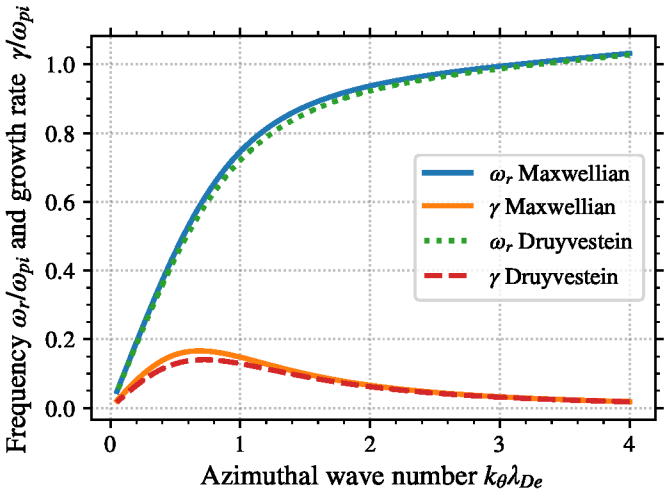

FIGURE 3.13 – IAW frequency and growth rate for a Maxwellian distribution function using the Freid and Conte function and a Druyvesteyn distribution evaluated with the numerical estimation of $\tilde{Z}$.

Figure 3.14 shows the evolution of the most growing wave with the electron drift velocity for both the Maxwellian and the Druyvesteyn EVDF. An illustration of the two distribution functions with a drift equal to the thermal velocity can be seen in Fig. 3.14.**b**. We see that, as obtained in the analytic dispersion relation Eq. (3.16), the growth rate is proportional to the drift velocity when $u_e \ll v_{th}$. In addition, the wave corresponding to the maximum growth rate depends only weakly of the drift velocity, and we find a good agreement with the analytic values $k_\theta\lambda_{De} = 1/\sqrt{2} \simeq 0.707$ and $\omega/\omega_{pi} = 1/\sqrt{3} \simeq 0.577$. Lastly, the shape of the EVDF seems to affect only weakly the result.

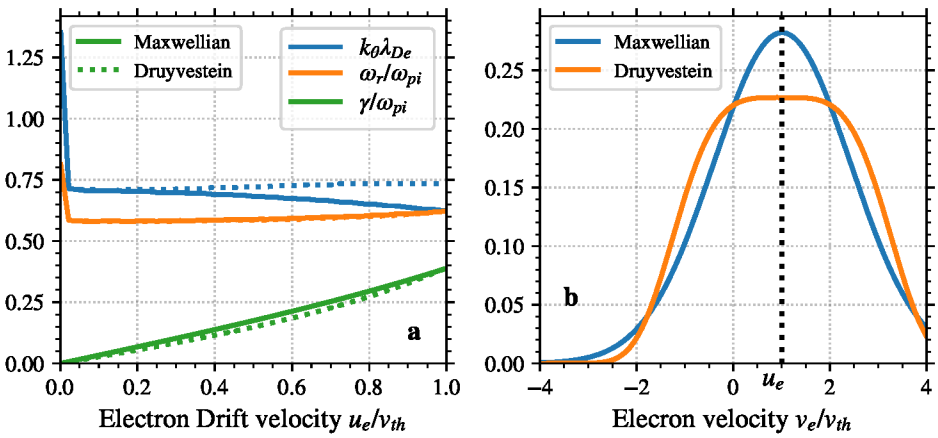

FIGURE 3.14 – (**a**) Evolution as a function of the electron drift velocity u_e of the maximum growth rate γ and the corresponding wavenumber k_θ and frequency ω of the IAW for both a Maxwellian and a Druyvesteyn EVDF, supposing the ions Maxwellian ;(**b**) the two distribution function for $u_e/c_s = 300$.

Electron Cyclotron Drift instability

Figure 3.15 shows the frequency and the grow rate for the ECDI, defined by Eq. (3.13), in the same conditions that the IAW results, with $k_r\lambda_{De} = 0.05$. The infinite sum over the cyclotron resonances is stopped at $N_{max} = 20$. We see in Fig. 3.15 that the cyclotron resonances are present for both distribution functions, and the wave frequency and the growth rate are not much affected by the shape of the EVDF. For very small radial wavenumber, the numerical resolution crashes, as the argument in $Z(\eta)$ diverges. However, in the limit $\eta \to \infty$, $Z(\eta) \to \frac{1}{\eta}$. Hence, we still obtain the cyclotron resonances, as shown in Janhunen et al. [65, Fig. 2].

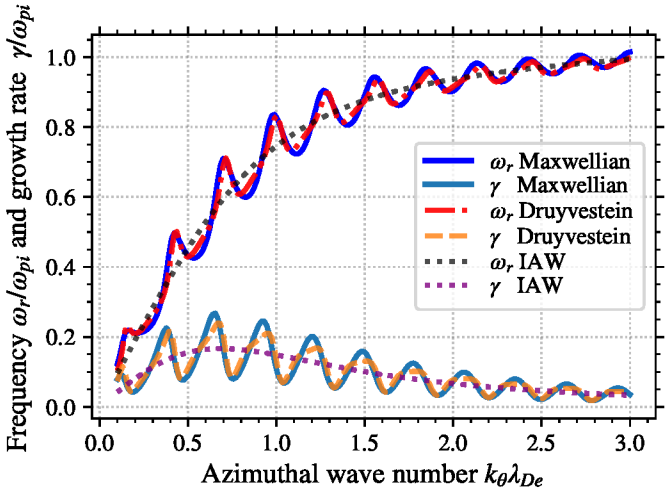

FIGURE 3.15 – ECDI frequency and growth rate for a Maxwellian distribution function using the Freid and Conte function and a Druyvesteyn distribution evaluated with the numerical estimation of $\tilde{Z}$, the radial wave number is $k_r\lambda_{De} = 0.05$. The IAW DR using Maxwellian VDFs is shown

We also see in Fig. 3.15 that the ECDI DR presents the resonances around the IAW DR. This is why in case of resonance broadening, the ECDI converged toward a IAW-like dispersion relation.

3.4 Comparison of the DR with the PIC simulations

In this section, we continue to analyze the simulation results described in Section 3.1. First, we described in Section 3.4.1 the velocity distribution functions (VDF) measured in the simulation. Then, we solve the relation dispersion with the measured VDFs, for both the ECDI (Eq. (3.13)) and the IAW waves (Eq. (3.15)), with the solved developed in Section 3.3.

3.4.1 Temporal evolution of the distribution functions in the PIC simulation

To begin with, we visualize and comment the distribution functions measured in the PIC simulation. Figure 3.16 shows at different times in the simulation the normalized electron azimuthal velocity distribution functions (the ion VDF is showed in Fig. 3.17). The velocities are normalized by the electron thermal velocity. To help reading the figure, the theoretical electron drift velocity $u_e = \frac{E_z}{B_r}$, normalized to the electron thermal velocity is shown. The distributions are averaged in time over 4 ns, and in space over all the azimuthal direction and over a small length in the radial direction at the center of the channel, between $r = 0.45\,\text{cm}$ and $r = 0.55\,\text{cm}$.

We can see in Fig. 3.16 that the electron mean velocity is always near the $E \times B$ drift velocity, which is of the order of one quarter of the electron thermal speed. The shape of the distribution functions is slightly different from the Maxwellian distribution, with smaller maximum and a wider distribution, similarly to a Druyvesteyn distribution.

Figure 3.17 shows at different times in the simulation the normalized ion azimuthal velocity distribution functions. As in Fig. 3.16, the mean velocity is shows, and a Maxwellian distribution of same density, mean velocity and temperature is shown.

At the beginning of the simulation the ions are Maxwellian with a zero mean velocity. Starting from $t = 0.8\,\mu\text{s}$, the ions are dragged in the same direction as the electron drift. This is characteristic of the ion-wave trapping [107]. Consequently, the ion distribution function is significantly different from the Maxwellian. Indeed, because of the particle-wave interactions a small population of high energy ions is generated. This leads to both an increase of the ion temperature, and the formation of a drift velocity in the azimuthal direction. The high energy ion population comes from ion-wave trapping, as we can see that their velocity is of the order of the ion sound speed, which is close to the wave phase velocity [87]. We can see that the trapped population is larger at $t = 1.6\,\mu\text{s}$ compared to $t = 2.44\,\mu\text{s}$. This is consistent with the discussion of Section 3.1.5, as we can see in Fig. 3.9 that at $t = 1.4\,\mu\text{s}$ the ion temperature is large, and the wave energy density ϵ_{wave} is large compared to the thermal energy density ϵ_{th}, while at $t = 2.4\,\mu\text{s}$ the ion temperature is small and we have $432\epsilon_{\text{wave}} \simeq \epsilon_{\text{th}}$.

As both electron and ion velocity distribution functions are different from a drifting Maxwellian, we will study the influence of both distributions in the calculations of the dispersion relation.

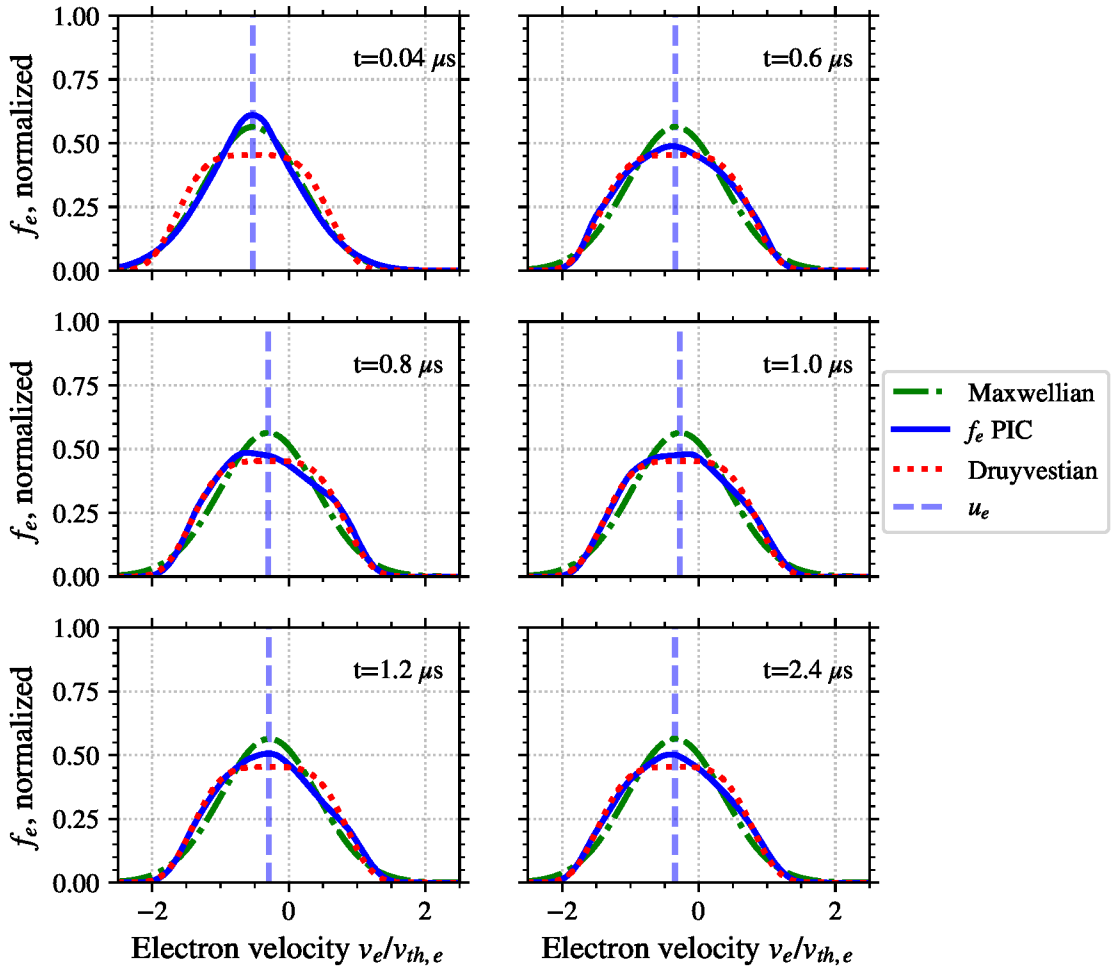

FIGURE 3.16 – (solid blue) Electron normalized azimuthal velocity distribution functions at different times of the simulation. The velocity is normalized by the electron thermal velocity ; (dashed light blue) The theoretical $E \times B$ drift velocity of the electrons $u_e = \frac{E_z}{B_r}$; (dotted-dashed green) Maxwellian distribution function with the same density, mean velocity and temperature as the measured EVDF.

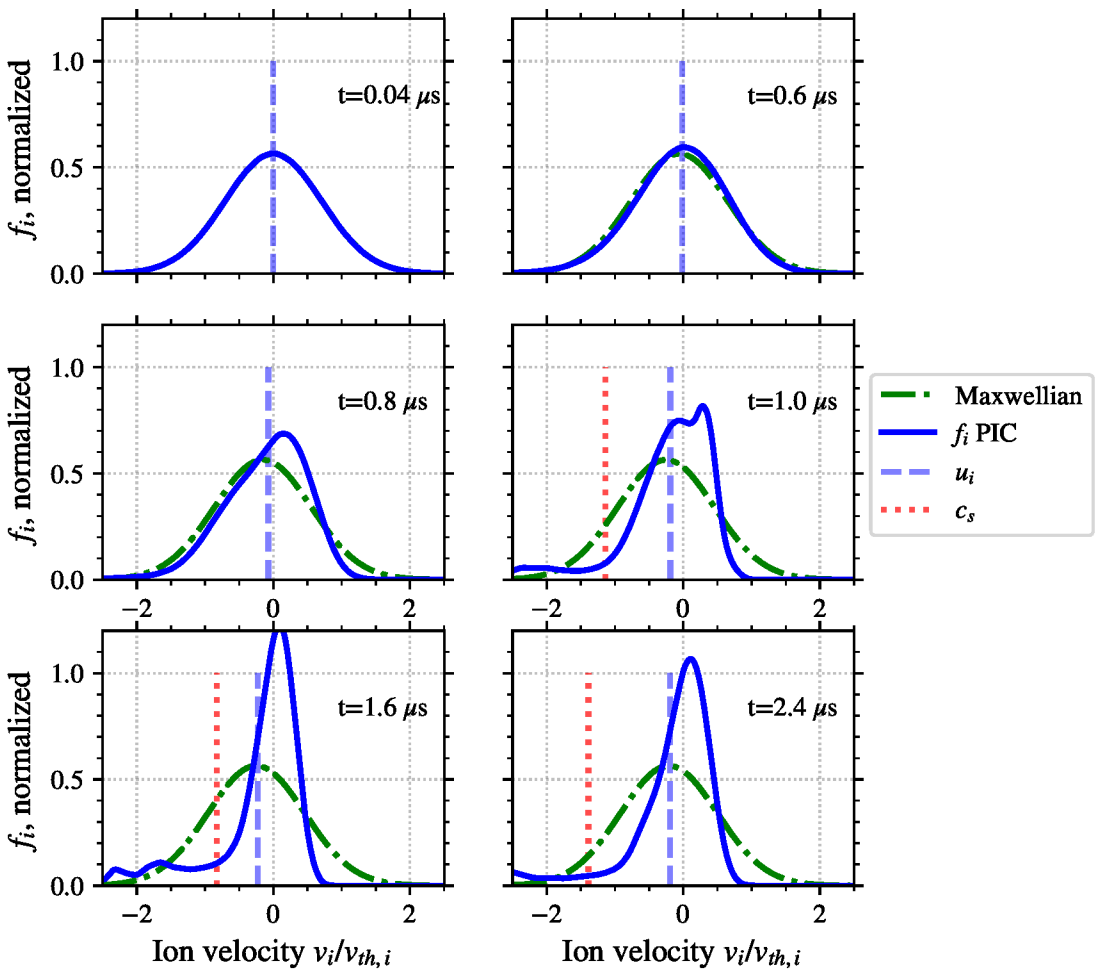

FIGURE 3.17 – Electron and ion normalized azimuthal velocity distribution functions at different times of the simulation. The velocity is normalized by the thermal speed of the corresponding species. The theoretical $E \times B$ drift velocity of the electrons $u_e = \frac{E_z}{B_r}$, and the ion sound speed c_s normalized by the ion thermal velocity are also displayed.

3.4.2 Resolution of the electron cyclotron drift instability

As observed in Section 3.1, the simulation begins with a linear growth of the instability. Previous results obtained with *LPPic* [18] showed no cyclotron resonances (also known as Bernstein resonances) during this period. However, these results were obtained with Lafleur's convection model, as introduced in Section 2.5. Here, the results were obtained with the modified model, inducing less noise.

We can see in Figure 3.18 a snapshot of the plasma potential fluctuation in the azimuthal direction

$$\delta\phi(r,\theta) = \phi(r,\theta) - <\phi(r,\theta)>_\theta,$$

at four different times during the growth of the instability. For these results, we increased the azimuthal length L_θ from 2.5 to 6.2 mm compared to the simulations of Section 3.1, so that the instability characteristics, as the wavenumber k_θ, are better resolved. We observe no significant differences on the simulation results. However, the simulation time is doubled in this case, so only the first microsecond have been simulated.

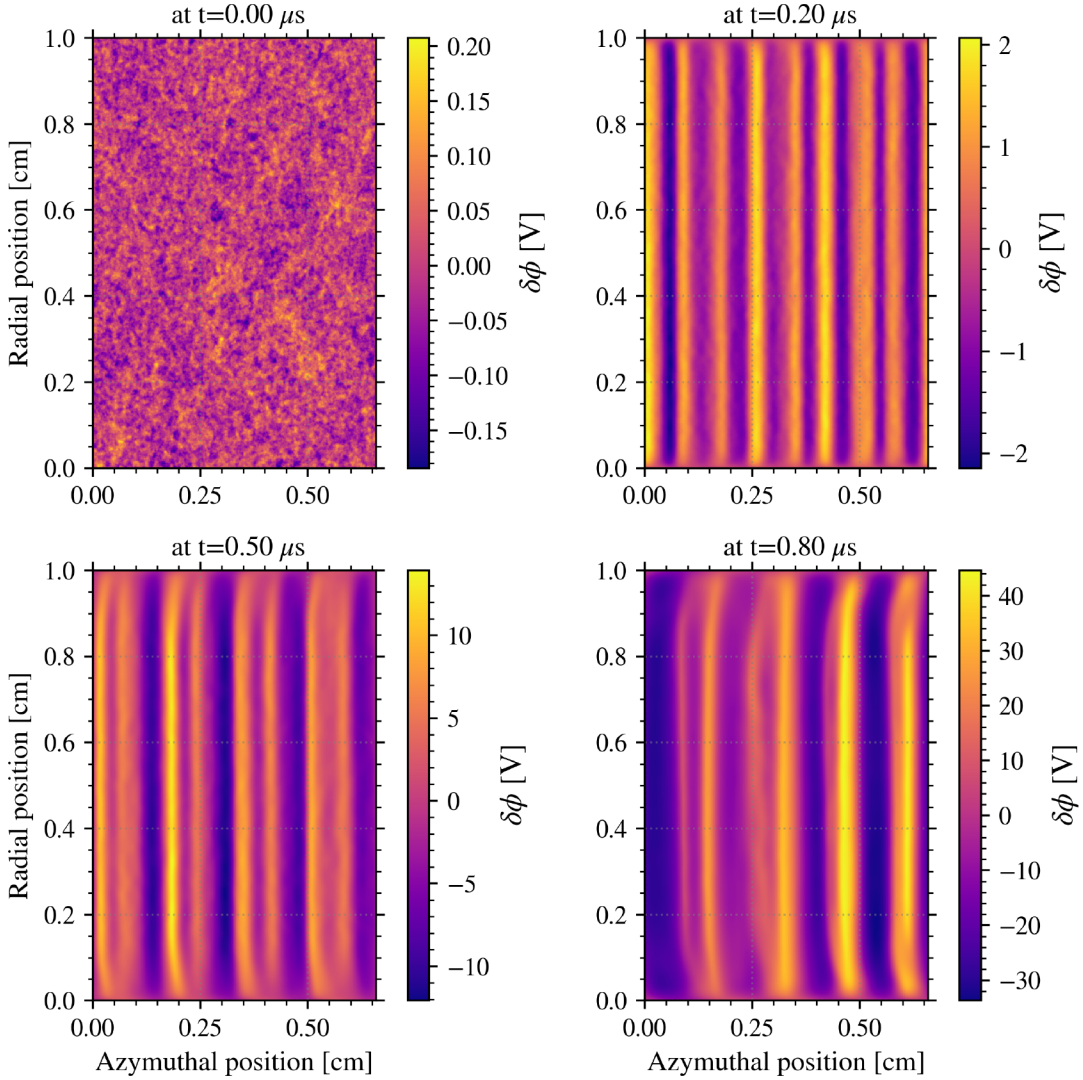

FIGURE 3.18 – Radial-azimuthal distribution of the oscillation of the plasma potential $\delta\phi(r,\theta) = \phi(r,\theta) - <\phi(r,\theta)>_\theta$ at different times during the linear phase of the simulation using an increased azimuthal length. The frequency spectra of each snapshot is shown in Fig. 3.19.

At the beginning, we see fluctuations that can be due to both thermal fluctuation [114] or numerical noise due to particle discretization. Then, the instability rises. We can see that it starts

with small wavelength ($\lambda \simeq 0.75\,\text{mm}$ at $t = 0.2\,\mu\text{s}$). After a short period, the short wavelength waves merge to form longer wavelength waves ($\lambda \simeq 1.5\,\text{mm}$ at $t = 0.7\,\mu\text{s}$).

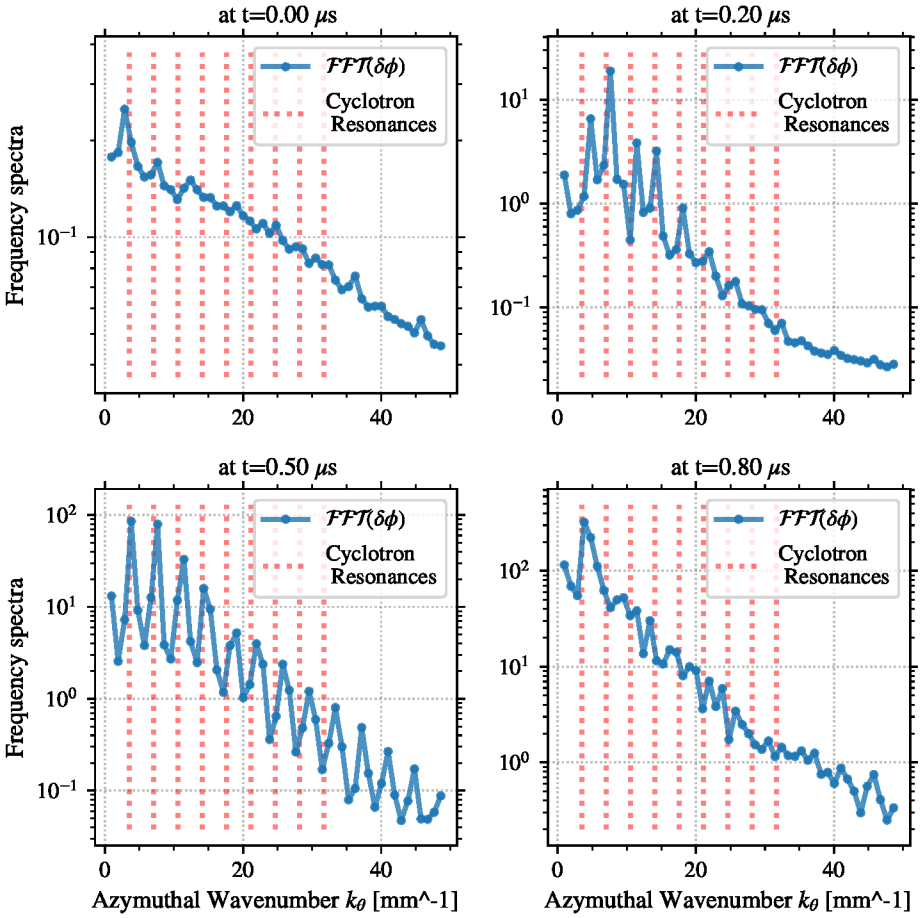

FIGURE 3.19 – Frequency spectra on the azimuthal instability presented in Fig. 3.18. Each spectrum is averaged in the radial direction. The red dotted lines represent the cyclotron resonances $k_\theta = n\dfrac{\omega_{ce}}{u_e}$ with $n \in \mathbb{N}$.

The evolution of the instability is also clearly seen on the frequency spectra, showed in Figure 3.19. The spectra are obtained with the FFT algorithm, and are averaged in the radial direction. We can see in the spectra the resonances at multiple of the cyclotron wavenumber $k_0 = \frac{\omega_{ce}}{u_e} \simeq 3.5\,\text{mm}^{-1}$. At $t = 0.2\,\mu\text{s}$, the most dominant mode is the second resonance, but the other resonances are also present. At $t = 0.5\,\mu\text{s}$, all the resonances are distinguishable, but their amplitude is strictly decreasing. Then, at $t = 0.8\,\mu\text{s}$, we can no longer see the resonances, except for the first one.

We now solve the ECDI dispersion relation of Eq. (3.13) for $t = 0.2, 0.4$ and $0.7\mu\text{s}$ using both the Maxwellian hypothesis for the ions and electrons, and the velocity distribution functions measured in the PIC simulations. The radial wavenumber taken is $k_r = 2\pi/L_R \sim 0.6/\text{mm}$ [85, 65]. This value corresponds to $k_r\lambda_{De} = 0.036$ at $t = 0.2\,\mu\text{s}$ and $k_r\lambda_{De} = 0.044$ at $t = 0.7\,\mu\text{s}$, as the electron temperature increases.

We can see in Figure 3.20 that the dispersion relation shows the cyclotron resonance at the beginning. However, the most growing wavelength is not the second harmonic, but the fourth. After $t = 0.5\,\mu\text{s}$, the resonances broaden, and disappear. This is in agreement with the measured spectra in Fig. 3.19, as no resonances are present at $t = 0.8\,\mu\text{s}$. This is correlated to the increases of the electron temperature, that increases the Debye length λ_{De} and hence affects the radial

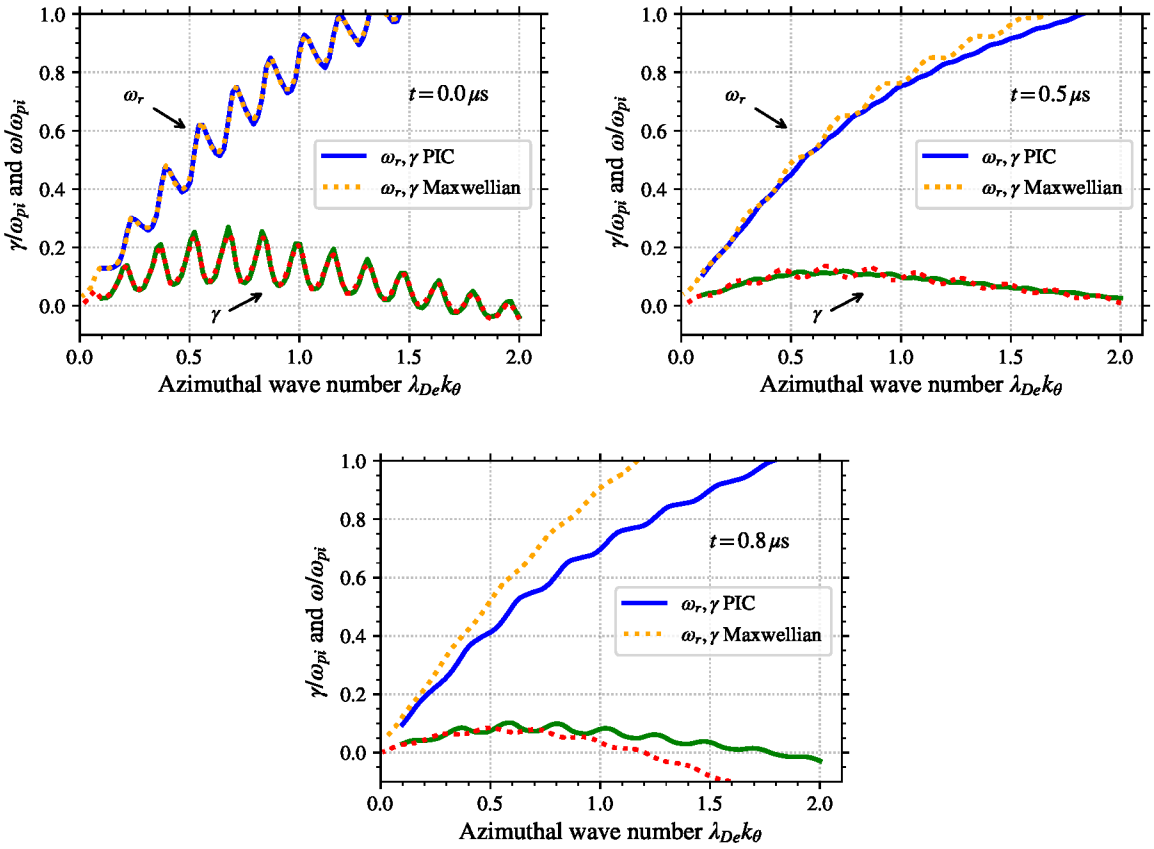

FIGURE 3.20 – Dispersion relation for the ECDI using (dotted lines) the Maxwellian hypothesis for the ions and electrons, and (solid lines) the velocity distribution functions measured in the PIC simulations. The wavenumber is normalized by the Debye length, and the pulsation and the growth rate are normalized to the ion pulsation frequency.

wave number [4, 36, 97]. The value of radial wavelength is discussed later in Section 3.5.

We can also observe that the deviation of the distribution function from the Maxwellian affects the DR. This has also been observed in an axial-azimuthal PIC simulation by Lafleur et al. [87]. This confirms that the exact distribution function should be used in the calculation of the dispersion relation, especially to determine the growth rate. Figure 3.21 shows a comparison of the 2D FFT of the azimuthal electric field FFT(E_θ) measured in the simulation computed between $t = 0.6\,\mu s$ and $t = 1.2\,\mu s$ with the three dispersion relations:

— the ECDI general DR obtained with the PIC EVDF at $t = 0.6\,\mu s$,
— the ECDI DR obtained with the Maxwellian hypothesis,
— the IAW DR using the analytic expression Eq. (3.16).

The two first DR are already showed in Fig. 3.20 with there corresponding growth rates.

From Figure 3.21, we can see that the instability observed in the PIC simulation does follow the ECDI DR with a very good correspondence. However, the differences between the three DR are not significant, compared to the resolution of the 2D FFT. On top of that, the IAW DR returns almost the same values than that of the ECDI DR, as the resonances are no more present. Therefore we will use the IAW DR in the next section.

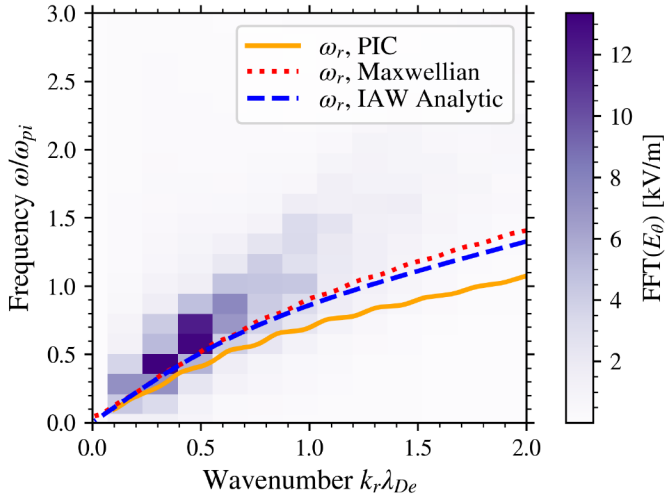

FIGURE 3.21 – Comparison of (purple image) the 2D FFT of the azimuthal electric field (E_θ) computed between $t = 0.6$ and $t = 1.2\,\mu s$ and averaged over the radial direction with the following dispersion relation: (orange solid) ECDI general DR obtained with the PIC VDFs at $t = 0.8\,\mu s$; (dotted red) ECDI DR obtained with the Maxwellian hypothesis; and (dotted blue) IAW DR using the analytic expression Eq. (3.16).

3.4.3 Resolution of the ion acoustic wave dispersion relation

We have seen in the previous Section 3.4.2 that the full ECDI dispersion relation is not needed, but can instead be approximated by the IAW [87, 65, 44]. The IAW relation can be solved with several hypotheses (see Section 3.2.1 for more details)

1. Simplified analytical values,
2. Maxwellian electrons, cold ion ($T_i = 0\,V$),
3. Maxwellian electrons and ions ($T_i > 0\,V$),
4. Non-Maxwellian electrons, Maxwellian ions ($T_i > 0\,V$),
5. Non-Maxwellian electrons and ions.

In the following, we will use all these cases and compare them to the PIC simulation results. We want to obtain the temporal evolution of the solution. In practice, we will only follow the evolution of the most growing wave. In order to find the most growing wave, we solve the dispersion relation for different values of k. Over all of the solutions obtained, we select the one corresponding to the maximum value of γ. We use 200 points between $k_\theta\lambda_{De} = 0.02$ and $k_\theta\lambda_{De} = 2$. Figure 3.22 illustrates how we select this dominant mode for one specific simulation time used for three different cases. We can see the maximum of the growing rate, and its frequency.

This process is repeated for the whole duration of the simulation. The velocity distribution functions, when used, are obtained from the PIC simulation the same way as in Section 3.4.1. Figure 3.23 shows the temporal evolution of the three characteristics of the most growing wave: the growth rate γ, the azimuthal wavenumber k and the frequency ω.

Three different behaviors are observed depending on the hypotheses used. First, the solution of the dispersion relation with Maxwellian electrons and cold ions (dashed green line in Fig. 3.23) presents a solution of ω and k constant in time, and very close to the analytic values, being $k_\theta\lambda_{De} = 1/\sqrt{2}$ and $\omega_r = \omega_{pi}/\sqrt{3}$. However, it also presents a constant growth rate.

Secondly, we observe that the solutions assuming Maxwellian ions of non-zero temperature are relatively similar for both the Maxwellian electrons (dotted red line) and using the electron velocity distribution function measured in the PIC simulation (dash-dotted orange line). In these cases, the growth rate decreases regularly to zero. Interestingly, the periods during which the growth rate is zero (firstly between $t = 1\,\mu s$ and $t = 2\,\mu s$, then around $t = 3\,\mu s$ and so on)

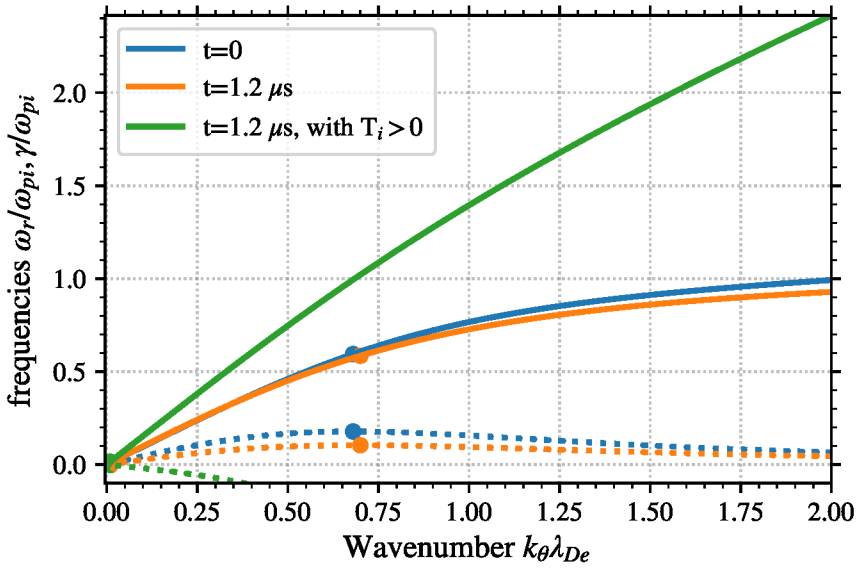

FIGURE 3.22 – Illustration of the IAW dispersion relation obtained at two different time ($t = 0$ and $t = 1.2\,\mu s$), (solid line) the wave frequency ω, and (dotted line) the growth rate γ, using the hypothesis of Maxwellian distribution functions for both electrons and ions. The electron temperature measured in the simulation is always used, but the ion temperature is only used once. The most growing solution is marked with a circle on the growth rate and the frequency.

correspond precisely to the periods during which the wave energy density decreases in Fig. 3.8. With the Maxwellian hypothesis, the decrease of the growth rate is only be due to the ion temperature, which corresponds to ion Landau damping. However, we must note that the value of the ion temperature T_i is mainly due to the population of ions trapped, as seen in Section 3.4.1.

To finish with, we solve the IAW dispersion relation without any hypothesis on the velocity distribution functions, by using the VDF measured in the PIC simulations (blue solid line in Fig. 3.23). In this case, the beginning ($t < 1\,\mu s$) is quite similar to the other results. Then for $t > 1\,\mu s$, the growth rate oscillates slightly around a mean value that is below the solution with cold ions, but above the result with warm ions. In order to determine which solution is the closest from the observation, we estimate the growth rate in the PIC simulation with the wave equation

$$\frac{\partial W_{\mathrm{PIC}}}{\partial t} + \nabla \cdot (\mathbf{u}_i W_{\mathrm{PIC}}) = 2\gamma_{eff} W_{\mathrm{PIC}} \tag{3.21}$$

with $W_{\mathrm{PIC}} = \sigma^2_{E_\theta}\epsilon_0/2$ the electrostatic wave energy measured in the PIC simulation. The spatial derivative can been approximated across the axial simulation direction by

$$\nabla \cdot (\mathbf{u}_i W_{\mathrm{PIC}}) = \frac{W_{\mathrm{PIC}} v_{i,\mathrm{out}}}{L_z}, \tag{3.22}$$

with $v_{i,\mathrm{out}}$ the ion outlet velocity

$$v_{i,\mathrm{out}} = \sqrt{\frac{2eU_z}{m_i}}, \tag{3.23}$$

with $U_z = E_z L_z$ the total potential difference in the axial direction. Therefore, the growth rate measured in the PIC simulation is

$$\gamma_{eff} = \frac{\partial_t W_{\mathrm{PIC}}}{W_{\mathrm{PIC}}} + \frac{v_{i,\mathrm{out}}}{2L_z}. \tag{3.24}$$

The effective azimuthal wave number k_{eff} is estimated by Fourier transform averaged in the the radial direction between $r = 0.4$ and $r = 0.6\,\mathrm{cm}$. Figure 3.24 shows the comparisons between the results of the dispersion relations and the PIC simulation results.

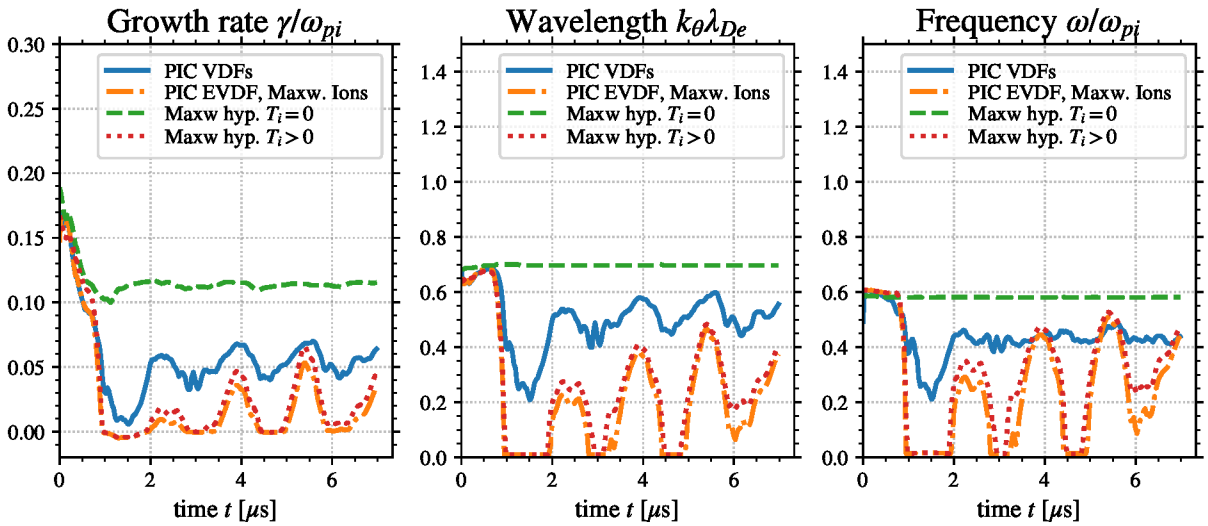

FIGURE 3.23 – Temporal evolution of the growth rate γ, the azimuthal wavenumber k and the frequency ω for the most growing wave, obtained with several hypotheses on the dispersion relation. See text for more details.

Figure 3.24.**a** shows the temporal evolution of the growth rate of the most growing mode (similar to the left panel of Fig. 3.23) obtained with the relation dispersion, and γ_{eff} the growth rate measured in the PIC simulation using Eq. (3.24). The value of γ_{eff} is averaged using a Gaussian kernel of standard deviation $\tau = 12\,\text{ns}$. We see in Fig. 3.24 that γ_{eff}, the growth rate measured in the simulation, follows the expected trend with an initial phase ($t < 1\,\mu\text{s}$) of growth, and then the oscillations with growing and damping phases. The values of γ_{eff} are closer to the growth rate obtained with the Maxwellian hypothesis and a non-zero ion temperature (label "Maxw, $T_i > 0$" in Fig. 3.24), compared to the values obtained with the PIC VDFs or with cold ions (label "Maxw, $T_i = 0$").

Figure 3.24.**b** shows the temporal evolution of the main wavenumber measured in the simulation and the wavenumber of the most growing mode obtained with the relation dispersion (similar to the central panel of Fig. 3.23). We see that the wavenumber of the instability observed in the simulation is of the good order of magnitude, and that is is in good agreement with the result of the DR that uses the velocity distribution functions measured in the simulation.

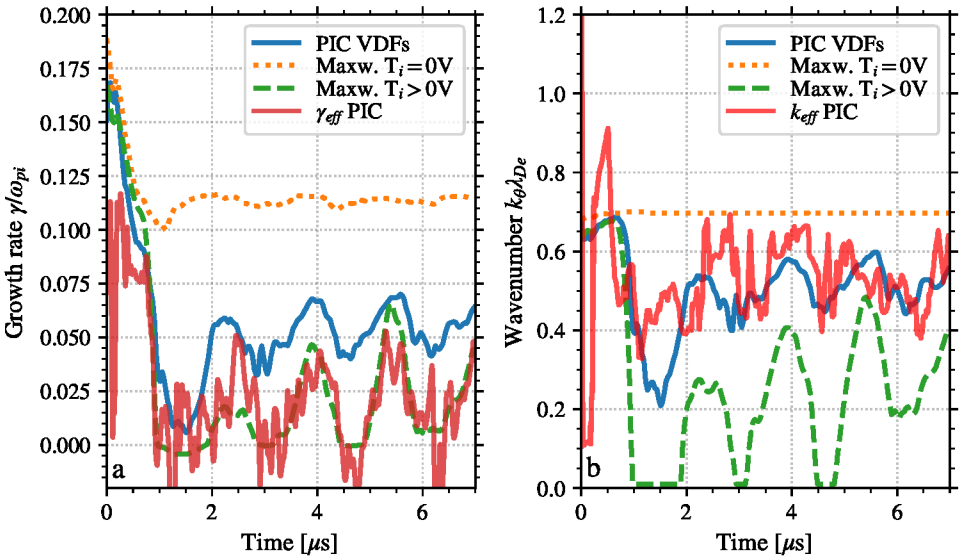

FIGURE 3.24 – Temporal evolution of (**a**) the growth rate and (**b**) the main wavenumber (red solid line) measured in the simulation using Eq. (3.24), and computed with the DR using (blue solid line) the VDF measured in the PIC simulation, (dotted orange line) the Maxwellian hypothesis with $T_i = 0\,V$, (dashed green line) the Maxwellian hypothesis with non-zero temperature ions. The result of the three DR are the same as in Fig. 3.23.

3.5 Discussion on the radial wavenumber

In the ECDI dispersion relation introduced in Section 3.2, the radial wavenumber must be non-zero. Hence, in Section 3.4, we have chosen a wavelength that fits between the two walls. On the other hand, the oscillation seen in Fig. 3.18 does not seem to present any oscillation in the radial direction. In this section, we investigate the interaction between the azimuthal instability and the wall in the radial direction.

3.5.1 Radial profile of the oscillation

In this section, we analyze the radial profile of the azimuthal instability described in the previous sections. Figure 3.25 shows the amplitude of the azimuthal instability on the plasma potential. It is defined as

$$\delta\phi^2 = 2\sigma_\phi^2 = \frac{2}{L_\theta}\int_0^{L_\theta} (\phi - <\phi>_\theta)^2\, d\theta, \tag{3.25}$$

Fig. 3.25 shows on the left the mean plasma potential $<\phi>$ averaged in time and in the azimuthal direction , and the amplitude of the fluctuation at each radial position. We see for $<\phi>$ the usual profile with the sheaths close to the wall characterized by a steep potential drop, and the presheaths in the plasma bulk with a more gentle variation. However, we see no radial pattern in the plasma potential nor the amplitude of the azimuthal plasma potential oscillation.

On the right panel of Fig. 3.25, we see the relative instability amplitude with respect to the mean plasma potential $\delta\phi/<\phi>$, in percent. We see that the amplitude of the oscillation follows the mean value of the plasma potential. Indeed, except close to the wall where ϕ reaches zero, the amplitude of the oscillation is approximately 8% of ϕ in all of the simulation domain. The oscillation to mean value ratio is compared to the analytic $\delta\phi \propto \sin(\pi\frac{r}{L_R})$ in Fig. 3.25. The sin profile corresponds to a radial wavelength twice as large large as the radial width. We can see that the sin profile decreases much faster toward the wall, compared to the simulation result.

The same constant ratio between the amplitude of the oscillation and the mean value is observed in the ion density, that can be seen in Figure 3.26. As a mater of fact, the phenomenon

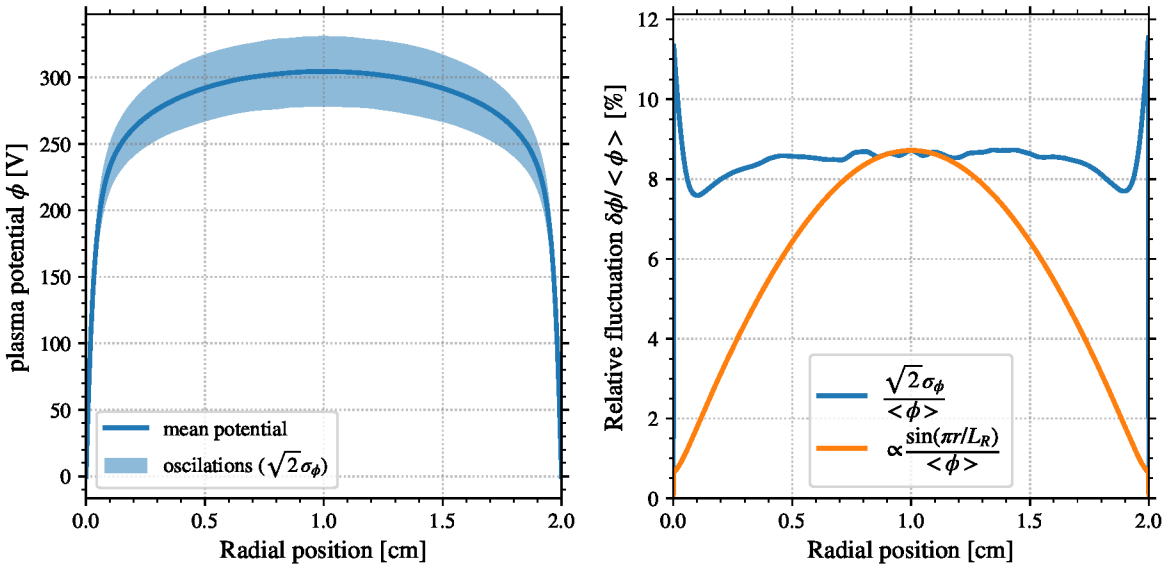

FIGURE 3.25 – (Left) Radial profile of the mean plasma potential averaged in the azimuthal direction and in time during the steady-state of the simulation ($t > 3.5\,\mu s$) and the average azimuthal instability amplitude. (Right) radial profile of the relative importance of the amplitude of the fluctuation to the mean plasma potential $< \phi >$.

is even more pronounced on the ion density, as the ratio $\delta n_i/n_i$ presents a radial profile almost constant everywhere, even at the wall. It can be explains by the fact that the ions reach the wall with a supersonic speed, so that the wall does not directly affect the ions.

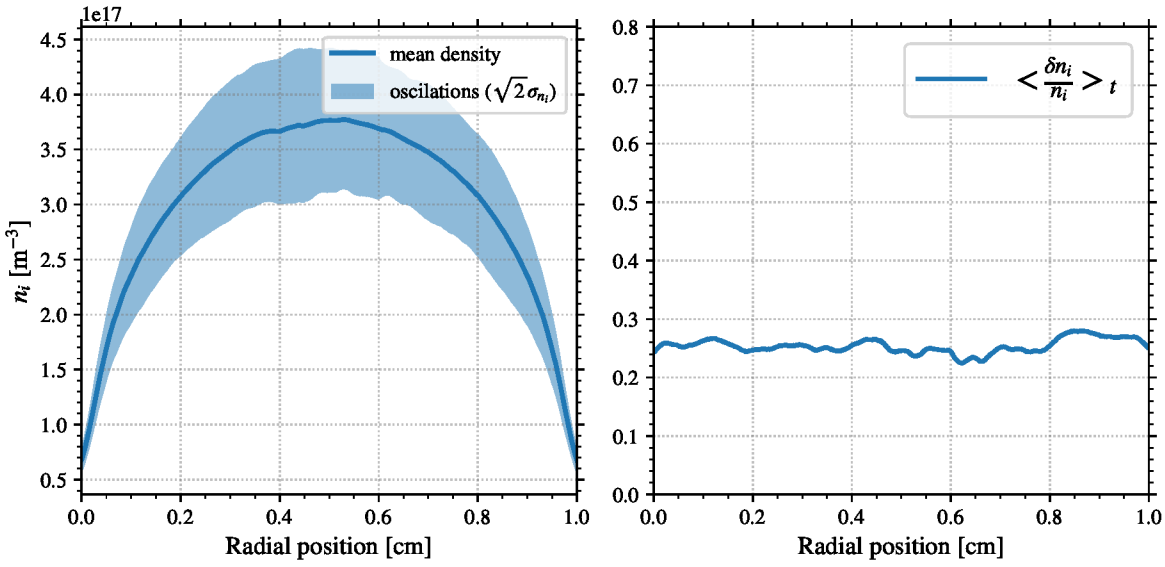

FIGURE 3.26 – Radial profile of (left) the mean ion density profile and δn_i the fluctuation amplitude and (right) the ratio between δn_i and n_i.

The fact that the amplitude of the oscillation is proportional to the mean azimuthal value may suggest that the sheaths significantly screen the oscillation from the walls . Therefore, the instability is not affected by the walls. A screening of the wall has been observed in Janhunen et al. [65], where the authors observed radial structures of wavelength larger than the radial length. However, here we observe no radial structure at all. The difference between Janhunen et al. [65]

and the results presented here may be due to the difference in the radial length ($L_R = 1\,\text{cm}$ is used here, against $L_R = 5.38\,\text{cm}$ in Janhunen et al. [65]).

3.5.2 Impact of the radial wavenumber on the DR

To highlight the impact of the radial wavenumber on the ECDI DR, Fig. 3.27 shows for three values of $k_r\lambda_{De}$ the evolution of the frequency ω, and the growth rate γ as a function of the azimuthal wavenumber k_θ. We see that when $k_r\lambda_{De}$ increases from 0.02 to 0.1, the cyclotron resonances decrease and broaden until they disappear.

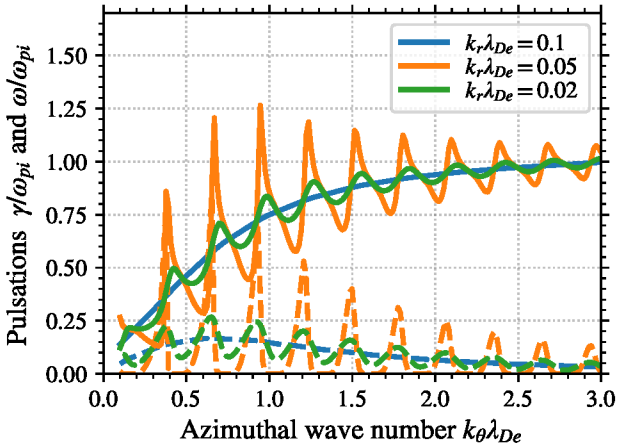

FIGURE 3.27 – Evolution as a function of the azimuthal wavenumber k_θ of (solid line) the frequency ω, and (dashed line) the growth rate γ for three values of the normalized radial wavenumber $k_r\lambda_{De}$ for the ECDI with Maxwellian electrons and cold ions.

This reduction of the resonances explains the observations of Fig. 3.20, where we saw similar reduction of the cyclotron resonances, due to the increase of λ_{De} from $\lambda_{De} = 4.3\times10^{-5}\,\text{m}$ at $t = 0$ to $\lambda_{De} = 7.0\times10^{-5}\,\text{m}$ at saturation, in agreement with the results in Lafleur et al. [4]. However, if the radial wavenumber k_r goes to zero, in agreement with the observations of Fig. 3.26, then the resonances would not smooth out for this reason. Instead, the resonances would stay.

As a conclusion, the interaction between the instability and the boundaries is still not clearly understood. The sheaths seem to screen the waves from the radial boundaries. In Section 4.4, we will discuss again the impact of the radial boundary condition (metallic versus dielectric electrode) on the oscillation.

As there is no radial structure observed in the simulation showed here, it means that the oscillation is purely azimuthal, or at least $\lambda_{De}k_r << 1$. In this case, the cyclotron resonances should non-longer disappear [36], except due to non-linear demagnetization of the electrons, as discussed before [8, 44]. The non-linear dispersion relations are out of the scope of the present work, but should be developed in order to better understand the evolution on the ECDI in the HET.

To understand the divergent observations of Hara [99], Janhunen et al. [65], and Taccogna et al. [44], a comparison of the simulation results using similar parameter and models should be undertaken. Such a comparison has been conducted between the different working groups on the axial-azimuthal simulation case [91]. A similar study in the radial-azimuthal geometry is current being devoloped.

3.6 Conclusion

Azimuthal instabilities have been observed in the PIC simulations presented here, as well as by several groups of the community [99, 65, 44]. As their nature remains unclear, we investigated in this chapter the PIC simulation results in order to obtain more insights on their nature and their behavior. The theoretical dispersion relations for the ECDI and the IAW have been used in both their simplified and general forms. The general form of the dispersion relation uses the particle velocity distribution function directly measured in the PIC simulations. The solver develop and used used is presented in Section 3.3.

At the beginning, the resonances typical of the ECDI are observed. After about 0.7 µs, they disappear, evolving towards the IAW dispersion relation. However, we show that the evolution from the ECDI to the IAW is not due to the larger radial wavenumber, as we observe no radial pattern in the simulation. Instead, it might be due to non-linear resonance broadening and electron demagnetization.

We also observed low frequency modulations of the amplitude of the instability. This oscillation is believed to be driven by the ion dynamic of the ion-wave trapping. Indeed, the oscillation period is of the order of $\tau = 1.5\,\mu s$, which is four times the ion bouncing period.

The oscillation of the growth rate is also observed with the dispersion relation when the ion temperature is used and that ions are supposed Maxwellian. However, when the ion velocity distribution function measured in the PIC simulation is used, the growth rate stays almost constant, with small oscillations. The growth rate in the simulation is estimated with the wave equation. The measured growth rate is in better agreement with the dispersion relation assuming Maxwellian distribution function, compared to the one using the VDF measured int he PIC simulation.

The origin of the discrepancy is unclear, as there are several possible reason. Firstly, to obtain the dispersion relations used here, we assumed small oscillations. However, the quasi-steady state is governed by non-linear phenomena, which probably have an affect the dispersion relation. Secondly, the estimation of the growth rate in the simulation uses a crude estimation of impact of the axial direction and the convection model on the wave. Lastly, the general dispersion relation solver use here has not been validated with distribution functions of complex shape, as the one observed in Fig. 3.17. A proper cross-validation with other solvers using complex distribution function is needed to confirm the result obtained. Another approach for the dispersion relation solver is to fit the VDF using a sum of analytic functions. Usually, one or few simple distribution functions are used, such as done by Rönnmark [109]. A general algorithm finding the best fit in a large ensemble of analytic functions could be used to analyze more complex distribution function as the one observed here in the PIC simulation.

The results observed here are globally similar with the other simulation results of the community discussed in Section 3.1.1. However, some differences remain, in particular during the non-linear stage. In order to conclude on the origins of the discrepancies, a precise comparison between the simulation codes and the parameters used will be conducted. A Benchmark is currently in construction, to compare some of these codes on the radial-azimuthal geometry similarly to the work done on the axial-azimuthal domain [91].

Chapter 4

Impact of the dielectric walls on the anomalous electron mobility

Part of the work presented in this chapter has been published in Tavant et al. [92].

In this chapter, we will now use the PIC simulation code described in Chapter 2 to perform a parametric study over two aspects of the dielectric walls: the secondary electron emission, and the modification of the electrostatic boundary condition. We study their impact on the electron cross-field mobility, the electron mean temperature and the sheath characteristics. The electrostatic boundary condition does not modify the results significantly. On the other hand, the electron emission increases the near-wall mobility while decreasing the mean electron temperature, which reduces the mobility due to the Electron Cyclotron Drift Instability (ECDI). A large discrepancy is observed between the sheath model of Section 2.7 and the PIC simulation results.

Contents

4.1 Presentation of the study

As introduced in Chapter 2, the Hall Effect Thruster (HET) behavior depends strongly on the axial electron transport toward the anode across the magnetic barrier. Two main phenomena are proposed to enhance the electron mobility,

— plasma instabilities and in particular the azimuthal ECDI, extensively studied in Chapter 3

— the electron induced electron emission from the wall

In order to compare quantitatively the relative importance of the two phenomena, we propose to conduct a parametric study on the dielectric wall characteristics. As highlighted in the introduction and in Chapter 3, the ECDI rises due to the $E \times B$ electron drift, but saturates due to both the axial convection which limits the electron heating, and the ion-wave trapping.

The first section describes the parameters of the simulation, while the second section highlights the main characteristics of the base simulation results (electron mobility, plasma potential, electron mobility, etc.). The other sections of the chapter present the results of the parametric study on the wall characteristics: first we study in Section 4.3 the influence of the dielectric layer, then in Section 4.5 the secondary electron emission is analyze, and lastly we combine the two characteristics in Section 4.7.

The simulation domain corresponds to the exit plane of the thruster. Hence, a neutral pressure P_n of 0.1 mTorr and a plasma density n_e of $1{\times}10^{17}$ m^{-3} are used. The fixed axial electric field and radial magnetic field are $E_z = 2{\times}10^4$ V/m and $B_r = 200$ G, respectively. The rectangular 2D domain measures $L_r = 2$ cm in the radial dimension and $L_\theta = 0.5$ cm in the azimuthal direction. The axial length used for the convection is set to $L_z = 1$ cm. It is important to note that the results shown in this chapter have been obtained at the beginning of my thesis, before the study of the convection presented in Chapter 2. Hence, in this chapter we use the convection model of Lafleur et al. [4]. However, we have validated that the convection model used does not modify the results under the conditions studied. The numerical parameters are chosen to respect the stability criterion of Particle In Cell (PIC) simulation, and are presented in Table 4.1

The simulation is initialized with a uniform density of particles, following a Maxwellian distribution with temperatures $\mathrm{T_{e,0}}$ and $\mathrm{T_{i,0}}$ for the electrons and the ions, respectively.

4.2 The base case

The *base* case corresponds to the case when the walls are grounded, and are fully absorbing. It is the reference case that will be extensively described and commented. Then, it will be used as reference to analyze and quantify the effects of two characteristics of the dielectric walls on the studied discharges : the secondary electron emission, and the modification of the electrostatic boundary condition.

4.2.1 Initial phase of the simulation: $t < 2\,\mu$s

The initial phase of the simulation corresponds to the growth of the ECDI, and the formation of the sheaths. Because of the growth of the instability, the electron transport increases as well, which increases the electron heating. The time scale of the sheath formation is governed by the ion inertia. It is roughly the same time scale as the saturation of the instability due to ion-trapping.

Figure 4.1 shows the temporal evolution of the electron mean kinetic energy decomposed over the three directions, $\mathcal{E}_{er}, \mathcal{E}_{e\theta}, \mathcal{E}_{ez}$, such that

$$\mathcal{E}_{ed} = \frac{1}{n}\frac{1}{2} m_e \iiint_{\mathbf{v}} v_{e,d}^2 f(\mathbf{v}) d^3v, \text{ with } d \in \{r, \theta, z\} \tag{4.1}$$

The mean kinetic energy is the sum of the thermal energy and the kinetic energy of the mean

TABLE 4.1 – Standard operating and numerical parameters used in the 2D PIC simulations of an HET. The simulation results are given as representative values.

Physical Parameter	notation	Value	Unit
Gas		Xenon	-
Domain dimensions	$L_x \times L_y \times L_z$	$2.0 \times 0.5 \times 1.0$	[cm^3]
Radial magnetic field	B_0	200	[G]
Axial electric field	E_0	2×10^4	[Vm^{-1}]
Mean plasma density	n_0	3×10^{17}	[m^{-3}]
Initial electron temperature	$\mathrm{T_{e,0}}$	10.0	[V]
Initial ion temperature	$T_{i,0}$	0.1	[V]
Secondary electron temperature	T_{see}	1.0	[V]
Neutral gas pressure	P_n	1.0	[mTorr]
Neutral gas temperature	T_n	300	[K]
Neutral gas density	n_g	3.22×10^{19}	[m^{-3}]
Simulation Parameter			
Time step	Δt	4×10^{-12}	[s]
Cell size	$\Delta x = \Delta y$	2×10^{-5}	[m]
Number of particles per cell	N/NG	80	[part/cell]
Typical quantities			
Electron plasma frequency	ω_{pe}	3.1×10^{10}	[rad/s]
Ion plasma frequency	ω_{pi}	36×10^6	[rad/s]
Electron cyclotron frequency	ω_{ce}	3.5×10^9	[rad/s]
Electron Larmor radius	r_{Le}	$6{\times}10^{-4}$	[m]

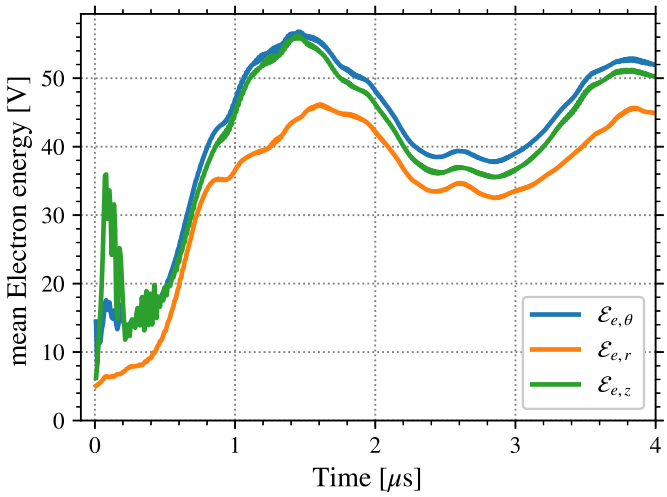

FIGURE 4.1 – Temporal evolution of the electron mean kinetic energy decomposed over the three directions. Only the beginning of the simulation is shown.

velocity. Because the electrons drift mainly in the azimuthal direction, we have

$$\begin{cases} \mathcal{E}_{er} \simeq \frac{\mathrm{T_{er}}}{2} \\ \mathcal{E}_{ez} \simeq \frac{\mathrm{T_{ez}}}{2} \\ \mathcal{E}_{e\theta} \simeq \frac{\mathrm{T_{e\theta}}}{2} + \frac{m_e}{2}\left(\frac{E_0}{B_0}\right)^2 \end{cases} \tag{4.2}$$

with $\frac{m_e}{2}\left(\frac{E_0}{B_0}\right)^2 \simeq 2.84\,\mathrm{V}$. We see that after some high frequency oscillations of $\mathcal{E}_{e\theta}$ and $\mathcal{E}_{ez}$ due to the cyclotron motion, the energies rise before stabilizing at $\mathcal{E}_e \simeq 45\mathrm{V}$. The radial kinetic energy $\mathcal{E}_{er}$ is less than $\mathcal{E}_{ez}$ and $\mathcal{E}_{e\theta}$, but only by a small difference of 5 V, corresponding to roughly 10%. The small difference between the azimuthal and the axial kinetic energy is of the order of 2 V, as expected from the cyclotron motion of the electrons and Eq. (4.2). This means that the electrons are almost isotropic.

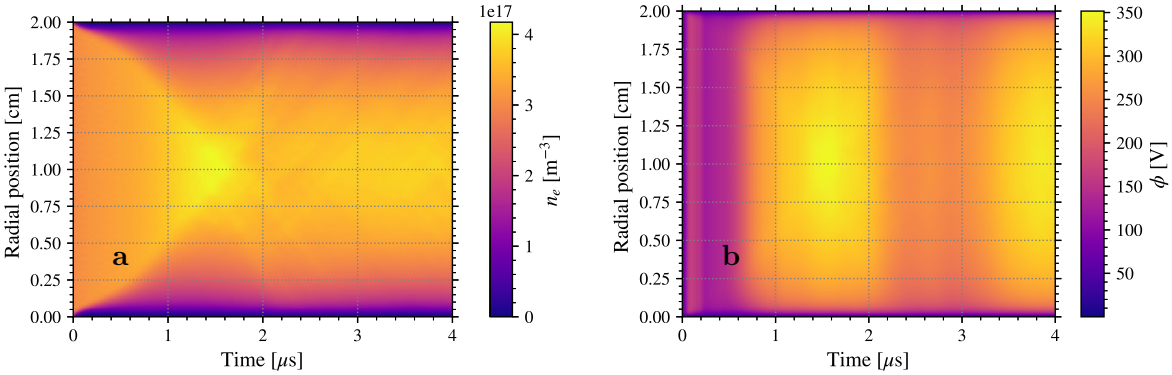

FIGURE 4.2 – Temporal evolution of the radial profile of the (**a**) electron density and (**b**) the plasma potential averaged azimuthally.

We can see in Figure 4.2 the evolution of the radial profile of the electron density on the plasma potential over the same period as Fig. 4.1. We observe on both quantities the formation of the sheath and the evolution toward a steady-state.

4.2.2 Saturated quasi steady-state: $t \geq 2\,\mu s$

After the relatively fast rise of the plasma characteristics, the simulation reaches a quasi steady-state, as we can see in Figure 4.3. We observe that after $t \simeq 2\mu s$, the electron energy $\mathcal{E}_e$ starts to oscillate around a mean value. The oscillations are then damped and reach their minimum amplitude at $t \simeq 7\mu s$ and then remain with a small amplitude as shown on simulations carried out up to 25 µs in Fig. 4.3 (the origin of these oscillations has been discussed in Section 3.1.5).

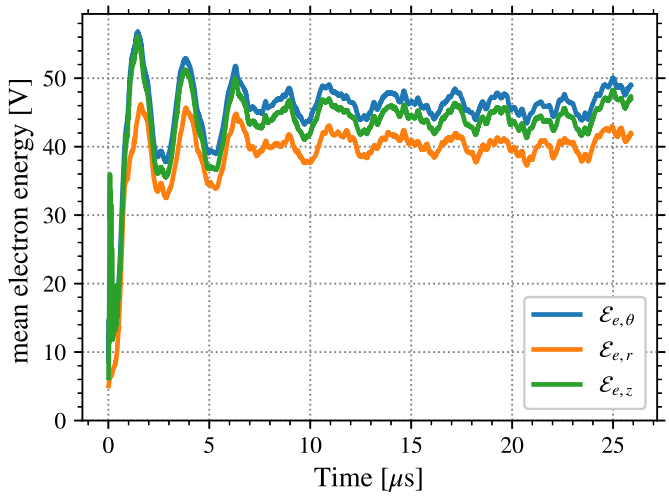

FIGURE 4.3 – Temporal evolution of the electron mean kinetic energy decomposed over the three directions, similar to Fig. 4.1 but for a longer period. We still see the difference between $\mathcal{E}_{ez}$ and $\mathcal{E}_{e\theta}$ due to the $E \times B$ drift, and the colder radial energy.

Figure 4.4 shows the azimuthally-averaged radial profiles of the electron and ion densities. The plasma is mostly quasineutral, except close to the walls, in the sheath, where the electron density falls more rapidly compared to that of ions. The sheath length can be roughly estimated to be 1 mm. The Debye length in our conditions is

$$\lambda_D = \sqrt{\frac{\epsilon_0 k_b T_e}{n_e e^2}} \sim 0.4\,\text{mm}, \tag{4.3}$$

which corresponds to the expected floating sheath length [115] (a few λ_{De}).

4.2.3 Enhanced electron transport

As introduced in Section 2.8, the electron cross-field axial transport is characterized by the electron mobility

$$\mu_\text{e} = \frac{u_{e,z}}{E_z} \tag{4.4}$$

with $u_{e,z}$ and E_z the electron mean axial velocity and the axial electric field, respectively. In PIC simulations, μ_e is computed at each time step by

$$\mu_\text{PIC} = \frac{1}{N E_z} \sum_N v_{e,z} \tag{4.5}$$

Figure 4.5 shows the temporal evolution of the electron mobility μ_PIC measured in the simulation with Eq. (4.5). We can see that it presents the same characteristics as the evolution of the electron energy $\mathcal{E}_e$ on Fig. 4.3. We recall that the classical electron mobility from the collisional theory developed in Eq. (1.7) is [4]

$$\mu_\text{classical} = \frac{\nu_m \frac{e}{m_e}}{\omega_{ce}^2 + \nu_m^2} \tag{4.6}$$

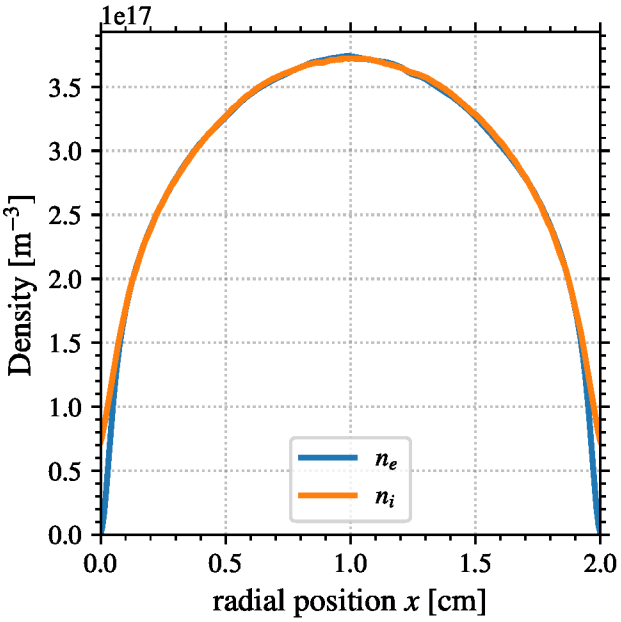

FIGURE 4.4 – Radial profile of the ion and electron densities at steady-state, averaged azimuthally and in time over the 5 last microseconds.

with ν_m the electron-neutral collision frequency and ω_{ce} is the electron cyclotron frequency. In the conditions of Table 4.1, $\mu_{\text{classical}} \simeq 0.8\ \text{m}^2(\text{sV})^{-1}$.

The measured electron mobility in the PIC simulation is one order of magnitude larger than the classical mobility. In the present case, as no electron is emitted from the wall, the enhancement can only come from the instabilities present in the plasma.

The oscillations can be seen in Fig. 2.4, which shows the azimuthal electric field observed at $T = 4\,\mu\text{s}$. It clearly features the oscillation of wavelength of the order of 1 mm, as observed in Héron and Adam [38], and Janhunen et al. [65]. Figure 4.6 shows the temporal evolution of the azimuthal electric field measured at the center of the channel. We can see that the instability rises and saturates quickly. Then, the oscillation remains quite stable. The Fourier Transform of the electric field presents a clear maximum at 14 MHz. The theoretical frequency of the ECDI

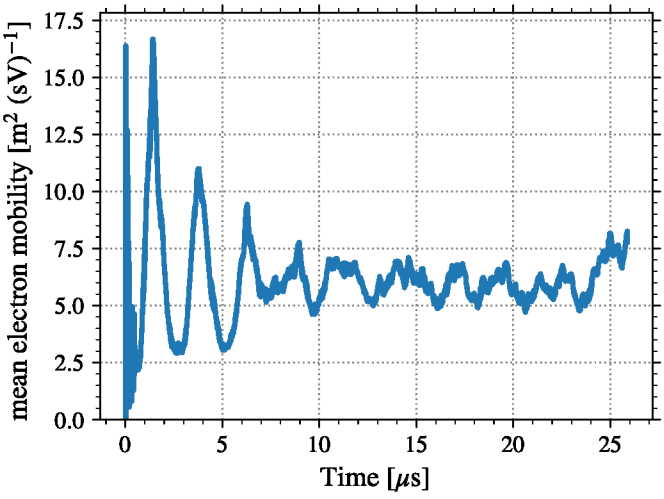

FIGURE 4.5 – Temporal evolution of the electron axial mobility computed in the PIC simulation.

instability is [102]

$$f_{\max} = \frac{\omega_{pi}}{\sqrt{3}} \simeq 21\,\text{MHz}, \tag{4.7}$$

which gives a relatively good agreement with the oscillation observed. The ECDI instability was the subject of Chapter 3, hence it will not be further discussed here.

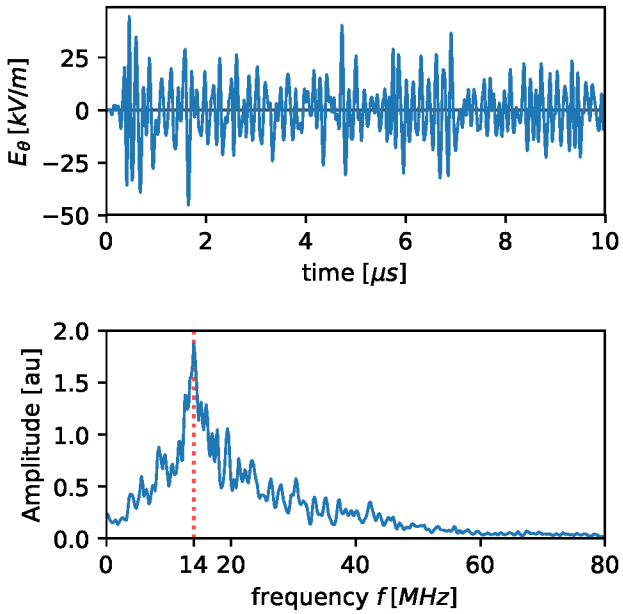

FIGURE 4.6 – Azimuthal instability: temporal evolution of the azimuthal electric field at the center of the simulations, and its frequency spectrum computed by FFT. The frequency for which the amplitude is maximum is highlighted.

The effective mobility μ_{eff} is determined by the correlation term $< \delta E_\theta \delta n_e >$ and the parameters of the simulations. The effective mobility at saturation μ_{eff}^{sat}, using the hypothesis of saturation by ion-wave trapping, only needs the electron temperature T_e. We can see that the three values $\mu_{\text{PIC}}, \mu_{\text{eff}}$, and μ_{eff}^{sat} are close from each-others.

TABLE 4.2 – Characteristics measured in the simulation at $t = 27\,\mu$s.

Quantity	Value
Correlation $< \delta E_\theta \delta n_e >$	$6{\times}10^{20}$ V/m^4
Effective mobility μ_{eff} from Eq. (2.61)	4.4 m^2(sV)$^{-1}$
Mobility saturation μ_{eff}^{sat} from Eq. (2.64)	3.3 m^2(sV)$^{-1}$
Measured mobility μ_{PIC} from Eq. (4.5)	6 m^2(sV)$^{-1}$

4.3 Modeling the dielectric layer

The first effect of the wall material studied is adding a layer of dielectric material with its own permittivity, as introduced in Section 2.4. The simulation parameters are the same as in the canonical case, presented in Section 4.2, but the plasma is separated from the ground wall by a dielectric layer of 3 mm. Hence, the distance between the grounded electrodes is 2.6 cm (instead of 2.0 cm in the base case). The relative permittivity of the dielectric is $\epsilon_R = 25$.

Figure 4.7 shows the radial profile of the radial electric field E_R at $t = 10\,\mu s$ (during the quasi steady-state) averaged in the azimuthal direction. The plasma domain starts at $r = 0$ and ends at $r = 2\,cm$. We note the jump in the value of the electric field at the plasma-wall transition. This jump is due to the surface charges and the change of permittivity. We can also notice that in the dielectric layer, in $r < 0$ and $r > 2\,cm$, the radial electric field is close to zero, compared to the value in the sheath.

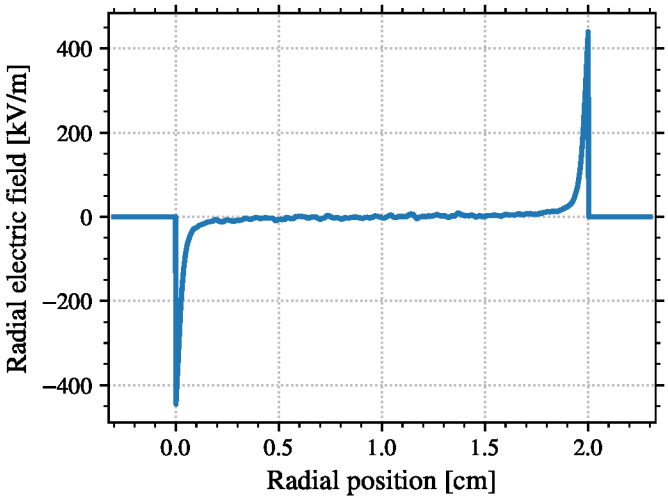

FIGURE 4.7 – Radial profile of the radial electric field E_R averaged in the azimuthal direction at $t = 10\,\mu s$. The plasma domain starts at $r = 0$ and ends at $r = 2\,cm$. The dielectric length is $L_{rmDiel} = 3\,mm$.

The next sections investigate the impact of the dielectric layer on the plasma characteristics, and highlight the plasma-wall interaction.

4.3.1 Effect of the dielectric layer

The simulation results are qualitatively the same as in the case without the dielectric layer. As an example, Figure 4.8 shows the temporal evolution of the axial electron mobility with and without the dielectric layers. We see that the results for the electron temperature and mobility are similar. The low amplitude oscillation of the case with the dielectric layer decreases slightly more slowly.

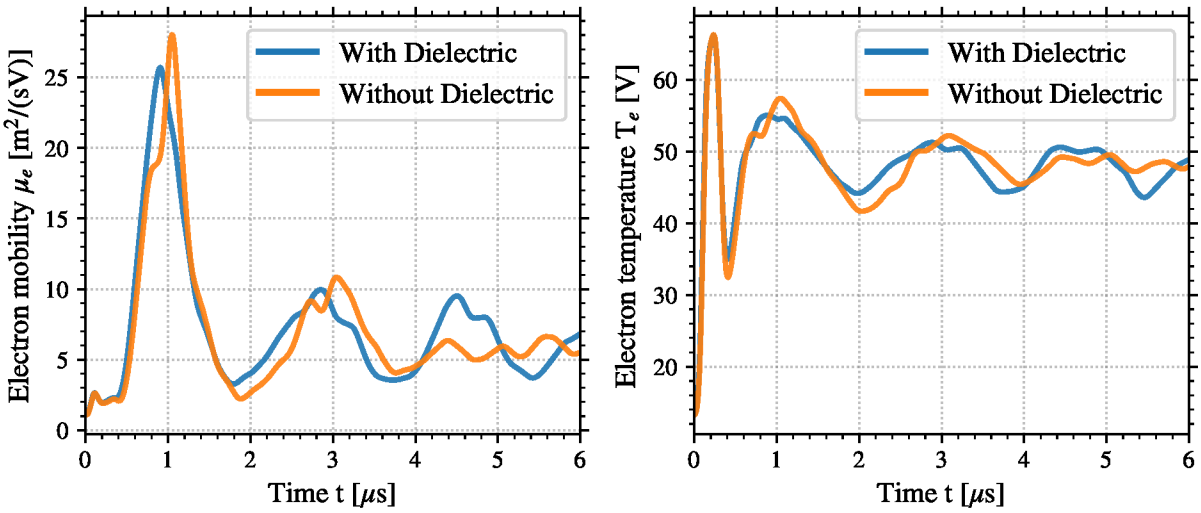

FIGURE 4.8 – Temporal evolution of the axial electron mobility (left), and the electron temperature (right) with and without the dielectric layer modeled.

4.3.2 Near-wall and in-wall parameters

In this section, we focus on the surface charge and the near-wall electric field. Figure 4.9 shows the temporal evolution of the surface charge at one point of the wall. The position has been chosen to be at the center ($L_\theta = 0.25$ cm) of the lower wall, but the observations are similar at other positions.

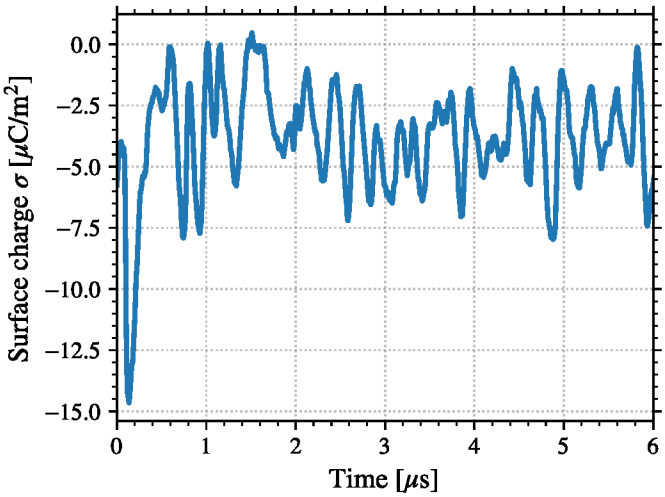

FIGURE 4.9 – Temporal evolution of the surface charge σ at one position of the lower dielectric wall

We can see in Fig. 4.9 that the value of the surface charge starts by decreasing significantly (increasing in absolute value), due to the hot electrons that reach quickly the walls. Then, σ grows (decreases in absolute value) and oscillates around a mean value close to $-3.5\,\mu C/m^2$ and with an amplitude of approximately $1.2\,\mu C/m^2$.

Fig. 4.10 shows the azimuthal evolution of the radial electric field inside the dielectric layer. The electric field is given at three different positions ($r = -0.2, -0.9$, and -1.8 mm away from the plasma-wall interface) to highlight its evolution. We can see that, first, the electric field is not homogeneous in the azimuthal direction and second, even though there is no charge in the dielectric, the amplitude of the electric field decreases when going further away from the plasma. This is due to the 2 dimensions (2D) Poisson equation, which smooth-out the inhomogeneity.

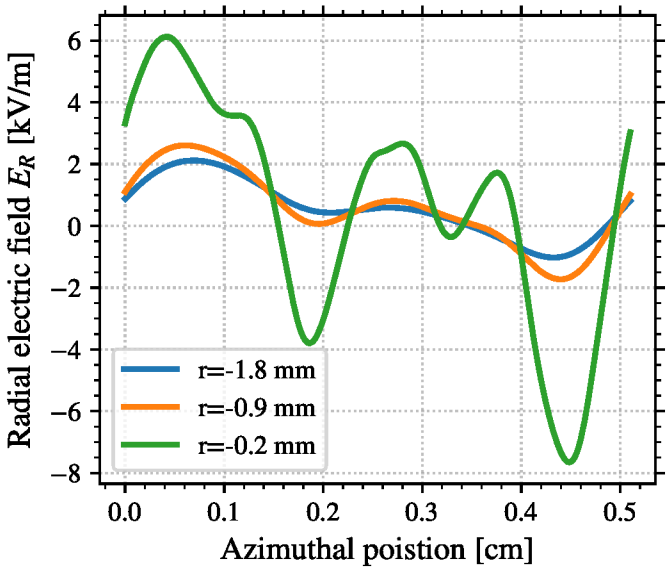

FIGURE 4.10 – Azimuthal evolution of the radial electric field inside of the dielectric layer at three different radial positions ; the reference $r = 0$ is the plasma-wall interface, the grounded electrode is located at $r = -3\,\text{mm}$.

4.3.3 Comparisons of different ways to model the effect of dielectric layers

As introduced in Section 2.4, a simplified approach to model the effect of the surface charges on the plasma is to use a Neumann boundary condition [44]

$$|E_r| = \frac{|\sigma|}{\epsilon_0}. \tag{4.8}$$

Equation (4.8) uses two approximations:

— one dimensional

— no electric field in the dielectric

We have already seen in Fig. 4.10 that the electric field in the dielectric is not zero, but instead it oscillates in respect to the azimuthal instability present in the plasma. Figure 4.11 shows the radial electric field at the wall and compares it to what is obtained by Eq. (4.8). We can see that the two values are of the same order of magnitude, close to -500 kV/m. However, the two values are not equal, as they oscillate around their mean value. We can see that the surface charge oscillates more than the actual electric field obtained by solving the Poisson equation.

As a conclusion, we have observed that the dielectric layer does not change the simulation results much, but it can modify the surface processes. The model used here for the dielectric layer does not modify the performance of the simulation, while allowing to take into account the 2D effects. In this section, no secondary electron emission has been taken into account. In Section 4.7, we will discuss the influence of using the simplified Eq. (4.8) in the case where secondary electron emission is important.

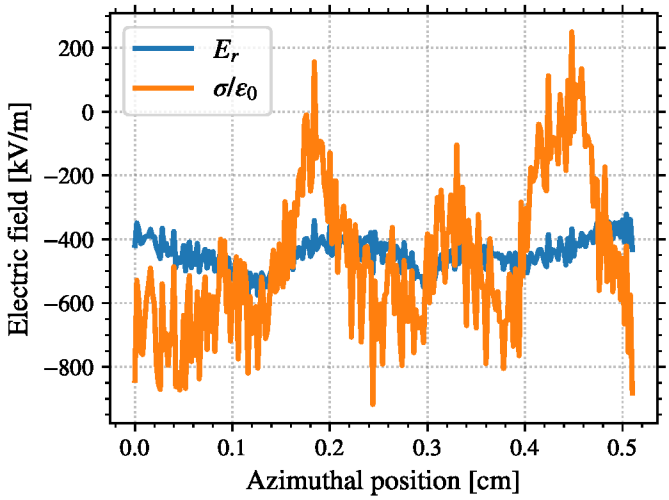

FIGURE 4.11 – Azimuthal evolution of the radial electric field at the plasma-wall interface (r=0) and the electric field that would result from surface charge according to Eq. (4.8).

4.4 Impact of the radial boundary conditions on the oscillations

In Section 3.5, we discussed the choice of the radial wavenumber of the instability observed. Changing the radial electric boundary condition could affect the instability. Therefore, we discuss in this section the impacts of the dielectric electrostatic boundary condition on the oscillations. We have seen in Section 4.3 that the dielectric boundary does not affect the macroscopic simulation results. Figure 4.12 shows the radial evolution in the first few cells from the wall of the amplitude of the oscillation of the azimuthal electric field on the left, and the ion density on the right, with grounded (metallic) wall and dielectric wall.

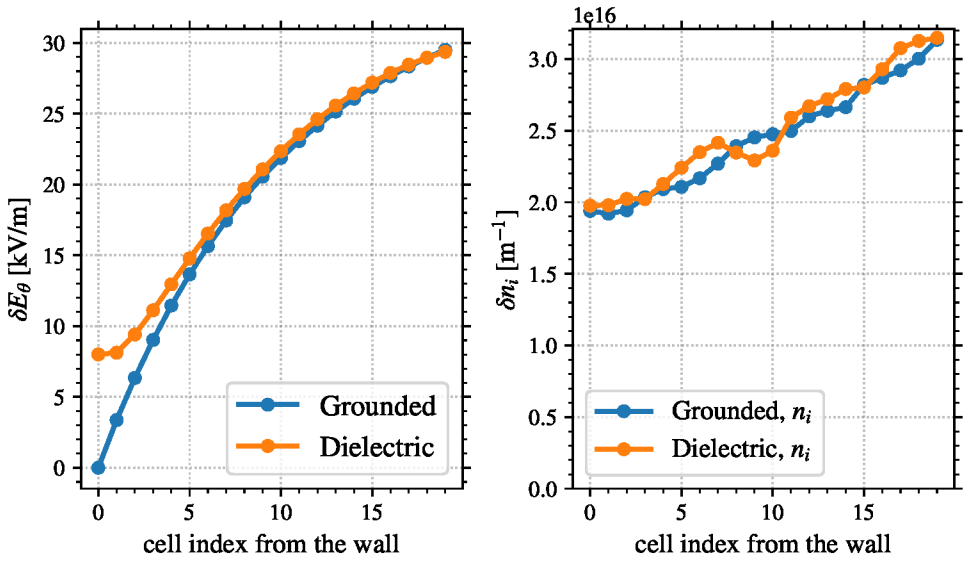

FIGURE 4.12 – Radial evolution in the first cells of the amplitude of the oscillation of (left) the azimuthal electric field and (right) the ion density, with grounded (metallic) wall and dielectric wall.

We can see in Fig. 4.12 that the boundary condition does not affect the ion oscillations. This is consistent with the observation made in Section 3.5.2 that the ion fluctuation was not affected by the wall. On the other hand, the azimuthal electric field has to go to zero when the wall is

grounded, which is not the case with a dielectric layer.

Nevertheless, the difference in E_θ between the two boundary conditions quickly disappears inside the plasma domain. Indeed, after a dozen cells from the wall, corresponding to a few Debye lengths, the amplitudes of δE_θ are equal for both cases. Hence, the electrostatic boundary condition induces only minor differences on the instability and therefore on the characteristics of the plasma discharge.

4.5 Effect of electron emission

In Section 4.2, the walls are not emissive. However, the dielectric ceramic used in HET can emit electrons [49, 6]. The electron emission model used, introduced in Section 2.6.2, has three parameters $\sigma_0, \epsilon^*, \sigma_{\max}$, such that the emission probability depends on the kinetic energy of the incident electron ϵ as

$$\sigma = \min\left(\sigma_0 + (1-\sigma_0)\frac{\epsilon}{\epsilon^*}, \sigma_{\max}\right). \tag{4.9}$$

The value of parameters are summarized in Table 4.3. The crossover energy ϵ^* is varied from as low as 4 V, corresponding to a very emissive material, to as high as 200 V, a weakly emissive material.

TABLE 4.3 – Parameters of the electron emission probability model

Parameter	value
σ_0	0.5
$\sigma_{\max}$	2.9
ϵ^*	4 – 200 V

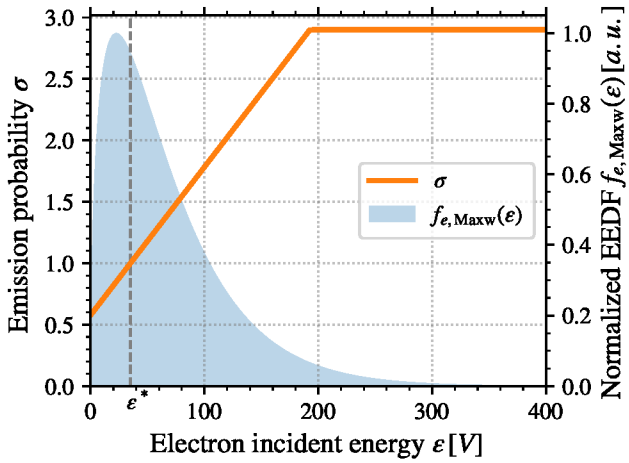

FIGURE 4.13 – Energy dependence of the electron emission model of Eq. (4.9) superimposed to a Maxwellian energy distribution function of temperature of 45 V, with $\epsilon^* = 35.04$ V.

Figure 4.13 shows the electron emission probability for $\epsilon^* = 35.04$ V (corresponding to Boron Nitride (BN)) superimposed to a Maxwellian Electron Energy Distribution Function (EEDF) of temperature $T_e = 45$ V (typical value obtained in the simulations). We can see that the saturation of σ at $\sigma_{\max}$ happens only for the very high energy tail. In the simulation, we can

evaluate the average electron emission yield, also named emission rate, defined as:

$$\bar{\sigma} = \frac{\Gamma_{\text{emitted}}}{\Gamma_{\text{incident}}} = \frac{\iiint v_r \sigma(\mathbf{v}) f(\mathbf{v}) d^3v}{\iiint v_r f(\mathbf{v}) d^3v}. \tag{4.10}$$

In general, Eq. (4.10) cannot be calculated analytically. However, if we assume that the EEDF is Maxwellian and we neglect the saturation at $\sigma_{\max}$, Eq. (4.10) can be integrated to give

$$\bar{\sigma}_{\text{Maxw}}(\mathrm{T_e}) = \sigma_0 + (1 - \sigma_0)\frac{2\mathrm{T_e}}{\epsilon^*}. \tag{4.11}$$

The saturation at $\sigma_{\max}$ can be neglected as we have seen that it only affects a small part of the electron population, see Fig. 4.13. The exact calculation and the relative error is given in Appendix B.

4.5.1 Impact of the electron emission on the mobility

The effects of the electron emission at the wall on the electron axial mobility are presented in Figure 4.14. The measured mobility μ_{PIC} is shown, as well as the effective mobility μ_{eff}, the saturation estimate μ_{eff}^{sat} and the classical mobility $\mu_{\text{classical}}$, defined in Section 2.8 respectively by Eq. (2.59), Eq. (1.8), Eq. (2.64) and Eq. (2.60). The values are averaged in time between $t = 5\mu$s and $t = 10\mu$s, and in space over the azimuthal and radial directions. For the canonical case, without electron emission, the values are presented in Table 4.2.

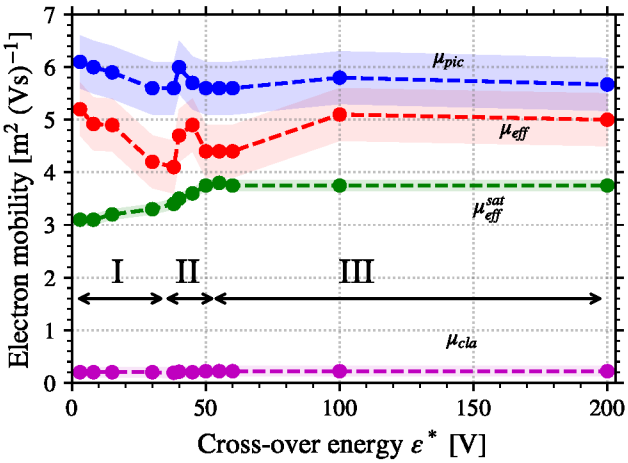

FIGURE 4.14 – Evolution of the electron mobility as a function of the crossover energy ϵ^*. In blue μ_{PIC} is the mobility measured in the simulations, while $\mu_{\text{classical}}$, μ_{eff} and μ_{eff}^{sat} in purple, red and green respectively are calculated with Eqs. (1.8), (2.59), (2.60) and (2.64). The three regimes **I, II** and **III**, described in Section 4.5.3 are identified.

As expected, the classical mobility in Fig. 4.14 is underestimated by more than one order of magnitude compared to μ_{PIC}. The effective mobility μ_{eff} and the effective mobility at saturation μ_{eff}^{sat} are much closer to μ_{PIC}, with an underestimation of roughly 10% and 30% respectively. The mobility measured in the simulation does not evolve much with the electron emission, even for very high emission rate, i.e very low values of ϵ^*.

On the other hand, μ_{eff}^{sat} decreases slightly when ϵ^* decreases from around 40V to lower values. However, it still provides a reasonable approximation of the electron enhanced mobility, even with high electron emission rate.

4.5.2 Near-wall conductivity

The results presented in Section 4.5.1 are spatially averaged. However, the mobility coming from the instability is expected to be higher where the instability is larger, hence at the center of the channel. On the other hand, the mobility due to wall emission is located close to the wall [46].

Figure 4.15 presents the radial profiles of the mobility measured in the PIC simulations without electron emission and for three values of ϵ^*. On the left, the measured mobility μ_{PIC} is shown and on the right it is the effective mobility μ_{eff} given by Eq. (1.8).

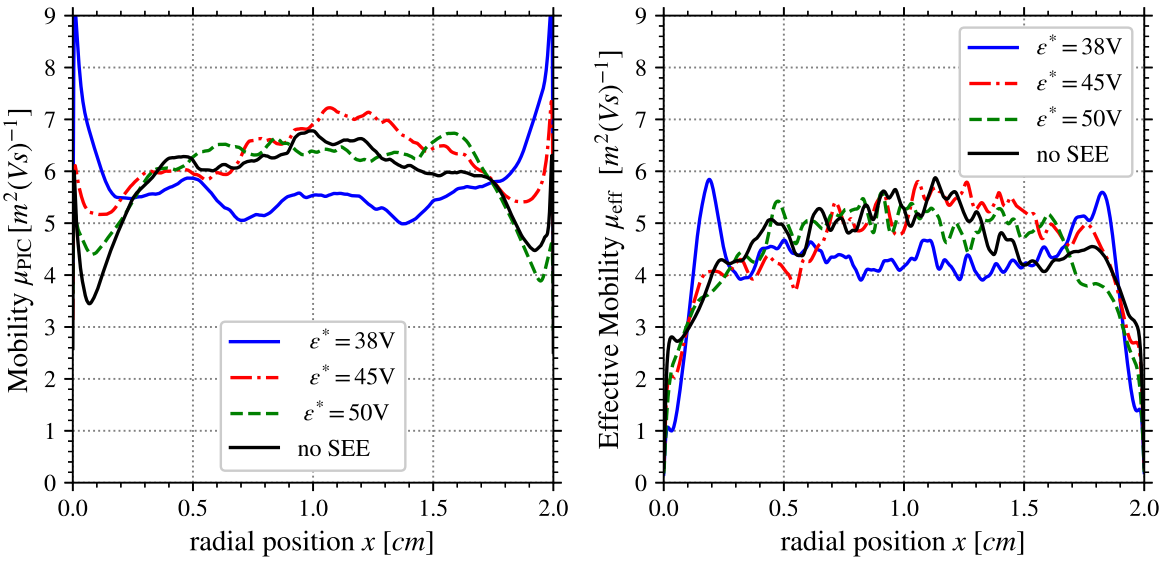

FIGURE 4.15 – Radial profile of the electron mobility (left) measured in the PIC simulations, and (right) given by Eq. (1.8), for different wall emissivities.

We can see in Fig. 4.15 that the mobility measured μ_{PIC} in the center decreases by roughly 20% as the emission rate increases. This observation is in agreement with μ_{eff}^{sat} observed in Figs. 4.14 and 4.15. This is due the electron temperature T_e which decreases from around $T_e = 45$V at $\epsilon^* = 200$V to $T_e = 30$V at low ϵ^* (the evolution of T_e can be seen in Fig. 4.19).

On the other hand, the near-wall mobility increases on μ_{PIC} almost by a factor of two between the case withour emission and $\epsilon^* = 38$ V. However, we do not see this evolution on μ_{eff}^{sat} which was derived from a theory with no Secondary Electron Emission (SEE), meaning that it indeed comes from another physical mechanism than the ECDI.

4.5.3 Three different regimes

In Figure 4.14, three regimes have been identified. Regime **I** corresponds to low values of ϵ^* (lower than 38V), during which μ_{eff}^{sat} increases with ϵ^* but μ_{PIC} and μ_{eff} decreases. Regime **III** corresponds to high values of ϵ^* (higher than 50V), during which μ_{eff}^{sat}, and μ_{PIC} are roughly constants, but μ_{eff} increases slightly. Regime **II** is a short transition regime, for $38 < \epsilon^* < 50$V.

The different regimes appear clearly on the temporal evolution of the different variables. Figure 4.16 presents the temporal evolution of the space average $\bar{\sigma}_{\text{PIC}}$ for three different values of ϵ^* , corresponding to the three different regimes we have identified. In regimes **I** and **III**, $\bar{\sigma}_{\text{PIC}}$ reaches a quasi steady-state after a few microseconds.

Regime **I**, with low ϵ^*, is characterized by a saturation of $\bar{\sigma}_{\text{PIC}}$ at a value between $\bar{\sigma}_{\text{cr}}$ and 1, which leads to a non-monotonic potential profile. Regime **III**, for higher ϵ^*, is characterized by a quasi steady-state with a SEE rate lower than $\bar{\sigma}_{\text{cr}}$.

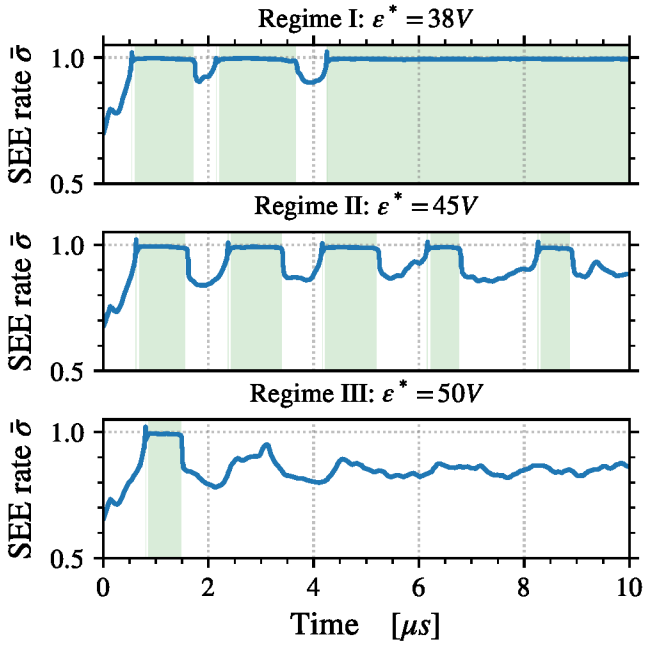

FIGURE 4.16 – Evolution as a function of time of the averaged electron emission rate $\bar{\sigma}_{\text{PIC}}$ in the three regimes observed (two stable ones, one with oscillations). The light green zones correspond to the periods when $\bar{\sigma}_{\text{PIC}} > \bar{\sigma}_{\text{cr}}$

The transition between these two stable regimes (monotonic and non-monotonic sheath) passes by regime **II**, an oscillating mode between the two stable regimes. As shown in Fig. 4.14, regime **II** is observed only in a narrow range of ϵ^*. The oscillations of regime **II** are shown in Fig. 4.16 up to 10µs but have been observed for more than 40µs. Note that regimes **I** and **III** in Fig. 4.16 are obtained for $\epsilon^* = 38$ V and $\epsilon^* = 50$ V respectively, i.e. near the boundary of the unstable window (see Fig. 4.14). Consequently, we observe a few oscillations before the quasi steady-state is reached, as these cases are close to the bifurcation.

The physical origin of the bifurcation can be seen with the help of Fig. 4.17, which shows the evolution of the potential drop to the wall as a function of the electron temperature. It is computed using Eq. (4.11) for $\bar{\sigma}$ and Eq. (2.53) for the potential drop, which is summarized as

$$\begin{cases} \bar{\sigma} = \bar{\sigma}_{\text{Maxw}} = \sigma_0 + (1-\sigma_0)\frac{2\text{T}_\text{e}}{\epsilon^*} \\ \Delta\phi = \text{T}_\text{e} \ln\left([1-\bar{\sigma}]\sqrt{\frac{m_i}{2\pi m_e}}\right) \end{cases} \tag{4.12}$$

Figure 4.17 shows the evolution of $\Delta\phi$ as a function of T_e obtained with Eq. (4.12) using four different values of ϵ^*. We can see that, starting from low electron temperature, the potential drop increases with the electron temperature, resulting in a better screening of the electrons. This corresponds to regime **III**. However, the $\Delta\phi$ reaches a maximum, after which it drops sharply to zero and below.

When the potential passes the maximum and decreases, the electrons are less screened by the sheath. Hence, the electrons reach the wall with a higher energy, resulting in a higher electron emission from the wall, hence a smaller potential drop. The sheath is unstable, and quickly attains a Space Charge Limited (SCL) regime [51]. In this regime, the sheath is not monotonic, and the model of Eq. (2.53) is no more valid, and the potential drop tends toward $\Delta\phi \simeq \text{T}_\text{e}$ [81, 84] [1], shown with the blue dotted line in Fig. 4.17. This corresponds to regime **I**.

However, during regime **I**, the electron power loss to the wall is very high, and can exceed the gain. Hence, the electron temperature decreases. If T_e decreases too much, the sheath can

1. see Section 2.7 for more details

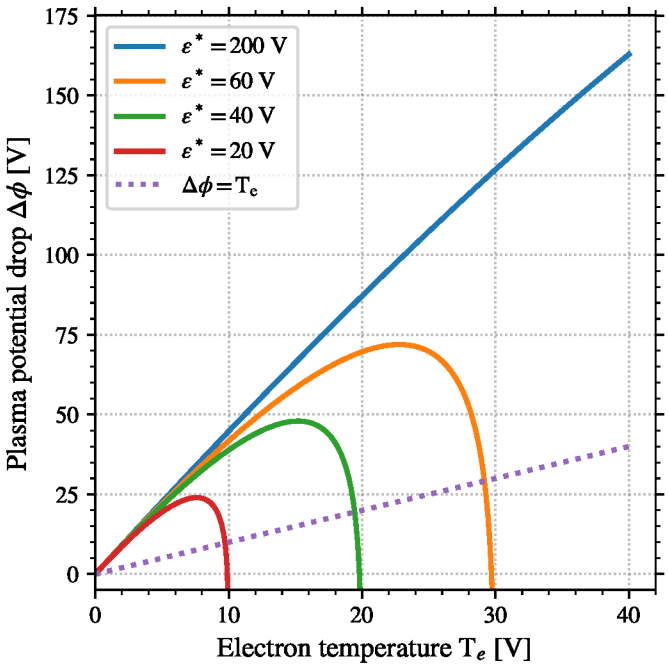

FIGURE 4.17 – Plasma potential drop to the wall as a function of the electron temperature for different values of the cross-over energy ϵ^* using Eq. (4.12). The dashed line is $\Delta\phi = T_e$.

come back to the previous regime **III**. The oscillations between regimes **I** and **III** define regimes **II**.

We can try to predict the threshold value of ϵ^* between regimes **III** and **II**. We have seen in Fig. 4.3 that without electron emission, T_e is of the order of 45 V. Using the different curves in Fig. 4.17, we can expect to observe the transition between regime **III** and **II** for $\epsilon^* > 60$ V, as we have for $\epsilon^* = 60$ V the maximum of $\Delta\phi$ is at $T_e \sim 25$ V, which is significantly lower than 45 V. However, we see in Fig. 4.16 that the transition appears at $\epsilon^* = 50$ V.

The reason for the discrepancy between the expected and the observed threshold values of ϵ^* could be that when $\bar{\sigma}$ increases, the electron power losses increase, and hence cause the electron temperature at equilibrium to decrease. The evolution of the temperature with $\bar{\sigma}$ is shown later in Fig. 4.19. We can see that even for very large SEE rates, the electron temperature only decreases down to $T_e = 30$ V. However, the curves of Fig. 4.17 still predict for $T_e = 30$ V a threshold value at $\epsilon^* = 60$ V. Consequently, even if T_e does indeed decrease when increasing ϵ^*, it remains too large to explain the discrepancy between the observed transition between regime **III** and **II** in Fig. 4.16 and the curves in Fig. 4.17.

Hence, the cause of the difference in the threshold value for regime **II** will be discussed again in Chapter 6, using a modified plasma-wall interaction model.

4.6 Validation of the sheath model

The PIC simulations used here do not need any sheath theory in order to model the plasma-wall interaction. Conversely, they rely on first principle models. Hence, they can be used in order to validate the sheath model introduced in Section 2.7 coming from the fluid theory.

This sheath model links with Eq. (4.12) the plasma potential drop $\Delta\phi$ with the electron temperature T_e and the electron emission rate $\bar{\sigma}$. Equation (4.11) can be used to estimate the electron emission rate given the mean electron temperature measured in the simulations, corresponding statistically to the plasma bulk temperature. In the PIC simulations, $\bar{\sigma}$ can be computed using Eq. (4.10) by counting the number of electrons attaining the wall and emitted during a time-step. We note $\bar{\sigma}_{PIC}$ this measurement.

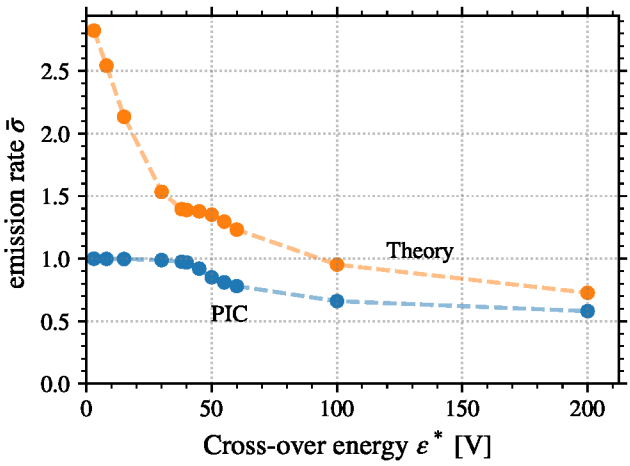

FIGURE 4.18 – Values of the electron emission rate $\bar{\sigma}_{\mathrm{PIC}}$ (blue) measured in the PIC simulations, and (orange) $\bar{\sigma}_{\mathrm{Maxw}}$ obtained with Eq. (4.11) using the electron temperature shown in Fig. 4.19.

We can see in Figure 4.18 that the mean electron emission rate in the simulations $\bar{\sigma}_{\mathrm{PIC}}$ lies between 0.6 for large ϵ^* and 1 at low ϵ^*. The saturation of $\bar{\sigma}_{\mathrm{PIC}}$ at 1 for high emissivity ($\epsilon^* < 50$V) was not expected from $\bar{\sigma}_{\mathrm{Maxw}}$ obtained with Eq. (4.11). Indeed, σ_{max} in Eq. (4.11) is equal to 2.9, and the electron temperature in the bulk measured, when used in Eq. (4.11), predicts a rate between 1.4 and 2.8. This discrepancy at low ϵ^* is due to the SCL regime. Hobbs and Wesson [81] predicted that in this regime, a potential well forms such that a fraction of the emitted electrons return to the wall, in order to maintain the effective emission rate to $\bar{\sigma}_{\mathrm{cr}} \sim 1$. However, for $\epsilon^* > 50$V, the sheath regime described in Section 2.7 should be valid.

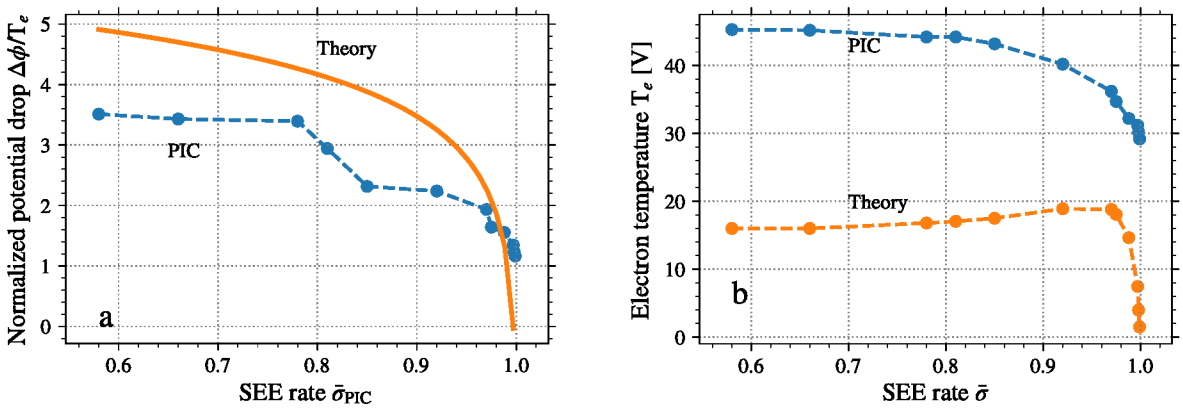

FIGURE 4.19 – (**a**) Plasma potential drop to the wall normalized by the electron bulk temperature as a function of the electron rate, and (**b**) the mean electron bulk temperature measured in the PIC simulations as a function of the electron emission rate $\bar{\sigma}$, measured in the simulations, and the effective temperature expected from Eq. (4.13).

The electron temperature measured in the bulk of the simulation is presented in Fig. 4.19.**b** for the same cases as in Fig. 4.18. An *effective* temperature that would correspond to the measured emission rate $\bar{\sigma}_{\mathrm{PIC}}$ in Eq. (4.12) is given by :

$$\bar{\sigma}_{\mathrm{Maxw}}(\mathrm{T}_{\mathrm{e},eff}) = \bar{\sigma}_{\mathrm{PIC}}, \text{ hence } \mathrm{T}_{\mathrm{e},eff} = \frac{\bar{\sigma}_{\mathrm{PIC}} - \sigma_0}{1 - \sigma_0} \frac{\epsilon^*}{2}, \tag{4.13}$$

We can see that when $\bar{\sigma}$ increases, the electron temperature in the bulk $\mathrm{T_e}$ monotonically decreases from 45V to around 30V. However, these values are not consistent with the measured emission

rate $\bar{\sigma}_{\mathrm{PIC}}$, even for $\epsilon^* > 50\mathrm{V}$. The bulk electron temperature is much higher than the effective $\mathrm{T}_{\mathrm{e},eff}$ obtained to correctly predict the emission rate.

Figure 4.19.**a** shows the evolution of the potential drop to the wall measured in the PIC simulation compared to the theory Eq. (2.53)). As expected by Eq. (2.57), $\Delta\phi$ measured in the simulation saturates to $\mathrm{T_e}$ for high emission rate ($\bar{\sigma}_{\mathrm{PIC}} \sim 1$). However, we see that at low emission rate, the potential drop is significantly lower than expected. The sheath model of Section 2.7 used two hypotheses:

— Maxwellian distribution function to obtain $\bar{\sigma}_{\mathrm{Maxw}}$ from Eq. (4.10),

— Isothermal electrons in the sheath.

These two hypotheses will be checked against the PIC simulations in the next chapter.

4.7 Full dielectric model with secondary electron emission

We have observed the effects of the electron emission and the electrostatic boundary condition separately in Sections 4.3 and 4.5, respectively. In Section 4.5, we observed three regimes depending on the emission rate. At high emissivity, the sheath is space-charge limited, resulting in an inverse sheath. At low emissivity, we obtain the standard sheath model with electron emission. The transition between the regimes passes by a oscillating regime.

In Section 4.3 we observed that when there is no emission, the dielectric boundary condition for the potential does not change the simulation results. In this section, we investigate the interaction between the two characteristics of the dielectric walls, especially with a high emission rate. More precisely, regime **II** is the most interesting, as it features a complex behavior. Hence, we use $\epsilon^* = 45\,\mathrm{V}$ to study the impact of the dielectric layer combined with the electron emission.

The dielectric layer thickness is $L_{\mathrm{Diel}} = 3\,\mathrm{mm}$, and the relative permittivity of the dielectric is $\epsilon_R = 25$. The dimensions of the plasma domain is not modified between the case with and without the dielectric layer. Instead, it is the width between the grounded electrodes that is increased.

4.7.1 Impact of the dielectric boundary condition on the mobility with electron emission

Figure 4.20 shows the temporal evolution of the electron mobility measured in the simulation μ_{PIC} for both cases, with and without the dielectric layer. We can see that the two variables are quite similar, with similar mean values and oscillation. Interestingly, the beginning of the simulations, up to $t = 3\,\mu\mathrm{s}$, are almost identical. After this, the values are no more in phase, but follow a similar behavior.

Hence, we conclude that results concerning the electron mobility obtained in Section 4.5 without the dielectric layer modeled will apply as well with the dielectric electrostatic boundary condition. In the next section, we analyze the plasma-wall interaction is more details.

4.7.2 Plasma-wall interaction

Figure 4.21 compares the temporal evolution of the mean electron emission rate $\bar{\sigma}_{\mathrm{PIC}}$ for the same parameter $\epsilon^* = 45\,\mathrm{V}$, with and without the dielectric wall modeled. As previously, the dielectric width is 3 mm, and the electrodes are now 2.6 cm apart (the geometry of the plasma domain is kept constant). As previously with the electron mobility, the two case present the same result at the beginning, up to $t = 2\,\mu\mathrm{s}$. After that, the value of $\bar{\sigma}_{\mathrm{PIC}}$ in the case with the dielectric layer oscillates lightly close to the critical value $\bar{\sigma}_{\mathrm{cr}}$, in contrast to the case without the dielectric layer that shows large variations. As Fig. 4.21 shows the values average over all of the wall, it can hide spatial variations. Hence the next figures present localized values.

Figure 4.22 shows the temporal evolution of the radial electric field in the sheath at the center of the azimuthal direction ($\theta = 0.25\,\mathrm{cm}$) for (**a**) the case with grounded wall, and (**b**) the

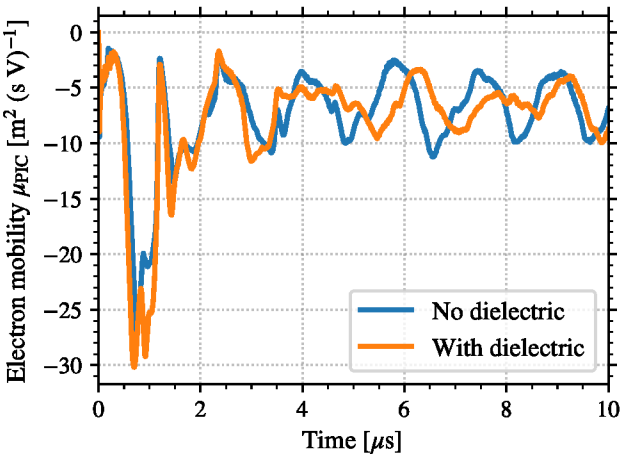

FIGURE 4.20 – Temporal evolution of the axial electron mobility measured in the PIC simulation with and without the dielectric layer between the plasma and the grounded electrodes. The crossover energy is $\epsilon^* = 45\,\mathrm{V}$, the length of the dielectric layer is $L_{\mathrm{Diel}} = 3\mathrm{mm}$ and its relative permittivity is $\epsilon_R = 25$.

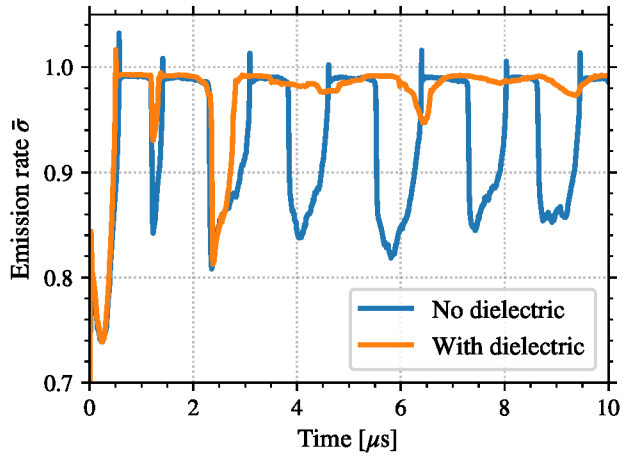

FIGURE 4.21 – Temporal evolution of the mean electron emission rate $\bar{\sigma}_{\mathrm{PIC}}$ averaged over all the wall surface with and without the dielectric layer modeled, for the same value $\epsilon^* = 45\,\mathrm{V}$.

case with dielectric layers. Only the two millimeters close to the walls are shown, as the radial electric field in the plasma bulk is close to zero. On both cases, we can see the sharp transitions between the sheath with high electric field (low $\bar{\sigma}_{\mathrm{PIC}}$) and the SCL regime with low electric field, for which $\bar{\sigma}_{\mathrm{PIC}} \simeq \bar{\sigma}_{\mathrm{cr}}$. Hence, in contrast to what could be understood from the mean SEE rate in Fig. 4.21, the case with dielectric layer do present the Relaxation Sheath Oscillation (RSO) oscillations. For the case without the dielectric layers (Fig. 4.22.**a**) the transitions between the left of the right wall are synchronous, as there appears simultaneously on the two walls.

On the other hand, the case with dielectric layers presents asynchronous transitions starting from $t = 2\,\mu\mathrm{s}$ and later. This is why the RSO oscillations could not be seen on $\bar{\sigma}_{\mathrm{PIC}}$ in Fig. 4.21. In addition, it seems that the left wall remains longer in the SCL regime compared to the right wall. Figure 4.23 shows the temporal evolution of the radial electric field at the right wall and along the azimuthal direction for (**a**) the case with grounded wall, and (**b**) the case with dielectric layers. We see that for the case without the dielectric layer modeled, the sheath changes from the standard regime to the SCL regime simultaneously along the radial direction. However, in the case with the dielectric layer, the sheath does not necessarily present the same regime at

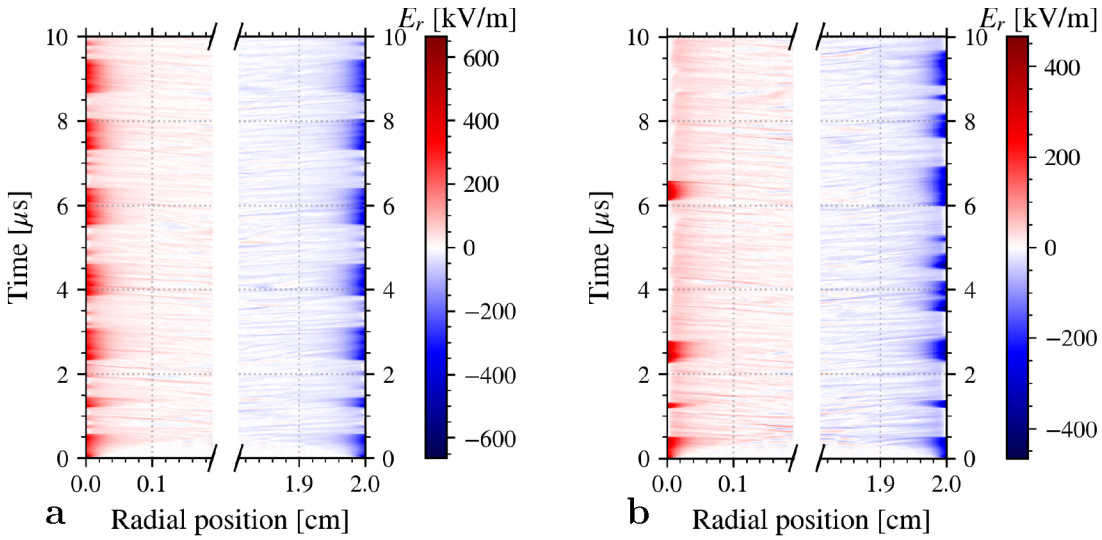

FIGURE 4.22 – Temporal evolution of the radial electric field over 2 mm from the wall at the center of the azimuthal direction ($\theta = 0.25$ cm) for (**a**) the case with grounded wall, and (**b**) the case with dielectric layers.

the same time along the azimuthal direction. This difference is due to the azimuthal electric field, that must be zero along the wall when the dielectric layer is not modeled, whereas it is not constrained with the dielectric layer modeled.

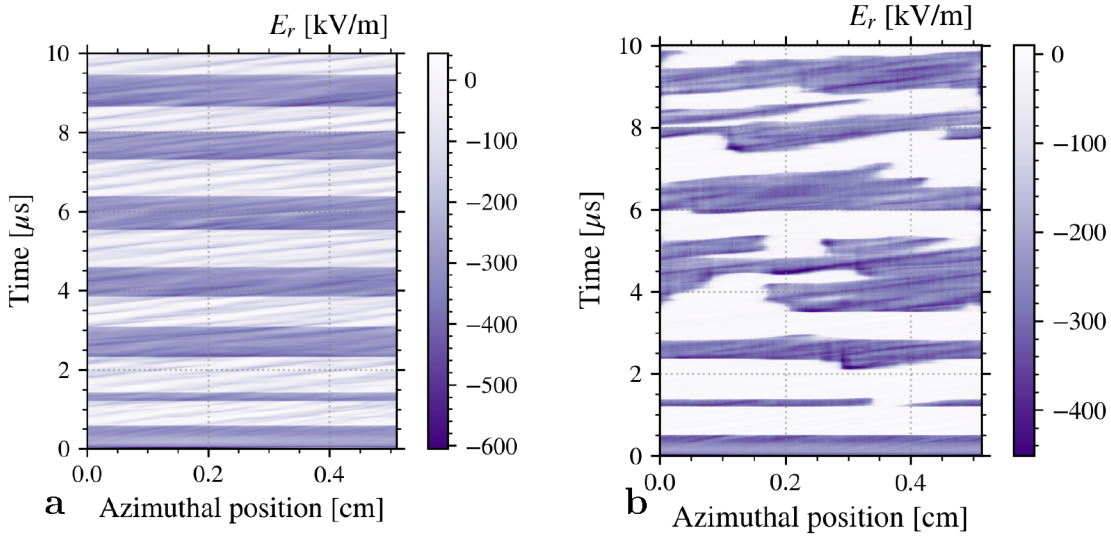

FIGURE 4.23 – Temporal evolution of the radial electric field at the wall along the azimuthal direction for (**a**) the case with grounded wall, and (**b**) the case with dielectric layers.

To finish with, we show in Figure 4.24 the temporal evolution of the electric field measured in the simulation at the wall and the electric field that corresponds to the surface charge $\frac{\sigma}{\epsilon_0}$ at the center of the azimuthal direction ($\theta = 0.25$ cm). While the surface charge follows slightly the transitions between the SCL and the usual sheath regime, it is significantly different from the measured electric field. Especially during the SCL regime, where the surface charge shows large oscillations that is not observed on the radial electric field.

To summarized, we have compared in this section the results of the regime **II** ($\epsilon^* = 45$ V) with and without the dielectric layer modeled. While the transitions between the SCL (regime **I** and the usual sheath (regime **III**) is seen in both cases, when the dielectric layer is modeled

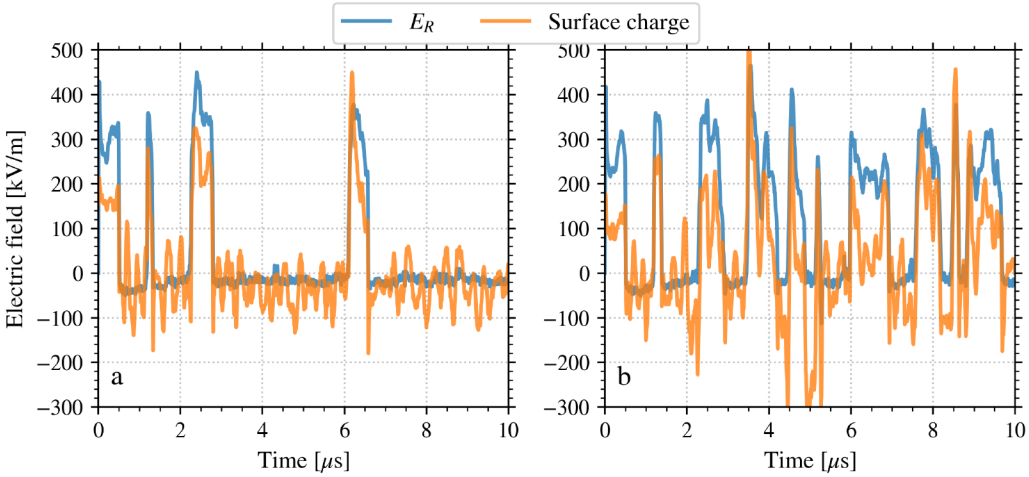

FIGURE 4.24 – Temporal evolution of (blue) the electric field at the wall and (orange) the electric field that corresponds to the surface charge $\frac{\sigma}{\epsilon_0}$ at the center of the azimuthal direction ($\theta = 0.25\,\text{cm}$) for (**a**) the left wall and (**b**) the right wall. The sign of the electric field is positive toward the wall.

the transitions are not synchronous between the two walls and along the azimuthal direction. Consequently, the sharp transitions of the averaged SEE rate $\bar{\sigma}_{\text{PIC}}$ observed in regime **II** without the dielectric layer is not observed. This could explain why this regime has not yet been observed experimentally, as it is very localized. Lastly, we observed that the surface charge does not present the same evolution than the radial electric field at the wall, especially during the SCL regime. This means that using the Neumann boundary condition to model the dielectric layer will certainly return different results.

4.8 Conclusion of the parametric study

Using the PIC simulation code introduced in Chapter 2, we studied the effects of the dielectric walls on the discharge, and more precisely the effects on the electron axial mobility. To begin with, a *base* case with metallic walls was defined and studied. The metallic walls correspond to grounded and non-emissive walls. For this reference case, we observed that the convection model used allows us to obtain a quasi steady-state. We observed an enhanced electron transport transverse to the magnetic field lines, because of the azimuthal instability. Both effects of the dielectric – the electron induced electron emission and the electrostatic boundary condition – were investigated. First, we only modeled the dielectric boundary condition. Then, we studied only the electron emission. Afterwards, the two phenomena have been studied together.

Electrostatic boundary condition

The electrostatic boundary condition is modeled by including in the domain of simulation the thickness of the wall ($L_{\text{Diel}} = 3\text{mm}$). Surface charges accumulate at the interface between the plasma and the wall. We observed that the modified boundary condition did not modify significantly the discharge and the axial cross-field electron mobility. Moreover, we saw that the boundary condition used results in a radial electric field E_r of the same order of magnitude than the Neumann boundary condition of Eq. (4.8) but the spatio-temporal evolution is not identical.

Indeed, when the secondary electron emission is modeled, the surface charges oscillates significantly compared to the radial electric field during the SCL regime. As the dielectric model

used here does not increase significantly the computational time, we recommend to use it instead of the Neumann boundary condition, that do not reproduce the same plasma-wall interaction.

Electron induced electron emission

The electron emission from the wall due to the impact of primary electrons reaching the wall is modeled using the model described in Section 2.6. The value of the crossover energy ϵ^* is varied from a large value (low emissivity) to small values (high emissivity). We observed in the simulations that when the electron emission rate increases, the mean electron temperature decreases. This decreases the amplitude of the ECDI at saturation, hence decreases the electron mobility in the plasma (see Fig. 4.15). However, electron emission induces Near-Wall Conductivity (NWC), which almost doubles the electron mobility close to the wall when ϵ^* varies from 200V to 30V. Consequently, the overall electron cross-field mobility is almost constant in our simulation.

We observed in our PIC simulations three different regimes depending on the values of ϵ^*. For high values of ϵ^*, the plasma stabilises with an emission rate $\bar{\sigma}_{\mathrm{PIC}} < \bar{\sigma}_{\mathrm{cr}}$. When ϵ^* is small, we observe a stable configuration with $\bar{\sigma}_{\mathrm{PIC}} \sim \bar{\sigma}_{\mathrm{cr}}$. Under these conditions, the sheath is space-charge limited. The transition between the two regimes is not stable, but instead passes by a bi-stable regime. In this third regime, the sheath oscillates between the two stable regimes.

Comparison with classical sheath model

The simulation results have been compared to the classical sheath model of Hobbs and Wesson [81]. We observed a significant discrepancy between the PIC simulations and the sheath model that comes from a fluid approach. In particular, the potential drop and the electron emission rate are both overestimated. These overestimations can lead to erroneous conclusion and prediction when using fluid models. Hence, a better understanding of the plasma-wall transition via the sheath is needed.

The sheath model currently used is based mainly on two hypothesis

— Maxwellian electron distribution function

— Isothermal electrons in the sheath

Both hypotheses will be questioned in the next chapter.

Chapter 5

Non-isothermal sheath model

The work presented in this chapter has been published in Tavant et al. [93].

In Chapter 4, discrepancies between the expected plasma-wall interaction quantities – as the plasma potential drop through the sheath and the electron emission rate – and the Particle In Cell (PIC) simulation results have been observed. In this chapter, we carry out a detailed analysis of the simulation results presented in Chapter 4 in order to gain more insight on the plasma-wall interaction. We focus on a simplified simulation in order to isolate the plasma-wall interaction from the other phenomena. This new PIC simulation is one-dimensional in space and three-dimensional in velocity (1D-3V), un-magnetized, and without electron emission. From this simplified simulation, we derived a non-isothermal sheath model, that describes well the kinetic simulations. We also extend the model to the case where ionization is self-consistent.

Contents

5.1 Insights from the PIC simulations

As mentioned in Section 4.6, the sheath model of Section 2.7 uses two hypotheses:
— Maxwellian electrons,
— Isothermal electrons.

When collisions can be neglected, as it is usually assumed in the sheath, these two hypotheses are linked. Indeed, the 1 dimension (1D) Maxwellian distribution function expressed as a function of the total energy is

$$f(\epsilon,\phi) \propto \exp\left(\frac{\epsilon-\phi}{\mathrm{T_e}}\right) \propto \exp\left(\frac{\epsilon}{\mathrm{T_e}}\right)\exp\left(\frac{-\phi}{\mathrm{T_e}}\right), \tag{5.1}$$

where ϵ and $\mathrm{T_e}$ are the electron kinetic energy and temperature expressed in Volt. We can see in Eq. (5.1) that the spatial variation (due to the plasma potential ϕ) only affects the amplitude of the distribution function, not its distribution in the energy space. Hence, the electron temperature is uniform, i.e. the electrons are isothermal. In addition, we find that $n_e \propto \exp(-\phi/\mathrm{T_e})$, which is the definition of Boltzmann electrons.

First we propose to check if these two hypotheses are valid in the 2 dimensions (2D) PIC-Monte Carlo Collision (MCC) simulation results

5.1.1 Electron distribution function

Using the kinetic information of the PIC simulations, we present in Figure 5.1 the mean electron energy probability functions (EEPF) in the case $\epsilon^* = 200\,\mathrm{V}$, for which the electron emission is of the order of $\bar{\sigma} = 0.6$. Figure 5.1.**a** shows the projections of the EEPF in the center of the simulations along the three directions. These projections are compared to the Maxwellian probability function of the same kinetic temperature. Figure 5.1.**b** shows the total EEPF for both the bulk and the sheath populations. The sheath length is defined as the location where the ions reach the Bohm speed, which is located about 0.4mm from the wall.

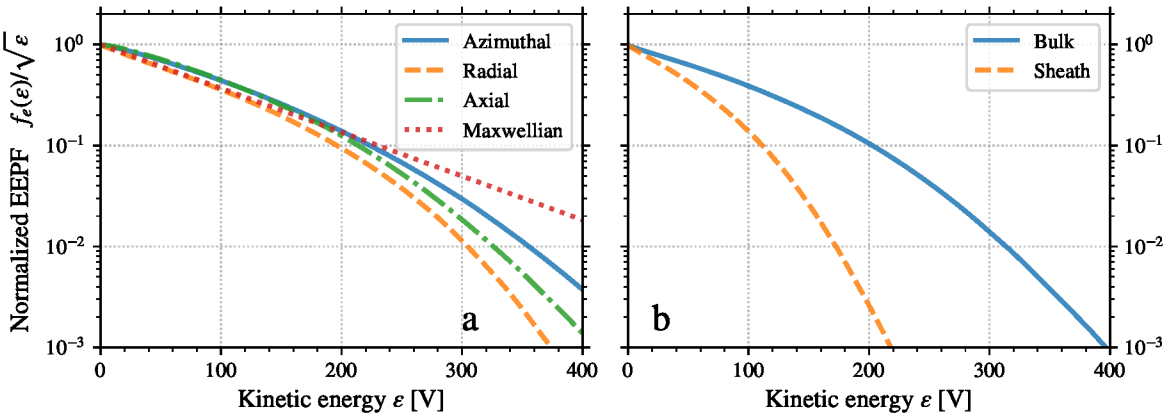

FIGURE 5.1 – Normalized electron energy distribution function of the electrons (**a**) in the bulk, in the three directions, and (**b**) in the bulk and in the sheath. In (**a**)the red dotted line is a Maxwellian distribution of $\mathrm{T_e} = 50\,\mathrm{V}$.

We see in Fig. 5.1.**a** that the electron energy distribution function in the bulk is not Maxwellian. In particular the high energy tails are depleted. In order to evaluate the effect of the non Maxwellian EEPF on the Secondary Electron Emission (SEE) rate $\bar{\sigma}$, we numerically integrate the EEPF from the PIC data using Eq. (4.10). The results (not shown) do not differ significantly from the values of $\bar{\sigma}_{\mathrm{Maxw}}$ obtained assuming a Maxwellian distribution, using Eq. (4.11). Hence, we can conclude that even if the Maxwellian hypothesis is not verified in the PIC simulations, it does not explain the differences observed on $\bar{\sigma}$ in Fig. 4.18.

Figure 5.1.**b** presents the EEPF for the bulk population as well as for the sheath population. We can see that the sheath population is colder than the population at the center. This observation was not expected, and could explain the difference of Fig. 4.18. This effect is assessed in the next section.

Surprisingly, we do not observe in Fig. 5.1 secondary electron beams in the radial direction, unlike previous observations of Sydorenko [63] with a 1D model or Héron and Adam [38] with a 2D model. On the other hand, we do observe SEE beams when we artificially remove the electron cyclotron drift instability by forcing $E_y = 0\,\mathrm{V/m}$ [5]. Hence, it seems that the ECDI, when simulated in 2D, quickly thermalizes the secondary electrons emitted from the walls. In addition, we can see in Fig. 5.1.**a** that the radial EEPF is close to the EEPF in the other directions, i.e the electron are almost isotropic. For instance, for $\epsilon^* = 200\,\mathrm{V}$ we measure $\mathrm{T}_{er} = 41.5\,\mathrm{V}$ while $\mathrm{T}_{e\theta} \sim \mathrm{T}_{ez} = 49\,\mathrm{V}$. The cause of the difference with Héron and Adam [38] is not clear yet, but their results were obtained at early times when saturation of the instability has not necessarily been reached, and no electron loss in the axial direction was accounted for. This is supported by Figs. 4.1 and 4.3 which show us that there is a larger anisotropy at the beginning of the simulation ($t < 2\mu\mathrm{s}$) than later. It is possible that when the instability is fully saturated, during the quasi steady-state, the electrons had sufficient time to isotropize. The energy transfer from the axial and azimuthal directions to the radial direction is not clearly understood yet [65], but we believe that it is due to the instability.

5.1.2 Radial evolution of the electron temperature

Figure 5.2 shows the radial profile of the electron temperature $\mathrm{T_e}$ averaged in time over $5\,\mu\mathrm{s}$ and over the azimuthal direction, for different emissivities. We can see that for all of the values of ϵ^* and even without electron emission, there is a steep gradient of the electron temperature in the sheath. Actually, the profile of $\mathrm{T_e}$ looks very similar to the profile of the plasma potential ϕ.

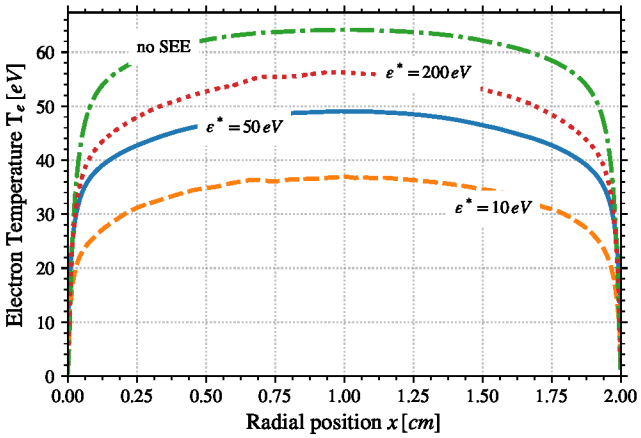

FIGURE 5.2 – Radial profiles of the electron temperature measured in the PIC simulations, without secondary electron emission (label "no SEE") and with different values of ϵ^*.

The significant difference between the value of the mean electron temperature in the whole simulation domain, used before in Section 4.6, and the electron temperature close to the wall can be responsible for the overestimation of $\bar{\sigma}$ compared to $\bar{\sigma}_{\mathrm{PIC}}$ on Fig. 4.18. Using this information, we compute an estimation of the electron emission rate $\bar{\sigma}$ with Eq. (4.11) using the electron temperature averaged over the last five cells of the PIC simulations. The results are presented in Figure 5.3.

We observe in Fig. 5.3 that now, the electron emission rate is well predicted (error less than 5%), except for $\epsilon^* = 10\,\mathrm{V}$ where a large error is still observed. As previously discussed, the case $\epsilon^* = 10\,\mathrm{V}$ presents a very high SEE rate which leads to a potential well close to the wall, the

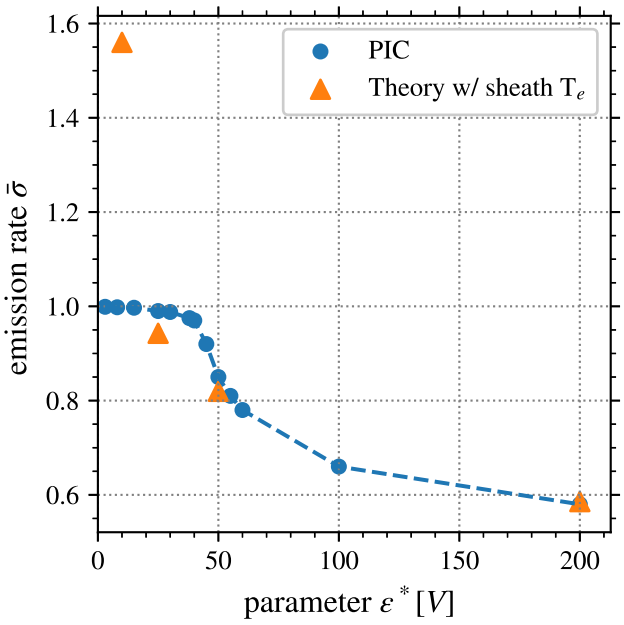

FIGURE 5.3 – Estimation of the electron emission rate $\bar{\sigma}$ as a function of ϵ^* using the values of the electron temperature close to the wall.

so-called Space Charge Limited (SCL) regime. Consequently, some secondary electrons emitted at low energy would be reflected back to the wall. Hence, since Eq. (4.11) does not take into account this local effect, it is not surprising that the SEE rate calculated using the mean electron temperature in the sheath is too high.

To summarize, Fig. 5.3 shows that when the sheath is not in the SCL regime, the SEE rate can be well predicted by Eq. (4.11) using the electron temperature close to the wall, which is lower than in the center of the domain. The particle and energy flux inducing the SEE rate are not well described if we use the electron temperature of the bulk as in the isothermal sheath model. This explains the overestimation of both $\bar{\sigma}$ and and $\Delta\phi$ presented in Figs. 4.18 and 4.19. Hence, the isothermal hypothesis used in the sheath model of Section 2.7 is denied by the PIC simulations.

In the next sections, we use a simplified PIC simulation to study in detail the origin of the electron temperature gradient in the sheath.

5.2 Simplified 1D PIC simulations

We have seen in Section 5.1 in Fig. 5.2 that the secondary electron emission is not responsible for the temperature radial profile. Hence, we neglect it in this section. The simulations are at low pressure, in which case the electrons are non-local [116, 117]. In low pressure bounded discharges, it is well-known that the EEDF is not Maxwellian in both capacitively coupled plasmas and inductively coupled plasmas [118, 119, 120, 73], in agreement with Fig. 5.1.

The impact of non-Maxwellian EEDF on the electron flux to the wall has been studied by Kaganovich et al. [121, 122]. They showed that the electron kinetics at low pressure can significantly reduce the electron flux to the wall, in agreement with kinetic simulations. The main parameter determining the electron flux was found to be the electron scattering frequency. However, to our knowledge no fluid model describes the sheath with non-Maxwellian EEDF.

The evolution of the electron temperature and the non-locality of the electrons in bounded plasmas has been studied in Meige and Boswell [120]. The authors showed that the high energy tail of the Electron Energy Distribution Function (EEDF) is depleted. They observed that the

Parameter	Value	Unit
Pressure P	$0.05, 0.1, 0.5, 2, 10$	mTorr
Initial density	1.10^{15}	m^{-3}
$\mathrm{T}_{\mathrm{e},inj}$	5	V
Domain length L	10	cm
gas	Argon	-

TABLE 5.1 – Simulation parameters for the 1D PIC simulations.

energy at which the depletion starts corresponds to the local plasma potential related to the wall. Hence, we will use in this chapter similar physical conditions, in order to compare our results to their observations.

5.2.1 Description of the 1D simulations

We use a 1D PIC simulation of an argon plasma confined between two walls separated by a length $L = 10$cm. The background pressure is varied between 0.05 and 10 mTorr. The direction of the simulation is x, and y, z are perpendicular to the simulation domain.

The same particle source model as in 2DPIC of the Hall Effect Thruster (HET) is used. In order to compensate the particle losses at the wall, we inject with a spatially uniform probability an electron-ion couple for every ion lost at the wall. This corresponds to the following ionization source term:

$$S_{iz} = \frac{1}{L} 2\Gamma_e \tag{5.2}$$

with Γ_e the electron flux to the wall. A second model will be used later, with a self-consistent heating and ionization.

Monte Carlo collisions (MCC) are still used, but we do not model the particle generation of the ionization process, but only the scattering and momentum transfer. As previously, Coulomb collisions are not included in the study as we are at low plasma density (at steady-state the electron density is around $n_e = 10^{15}\mathrm{m}^{-3}$).

To satisfy generally accepted accuracy conditions for the cell size and time step [70], a time step of $3.7 \cdot 10^{-11}$ s is used with a cell length of $1.7 \cdot 10^{-5}$ m. This allows us to resolve properly the plasma frequency $\frac{2\pi}{\omega_{pe}} = 3.5 \cdot 10^{-9}$ s and the Debye length $\lambda_{De} = 3.10^{-4}$ m. Around 300 particles per cell are used for the simulations, and statistical convergence has been verified for both the cell length and the number of particles per cell.

5.2.2 Simulation results of the 1D PIC simulation

Figure 5.4 shows the results of the simulation for a neutral pressure $P = 0.1$mTorr. The results obtained with the different pressures of Table 5.1 show the same characteristics, and the effect of the pressure is further discussed in Section 5.3.3.

On the left-hand side we observe the electron and ion density profiles, while on the right the plasma potential and the electron temperature, defined with Eq. (1.18), are shown. In Fig. 5.4, the electron and ion densities and the plasma potential feature the usual symmetric profiles with a pre-sheath and a sheath. However, while the electron temperature is almost constant in the plasma bulk at the center of the simulation domain, we observe a steep decrease in the sheath. The electron temperature gradient should affect the density profile in the sheath and the electron heat flux to the wall.

For isotropic distribution functions, it is convenient to introduce the electron energy distribution function (EEDF) f_ϵ [123]:

$$f_\epsilon(\epsilon)d\epsilon = 4\pi v^2 f_e(\mathbf{v})dv \tag{5.3}$$

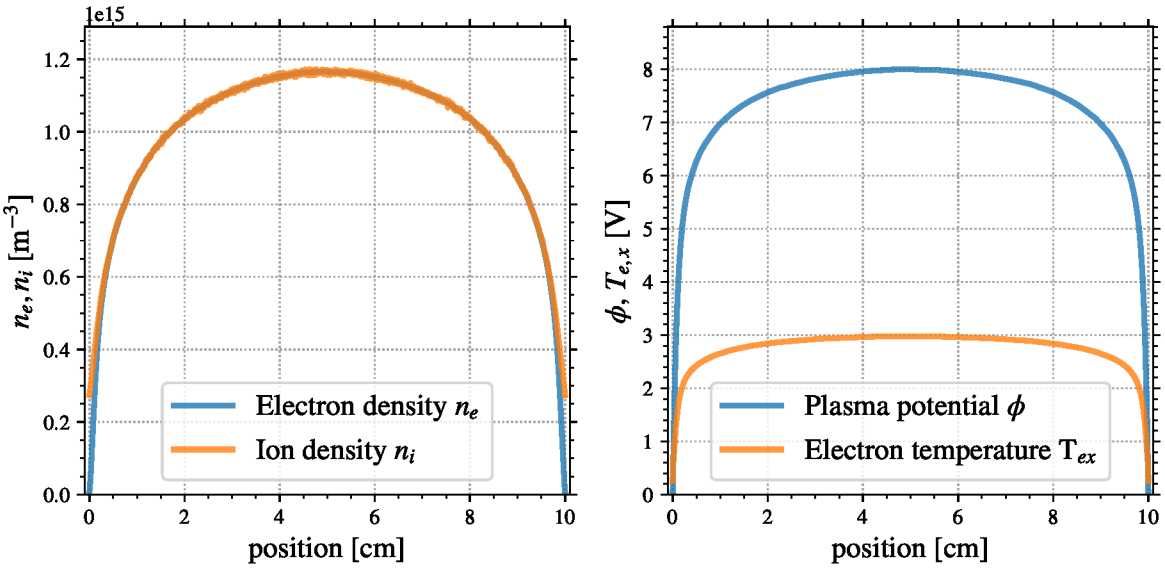

FIGURE 5.4 – Profile of the electron and ion densities (left) and the plasma potential and electron temperature in the PIC simulation with the parameters of Table 5.1, with $P = 2$mTorr.

It is related to the electron energy probability function (EEPF) f_P by (see Eq. (1.14))

$$f_P(\epsilon) = \epsilon^{-1/2} f_\epsilon \tag{5.4}$$

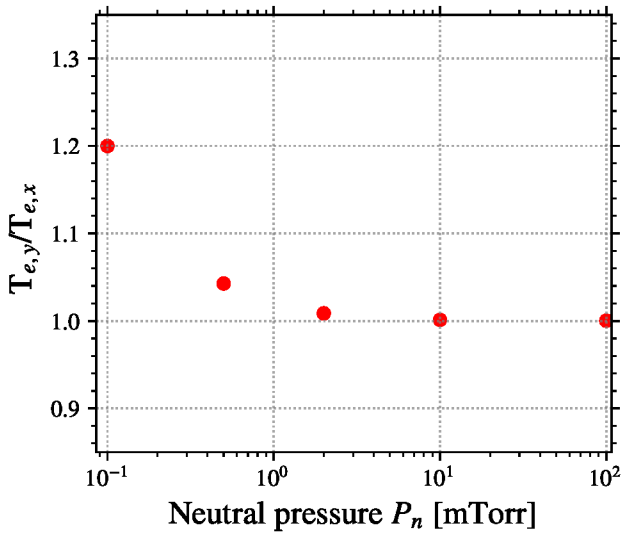

FIGURE 5.5 – Evolution of the temperature ration between the y direction (parallel to the wall) and the x direction (normal to the wall) as a function of the neutral pressure

At low pressure, the distribution function can be anisotropic. Figure 5.5 shows the evolution as a function of the neutral background pressure of the ratio between the electron temperature parallel to the wall $T_{e,y}$ and the temperature normal the the wall $T_{e,x}$. We can see that when the pressure decreases, the distribution function becomes less isotropic. As the distribution function can be anisotropic, and since the direction of interest is the x direction, we focus here on $f_{Px}(\epsilon_x)$ the EEPF in the x direction, with $\epsilon_x = \frac{m_e v_{e,x}^2}{2}$.

Figure 5.6 presents the EEPF measured in the PIC simulations at different positions. As the system is symmetric around x=5cm, the positions have been chosen arbitrarily in the left

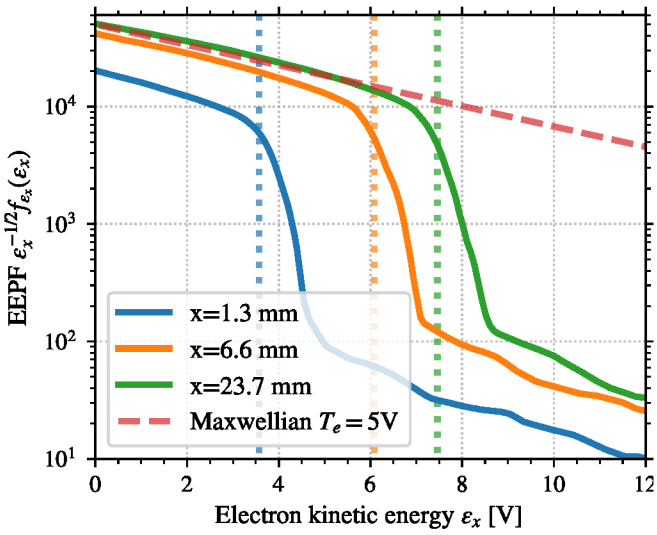

FIGURE 5.6 – Electron energy probability function at different positions in the simulation: at $x = 1.3, 6.6$ and 23.7 mm in blue, orange and green respectively. Also shown are the Maxwellian distribution of temperature $T_e = 5\,V$ (red dashed line), as well as the local plasma potential relative to the wall $\Delta\phi$ (dotted lines).

sheath, and their values correspond to the positions of the cell centers. We can see that the low energy population ($\epsilon < e\Delta\phi$) is nearly Maxwellian, of temperature $T_e = 5\,V$ which is the injection temperature $T_{e,inj}$. This population corresponds to the electrons confined by the sheath. However, the high energy tail ($\epsilon > e\Delta\phi$) is depleted due to the absorption at the wall [120, 122, 124]. This results in a non-Maxwellian EEPF of temperature, defined with Eq. (1.18), lower than $T_{e,inj}$. The small population of electrons with very high energy corresponds to the electrons newly generated that have not reached the walls yet.

5.2.3 A model for the observed EVDF

In order to describe the EEPF seen in Fig. 5.6, it is possible to use a two-T_e distribution [124, 118, 125]:

$$f_{Px}(\epsilon_x) = A\epsilon_x^{1/2} \begin{cases} \exp(-\frac{\epsilon_x}{T_1} - \frac{\epsilon_b}{T_2}), \ \epsilon_x < \epsilon_b \\ \exp(-\frac{\epsilon_x}{T_2} - \frac{\epsilon_b}{T_1}), \ \epsilon_x > \epsilon_b \end{cases} \tag{5.5}$$

with ϵ_b the energy of the knee, T_1 and T_2 the two temperatures, and A a normalization constant. In the case of absorption by the walls, we can assume that $\epsilon_b = \Delta\phi$ as the absorption only occurs for the electrons of energy higher than $\Delta\phi$. For the case of Fig. 5.6, we find $T_1 = 5$eV and $T_2 = 0.5$eV. This model is closer to the PIC EEPF, but neglects the tails of newly generated electrons of high temperature, as we can see if in Figure 5.7.

In the next section, we investigate a way of taking into account this non-local kinetic phenomenon in a fluid model.

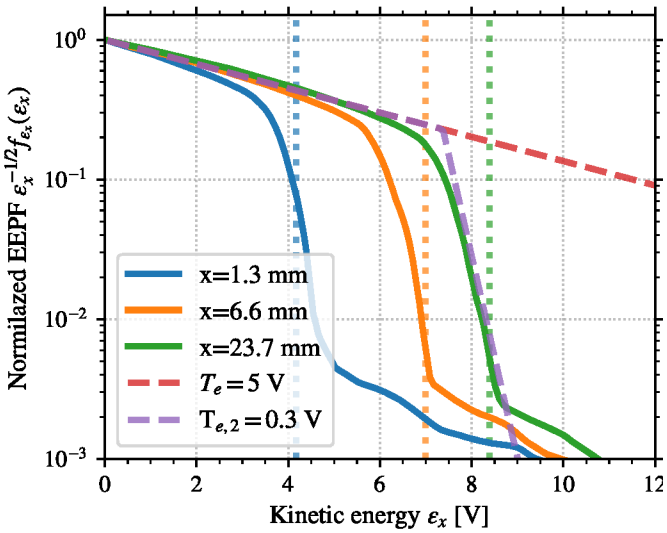

FIGURE 5.7 – Electron energy probability function at different positions in the simulation, as in Fig. 5.6, but overlaid with a 2-temperature distribution function.

5.3 Collisionless kinetic model and polytropic state law

The previous section showed that in the 1D PIC simulations the electrons are not Maxwellian, similarly to the 2D results. In this section, we use the 1D kinetic equation in order to highlight the important phenomena needed to describe the sheath.

5.3.1 Vlasov equation for the sheath

Because the sheath is thin and the neutral pressure is low, we neglect the collisions in the sheath, so that we only need to solve Vlasov's equation. The stationary 1D-3V Vlasov equation for the EVDF reads:

$$v_x \cdot \partial_x f_e \mathbf{e}_x + \frac{e}{m_e} \nabla\phi \cdot \nabla_v f_e = 0, \tag{5.6}$$

Since the electrostatic potential depends only on x, Eq. (5.6) becomes,

$$v_x \partial_x f_e + \frac{e}{m_e} \partial_x \phi \partial_{v_x} f_e = 0 \tag{5.7}$$

The variables v_y and v_z do not play any role, such that they can be hold constant, and we can solve Eq. (5.7) with f_e as a function of x and v_x only.

In order to solve Eq. (5.7) in the sheath, we use the following boundary conditions:

1. At the plasma sheath boundary ($x = x_s$) the EEDF is imposed:

$$f_e(x_s, v_x) = f_0(v_x), \tag{5.8}$$

2. At the wall ($x = x_w$) the particles are absorbed, such that

$$f(x_w, v_x < 0) = 0 \tag{5.9}$$

The partial derivative equation (5.7) can be solved by the method of the characteristics. We introduce the function $\gamma(x)$ such that

$$\frac{df_e(x, \gamma(x))}{dx} = \partial_x f_e + \gamma' \partial_{v_x} f_e = 0 \tag{5.10}$$

Combining this equation with Eq. (5.7) for $v_x = \gamma(x)$,

$$\left(\frac{e\phi'}{m_e} - \gamma\gamma'\right)\partial_{v_x} f_e = 0 \tag{5.11}$$

In general $\partial_{v_x} f_e \neq 0$ such that $(e\phi'/m_e - \gamma\gamma')$ can be integrated

$$\frac{\gamma(x)^2}{2} - \frac{e\phi(x)}{m_e} = \frac{\gamma(x_s)^2}{2} - \frac{e\phi_s}{m_e} \tag{5.12}$$

Since the EVDF is conserved along the contour γ,

$$f_e(x, \gamma(x)) = f_e(x_s, \gamma(x_s)) \tag{5.13}$$

and

$$\gamma(x_s) = \left[\gamma(x)^2 - \frac{2e(\phi(x) - \phi_s)}{m_e}\right]^{1/2} \tag{5.14}$$

with ϕ_s the plasma potential at the sheath edge. Using Eq. (5.8),

$$f_e(x, v) = f_0\left(\left[v^2 - \frac{2e(\phi(x) - \phi_s)}{m_e}\right]^{1/2}\right) \tag{5.15}$$

Condition (5.9) yields a condition on f_0:

$$\text{for all } v > \left(\frac{2e\phi_s}{m_e}\right)^{1/2}, f_0(v) = 0 \tag{5.16}$$

This simple collisionless model explains rigorously how the tail of the EVDF is cut by the wall absorption. This asymmetry of the Electron Velocity Distribution Function (EVDF) could press us to separate the electrons into the population going toward the wall and the one going away from the wall. Figure 5.8 shows the EEPF of the electron going toward and from the wall. We can see that there is only a small difference between the EEPF of the two populations. Indeed, as the domain is symmetric and bounded in the two directions, the population coming toward the wall is also depleted by the opposite wall. Hence in the following, we will neglect this asymmetry due to the wall.

Figure 5.9 compares the EEPF from Eq. (5.15) with the PIC simulations between the position $x = 1.3\,\text{mm}$ and $x = 23.7\,\text{mm}$. The plasma potential reads $\phi(x = 1.3\,\text{mm}) = 4.1\,\text{V}$ and $\phi(x = 23.7\,\text{mm}) = 7.7\,\text{V}$. We can observe a very good agreement between the actual evolution of the EEPF measured in the simulations and the prediction of Eq. (5.15). This confirms the possibility to neglect the collisions in the sheath.

5.3.2 Polytropic state law for the electrons

The evolution of a two-T_e EEDF in a collisionless potential drop has been studied by Zhang et al. [125]. The authors have shown that the evolution of the electron population can be described using a polytropic index γ, such that:

$$\nabla_x \left(p_{e,x}(x) n_e(x)^{-\gamma}\right) = 0 \tag{5.17}$$

with $p_{e,x} = n_e \mathrm{T}_{\mathrm{e},x}$ the electron pressure in the x direction. The value of γ is related to the two temperatures T_1 and T_2, and for $T_1 > T_2$, we have $\gamma > 1$.

Figure 5.10 shows the PIC simulation results presented in Fig. 5.4 in log scale. Each marker represents one cell of the PIC simulation. Overlaid is a linear regression which slope is the polytropic index γ. The regression is conducted over the whole simulation domain. We can see that the linear regression fits the simulation results with a very good agreement ($\mathrm{R}^2 = 0.999$). The value $\gamma = 1.43$ is significantly higher than the isothermal case ($\gamma_{\text{isothermal}} = 1$). Interestingly,

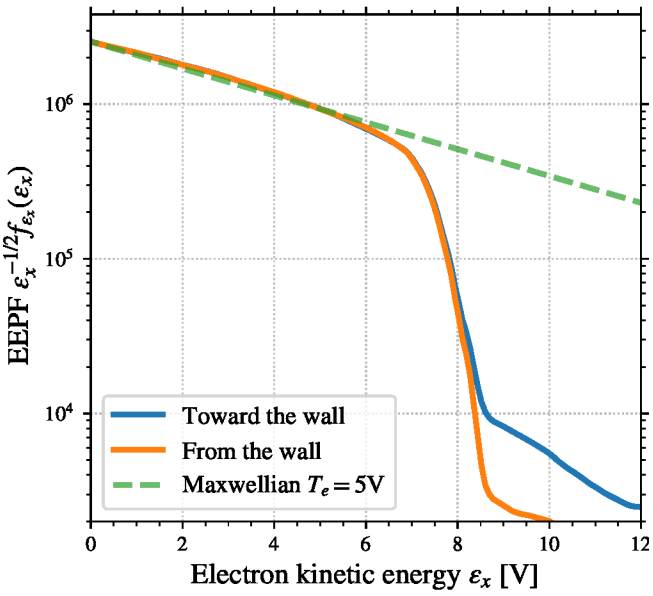

FIGURE 5.8 – EEPF measured in the PIC simulations of the electrons going toward and from the wall at $x = 23.7mm$. The green dashed line corresponds to a Maxwellian distribution of 5 V.

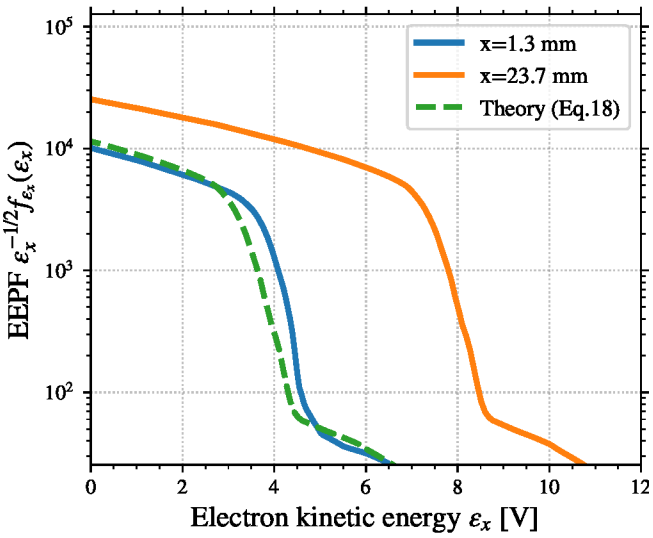

FIGURE 5.9 – Evolution of the EEPF between 1.3mm (in blue) and 23.7mm (in orange) from the wall. Is overlaid (in dashed green) the expected EEPF at $x = 1.3$mm using the EEPF at $x = 23.7$mm and the potential difference in Eq. (5.15).

while the polytropic law observed in Zhang et al. [125] was only for a collisionless evolution, here the polytropic law is observed in both the collisionless sheath and the weakly collisional plasma region.

The polytropic law of Eq. (5.17) can be used in order to close the fluid equation without the isothermal hypothesis. The non-isothermal fluid model for the sheath is the subject of Section 5.4. A polytropic index for the ions has already been proposed in order to link the ions kinetics and the fluid parameters [126, 127]. The approach here is essentially the same but applied to the electrons.

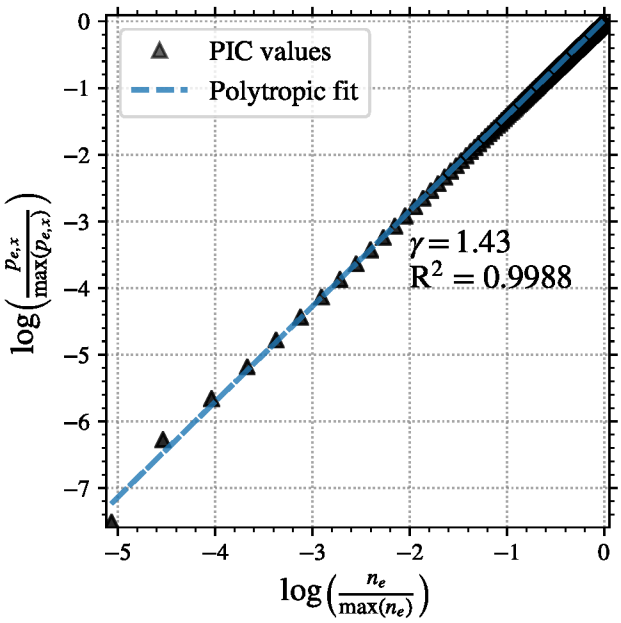

FIGURE 5.10 – Electron pressure as a function of the electron density observed in the PIC simulations of Fig. 5.4 (black markers), and the linear fit (blue dotted line) in order to determine γ.

5.3.3 Evolution of the polytropic index

We investigate the effect of the neutral pressure on the polytropic index γ for the 5 pressure conditions of Table 5.1. We recall that the electron elastic scattering and momentum transfer are modeled, while the ionization and the heating are not self-consistent, but they are similar to the 2D PIC models of Chapter 4. Figure 5.11 presents the evolution of γ as a function of the pressure. We can see that the polytropic index decreases from 1.7 to 1.4 as the pressure increases from 0.05 to 10 mTorr. This is in agreement with the fact that the high energy electron population is mostly replenished by the electron-neutral scattering, in agreement with Kaganovich et al. [122]. Increasing the collisions while keeping the other parameters constant provides more electrons to the high energy tail, hence reducing the polytropic index, as observed by Zhang et al. [125].

Other parameters are also expected to modify γ. For instance the size of the simulation, the electron mean energy, and the nature of the gas.

5.3.4 Coulomb collision and possible improvements

In the PIC simulations, the Coulomb collisions (electron-electron, electron-ion, and ion-ion) are not modeled. However, they are known to modify the distribution function. More precisely, they isotropize the distribution and tend toward a Maxwellian [128, 80].

Using the density $n_e = 1{\times}10^{15}\,/\mathrm{m}^3$ and the electron temperature $\mathrm{T_e} = 3\,\mathrm{V}$ we find the electron-electron Coulomb collision at 90° [56, 42]

$$\nu_{90} = 15\,\mathrm{kHz} \tag{5.18}$$

which is significantly smaller than the electron-neutral scattering frequency. However, it is known that the Coulomb collisions cross-section is highly dependent on the electron velocity.

Figure 5.12 shows the evolution of the mean free path for the electron-electron Coulomb collision $l_{CC} = v_e/\nu_{90}$. We can see that it is of the order of the domain size ($L = 10\,\mathrm{cm}$) only for very low energy. On the other hand, the collision frequency for small angle is higher. In Sydorenko et al. [80], the authors showed that under some conditions, the Coulomb collisions can modify

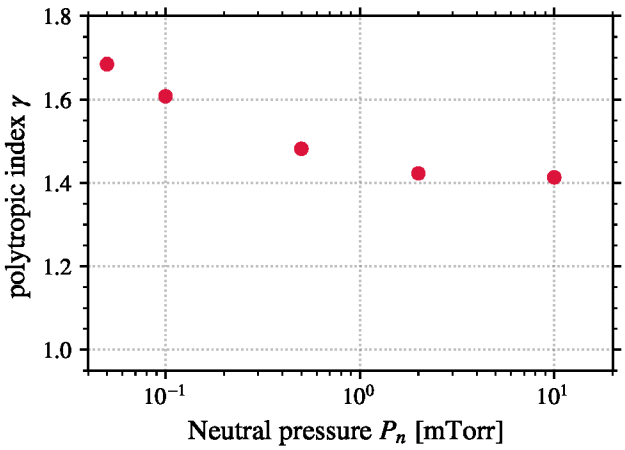

FIGURE 5.11 – Effect of the background neutral pressure over the polytropic index γ in the 1D PIC simulations, under the conditions of Table 5.1. As a reminder, the isothermal case corresponds to $\gamma = 1$.

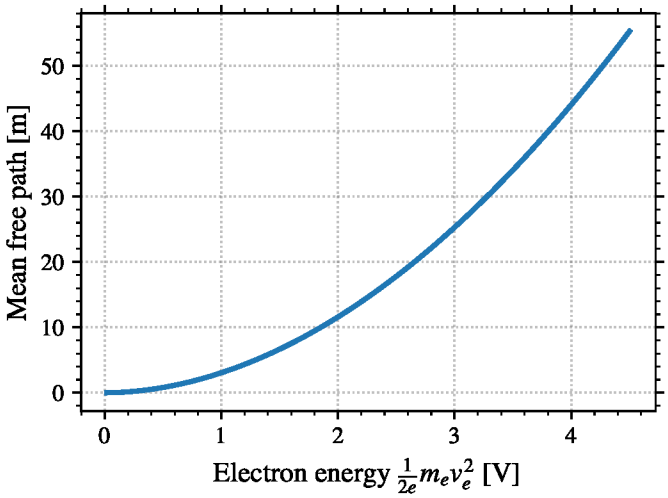

FIGURE 5.12 – Mean free paths of the Coulomb collision as a function of the electron energy.

the simulation results by a few tens of percent. Hence, the impact of the small angle Coulomb collisions on the distribution functions should be asserted in future work. Modeling the Coulomb collision in PIC simulations currently require a different model than the MCC algorithm, thus requires more time to be implemented and tested before being used.

5.4 Non-isothermal fluid model

We have seen in Section 5.3 that the polytropic law presented in Eq. (5.17) can be used to describe the evolution of the electron temperature, hence closing the fluid equations. Provided that the electron pressure is $p_e = en_e\mathrm{T_e}$, assuming that the sheath is collisionless, and neglecting the electron mean velocity compared to the thermal velocity, the electron momentum conservation

$$\nabla(n_e\mathrm{T_e}) + n_e\nabla\phi = 0 \tag{5.19}$$

results in

$$\nabla\mathrm{T_e} = -\frac{\gamma - 1}{\gamma}\nabla\phi \tag{5.20}$$

Integrating Eq. (5.19) from the sheath edge, the electron density is hence :

$$n_e(\phi) = n_0 \left[1 + \frac{(\gamma - 1)(\phi - \phi_0)}{\gamma \mathrm{T_{e0}}}\right]^{\frac{1}{\gamma - 1}} \tag{5.21}$$

with the subscript 0 corresponding to the sheath edge. In Eq. (5.21), we need to have γ strictly greater than one. For $\gamma = 1$, we find the usual Boltzmann electrons :

$$n_e(\phi) = n_0 \exp(-\frac{(\phi - \phi_0)}{\mathrm{T_e}}) \tag{5.22}$$

corresponding to the isothermal model.

5.4.1 Comparison with the PIC simulations

The PIC simulations of Section 5.2 can be modeled using a 1D low pressure fluid model with collisionless ions. We use the solver described in Riemann et al. [129], modified to take into account the new electron closure. We simply need to add one equation for the temperature, and the ionization source term is fixed constant in space.

Using the normalized variables and parameters :

$$\lambda = \frac{S_{iz} L}{c_s}, \qquad \Phi = -\frac{e\phi}{\mathrm{T_{e,c}}}, \qquad u = \frac{v_i}{c_s} \tag{5.23}$$

$$n = \frac{n_i}{n_{e,c}}, \qquad \chi = \lambda \frac{x}{L}, \qquad \epsilon = \lambda \frac{\lambda_{De}}{L} \tag{5.24}$$

$$\tag{5.25}$$

with $\mathrm{T_{e,c}}, n_{e,c}$ the electron temperature and density at the center, $c_s = \sqrt{\frac{\mathrm{T_{e,c}}}{m_i}}$ the ion sound speed, v_i, n_i the ion speed and density, and S_{iz} the ionization frequency, we can write the set of equations as [129] :

$$\begin{cases} d_\chi(nu) & = \lambda \\ d_\chi(u) & = \frac{d_\chi(\phi)}{u} - \frac{\lambda}{n} \\ d^2_\chi(\Phi) & = \frac{(n - n_e)}{\epsilon^2} \\ S_{iz} & = cst \\ n_e & = \left[1 + \frac{(\gamma - 1)\Phi}{\gamma}\right]^{\frac{1}{\gamma - 1}} \end{cases} \tag{5.26}$$

Starting from the center, and using the results of the PIC simulations to determine γ, we can use the system of Eq. (5.26) to compute the profile of each variable. The plasma potential is self consistently computed from an arbitrary value at the center. It is then shifted to set the wall potential to 0V. The integration uses the 4^{th} order Runge-Kutta integration scheme of the python package `scipy`.

Figure 5.13 shows the comparison of the electron temperature and the plasma potential with the resolution of the set of Eq. (5.26). We can see a very good agreement between the model and the PIC simulations.

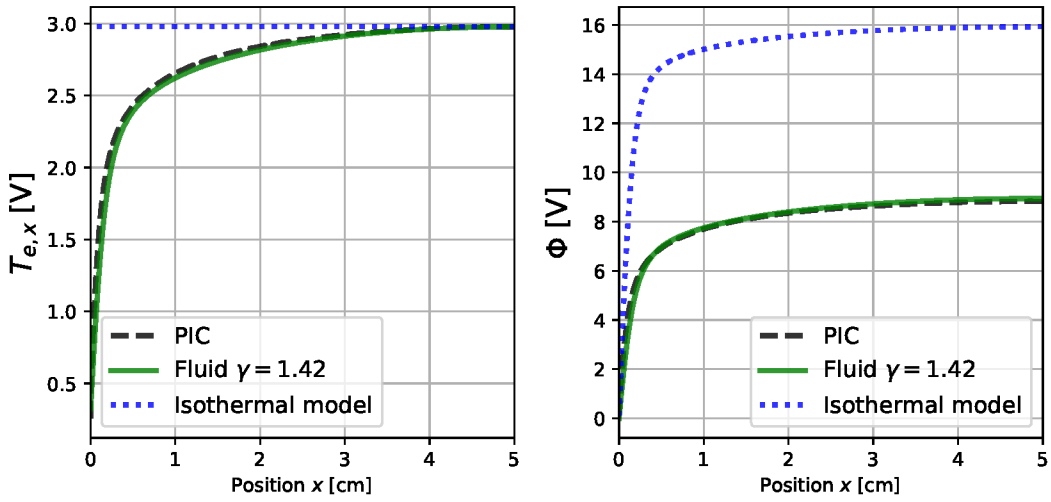

FIGURE 5.13 – Comparison of the electron temperature and plasma potential measured in the PIC simulation with the prediction of the polytropic model with $\gamma = 1.42$.

5.4.2 Modified Bohm criterion

The Bohm criterion expresses a necessary condition on the ion velocity at the sheath edge for the formation of a stationary sheath [130]. As discussed in the appendix, it is possible to derive a modified Bohm criterion for the polytropic electrons :

$$\mathcal{M}^2 = \left(\frac{u_0}{c_s}\right)^2 \geq \gamma \tag{5.27}$$

with $\mathcal{M}$ the Mach number, u_0 the ion mean velocity at the sheath edge and $c_s = \left(\frac{e\mathrm{T_{e0}}}{m_i}\right)^{1/2}$ the ion acoustic velocity at the sheath edge. The derivation of this modified Bohm criterion is analogous to the isothermal case. In the same way as for the isothermal Debye sheath, we assume that the sheath criterion is saturated :

$$\mathcal{M}^2 = \gamma. \tag{5.28}$$

In addition, the ion flux at the wall is equal to the flux at the sheath edge :

$$\Gamma_i = n_0 \sqrt{\frac{\gamma e \mathrm{T_{e0}}}{m_i}} \tag{5.29}$$

5.4.3 Plasma potential drop to the wall

The electron flux at the wall is the thermal flux :

$$\Gamma_e = \int_0^{+\infty} v f_e(x = x_w, v) dv \tag{5.30}$$

Using the model of two-Te EEDF described in Section 5.2.3, we obtain

$$\Gamma_e = \frac{1}{4} n_{e,w} \bar{v}_w \tag{5.31}$$

with $n_{e,w}$ the electron density at the wall, and $\bar{v}_w = \sqrt{\frac{8e\mathrm{T_{e,w}}}{\pi m_e}}$ the mean electron speed at the wall, using $\mathrm{T_{e,w}}$ the electron temperature at the wall. Using Eq. (5.20), we have :

$$\mathrm{T_{e,w}} = \mathrm{T_{e0}} \left(1 - \frac{\gamma - 1}{\gamma} \frac{\Delta\phi_0}{\mathrm{T_{e0}}}\right) \tag{5.32}$$

with $\Delta\phi_0$ the potential drop between the sheath edge and the wall. Using the current equality : $\Gamma_i = \Gamma_e$ at the wall we find with Eqs. (5.29), (5.31) and (5.32) :

$$\left[1 + \frac{\gamma - 1}{\gamma}\frac{\Delta\phi_0}{\mathrm{T_{e0}}}\right]^{\frac{1}{\gamma-1}} \sqrt{1 - \frac{\gamma - 1}{\gamma}\frac{\Delta\phi_0}{\mathrm{T_{e0}}}} = \sqrt{\frac{2\gamma\pi m_e}{m_i}} \tag{5.33}$$

Equation (5.33) cannot be solved analytically, but it can be solved numerically. We use the function `fsolve` from python package `scipy.optimize` to plot the solution of Eq. (5.33) in Fig. 5.14. Meanwhile, we estimate $\frac{\Delta\phi_0}{\mathrm{T_{e0}}}$ using the fluid model of Section 5.4 by reading the potential at the position for which the ions reach the modified Bohm velocity. The small difference between the solution of Eq. (5.33) and the fluid solution is due to the presence of ionization in the sheath.

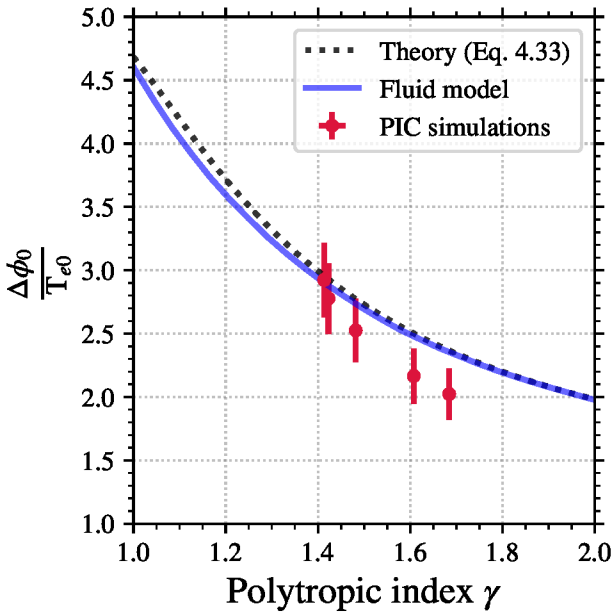

FIGURE 5.14 – Evolution of the potential drop normalized to the electron temperature as a function of the polytropic index γ from the theory of Eq. (5.33), from the fluid model of Section 5.4.1 and from the PIC simulations results (the same cases as in Fig. 5.11). Errors correspond to 10% .

Figure 5.14 shows the evolution of normalized plasma potential drop to the wall $\frac{\Delta\phi_0}{\mathrm{T_{e0}}}$ as a function of γ. Error bars indicate an uncertainty of 10%. This uncertainty value corresponds to an aggregation of the numerical fluctuation of the PIC simulation (that decreases when more particles per cell are used), and the estimation of the sheath edge position. A more accurate estimation of these uncertainties would require a dedicated study with many additional simulations, hence we choose the reasonable value of 10% [70]. We can see that in the limit where $\gamma \to 1$, we find with Eq. (5.33) the usual isothermal value $\frac{\Delta\phi_0}{\mathrm{T_{e0}}} \simeq 4.68$ for argon. The value observed in the fluid model is very close to the results of Eq. (5.33). This is due to the very small size of the sheath, as seen in Fig. 5.4. When γ increases, $\frac{\Delta\phi_0}{\mathrm{T_{e0}}}$ decreases significantly. The decrease of $\Delta\phi_0$ is consistent with the depletion of the high energy tail of the electrons distribution function, as the plasma needs less screening of the electrons in order to remain quasi-neutral.

Figure 5.14 also presents the potential drop measured in the same PIC simulations as presented in Fig. 5.11. The error bars correspond to an estimate of the aggregation of the uncertainties from the PIC simulation and the averages. The sheath edge is defined using the modified Bohm criterion (Eq. (5.28)), as for the fluid model. We can see a very good agreement with the theories. The trend of decreasing potential drop with increasing γ is clearly observed, and the values agree

within about 10%. This is significantly more accurate than the 50% discrepancy with respect to the isothermal model.

The solutions of Eq. (5.33) can be fitted between $\gamma = 1$ and $\gamma = 2$ with a good precision ($R^2 = 0.98$) by :

$$\frac{\Delta\phi_0}{\mathrm{T_{e0}}} = 0.7 + \frac{4.1}{\gamma^{1.7}} \tag{5.34}$$

5.4.4 Power losses at the wall

As expressed in the previous section, the electron flux to the wall is equal to the ion flux :

$$\Gamma_e = \Gamma_i = n_0 \sqrt{\frac{\gamma e \mathrm{T_{e0}}}{m_i}} \tag{5.35}$$

with $n_{e,0}$ and $\mathrm{T_{e0}}$ the electron density and temperature at the sheath edge. Following the two-$\mathrm{T_e}$ EEDF as described in Section 5.3, the electron energy flux to the wall is a thermal flux from a Maxwellian distribution function of temperature $\mathrm{T_{e}}_w$. Hence it reads [123] :

$$Q_e = \Gamma_e 2\mathrm{T_{e}}_w \tag{5.36}$$

Using Eq. (5.32), we obtain

$$\frac{Q_e}{\Gamma_e} = 2\mathrm{T_{e0}} \left[1 - \frac{(\gamma - 1)}{\gamma} \frac{\Delta\phi_0}{\mathrm{T_{e0}}}\right] \tag{5.37}$$

with $\frac{\Delta\phi_0}{\mathrm{T_{e0}}}$ calculated from either Eq. (5.33) or Eq. (5.34). From Eq. (5.37) we see that in the isothermal limit we find the usual $2\mathrm{T_e}$ mean energy by electron leaving the plasma. However, for $\gamma > 1$, the mean energy by electron decreases.

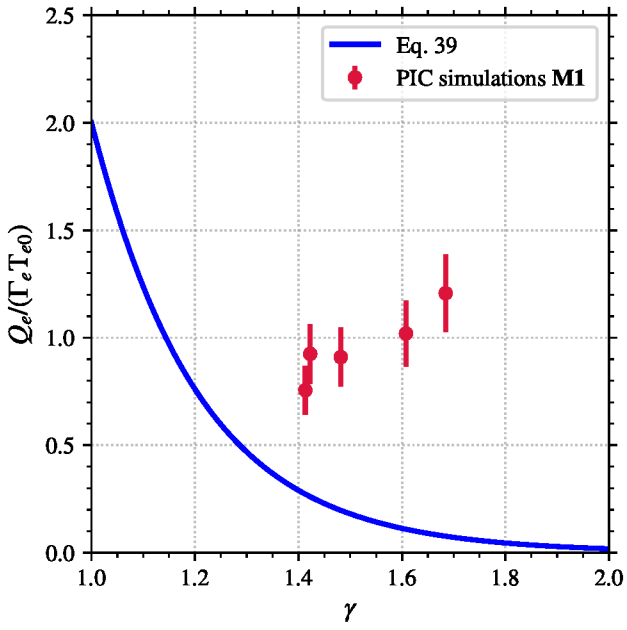

FIGURE 5.15 – Evolution of the mean energy per electron leaving the plasma at the wall normalized to the electron temperature at the sheath edge as a function of the polytropic index γ from the theory of Eq. (5.37) and from the PIC simulations results (the same cases as in Fig. 5.11) .

Figure 5.15 shows the evolution of the average energy of electrons leaving the plasma at the wall normalized to the electron temperature in the plasma bulk from Eq. (5.37). We can see

that the ratio is significantly lower than the isothermal value $\frac{Q_e}{\Gamma_e} = 2\mathrm{T_{e0}}$ when $\gamma > 1$. Overlaid in Fig. 5.15 are the PIC simulation results. We can see that the PIC results are lower than the isothermal value, but do not agree well with Eq. (5.37). The discrepancy could be due to the two-Te hypothesis used in Eq. (5.36). Indeed, we can see in Fig. 5.8 that there is a small population of high energy electrons. This population is not big enough to modify the electron flux to the wall, hence the potential drop [131], but may increase the mean energy of electron leaving the plasma. We tested the hypothesis for one case ($P_n = 2$ mTorr). Once the steady-state was reached, we stopped generating the electron-ion couples. We observed that during a transition time of around 0.74μs, the mean energy per electron decreased significantly from $0.9\mathrm{T_{e,0}}$ to $0.3\mathrm{T_{e,0}}$, while the electron flux to the wall Γ_e and the electron temperature $\mathrm{T_{e,0}}$ was not yet affected. Another phenomena is the anisotropy of the EVDF, as shown in **??** for low pressure, hence large polytropic index (see Fig. 5.11). This could explain why the mean energy per electron in the PIC simulations increases with increasing γ.

This is more consistent with the value given by Eq. (5.37) shown in Fig. 5.15, and seems to confirm the hypothesis, but more investigations on the heat flux are needed.

5.5 Realistic heating and ionization

In the study of Section 5.2, the ionization and the heating mechanism are not self-consistent, but allowed us to obtain quickly a steady-state as in the simulations of Chapter 2. We now study the impact of the wall absorption in a case of self-consistent heating and ionization. The electrons are heated "inductively" with a radio-frequency (RF) electric field in the direction normal to the simulation grid [120, 94, 132]. The electrons are heated in the y direction, and momentum is transferred to the x and z axis via electron-neutral collisions. The heating electric field $\mathbf{E_{rf}} = E_{rf}\mathbf{e_y}$ is independent of x in the simulation domain, its frequency is 13.56 MHz, and its amplitude is adjusted in order to obtain the desired absorbed power $P_{abs} =< \mathbf{J_e} \cdot \mathbf{E_{rf}} >$.

Parameter	value	unit
Pressure	0.1	mTorr
P_{abs}	0.25	$\mathrm{W/m^{-3}}$
Length L	10	cm

TABLE 5.2 – Input parameters for the simulation using the self-consistent model.

Figure 5.16 presents the simulation results for the electron density, plasma potential and electron temperature using the parameters of Table 5.2. We can see that the different variables (density, electron temperature and the plasma potential) are not much affected compared to the results of Section 5.2.

Figure 5.17 presents the electron pressure as a function of the electron density measured in the simulation in log scale. We see that the trend is not purely linear. Hence, the linear regression used in order to obtain the polytropic index is conducted twice:

— In the whole domain: $\gamma = 1.5$

— Only in the sheath: $\gamma = 1.6$

The linear relation conducted on the whole domain is less accurate than for the simulation result of Section 5.2 ($R^2 = 0.992$). However, we can see that the linear relation still describes quite well the electron evolution in the sheath. The polytropic indexes obtained with the self-consistent model are close to the one of the simulation of Section 5.2 at the same pressure.

Figure 5.18 shows the comparison of the electron temperature and the plasma potential in the PIC simulation using the self-consistent model with the prediction of the fluid model of Section 5.4. We can see that the agreement between the PIC results and the fluid models is less

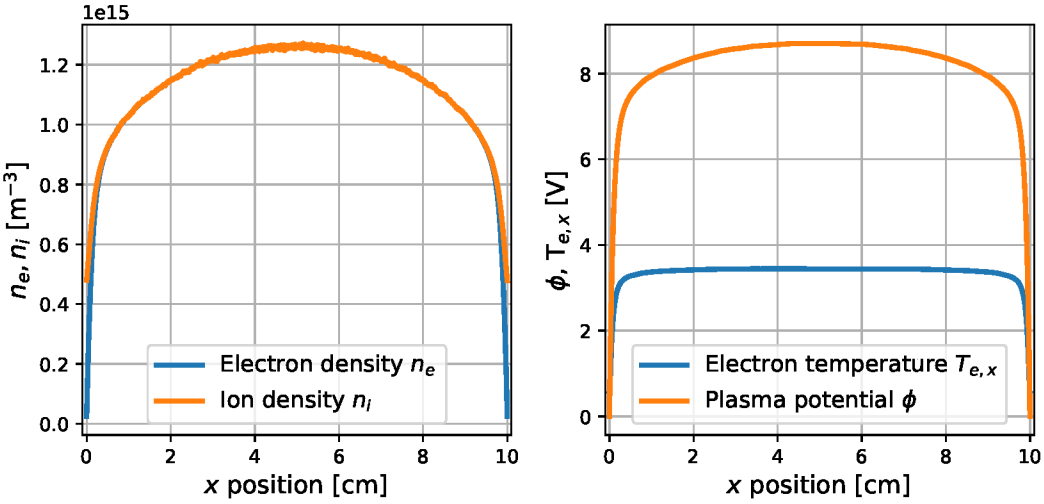

FIGURE 5.16 – Results of the PIC simulation for the self-consistent model, using RF inductive heating.

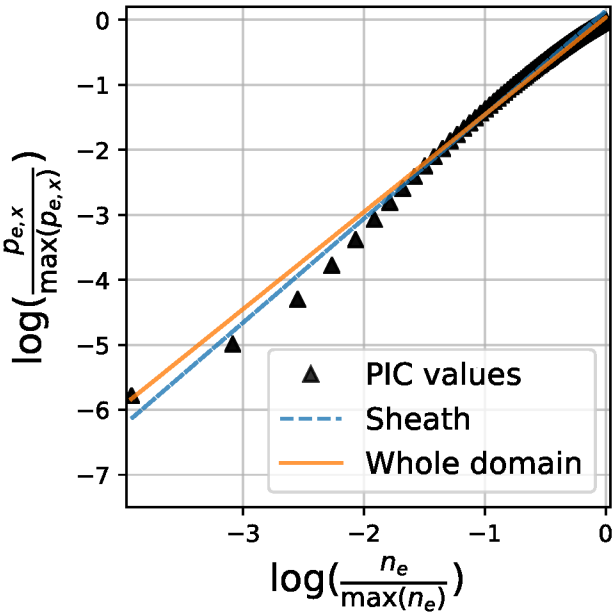

FIGURE 5.17 – Estimation of the polytropic index in the sheath and in the whole domain in the PIC simulation using the self-consistent model.

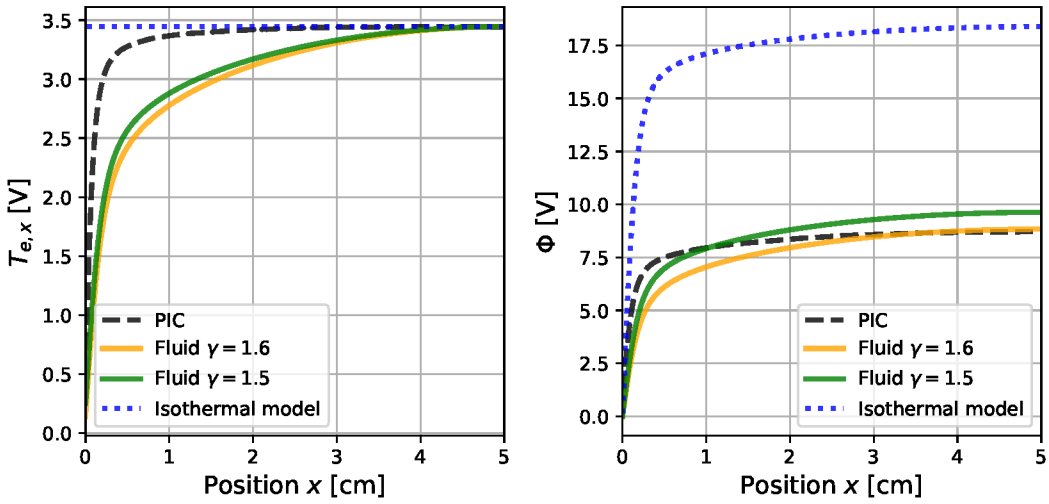

FIGURE 5.18 – Comparison of the electron temperature and plasma potential measured in the PIC simulation with the prediction of the fluid model with $\gamma = 1.5$ (average index in the domain) and $\gamma = 1.6$ (index in the sheath).

satisfactory than in Fig. 5.13 but it is still significantly better than the isothermal model. Hence, even with a self-consistent heating and ionization in the plasma, the polytropic model stands as a better model for the sheath and the pre-sheaths.

5.6 Monte Carlo computation of the EVDF

The 1D PIC simulations were computed faster than the 2D simulations, as the latter needed around a week to compute 10 µs on 360 CPUs, while the former needed only a few days on 64 CPUs to compute 20 µs of physical time. However, they still take a rather long time, especially when compared to fluid models that can be solved from under one second to around one day on a single core, depending on the hypotheses used.

We have seen that the polytropic index depends on several conditions, as the background pressure (see Fig. 5.11) but also the densities, sizes, heating mechanism, and so on. We have seen in Section 5.4 that the only value of the polytropic index γ is enough to describe the PIC simulation. As the value of γ depends on the EVDF, we propose here a Monte Carlo approach that could be used in order to obtain the EVDF faster than with a PIC simulation. A possible application would be similar to Kushner [133], where the author uses a small population of electrons (typically 300-500) and observes their evolutions in a given plasma potential.

This method gets rid of the Poisson equation, which can take between 30% and 50% of the total simulation time. Hence, the Debye length does not have to be highly resolved anymore for stability and numerical heating. However, we still need to resolve the sheath, which length is of the order of 5 Debye lengths [115]. Consequently, a coarser mesh of cell size 5 times larger can be used. The condition on the time step is also reduced. This results in a much faster computation.

5.6.1 Description of the Monte Carlo simulation used

In order to validate the Monte Carlo approach, we use as reference the converged simulation of the 1D PIC model at a background pressure of $P_n = 1\,\text{mTorr}$. We use the plasma potential ϕ computed self-consistently at the end of the PIC simulation. The Monte Carlo simulation uses the same modules of *LPPic* as the PIC simulation for the particles, but the fields (charge density, electric field, etc.) are not computed. Similarly to the PIC simulation, the Monte Carlo simulation is initialized with uniform Maxwellian electrons. The electrons motion and collisions are computed as described in Section 2.1. When an electron is collected at the wall, it is re-injected uniformly.

We validate the Monte Carlo computation by comparing the distribution function obtained with the one measured at the end of the PIC simulation. Figure 5.19 shows the expected EEPF obtained in the PIC simulation with a background pressure of $P = 1\,\text{mTorr}$. The maximum plasma potential, at the center of the domain, is $\max(\phi) = 12.2\,\text{V}$. Is also shown in Fig. 5.19 the EEPF at the beginning of the Monte Carlo computation, which corresponds to the Maxwellian distribution of temperature $\text{T}_\text{e} = 5\,\text{V}$. The results of the Monte Carlo simulation are presented in Section 5.6.2.

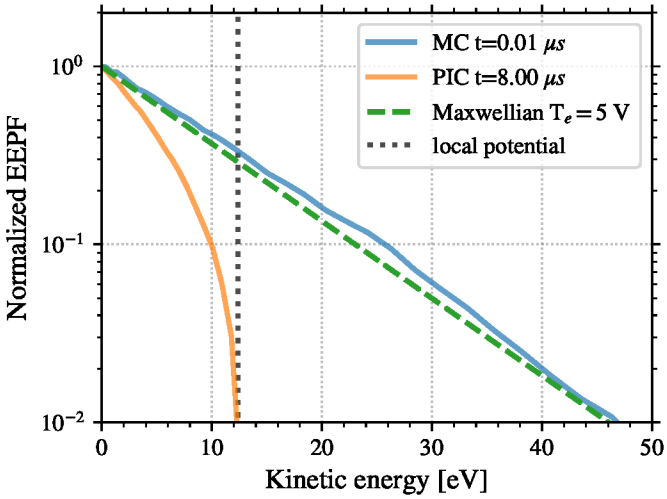

FIGURE 5.19 – Electron energy probability function obtained from (orange) the PIC simulation after convergence, and (blue) at the beginning of the Monte Carlo simulation. A Maxwellian distribution function at the $\text{T}_{\text{e},inj}$ and the local plasma potential are also given.

5.6.2 Results of the Monte Carlo computation

In this section, we describe the temporal evolution of the EEPF in the Monte Carlo (MC) simulation, compared to the EEPF measured in the PIC simulation.

Beginning of the simulation

We start by analyzing the evolution of the EEDF at the very early time of the simulation, from $t = 0.01$ to $0.08\,\mu\text{s}$. Figure 5.20 shows the measured electron energy probability function (EEPF) at 3 cm from the left wall. The energy of the electrons is oriented, meaning that the electrons with positive energy are coming from the wall, while the negative energy is used for the electrons going toward the wall.

Two phenomenon can be seen in Fig. 5.20. The first is the rapid decrease of the tail of the distribution function, for energies higher than the plasma potential. The tail for positive energy decreases faster than for negative energy, as the EEPF is measured closer to one wall than the other ($x = 3\,\text{cm}$ against $L - x = 7\,\text{cm}$). After $T \simeq 0.06\,\mu\text{s}$ the two tails are largely depleted, as they are one order of magnitude smaller than the initial Maxwellian EEPF.

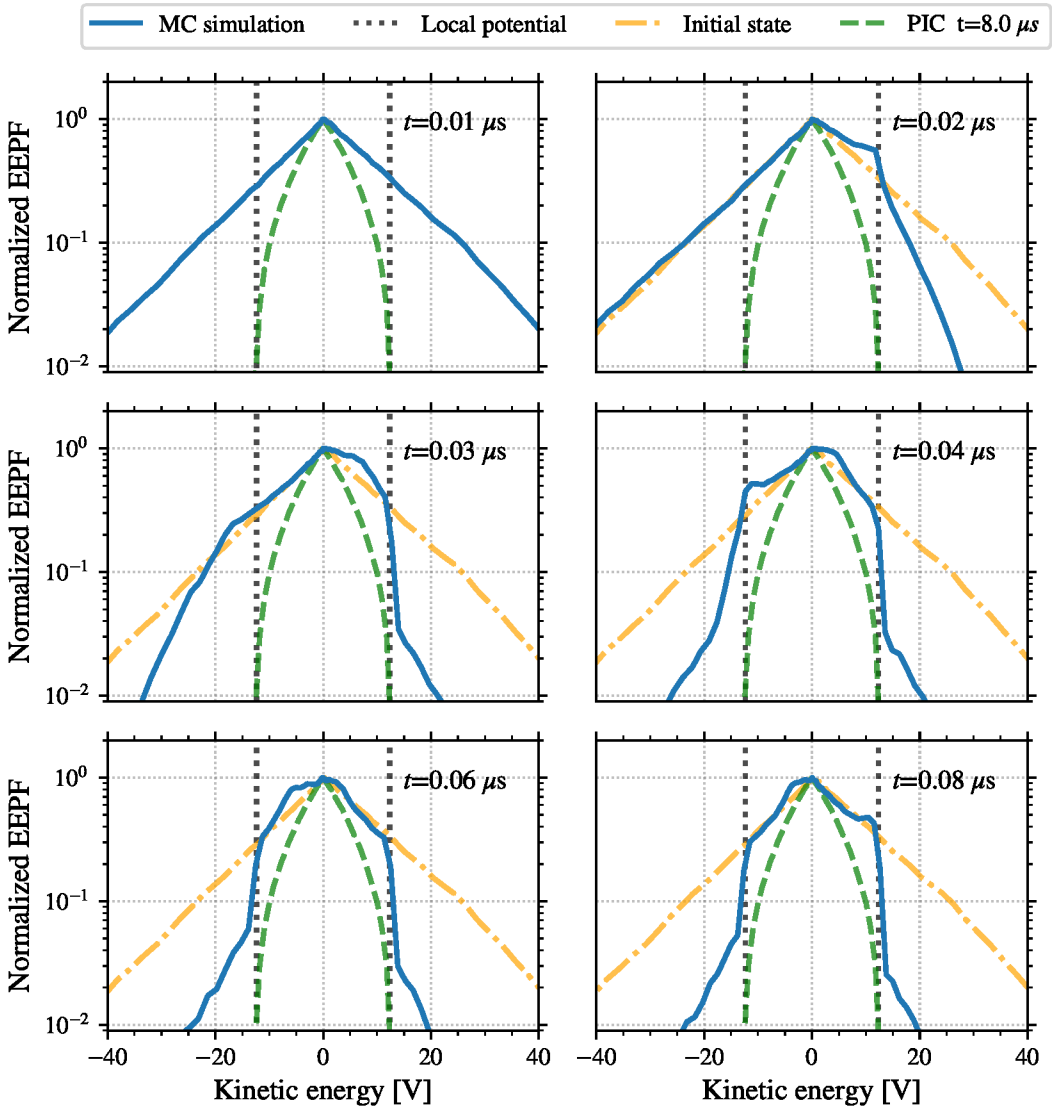

FIGURE 5.20 – Evolution of (blue) the directed EEPF measured at $x = 3\,\text{cm}$ from the left wall in the Monte Carlo simulation. The positive energy is used for the electrons going from the wall, while the negative energy represents the electrons moving toward the wall. The dotted lines correspond to the local potential. Are overlaid (dash-dotted orange) the initial Maxwellian distribution (Maxwellian at $T_e = 5\,\text{V}$) and (dashed green) the EEPF obtained at the end of the PIC simulation ($t = 8\,\mu\text{s}$).

The second phenomena is the presence of waves in the velocity space that can be seen in the low energy populations. They are due to the plasma potential profiles. Indeed, the electrons are initialized uniformly with a fixed temperature, hence their total energy depends on the local plasma potential.

Convergence of the simulation

Figure 5.21 shows the evolution of the EEDF over a longer time scale from $t = 0.1$ to $3.5\,\mu s$ (compared to $t = 0.01$ to $0.08\,\mu s$ in Fig. 5.20). We can see the slow evolution of the low energy population from the initial, but slightly perturbed, Maxwellian distribution toward a distribution of smaller temperature. After $t = 1.5\,\mu s$, the EEPF of the Monte Carlo computation is fairly close to – and converges slowly towards – the EEPF measured at $t = 8\,\mu s$ in the PIC simulation.

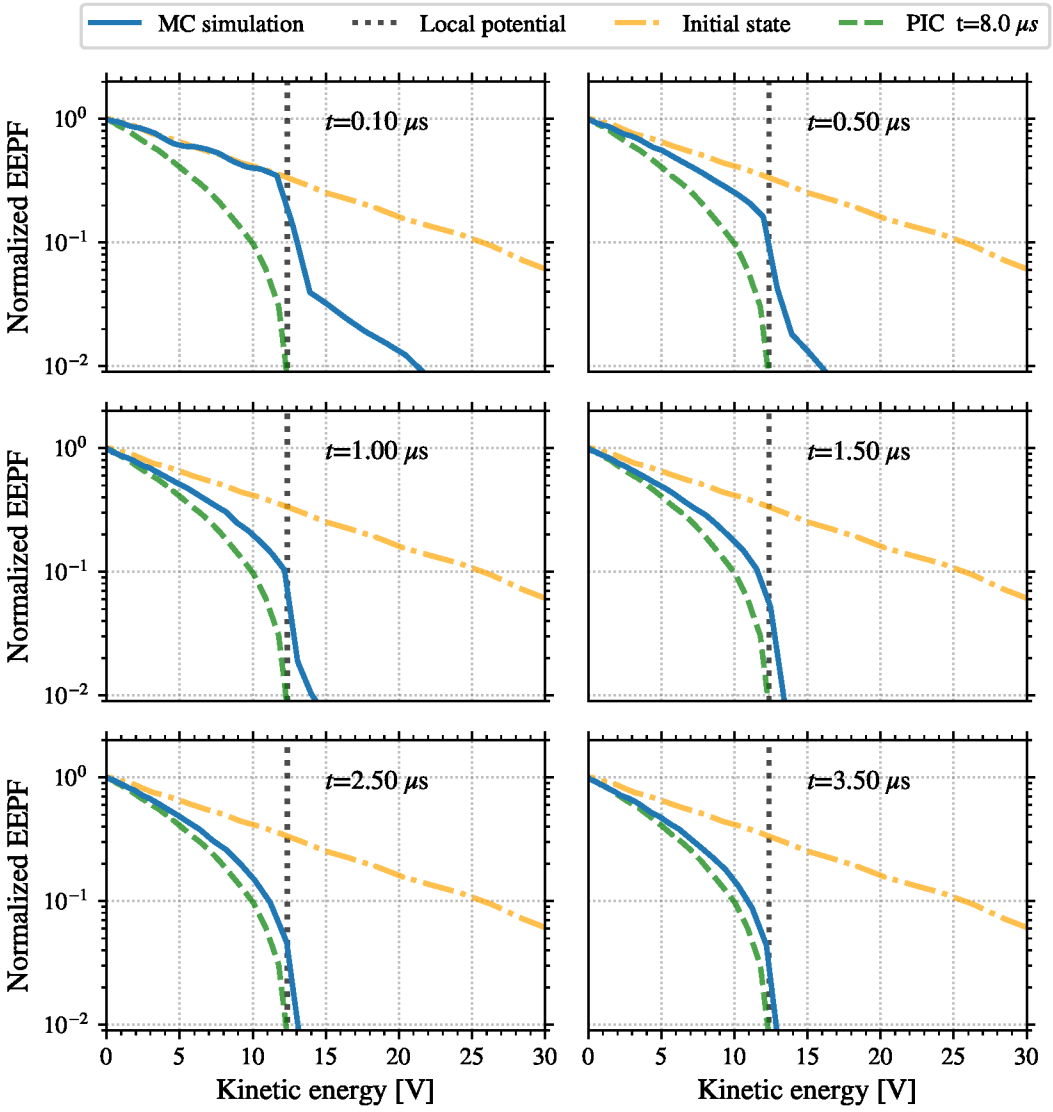

FIGURE 5.21 – Evolution of (blue) the EEPF measured at $x = 3\,cm$ from the left wall in the Monte Carlo simulation. The dotted line corresponds to the local potential. Are overlaid (dash-dotted orange) the initial Maxwellian distribution and (dashed green) the EEPF obtained at the end of the PIC simulation ($t = 8\,\mu s$).

This Monte Carlo investigation has shown that in the 1D model at $P_n = 1\,mTorr$, the EEPF depends on the absorption at the wall but also on the electron-neutral collisions. The final shape of the distribution is not simple, and is difficult to describe and predict analytically. However, given the profile of the plasma potential, the Monte Carlo computation reproduces the same distribution in a much shorter time compared to the PIC simulation. The obtained EEPF can then be used to determine the electron density and temperature evolution in a low pressure plasma where electrons are non-local. This could be used to determine efficiently, and precisely, the electron polytropic coefficient to use in a fluid model.

5.6.3 Discussion on the different time scales

The results presented in the previous section show two main time scales. In this section, we compare the observed time scales with the theoretical times. The electrons collected at the wall have a kinetic energy at least equal to the potential drop to the wall $\epsilon = e\Delta\phi$, which corresponds in our case to a limit velocity of $v_{\text{lim}} = 1.5{\times}10^6\,\text{m/s}$. Hence, the limit time of flight between the two boundaries is

$$T_{\text{flight}} = \frac{L}{v_{\text{lim}}} = 0.068\,\mu\text{s}.$$

This is in agreement with the results of Fig. 5.20, where we see that the high energy tails are depleted around $t = 0.06\,\mu\text{s}$.

The electron-neutral scattering frequency is computed for a background pressure of 0.13 Pa (1 mTorr) at the temperature of 300 K, which corresponds to a neutral density of

$$n_g = 3.2{\times}10^{19}\text{m}^{-3}.$$

For an electron temperature of 5 V, the thermal electron-neutral elastic scattering frequency for argon is [56, p.73]

$$\nu_{\text{ela}} = 4.70\,\text{MHz},$$

which corresponds to a period of $\tau_{\text{ela}} = 0.2\,\mu\text{s}$. This period is shorter than the one observed in the Monte-Carlo simulation, as we see in Fig. 5.21 that the low energy part of the EEPF is significantly affected after $t = 1\,\mu\text{s}$.

This discrepancy can be due to two reasons. First, at high energy the electron-neutral scattering is not isotropic, but instead gives mostly small angles (forward scattering) [66]. Hence, a large number of collisions is required for the isotropization to be observable. Secondly, the argon presents a significant Ramsauer minimum (a quantum mechanical resonance [56]) at 0.3 V, were the cross-section is two orders of magnitude lower than at 5 V.

Numerical artifacts

In PIC simulations, numerical parameters can induce numerical heating and thermalization [134]. The numerical heating has been studied in detail [69]. It is due to aliasing effects, and depends on the grid size, time step and number of particles per cell. It is important to carefully choose these parameters to reduce the effect of the heating.

The thermalization is the fact that the distribution of the particle tends toward a Maxwellian. It originates from fluctuations of the electric field due to the discretization of the particles. The first studies showed that the thermalization time τ_T depends on N_D the number of (numerical) particles per Debye sphere [135, 136]. The presence of collisions can affect τ_T [71, 134]. In Turner [71], the author observed the evolution of the thermalization time with N_D as

$$\tau_T = \frac{1}{\omega_{pe}} \frac{34.4}{N_D^{-2} + 28.0 N_D^{-1} \frac{\nu_m}{\omega_{pe}}} \tag{5.38}$$

which gives in our condition a time-scale several orders of magnitude larger than the typical simulation time. We confirmed it by doubling the number of particle per cell for one pressure condition, and no observable impact has been detected. Hence, the effects of numerical parameters on the simulation results are expected to be negligible.

5.7 Conclusion

Using the kinetic informations from the PIC simulations, we have seen that the electrons are not Maxwellian, in contrast with the hypothesis of the usual models for plasma wall interactions. The electron distribution function is affected by two phenomena:

— the absorption of high energy electrons at the wall
— the electron-neutral scattering

The absorption depletes rapidly the high energy tail of the EEPF for energies higher than the local plasma potential relative to the wall. However, the low energy population is not affected by the wall.

The collisions affect the electrons more slowly, by replenishing the high energy tail by scattering. Indeed, in the directions parallel to the wall, the high energy tail is not depleted. However, for large energies ($\epsilon > 10\,\mathrm{V}$), the electron-neutral scattering angle is small [66], hence the time scale over which the collisions impact the EEPF is much longer than the typical time between two collisions.

The electron trajectory in the discharge chamber is hence mostly collisionless. We have successfully confirmed this by confronting the EEDF measurements to the 1D stationary Vlasov equation. Following the work of Zhang et al. [125] on the collisionless evolution of non-Maxwellian electron through a potential drop, we have found that a polytropic closure for the electron describes very accurately the electron temperature evolution:

$$\mathrm{T_e} n_e^{1-\gamma} = cst, \text{ with } \gamma \text{ the polytropic index}$$

The polytropic state law for the electrons, when used in fluid model, allows to obtain the same densities and plasma potential as in the PIC simulation. This paves the way for a modified sheath model to compare to the 2D PIC simulation of the HET of Chapter 4.

We have also seen in Section 5.5 that the polytropic state law also stands when a self-consistent heating mechanism is used, even if the agreement is not as good as in the other case.

In Section 5.7, the value of the polytropic index γ depends on the shape of the EVDF. We showed in Section 5.6 that a Monte Carlo computation can be used in order to obtain the EVDF for a given plasma potential profile and neutral pressure. As the Monte Carlo approach does not need the Poisson equation to be solved, it produces the EVDF much faster than a PIC simulation. Hence, we could couple the Monte Carlo calculation with a fluid model to accurately take into account the real shape of the EVDF in the closure of terms in fluid models.

Chapter 6

Polytropic sheath model in the presence of electron emission

In this Chapter, we add to the non-isothermal sheath model developed in Chapter 5 the secondary electron emission. Using the Particle In Cell (PIC) simulations with secondary emission, we observe that the electrons are well described by a polytropic state law, which index is almost constant when varying the cross-over energy ϵ^*. Hence, we derive the sheath characteristics using the same fluid approach. We note that this model allows multiple solutions for a given electron temperature, which could explain the oscillations observed in regime **II** observed in Chapter 4, as shown in Fig. 6.12. The predictions of the polytropic sheath model are successfully compared to the PIC simulation results presented in Chapter 4.

Contents

6.1 Objectives of the chapter

In Section 4.6, we have seen that the plasma-wall interaction observed in the 2 dimensions (2D) PIC simulations are different from the classical sheath models. We recall here the main observations of Chapter 4. We have conducted a parametric study on the wall emissivity by varying the crossover energy ϵ^* in the emission probability

$$\sigma = \sigma_0 + (1 - \sigma_0)\frac{\epsilon}{\epsilon^*},$$

with ϵ the electron kinetic energy. The Secondary Electron Emission (SEE) rate (or yield) $\bar{\sigma}$ is the emission probability σ averaged over the electron flux at the wall. With a Maxwellian flux of temperature $\mathrm{T_e}$, we have

$$\bar{\sigma}_{\mathrm{Maxw}} = \sigma_0 + (1 - \sigma_0)\frac{2\mathrm{T_e}}{\epsilon^*}. \tag{6.1}$$

The sheath model with SEE predicts a potential drop between the sheath-edge and the wall of [84, 81]

$$\Delta\phi = \mathrm{T_e} \log\left([1-\bar{\sigma}] \sqrt{\frac{m_i}{2\pi m_e}} \right). \tag{6.2}$$

In Chapter 4, Fig. 4.18 and Fig. 4.19.**a** (reproduced here in Fig. 6.1 to ease the reading of the chapter) show both the plasma potential $\Delta\phi$ and the SEE rate $\bar{\sigma}$ measured in the PIC simulations and obtained from Equations (6.1) and (6.2). We see that the plasma potential is overestimated for low values of $\bar{\sigma}$ by around 30%. Moreover, the SEE rate is also overestimated.

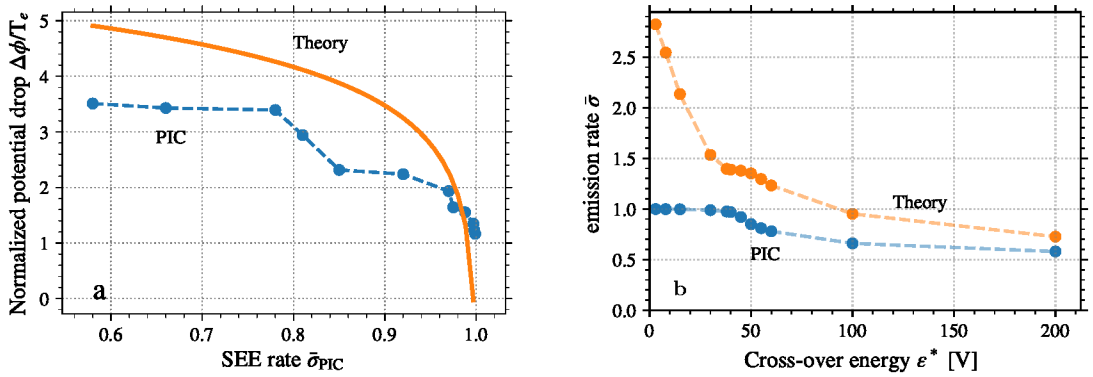

FIGURE 6.1 – (**a**) Plasma potential drop to the wall $\Delta\phi$ normalized by the electron bulk temperature $\mathrm{T_e}$ as a function of the electron rate (blue) measured in the PIC simulations and (orange) calculated with Eq. (6.2); (**b**) the SEE rate $\bar{\sigma}$ (blue) measured in the PIC simulation, and (orange) calculated with Eq. (6.1).

The discrepancy is most certainly due to the isothermal hypothesis. In Chapter 5, we have developed a sheath model without the isothermal hypothesis, but instead the polytropic state law. The objective of this chapter is to add to the polytropic sheath model of Chapter 5 the electron emission from the wall, in order to better predict the plasma-wall interaction.

6.2 Polytropic electrons in the presence of SEE

The sheath model developed in Chapter 5 uses a polytropic state law for the electrons instead of the usual isothermal approximation. Indeed, the results of the 1 dimension (1D) PIC simulations presented a polytropic evolution of the electrons. This model successfully reproduced the sheath characteristics when no secondary electron emission was modeled (fully absorbing walls). Before adapting this sheath model to the case with SEE, we need to validate the polytropic hypothesis in the presence of SEE.

6.2.1 Determination of the polytropic index from PIC simulations

The 2D PIC simulation is described in Chapter 4, but we recall here the main parameters. The bidimensional domain length is 2 cm in the radial direction, and 0.25 cm in the azimuthal direction. A radial magnetic field $B = 200\,\mathrm{G}$ and an axial electric field $E = 20\,\mathrm{kV/m}$ are applied. The mean plasma density is $n_e = 3{\times}10^{17}\,\mathrm{m}^{-3}$. The radial direction is closed by grounded wall, but we model the electron induced electron emission from the wall. The model used is described in Section 2.6, using the parameters of Table 4.3. In addition, the axial convection is modeled using Lafleur's model of convection, as discussed in Section 2.5.

Figure 6.2 shows the electron density and the electron temperature obtained at the end of the simulation ($t = 10\,\mu\mathrm{s}$) in the case $\epsilon^* = 200\,\mathrm{V}$. We can see the azimuthal instability on both n_e and $\mathrm{T_e}$. However, these azimuthal oscillations will be averaged in the following development.

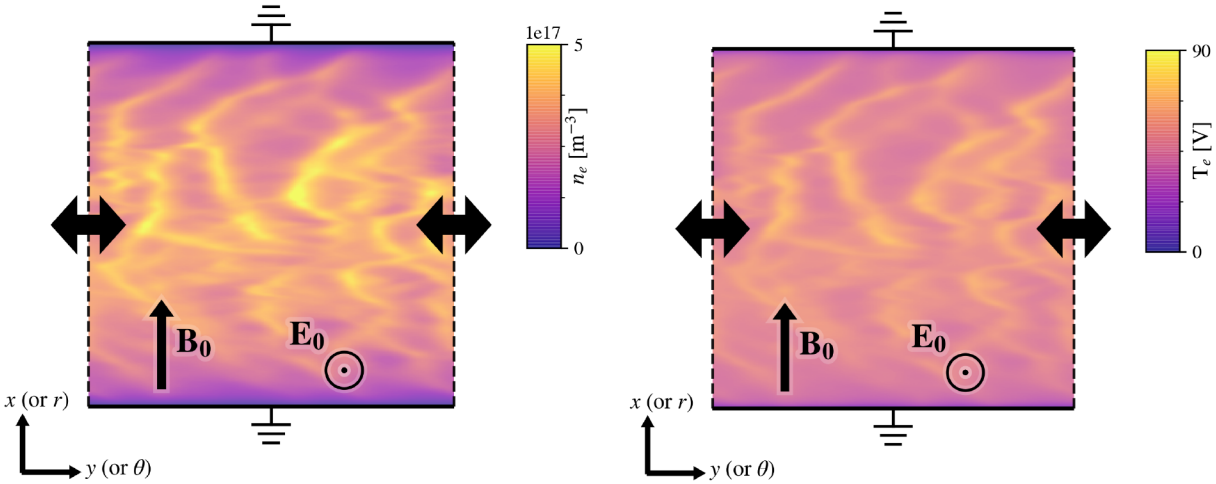

FIGURE 6.2 – Maps of the (left) electron density n_e and (right) electron temperature T_e at $t = 10\,\mu s$ in the 2D simulation domain with $\epsilon^* = 200\,V$.

As previously done in Chapter 5, we use the mean values of the electron density n_e and the electron pressure $p_e = en_eT_e$ to find the value of the polytropic index. Figure 6.3 shows the radial profiles of the electron density and temperature for different values of the cross-over energy ϵ^*. The three values of ϵ^* used are representative of the observed behaviors in Chapter 4. Indeed, $\epsilon^* = 200\,V$ and $\epsilon^* = 50\,V$ correspond to the upper and lower limits of regime **III**, corresponding to low emission rate $\bar{\sigma}$, while regime **I** corresponds to the case $\epsilon^* = 10\,V$. Regime **II** is not presented, as the oscillating nature of the sheath is not taken into account by the stationary sheath model developed here.

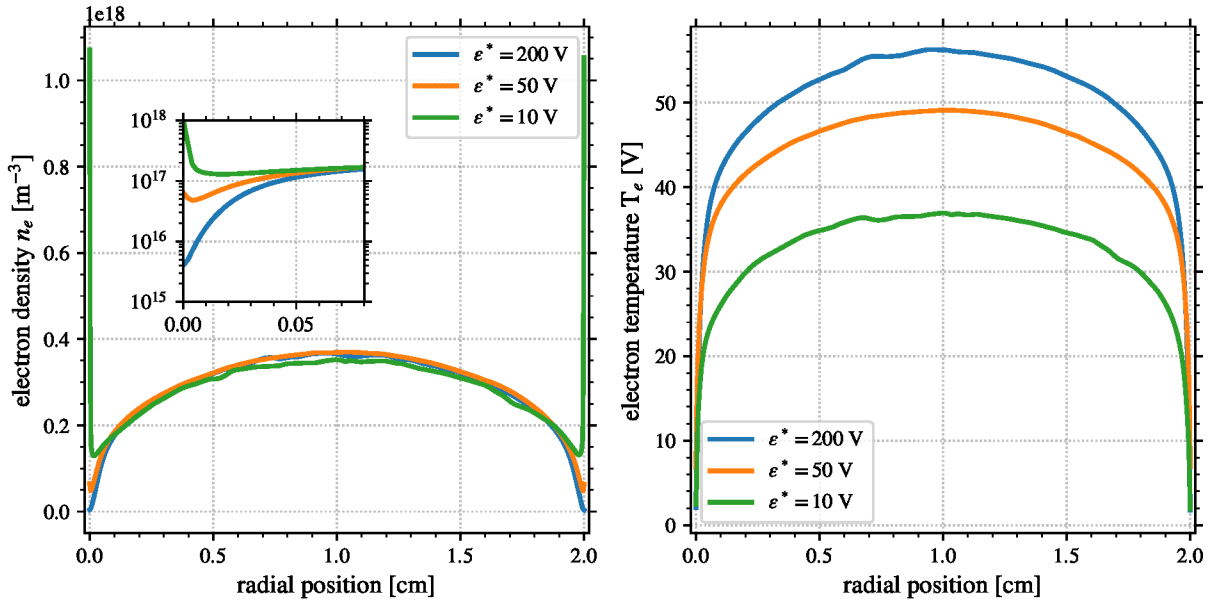

FIGURE 6.3 – Radial profiles of (left) the electron density and (right) the electron temperature, for different values of ϵ^*. The variables are averaged over the azimuthal direction and in time between $t = 5\,\mu s$ and $t = 10\,\mu s$.

We see in Fig. 6.3 that the electron temperature presents a monotonic profile for all the values of ϵ^*. However, for low values of ϵ^* the electron density is not monotonic, but instead presents an increase close to the wall. This is clearly visible in Fig. 6.4, which presents the electron pressure p_e as a function of the electron density n_e, in log scale and normalized by the values at the center. We see that close to the wall, where the electron pressure is the lowest, the curves present an

inversion, in contrast with the case without electron emission seen in Fig. 5.10. Otherwise in the rest of the domain, the curves are almost linear, corresponding to a polytropic state law.

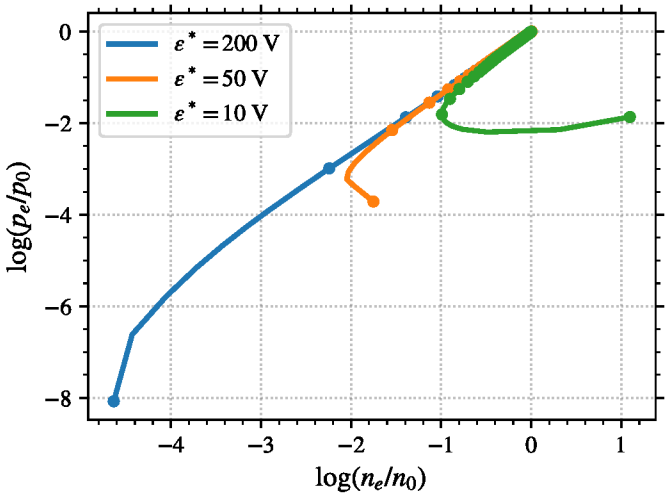

FIGURE 6.4 – Electron pressure as a function of the electron density normalized by the center variable, in log scale. The data corresponds to the same as Fig. 6.3. Markers are used every 10 cells (corresponding to around one Debye length λ_{De})

In Figure 6.4, the increase of the electron density close to the wall for $\epsilon^* = 50\,\mathrm{V}$ is due to the cold secondary electron population, that resides next to the wall before being accelerated through the sheath toward the plasma. In addition, under the Space Charge Limited (SCL) regime observed at $\epsilon^* = 10\,\mathrm{V}$ the plasma potential presents a local minimum close to the wall, that reflects secondary electrons back to the wall. However, we see that it happens only over the last Debye length λ_{De}. Consequently, in the following we neglect this increase of the electron density to derive the polytropic index of the plasma.

We determine the value of the polytropic index γ from the PIC simulations with a least mean square linear regression. The results of the regressions are displayed in Fig. 6.5, and the polytropic indexes obtained are summarized in Table 6.1.

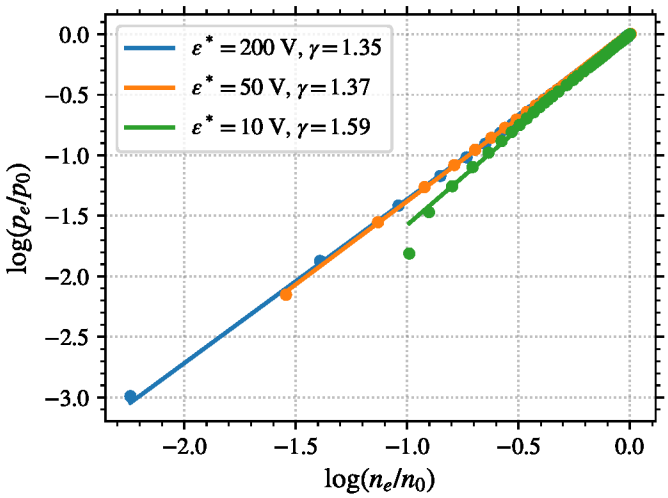

FIGURE 6.5 – Polytropic linear regression for different values of ϵ^*, in the same conditions as Fig. 6.4, but the last 10 cells near the wall are removed. The values of γ fitted on the PIC simulation data are given in the legend.

We can see that the value of γ does not evolve significantly in regime **III**, as it evolves from $\gamma = 1.35$ to 1.37 when ϵ^* vary from 200 to 50 V. For $\epsilon^* = 10\,\mathrm{V}$, the value of the polytropic index

TABLE 6.1 – Polytropic index extracted from the 2D PIC simulations

Crossover energy ϵ^*	Polytropic index γ
200 V	1.35
50 V	1.37
10 V	1.59

in the linear stage is $\gamma = 1.59$, which is not so different from the values in regime **III**. However, we will see later that during the regime **I**, the characteristics of the sheath is not affected by the polytropic index. Consequently, we assume in the following that the polytropic index in the PIC simulation with secondary electron emission is constant and equals $\gamma = 1.36$ for all values of ϵ^*. It will be used in the next sections to compare the PIC results with a fluid model of the sheath.

6.2.2 Evolution of the forward electron population

The electron density n_e and temperature T_e shown in Section 6.2.1 (Figs. 6.3 to 6.5) include both the primary electrons going toward the wall and the secondary electrons emitted from the wall. However, the SEE rate only depends on the primary electrons reaching the wall. In order to separate the two populations, we use the Electron Velocity Distribution Function (EVDF) obtained in the simulations. Figure 6.6 presents the EVDF measured at the center of the simulation domain. We see that the EVDF presents similar profiles for the three cases, except for the mean energy that increases with increasing values of ϵ^*.

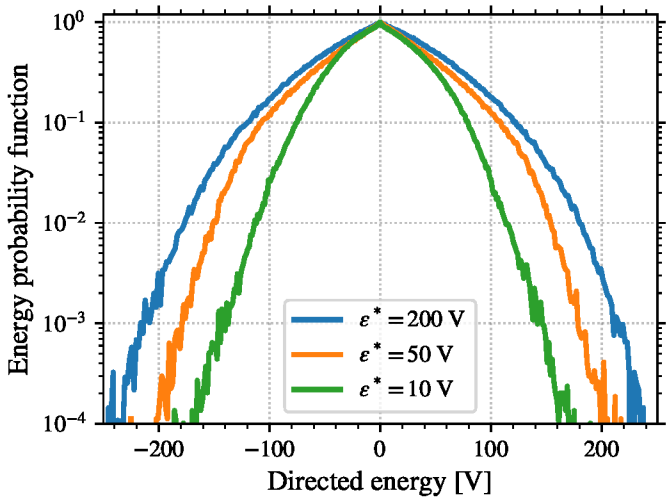

FIGURE 6.6 – Electron velocity distribution function at the center of the simulation, with the same parameters as the cases of Figs. 6.4 and 6.5. The sign of the energy corresponds to the direction of the motion.

We note that no beam is present here, even in the case of very large electron emission at $\epsilon^* = 10$ V, in contrast with observations of 1D PIC simulations [80, 52], but in agreement with the 2D results of Héron and Adam [38]. This seems to infer that the instability, self-consistently modeled in the 2D simulations, thermalizes the secondary electron population.

Using the solution of the stationary Vlasov equation Eq. (5.15), we compute the evolution of the density and temperature of the primary electron population going toward the wall through

the plasma potential ϕ

$$\begin{cases} f(\phi, v_e) = f\left(0, \sqrt{v_e^2 + \dfrac{2e}{m_e}\phi}\right) \\ n_e(\phi) = \displaystyle\int_0^{+\infty} f(\phi, v_e) dv_e \\ p_e(\phi) = \dfrac{m_e}{e} \displaystyle\int_0^{+\infty} v_e^2 f(\phi, v_e) dv_e \end{cases} \tag{6.3}$$

The results obtained by the system of equations (6.3) are shown for the three cases in Fig. 6.7. We see that the forward electron population follows a polytropic law. For $\epsilon^* = 200$ and 50 V, the corresponding polytropic index is $\gamma = 1.28$, while for $\epsilon^* = 10$ V we measure $\gamma = 1.35$.

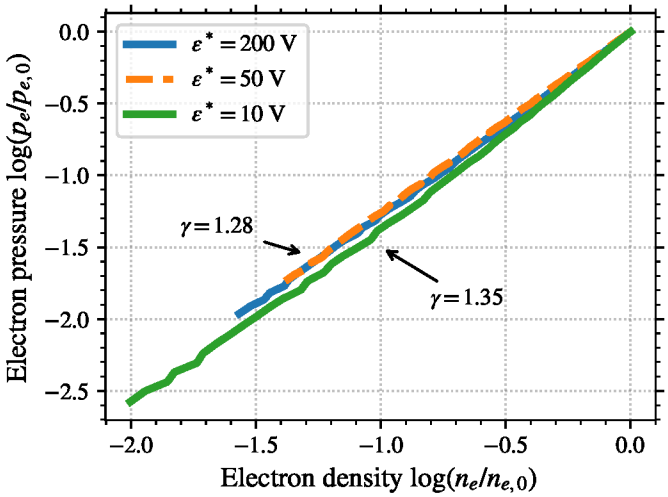

FIGURE 6.7 – Electron pressure as a function of the electron density in log scale of the forward (primary) electron population using the stationary Vlasov equation Eq. (6.3) for (blue) $\epsilon^* = 200$ V, (dashed orange) $\epsilon^* = 50$ V, and (green) $\epsilon^* = 10$ V.

The fact that the polytropic index of the primary electrons is lower than that of the total electron population ($\gamma = 1.28$ versus 1.36) means that the electron temperature of the primary electron population going toward the wall decreases more slowly than the total electron pressure. This is certainly due to the partial absorption and emission of secondary electrons at the wall, injected at $T_{SEE} = 2$ V which is small compared to T_e. Hence, we can expect that the emission rate $\bar{\sigma}$, which directly depends on the forward electron population, is better described with the polytropic index $\gamma = 1.28$, computed in Fig. 6.7, than with $\gamma = 1.36$ from Section 6.2.1.

6.3 Sheath model with polytropic electrons and electron emission

6.3.1 Definition of the sheath equation

We have seen in Section 6.2 that even in the presence of electron emission from the wall, the electrons can be described using a polytropic state law. The value of the polytropic index obtained from the mean electron density and temperature is for $\epsilon^* \geq 40$ V is $\gamma \simeq 1.36$. Hence, we modify the polytropic sheath model of Section 5.4 to take into account the electron emission from the wall. This modifies the current equality at the wall to

$$\Gamma_i = (1 - \bar{\sigma})\Gamma_e. \tag{6.4}$$

Sheath model with constant emission rate

Using Eqs. (5.29), (5.31) and (5.32) for Γ_i and Γ_e, we obtain the equality

$$(1-\bar{\sigma})\left[1+\frac{\gamma-1}{\gamma}\frac{\Delta\phi_0}{\mathrm{T_{e0}}}\right]^{\frac{1}{\gamma-1}}\sqrt{1-\frac{\gamma-1}{\gamma}\frac{\Delta\phi_0}{\mathrm{T_{e0}}}}=\sqrt{\frac{2\gamma\pi m_e}{m_i}} \tag{6.5}$$

Similarly to the case without electron emission in Section 5.4, Eq. (6.5) cannot be solved analytically, but it can be solved numerically. The solution for $\bar{\sigma}=0.8$ is compared to the case without electron emission ($\bar{\sigma}=0$) for a xenon (Xe) plasma in Fig. 6.8. As expected, the potential difference decreases with increasing $\bar{\sigma}$. We see that the gap between the two cases decreases when γ increases from 1 to 2.

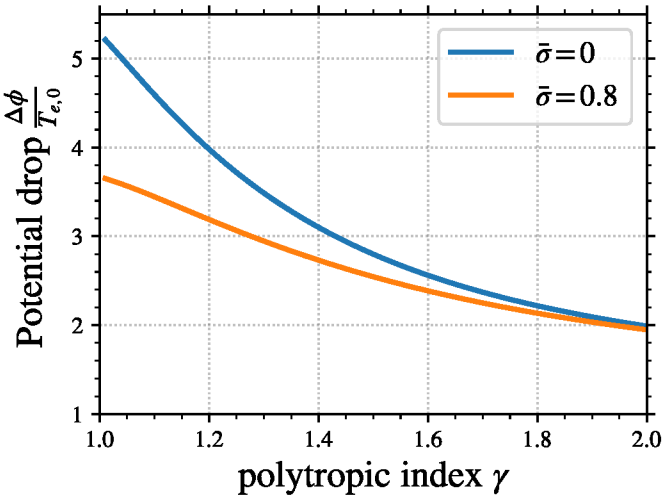

FIGURE 6.8 – Potential drop $\Delta\phi$ normalized by the bulk electron temperature $\mathrm{T_{e0}}$ as a function of the polytropic index γ for a xenon plasma ($m_i = 131\,\mathrm{u}$). The emission rate $\bar{\sigma}$ is fixed either at $\bar{\sigma}=0$ or $\bar{\sigma}=0.8$.

Sheath model with varying emission rate

In fact the electron emission rate is a function of the electron temperature at the wall. Using the same hypothesis as in Eq. (5.31) (mostly a Maxwellian EVDF at the wall), we define the emission rate from Eq. (4.11) by

$$\bar{\sigma}=\begin{cases}\bar{\sigma}_{\mathrm{Maxw}}(\mathrm{T_{e,wall}})=\sigma_0+(1-\sigma_0)\frac{2\mathrm{T_{e,wall}}}{\epsilon^*}\\ \bar{\sigma}_{\mathrm{cr}}\quad\text{, if } \bar{\sigma}_{\mathrm{Maxw}}(\mathrm{T_{e,wall}})>\bar{\sigma}_{\mathrm{cr}}\end{cases} \tag{6.6}$$

with $\bar{\sigma}_{\mathrm{cr}}=0.983$ corresponding to the SCL regime, and the electron temperature at the wall

$$\mathrm{T_{e,wall}}=\mathrm{T_{e,0}}-\frac{\gamma-1}{\gamma}\Delta\phi. \tag{6.7}$$

Noting $\chi=\frac{\gamma-1}{\gamma}\frac{\Delta\phi_0}{\mathrm{T_{e,0}}}$, we finally obtain the sheath equation to be solved

$$f(\chi)=[1+\chi]^{\frac{1}{\gamma-1}}\sqrt{1-\chi}-\frac{\sqrt{2\gamma m_e/m_i}}{1-\bar{\sigma}(\mathrm{T_{e,0}},\chi)}=0. \tag{6.8}$$

Equation (6.8) depends now explicitly on $\mathrm{T_{e,0}}$ through the value of $\bar{\sigma}$. Hence, the solution of $f(\chi)=0$ is no longer independent of $\mathrm{T_{e,0}}$, which adds a free parameter when solving the sheath equation. Figure 6.9 shows the evolution of $f(\chi)$ of Eq. (6.8) for $\gamma=1.36$, $\mathrm{T_{e,0}}=45\,\mathrm{V}$ and $\epsilon^*=50\,\mathrm{V}$.

We see that $f(\chi)$ of Eq. (6.8) is rather complex. Five points of interest are marked and labeled in Fig. 6.9 to ease the reading:

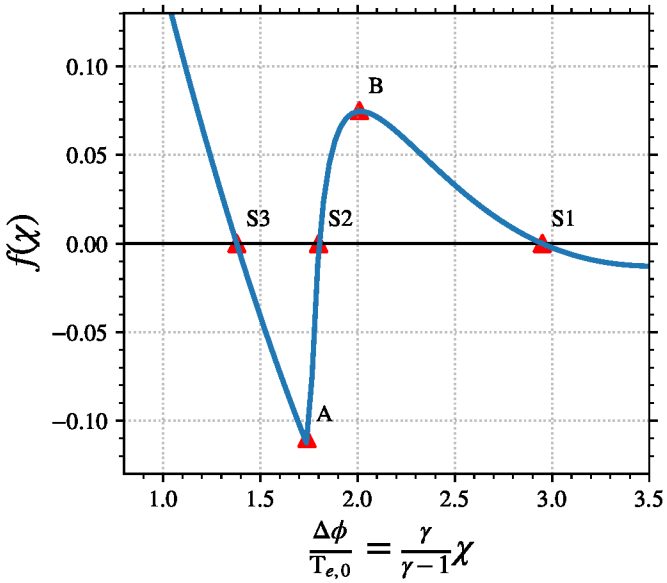

FIGURE 6.9 – Value of $f(\chi)$ of Eq. (6.8) for $\gamma = 1.36$, $\mathrm{T_{e,0}} = 45\,\mathrm{V}$ and $\epsilon^* = 50\,\mathrm{V}$. The five red triangular markers represent five points of interest: the three markers S1, S2, and S3 are solutions of $f(\chi) = 0$; and the markers A and B are two local extrema.

1. S1, S2, and S3 represents the points at which $f(\chi) = 0$, i.e. the solutions of Eq. (6.8)
2. A and B are two local extrema.

The curve $f(\chi)$ is composed of two continuous branches that join at the point A in Fig. 6.9. The two branches corresponds to the two cases of Eq. (6.6). Hence, the point A corresponds to the value of $\Delta\phi/\mathrm{T_{e,0}}$ for which

$$\sigma_0 + (1 - \sigma_0)\frac{2\mathrm{T_{e,wall}}}{\epsilon^*} = \bar{\sigma}_{\mathrm{cr}} = 0.983.$$

The branch at the left of A corresponds to the SCL regime, and has one solution S3 to $f(\chi) = 0$ at $\Delta\phi/\mathrm{T_{e,0}} \simeq 1$. This solutions is the same as in the isothermal case [81]. The branch at the right of A passes by a local maximum B and presents two roots S1 and S2.

The existence of the three solutions depends on the values of ϵ^*, $\mathrm{T_{e,0}}$ and γ. Figure 6.10 shows the impact of the evolution of $\mathrm{T_{e,0}}$ and ϵ^*, with γ constant. We can see that when $\mathrm{T_{e,0}}$ decreases, or ϵ^* increases, the points A and B move upward. Consequently, for low values of $\mathrm{T_{e,0}}$ (respectively large values of ϵ^*) the point A can be above the line $f(\chi) = 0$, hence Eq. (6.8) presents only the root S1. In contrast for high values of $\mathrm{T_{e,0}}$ (respectively low values of ϵ^*) the point B is below $f(\chi) = 0$, so that only S3 is solution of Eq. (6.8). For intermediate values of $\mathrm{T_{e,0}}$ and ϵ^*, A and B are located on both sides of $f(\chi) = 0$, so that the three roots S1, S2, and S3 exist.

Figure 6.11 illustrates the three coexisting sheath solutions. The red solid line with the largest potential drop to the wall represents the solution S1, which is the standard sheath. This solutions leads to the largest electron temperature drop to the wall, hence the smallest SEE rate. The dashed blue line, with a potential well close to the wall, corresponds to the root S3 in the SCL regime, for which $\bar{\sigma} = \bar{\sigma}_{\mathrm{cr}}$ and with $\Delta\phi \simeq \mathrm{T_{e,0}}$. Lastly, the dash-dotted green line represents S2 the intermediate solution.

Figure 6.12 shows the evolution of the sheath potential drop and the SEE rate as a function of $\mathrm{T_{e,0}}$ for the case $\epsilon^* = 50\,\mathrm{V}$. Both the isothermal sheath and the polytropic model using $\gamma = 1.36$ are shown. The result of the isothermal sheath model was previously shown in Fig. 4.17 in Chapter 4. For the solution of the polytropic sheath model, the branches corresponding to the three solutions S1, S2, and S3 are labeled. The light green area highlights the temperature range

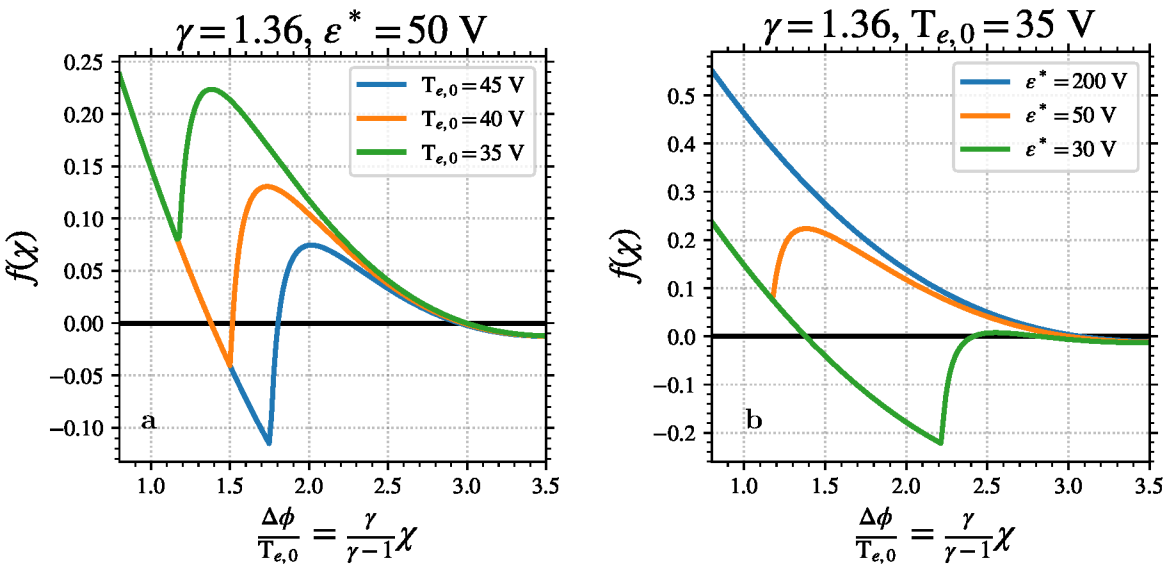

FIGURE 6.10 – Value of $f(\chi)$ of Eq. (6.8) for $\gamma = 1.36$ and different values of $T_{e,0}$ and ϵ^*. (**a**) shows the impact of the evolution of $T_{e,0}$ with $\epsilon^* = 50\,V$, and (**b**) shows the impact of the evolution of ϵ^* with $T_{e,0} = 35\,V$.

with the three coexisting solutions. The lower bounds of the area is noted $T_e^{(2)}$ and the upper bound is noted $T_e^{(1)}$

We see in Fig. 6.12.**a** that $\Delta\phi$ is significantly impacted by the polytropic law. In particular the maximum potential drop which is more than twice as high as the isothermal maximum. In addition, we see in Fig. 6.12.**b** that the polytropic sheath model predicts a SEE rate smaller than the isothermal model. This is due to the fact that the polytropic state law reduces the electron temperature at the wall, hence decreases the electron emission rate for a given $T_{e,0}$. Consequently, the electron bulk temperature can reach higher temperature, compared to the one observed in Fig. 4.17.

6.3.2 Theoretical values of the critical electron temperatures

As shown in Fig. 6.9, for a given $T_{e,0}$, $f(\chi)$ defined by Eq. (6.8) presents a local minimum and a local maximum, labeled A and B respectively in Fig. 6.9. Therefore, there exist two values of $T_{e,0}$ for which either the minimum or the maximum of the $f(\chi)$ crosses exactly the horizontal axis. These values, noted $T_e^{(1)}$ and $T_e^{(2)}$ correspond respectively to the upper and lower bounds of the electron temperature range over which the three solutions coexist. These threshold temperatures can be seen for $\gamma = 1.36$ in Fig. 6.12, where $T_e^{(1)} \simeq 55\,V$ and $T_e^{(2)} \simeq 35\,V$

Maximum electron temperature value for regime III, $T_e^{(1)}$

The first critical electron temperature $T_e^{(1)}$ corresponds to the maximum temperature of the root S1, which is the usual monotonic sheath (corresponding to regime **III**). It is defined as the temperature for which the local maximum B crosses the line $f(\chi) = 0$. As it is a double solution, it corresponds to the solution of Eq. (6.8) that is also a solution of its derivative with respect to χ:

$$\frac{\partial f(\chi)}{\partial \chi} = 0.$$

Once again, the equation is not trivial, and cannot be solved analytically, thus we solve it numerically.

Figure 6.13 shows the variation of $T_e^{(1)}$ as a function of ϵ^* and γ. We see that the maximum temperature $T_e^{(1)}$ increases linearly with ϵ^*. This was expected, as in Eq. (6.8), the only time

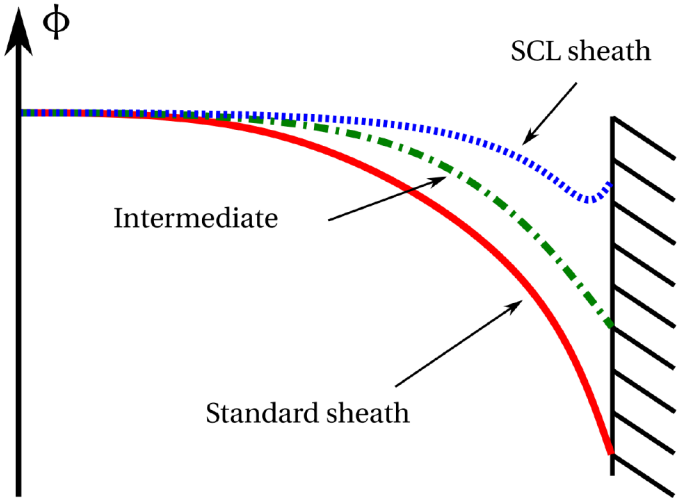

FIGURE 6.11 – Schematic representation of the plasma potential profile in the sheath to the wall for the three coexisting solutions. The red solid line is the standard solution, with the lowest SEE rate ; the dashed blue line corresponds to the SCL regime, with $\bar{\sigma} = \bar{\sigma}_{\rm cr}$; the dash-dotted green line is the intermediate solution, with an intermediate SEE rate.

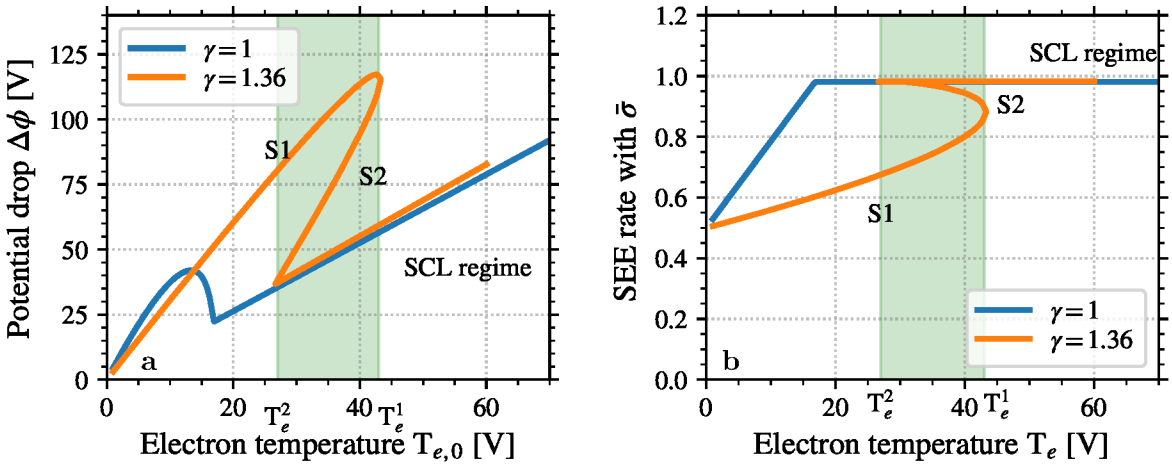

FIGURE 6.12 – Evolution as a function of the electron temperature T_e for $\epsilon^* = 35\,V$ of (**a**) the plasma potential drop to the wall $\Delta\phi$, and (**b**) the SEE rate $\bar{\sigma}_{\rm Maxw}$ using the polytropic sheath model ($\gamma = 1.36$) and the isothermal sheath model. The labels S1, S2 and SCL regime correspond to the three solutions illustrated in Fig. 6.11. The light green area highlights the temperature range with three solutions.

that $T_{e,0}$ is explicitly present is in the term $\frac{T_{e,0}}{\epsilon^*}$. On the other hand, the variation with γ follows a power law, monotonically increasing from 30 V for $\gamma = 1.2$ to 50 V for $\gamma = 1.4$ in the case $\epsilon^* = 45\,V$.

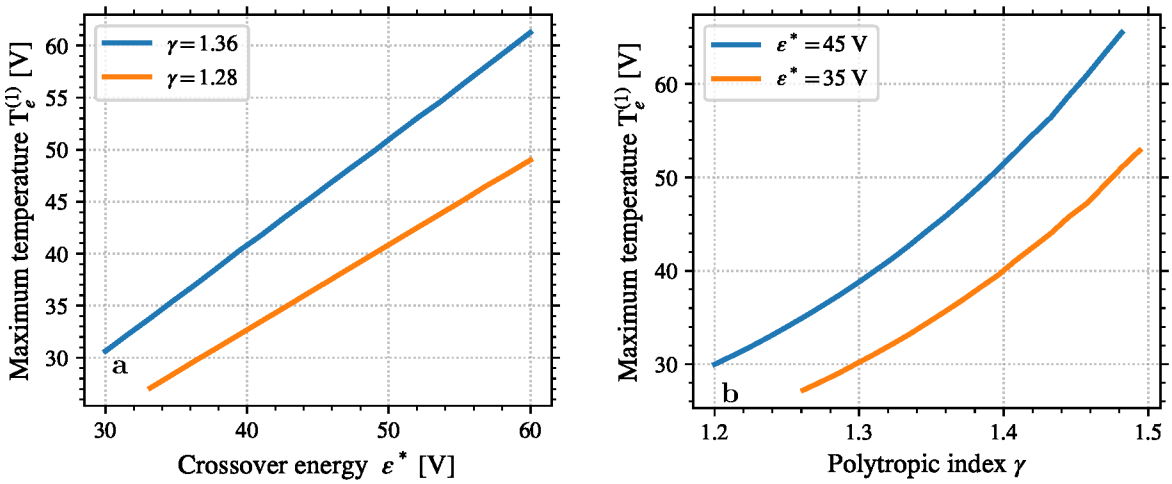

FIGURE 6.13 – Variation of $T_e^{(1)}$ (**a**) as a function of ϵ^* for two values of γ, and (**b**) as a function of γ for two values of ϵ^*.

Minimum electron temperature value for regime I, $T_e^{(2)}$

The minimum electron temperature value for regime **I**, $T_e^{(2)}$, corresponds to the case where the electron temperature at the wall induces exactly an emission rate $\bar{\sigma}_{\mathrm{Maxw}}(T_{e,\mathrm{wall}}) = \bar{\sigma}_{\mathrm{cr}}$. Noting $C_1 = \frac{\bar{\sigma}_{\mathrm{cr}}-\sigma_0}{1-\sigma_0} = 0.964$, we obtain

$$(1-\bar{\sigma}_{\mathrm{cr}})\left(2-\frac{C_1\epsilon^*}{2T_e^{(2)}}\right)^{\frac{1}{(\gamma-1)}}\sqrt{\frac{C_1\epsilon^*}{2T_e^{(2)}}} = \sqrt{\frac{2\gamma\pi m_e}{m_i}} \tag{6.9}$$

Equation (6.9) is solved numerically. The solutions for different values of ϵ^* and γ are shown in Fig. 6.14. As for $T_e^{(1)}$, $T_e^{(2)}$ increases linearly with ϵ^*. It also increases slowly with γ, from 24 V for $\gamma = 1.2$ to 39 V for $\gamma = 1.4$ in the case $\epsilon^* = 45$ V. We note that $T_e^{(2)}$ increases more slowly with γ compared to $T_e^{(1)}$, hence the range of temperature with the three coexisting solutions widen when γ increases.

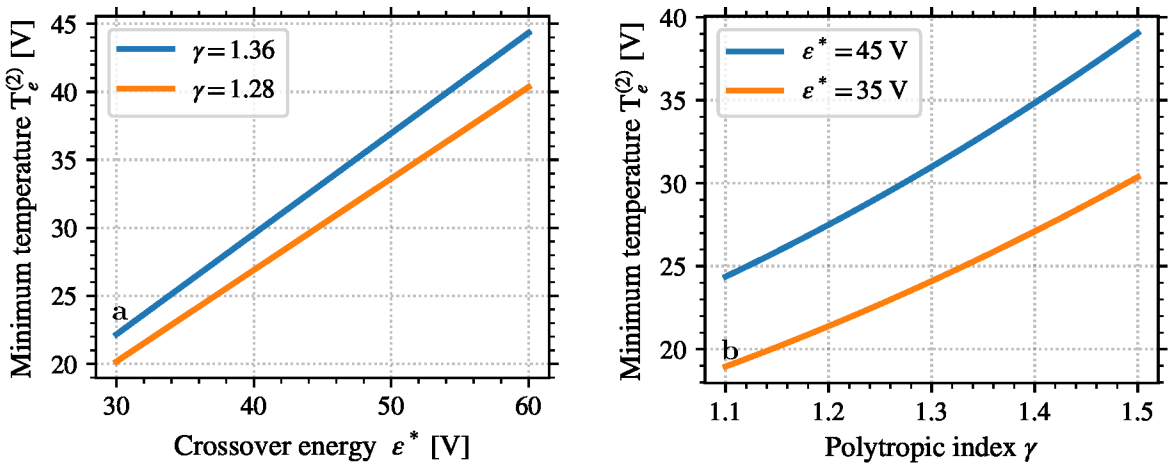

FIGURE 6.14 – Variation of $T_e^{(2)}$ (**a**) as a function of ϵ^* for two values of γ, and (**b**) as a function of γ for two values of ϵ^*.

6.4 Comparison of the sheath model with PIC simulations

We compare in this section the characteristics of the plasma wall interaction observed in the PIC simulations with the fluid model developed in Section 6.3. We first compare the mean values in the parametric study over the crossover energy ϵ^*, then we investigate the oscillations of regime **II**.

6.4.1 Parametric study of the modified sheath model

The variables of interest to characterize the plasma-wall interaction are the averaged electron emission rate $\bar{\sigma}$ and the plasma potential drop to the wall. The only inputs of the modified sheath model are the electron mean temperature in the bulk $T_{e,0}$, as well as the polytropic index γ. As seen in Section 6.2.1, the polytropic index of the total electron population is measured in the PIC simulations to be $\gamma = 1.36$. However, the electrons going toward the wall present a different index, measured from the bulk EVDF to $\gamma = 1.28$. These two values will be compared.

One polytropic index : $\gamma = 1.36$

Using the mean electron temperature measured in the PIC simulations, we first compute the plasma potential drop $\Delta\phi$ by solving Eq. (6.8) with $\gamma = 1.36$. As shown in Fig. 6.14, up to three solutions are possible. The emission rate $\bar{\sigma}$ is computed using Eq. (6.6). As discussed previously, the rate is limited to $\bar{\sigma}_{cr} = 0.982$ to take into account the SCL regime.

The results of the sheath modeled are compared to the PIC simulation results in Figure 6.15. The plasma potential drop in Fig. 6.15.**a** is increased by $\sqrt{\gamma}T_{e,0}/2$ to account for the pre-sheath drop.

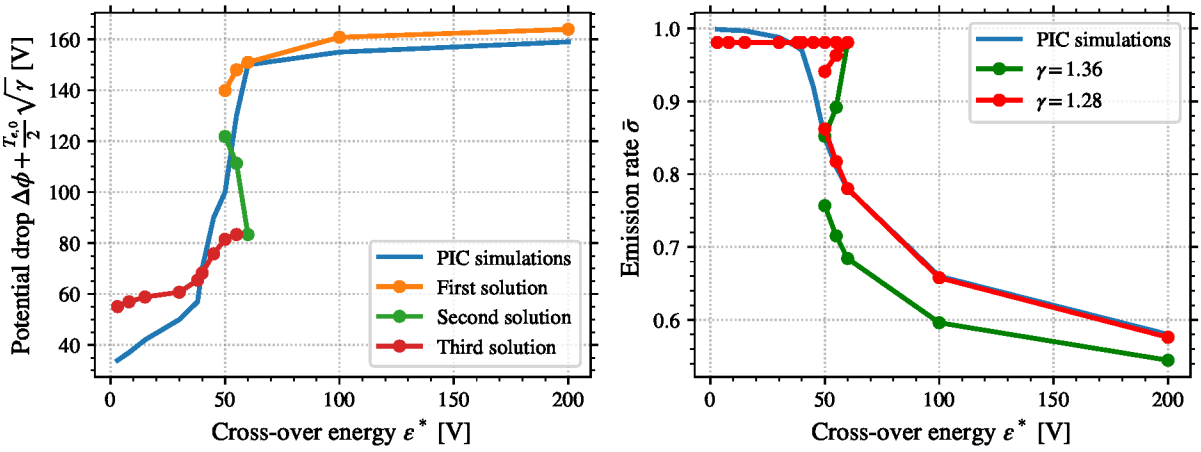

FIGURE 6.15 – Comparison of the PIC simulations and the sheath model using $\gamma = 1.28$ for (**a**) the plasma potential drop from the center to the wall, and (**b**) the electron emission yield calculated with Eq. (6.6). On the panel (**b**) the red dotted line correspond to the value of $\bar{\sigma}_{Maxw}$ obtained with Eq. (6.6) using the value of $\Delta\phi$ showed on the panel (**a**).

Concerning $\Delta\phi$, we see that the sheath model combining the polytropic state law and the electron emission is in good agreement with the PIC simulations. We see that the region where the three solutions coexist corresponds well with the regime **II**.

Concerning the emission rate $\bar{\sigma}$, we observe that the value $\gamma = 1.36$ under estimates $\bar{\sigma}$ compared to the values of the PIC simulations for $\epsilon^* > 70\,V$. On the other hand, $\gamma = 1.28$ is in very good agreement on the whole range of ϵ^*. Interestingly, the saturation of the mean electron emission rate for low values of ϵ^* in the PIC simulation is greater than the critical value $\bar{\sigma}_{cr}$. This is because the critical value corresponds to the start of the SCL regime, with a radial electric at the wall equal to zero. However, we observe in the PIC simulation a small potential well, meaning that the SEE rate is slightly above $\bar{\sigma}_{cr}$.

Two polytropic index : $\gamma = 1.36$ and 1.28

We saw in Fig. 6.15 that $\bar{\sigma}$ is better described using $\gamma = 1.28$. Therefore, we modify the sheath model to take into account two polytropic index: $\gamma = 1.36$ is used to described the electron density, but now $\gamma = 1.28$ is used to compute the temperature at the wall of the forward electron population, hence the SEE rate. The results of the modified sheath model is shown in Figure 6.16. We see that the modified sheath modeled using two values of γ does not affect significantly the value of the sheath potential drop $\Delta\phi$. However, the secondary electron emission rate is in better agreement with the PIC simulation results.

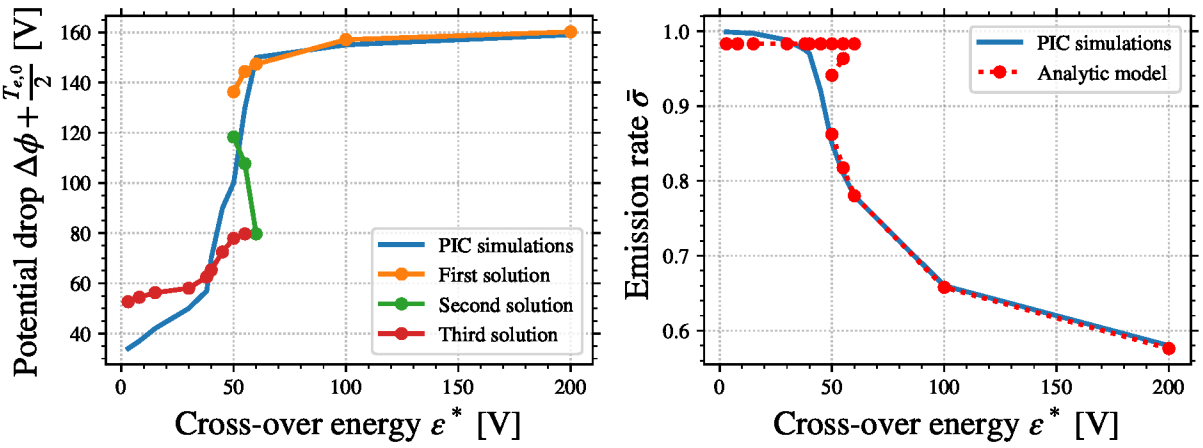

FIGURE 6.16 – Comparison of the PIC simulations and the sheath model using two values of γ ($\gamma = 1.36$ for the electron density, and $\gamma = 1.28$ for the forward electron temperature at the wall) for (**a**) the plasma potential drop from the center to the wall, and (**b**) the electron emission yield calculated with Eq. (6.6).

6.4.2 Sheath oscillations of regime II

The regime **II** is characterized by the presence of oscillations between two meta-stable regimes **III** and **I**, one with a low emissivity and the other with a high emissivity. Figure 6.17 shows the temporal evolution of the electron temperature and the plasma potential relative to the wall for $\epsilon^* = 45\,\mathrm{V}$. The electron temperature is computed over the whole electron population in the PIC simulations. Both the radial temperature $\mathrm{T}_{\mathrm{e},R}$ and the total temperature T_e are shown (see Eq. (1.19) for their definition). The plasma potential $\Delta\phi$ shown is measured at the center of the radial direction of the simulation, averaged over the azimuthal direction.

We clearly see in Fig. 6.17 the quasi-periodic oscillations between the two states. We observe that the electron temperature is slightly anisotropic, with the radial temperature smaller than the axial temperature. This anisotropy observed was not taken into account in the sheath model developed in this chapter. More precisely, the radial temperature $\mathrm{T}_{\mathrm{e},R}$ is linked to the thermal flux of electron toward the wall, while the total temperature T_e changes the electron emission rate $\bar{\sigma}_{\mathrm{Maxw}}$. However, the degree of anisotropy is not very high, as it is of the order of 10% when the sheath is not inverted. When the sheath is inverted, the anisotropy is of the order of 25%, as the electrons with a large radial energy are quickly absorbed. However in the SCL regime, we assume that the electron emission rate saturates at $\bar{\sigma} = \bar{\sigma}_{\mathrm{cr}}$, hence in this regime the impact of the total energy is less important with respect of the radial energy. Hence, we will compare the prediction using only the radial temperature $\mathrm{T}_{\mathrm{e},R}$ or the total, averaged, temperature T_e, but not the two of them together.

Figure 6.18 shows the potential drop as a function of the radial electron temperature $\mathrm{T}_{\mathrm{e}R}$ and the total electron temperature $\mathrm{T}_\mathrm{e} = (\mathrm{T}_{\mathrm{e}R} + \mathrm{T}_{\mathrm{e}\theta} + \mathrm{T}_{\mathrm{e}z})/3$ measured in the PIC simulation (same case as Fig. 6.17). Is also shown the theoretical solutions obtained with the model of Section 6.3

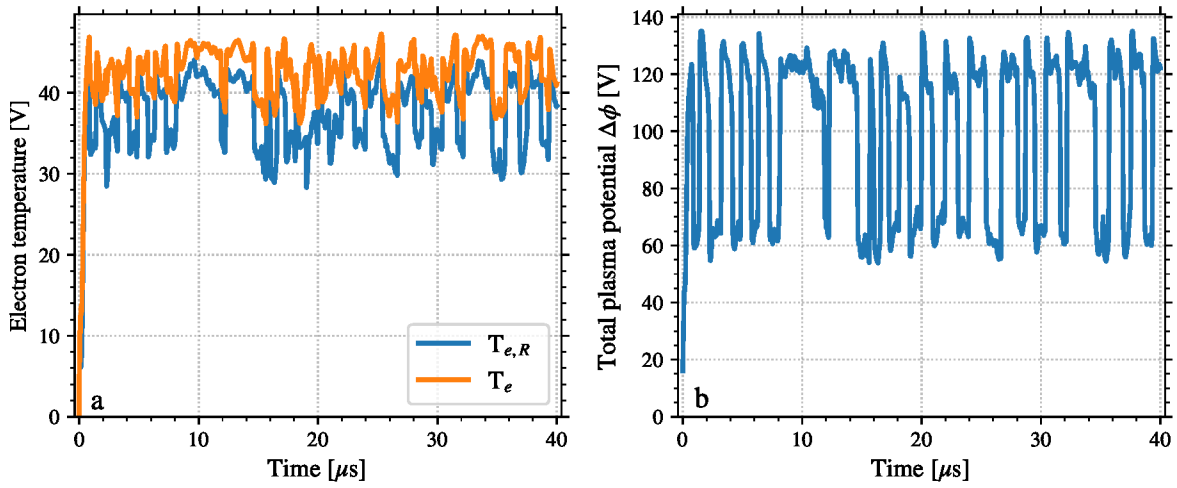

FIGURE 6.17 – Temporal evolution of (**a**) the plasma potential $\Delta\phi$ and (**b**) the electron temperatures: $T_{e,R}$ is the radial temperature, and T_e is the total temperature.

using constant polytropic indexes $\gamma = 1.36$ and 1.28, and $\epsilon^* = 45\,\mathrm{V}$, and a pre-sheath potential drop of $T_{e,0}/2$.

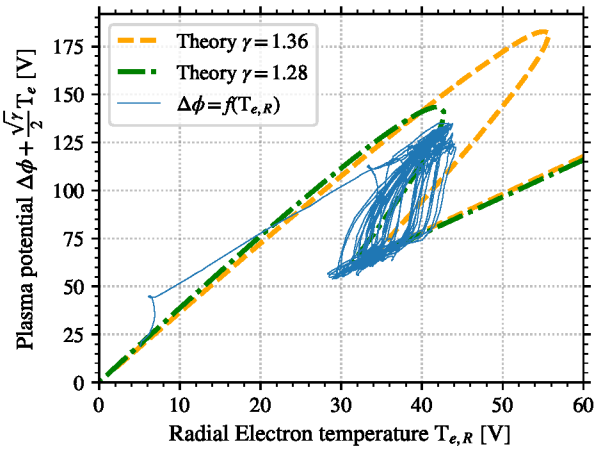

FIGURE 6.18 – Plasma potential as a function of (left) the radial electron temperature T_{eR} and (right) the total electron temperature. The blue line is the PIC results presented in Fig. 6.17, the orange dashed lines correspond to the theoretical values with $\gamma = 1.36$, and the green dotted-dashed line is computed with $\gamma = 1.28$.

We see in Fig. 6.18 that the sheath characteristics observed in the PIC simulations match relatively well the theoretically values obtained from the sheath model. In particular, we see the co-existence of the two solutions of $\Delta\phi$ observed for the same electron temperature, which corresponds to the domain of electron temperature for which the sheath model also predicts multiple solutions.

During the state corresponding to regime **III** (high value of $\Delta\phi$), the PIC values are too noisy to clearly determine if the sheath follows the first or the second branch of the solutions. On the other hand, we see relatively well the correspondence between the PIC results and the theory for the regime **I** (low value of $\Delta\phi$. The agreement with the polytropic sheath model using $\gamma = 1.36$ is better during the standard sheath regime, as the maximum electron temperature $T_e{}^{(1)}$ observed in the simulation is higher than the value at $\gamma = 1.28$. However, during the SCL regime the two values return the same plasma potential.

Electron power balance

The total electron power balance integrated aver the simulation domain can be expressed as

$$\frac{\partial}{\partial t}\left(\frac{3}{2}Vn_e e\mathrm{T_e}\right) = P_{\mathrm{abs}} - P_{\mathrm{loss}}, \tag{6.10}$$

with V the volume of the simulation domain, n_e the average electron density, P_{abs} the total absorbed power, and P_{loss} the total power lost. The absorbed power P_{abs} is assumed to be the Joule heating

$$P_{\mathrm{abs}} = Vn_e e\mathbf{v}_e \cdot \mathbf{E} = Vn_e e v_{e,z} E_z = Vn_e e\mu_e E_z^2 \tag{6.11}$$

with E_z the imposed axial electric field and μ_e the electron axial mobility. From the parametric study of Chapter 4, we have $\mu_e \simeq 5.6\,\mathrm{m^2/V/s}$. As E_z is imposed and the electron density is constant, then the absorbed power is constant.

The power loss P_{loss} is assumed to be governed by losses at the wall. Hence, as developed in Section 5.4

$$P_{\mathrm{loss}} = S\frac{1}{4}hn_e u_b 2e\mathrm{T_{e,wall}} \tag{6.12}$$

with S the surface of the wall of the simulation domain, $h \sim 1$ is the ratio between the mean plasma density and the plasma density at the sheath edge, $u_b = \sqrt{\frac{\gamma e\mathrm{T_e}}{m_i}}$ is the modified Bohm velocity and $\mathrm{T_{e,wall}}$ is the electron temperature at the wall. Hence, we have

$$\frac{\partial}{\partial t}\mathrm{T_e} = \frac{2}{3}\mu_e E_z^2 - \frac{S}{V}\frac{1}{3}\sqrt{\frac{\gamma e\mathrm{T_e}}{m_i}}\left(\mathrm{T_e} - \frac{\gamma-1}{\gamma}\Delta\phi\right), \tag{6.13}$$

where $\frac{V}{S} = L_R$. Equation (6.13) is coupled with the sheath model that returns $\Delta\phi$ as a function of $\mathrm{T_e}$. Concerning the three co-existing solutions, we assume that the sheath follows the same branch until the threshold temperature $\mathrm{T_e}^{(2)}$, or $\mathrm{T_e}^{(1)}$, is reached when the electron temperature increases, or decreases, respectively. When $\mathrm{T_e}^{(1)}$ or $\mathrm{T_e}^{(2)}$ is reached, the sheath jumps to the other solution.

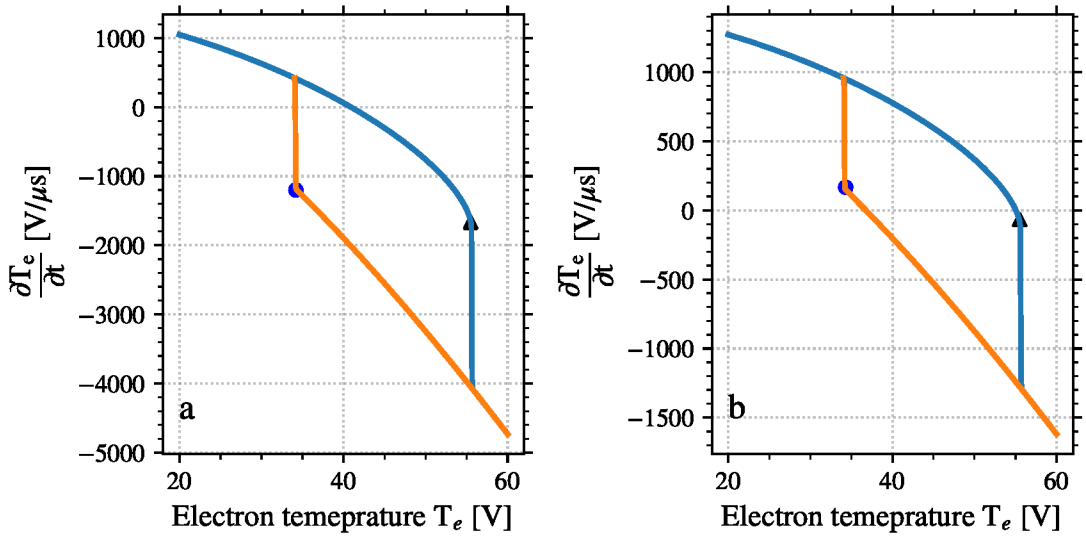

FIGURE 6.19 – Evolution of the power balance $P_{\mathrm{abs}} - P_{\mathrm{loss}}$ as a function of the electron temperature for (**a**) $L_R = 2\,\mathrm{cm}$ and (**b**) $L_R = 4\,\mathrm{cm}$, with $\epsilon^* = 45\,\mathrm{V}$. The blue line corresponds to the increasing temperature for the standard sheath solution, and the orange line correspond to the decreasing temperature in the inverted sheath solution. The markers represent the limit values of the power balance.

Figure 6.19 shows the evolution of the power balance with the electron temperature for two values of $L_R = 2$ and $4\,\mathrm{cm}$. We see for $L_R = 2\,\mathrm{cm}$ in Fig. 6.19.**a** that starting from $\mathrm{T_e} = 20\,\mathrm{V}$ the

power balance is positive until $T_e \simeq 50\,V$. In this condition, the system present a stable solution at that temperature. In contrast for $L_R = 4\,cm$ in Fig. 6.19.**b** the power balance is positive along all of the blue curve, meaning that the electron temperature will rise until the sheath jumps to the SCL regime. There, the power balance is negative, so the electron temperature will decreases until $T_e \simeq 35\,V$ for which the power is balanced.

The power balance of Eq. (6.13) cannot present an oscillating evolution, as there is a temperature for which the power is balance. This is because the maximum power balance in the SCL regime (blue circle markers in Fig. 6.19) is above the minimum value in the standard regime (black triangular markers) In order to observe the oscillations, one should have the circle marker below the triangular one.

Ion dynamics

One has to note that the modified sheath model is stationary, while the oscillations observed are relatively fast. The ion dynamics can be estimated to be

$$\tau_i = \frac{2\pi}{\omega_{pi}} = 0.1\,\mu s. \tag{6.14}$$

Another estimation of the ion time scale is the time needed by an ion to reach the sheath edge from the center of the discharge. Assuming a constant electric field $E_{ps} = \frac{T_e}{L_R}$ in the pre-sheath, we have

$$t_{flight} = L_R \sqrt{\frac{m_i}{eT_e}} = 3.7\,\mu s. \tag{6.15}$$

with $L_R = 2\,cm$ and $T_e = 40\,V$. The period of the sheath oscillations observed $T = 2\,\mu s$ is between τ_i and t_{flight}. Hence, we can expect the ion dynamics to affect the plasma sheath characteristics during the sheath oscillations of the regime **II**.

The sheath oscillations of regime **II** have been observed in Croes [5] with three different ion masses : xenon, krypton and argon. The results are shown in Fig. 6.20. We see that the period of the oscillations vary with the ion mass. More precisely, the period of oscillations decreases with the decrease of the ion mass. This observation confirms that the ions have a role in the dynamics of the oscillations.

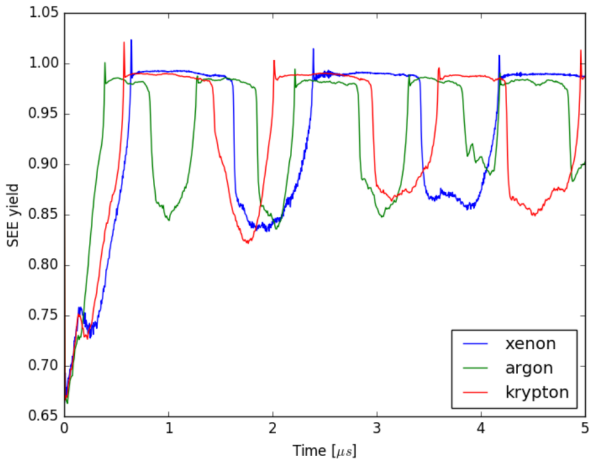

FIGURE 6.20 – Temporal evolution of the SEE rate $\bar{\sigma}$ measured in the PIC simulations for different gases (xenon, krypton, and argon), taken from Croes [5].

6.5 Maximum electron temperature in experiments

In Raitses et al. [7], the authors compare the maximum of the axial profile of the electron temperature $\hat{T}_e$ measured in a Hall Effect Thruster (HET) with two different wall materials: one with a very low emissivity (carbon velvet material), the other is the conventional Boron Nitride (BN) ceramic. Figure 6.21 reproduces the results obtained in Raitses et al. [7].

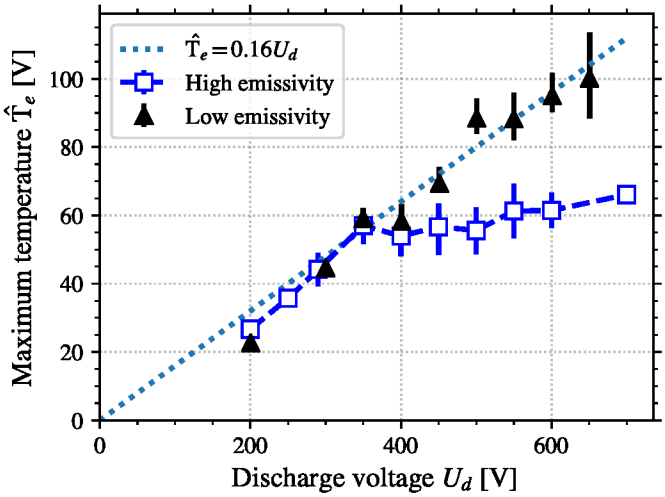

FIGURE 6.21 – The dependence of the maximum electron temperature on the discharge voltage for a conventional thruster with high-SEE BN channel walls and the segmented thruster with low-SEE floating segmented electrodes made of carbon velvet material. Reproducibility of measurements is shown by error bars. Adapted from Raitses et al. [7, Fig. 3]

They observed that with the BN ceramic the values of $\hat{T}_e$ reach a plateau. The value of the plateau is $\hat{T}_e{}^1 = 55 \pm 6\,\mathrm{V}$, the error corresponds to reproducibility of the measurements. In contrast the results with the low emissivity material do not present such behavior, but instead the electron temperature $\hat{T}_e$ keeps increasing linearly with the discharge voltage.

The saturation of the temperature is expected to be due to the SCL regime, which increases the electron power losses. Hence, we expect that the plateau to be the related to $T_e{}^{(1)}$ the maximum electron temperature for the first root S1 to exist. For the BN ceramic we have $\epsilon^* \simeq 35\,\mathrm{V}$ [137], hence using $\gamma = 1.36$ we have $T_e{}^{(1)} = 45\,\mathrm{V}$. This value is lower than $\hat{T}_e{}^1$ observed experimentally, but the agreement is significantly better than with the isothermal sheath model prediction:

$$T_{e,\mathrm{isothermal}}^{(1)} \simeq \frac{\epsilon^*}{2} \simeq 17.5\,\mathrm{V}. \tag{6.16}$$

In order to assess the discrepancy between $T_e{}^{(1)}$ and $\hat{T}_e{}^1$, we need to know the polytropic index observed experimentally. In addition, several phenomena are neglected in the 2D PIC simulation of the sheath model, as the magnetic mirror and the channel curvature [38, 73].

6.6 Conclusion

We observed using the 2D radial-azimuthal PIC simulations of the exit plane of the HET with secondary electron emission that the plasma-wall interaction was not modeled accurately using classical sheath models. This is certainly due to the decrease of the averaged electron temperature from the center to the wall. We saw that the polytropic law could be used to describe this radial evolution of the electrons. The polytropic index is observe to be close to $\gamma = 1.36$ and depends weakly on the SEE rate $\bar{\sigma}$. We have noted that the primary electrons, going from the plasma center toward the wall, presented a lower polytropic index, of the order of $\gamma = 1.28$. This is consistent with the fact that the secondary electrons are emitted with a Maxwellian flux distribution of temperature $\mathrm{T_e} = 2\,\mathrm{V}$.

We have derived a sheath model that uses the polytropic state law to close the electron equations, and the SEE rate is computed with the electron temperature at the wall, with a local Maxwellian hypothesis. This model gives an equation of the potential sheath drop $\Delta\phi$ between the sheath edge and the wall. Depending on the electron temperature $\mathrm{T_{e,0}}$ and the crossover energy ϵ^*, the equation can have one or three solutions.

Confronted to the PIC simulation, the polytropic model was able to predict accurately the characteristics of the plasma-wall interaction observed in the PIC simulation. Using only the electron temperature and the polytropic index of the PIC simulations, we obtain a good correspondence for both the plasma potential drop to the wall $\Delta\phi$ and the secondary electron emission rate $\bar{\sigma}$ between the sheath model and the PIC simulations.

We also observed a good correspondence between the multiple solutions of the sheath model and the sheath oscillations observed in regime **II**. Indeed, we observe that the electron temperature rises following the first branch of the solution, corresponding to regime **III**. When the electron temperature crosses the maximal temperature $\mathrm{T_e}^{(1)}$, the sheath jumps to the third branch, which corresponds to regime **I**. In regime **I**, the electron power losses increase drastically, which reduces the electron temperature until the minimum electron temperature $\mathrm{T_e}^{(2)}$. There, the sheath jumps back to the first branch of the solutions.

In the model developed here, the anisotropy between the temperature parallel and perpendicular to the magnetic field line has not been taken into account. However, the electron flux to the wall is governed by the parallel electron temperature, while the SEE rate depends on the two temperatures. Hence, the electron anisotropy could modify the results of the current sheath model. However, the radial evolution of the perpendicular electron temperature is not clearly understood. Figure 6.22 shows the radial evolution of the electron temperature anisotropy $\frac{\mathrm{T_{e,}}_R}{\mathrm{T_{e,}}_\perp}$ for three values of the crossover energy ϵ^*. We see that the electron anisotropy increases with the increases of the SEE rate. This is expected, as the radial losses, which increases with increasing SEE rate, reduces the electrons with a high radial energy, without effects on the perpendicular energy. Another observation in Fig. 6.22 is the anisotropy radial profile, which is almost uniform. This is not consistent with the current understanding of the collisionless evolution of the electron described with the Vlasov equation developed in Section 5.3. The reason of this constant anisotropy could be the azimuthal instability, which presents radial structures during the saturated state. The importance of the instability on the radial electron energy is further discussed in the next chapter, especially in Section 7.5.1.

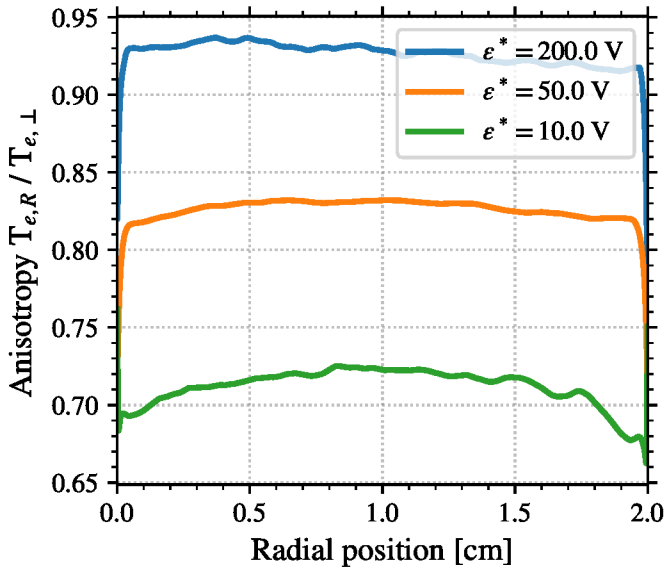

FIGURE 6.22 – Radial evolution of the electron anisotropy $\frac{T_{e,R}}{T_{e,\perp}}$ for the three values of the crossover energy $\epsilon^* = 200, 50$, and 10 V.

Chapter 7

Modeling the radial losses in a 2D axial-azimuthal PIC simulation

In this chapter, we modify the simulation code *LPPic* in order to simulate the axial-azimuthal plane of the Hall Effect Thruster (HET). This allows us to challenge the conclusion obtained from the results of the radial-azimuthal simulations. The impact of the radial plasma-wall interaction is also studied, using a simple model that reproduces the particle radial losses. Its effects on the plasma characteristics and the Electron Cyclotron Drift Instability (ECDI) are studied. The axial transport of the wave and the question of the energy transfer between the three directions are discussed.

Contents

7.1 Presentation of the axial-azimuthal simulation

The bi-dimensional (2D) simulation plane used so far in this work was the radial-azimuthal plane so that the plasma-wall interaction could be studied while obtaining self-consistently the azimuthal instability responsible for the axial electron transport. In this configuration, we have implemented an algorithm that models the axial convection of the particles. However, there are other missing mechanisms of the axial direction in this simulation, in particular: the axial electric field is imposed; the wave is not convected axially; the impact of the axial gradients, such as the diamagnetic drift, are not included; the ionization region is not modeled.

The axial-azimuthal 2 dimensions (2D) simulation domain is used to study these mechanisms, and there are several studies in the literature that focused on modeling this specific simulation plane [35, 86, 8, 44]. However, in these models, the impact of the radial direction is now missing. Therefore, we propose in this chapter a first step to incorporate the radial direction in the axial-azimuthal simulation.

After presenting the simulation domain and its characteristics in Section 7.1, we compare the impact of the radial losses modeled on the simulation results. First, we analyze the discharge characteristics in Section 7.2, then we focus in Section 7.3 on the azimuthal instability.

7.1.1 Description of the simulation domain

To ease the understanding of the different simulation domains, Figure 7.1 shows the simplified HET annular channel with both the radial-azimuthal and the axial-azimuthal $(\mathbf{Z} - \theta)$ domain. The third 2D domain, the radial-axial domain, is not represented. Indeed, it does not model the electron transport due to the azimuthal instability, hence we discard it.

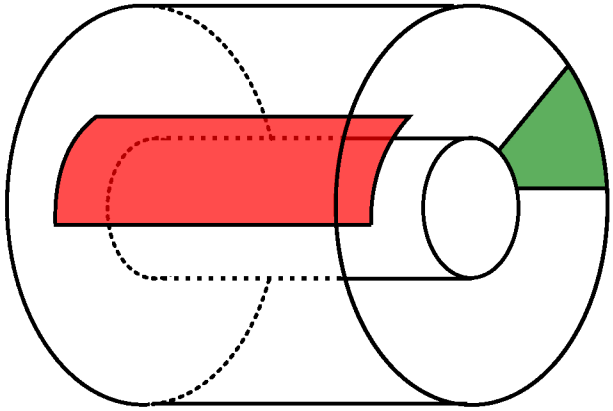

FIGURE 7.1 – Schematic representation of the HET chamber with (green) the radial-azimuthal and (red) the axial-azimuthal 2D domains.

The 2D $(\mathbf{Z} - \theta)$ domain is located at the mean radius of the channel (channel centerline) and we neglect its curvature. Figure 7.2 presents a schematic representation of the $(\mathbf{Z} - \theta)$ simulation domain. The anode side is closed by a metallic fully absorbing electrode, with a fixed non-zero potential. On the other side of the domain, the near-plume region (a few centimeters from the exit plane) is modeled. The boundary located in the near-plume is also a Dirichlet boundary condition, this time grounded. The azimuthal direction is closed with periodic boundaries for both the particles and the fields.

The axial and azimuthal electric fields are self-consistently computed from the charge density by solving the Poisson equation. Consequently, the simulation domain is not so different from the radial-azimuthal simulation domain. This allowed us to adapt the code *LPPic* to simulate both domains using the same core functions. Three particular aspects have been developed:

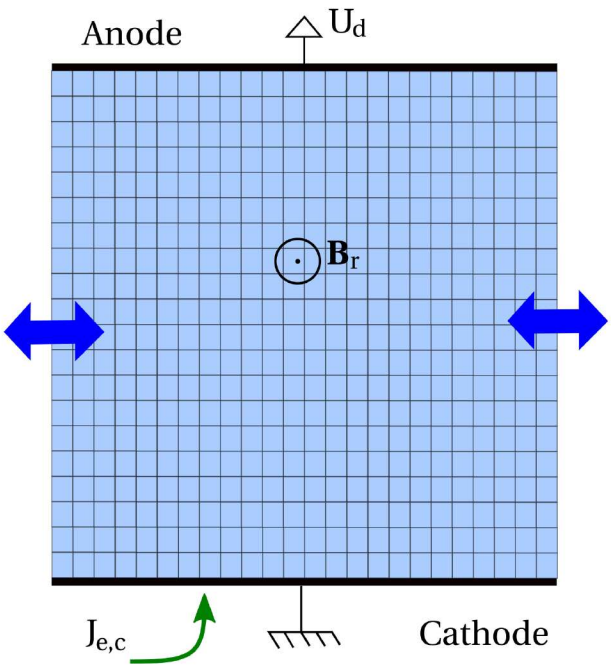

FIGURE 7.2 – Schematic representation of the 2D $(\mathbf{Z} - \theta)$ simulation domain. The anode is at the top, and the cathode at the bottom of the figure. The radial magnetic field perpendicular to the simulation plane is imposed. The azimuthal direction is closed by periodic boundary condition. The electron current density emitted by the cathode $J_{e,c}$ is injected in the simulation domain at the cathode side.

the cathode electron emission, the dynamic computational load balancing, and the electron sub-cycling.

Cathode electron emission

In the HET, the cathode is mostly used to neutralize the ion beam, but a significant fraction of the emitted electrons enters the channel and travels toward the anode, in order to sustain the discharge. Consequently in the simulation, electrons are injected close to the cathode boundary following a Maxwellian distribution of a few electron volts. The number of electrons to inject at each time step is computed by closing the eternal circuit between the anode and the cathode.

In the experimental set-up, a circuit (filter) is placed between the thruster and the generator [138], originally to protect the power supply against AC current. While this external circuit can be modeled [139], and is susceptible to impact the thruster behavior [138, 140], it is not included in this study. Thus, the cathode current equals the anode current

$$I_a = I_c.$$

Dynamic computational load balancing

The axial profile of the plasma density presents a maximum that can be one order of magnitude higher than the mean plasma density. Consequently, a static MPI domain decomposition would produce an unbalance in the number of numerical particles per CPU, which would reduce the efficiency of the code.

One possibility is to modify dynamically the weight of the numerical particles relative to the plasma density, in order to keep a relatively constant number of particles per cell. This can be done by merging the particles when they are too numerous, or by splitting them in smaller particles when they are too few [141, 142]. However, such algorithm can modify the charge, momentum, or the energy of the system if it is not done carefully. In Vranic et al. [143], the authors present an algorithm claimed to conserve these quantities. However, we chose not to implement it because of its error-prone complexity.

Instead, we implemented a dynamic redistribution of the CPU domain, so that every CPU owns approximately the same number of particles. As the density gradient is principally in the axial direction, we only change the axial size of the CPU domains. The dynamic load balancing is done every 150 000 time steps.

Electron time-step sub-cycling

Due to the large mass ratio between the ions and the electrons, the ion dynamic is much slower than the electron dynamic that constrained the time step Δt. In Adam et al. [144], the authors propose to reduce the computational time by using a different time-step for the ions Δt_i and the electrons Δt_e. They show theoretically and numerically that numerical instabilities rise when $\omega_{pe}\Delta t_i \sim \pi$. With the stability criterion on Δt_e (Eq. (2.5)), we find the stability criterion

$$\frac{\Delta t_i}{\Delta t_e} < \frac{\pi}{0.2} \simeq 15.7. \tag{7.1}$$

Consequently, we use $\frac{\Delta t_i}{\Delta t_e} = 11$ in what follows. We verified for one case that using the same time-step for the ions and the electrons produces the same solution.

7.1.2 Facing the breathing mode

The breathing mode comes from the coupling between the neutral gas flow and the plasma dynamics, via the ionization. Under the typical conditions of the HET, this oscillation is observed with a low frequency, around $10 - 30$ kHz, and a large amplitude, as the plasma density can change up to one order of magnitude during the oscillation period [6, 27]. This oscillation is much slower than the ECDI, and is present throughout the entire channel.

If these oscillations are not problematic for the fluid or Direct Kinetic (DK) simulations, they are for Particle In Cell (PIC) simulations. Indeed, the total number of numerical particles is proportional to the plasma density, and a minimal number of particles is required to limit the numerical heating [71]. Thus, when the mean plasma density oscillates, the number of numerical particles (hence the amount of memory used) can change drastically. This reduces significantly the performance of the simulation code, and can lead to memory overflow if the memory available is not high enough to store all the particles during the peak of density of the oscillation. The *merging-splitting* of the particles can be used to reduce the variation of the number of numerical particles, but it is not used for the same reason than discussed above.

In addition to the number of particles, the numerical parameters (time step and cell size) have to be chosen to satisfy the stability criteria during all the simulation, which also reduces significantly the performance of the simulation. This could be overcome by adapting dynamically the mesh and the time step. However, too few studies of the consequences of the use of adaptive mesh and time step on the simulations have been conducted. Thus, we have chosen not to modify the PIC algorithm. Two other approaches have been followed to reduce the computational cost of axial-azimuthal simulations:

1. the approach used by Coche and Garrigues [86]: using a scaling of the permittivity to reduce the computational load to simulate the breathing mode,
2. the approach of Boeuf and Garrigues [8]: using an imposed ionization source term to obtain a steady-state without breathing mode.

Since we want to get insights on the radial wall effects in a reasonable computational time, we use in this study the test-case of Boeuf. It is interesting to note that a very close configuration has been used as a international benchmark published recently in Charoy et al. [91].

7.1.3 Description of the simulation test-case of Boeuf

In Boeuf and Garrigues [8], the authors used a simplified simulation set-up in order to study the azimuthal instabilities. The simulation is collisionless and the ionization profile is not-self-consistent but is rather given as an input. This removes the breathing mode oscillations from the discharge, and simplifies the parametric study. The ionization source term S_{iz} used follows a cosine profile

$$S_{iz} = \max\left(0, S_0 \cos\left[\pi \frac{z - z_M}{L_S}\right]\right), \tag{7.2}$$

with the parameters S_0, z_M , and L_S given in Table 7.1. The simulation domain is small, reducing again the computational load. Indeed, the axial length in this case is $L_z = 2.5\,\text{cm}$, with $L_{ch} = 0.75\,\text{cm}$ of the chamber included in the simulation domain, against $L_{ch} = 2.5\,\text{cm}$ in a typical HET. Figure 7.3 presents the simulation domain, the axial profile of the ionization source term S_{iz}, and the magnetic field profile.

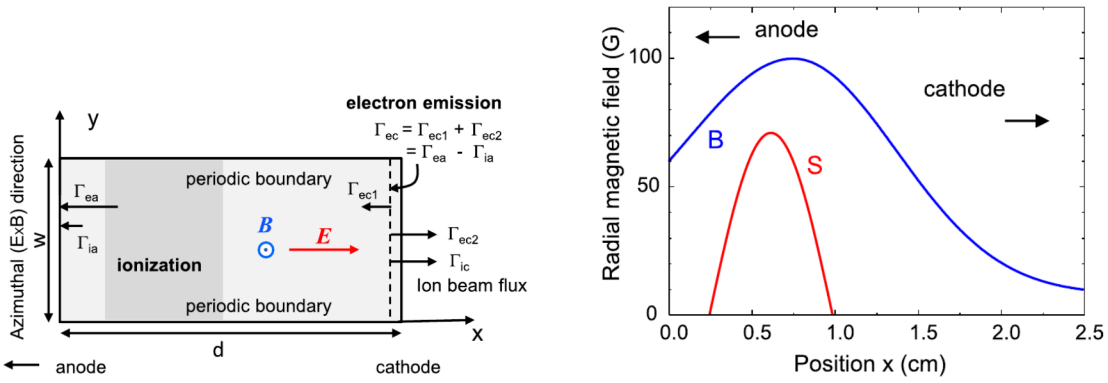

FIGURE 7.3 – (left) the 2D axial azimuthal domain, with in dashed line the cathode electron injection plan; (right) the axial profile of the magnetic field and the ionization source term profiles, taken from [8].

The electrons emitted by the cathode are injected inside the simulation domain, at 1 mm from the boundary. Since the electron injection is not located at the cathode boundary, a large cathode sheath is present. Therefore, the plasma potential is corrected so that the potential is $\phi = 0$ at the location of injection, at 1 mm from the boundary. This is done by substracting the azimuthally averaged plasma potential at the injection plane, from the potential calculated with the Poisson equation. The large cathode sheath that forms between 2.4 and 2.5 cm has been shown not to affect the discharge behavior and hence, it won't be studied here. The physical and numerical conditions used for the simulation are given in Table 7.1. More details can be found in Boeuf and Garrigues [8] and Charoy et al. [91].

7.1.4 Models for the radial losses

In this section, we address the issue of adding to the purely 2D axial-azimuthal PIC simulation the impact of the radial walls. The first effect that we want to model is the particle and power losses to the wall. Thus, as previously done in the radial-azimuthal simulation, the particles are tracked in the three directions, and a finite radial length is used to limit the radial direction. When an ion crosses the boundary, it is removed from the simulation. The electrons are partially reflected, such that the electron flux absorbed at the wall equals the ion flux. We do not model the secondary electron emission. We assume that the sheath is infinitely thin, so that the wall corresponds to a partially reflecting surface. Two approaches have been investigated to model efficiently the effect of the sheath.

TABLE 7.1 – Physical and numerical parameters used in the 2D PIC simulations of an axial and azimuthal ($\mathbf{Z} - \theta$) plane of a HET.

Physical Parameter	notation	Value	Unit
Gas		Xenon	-
Domain dimensions	$L_\theta \times L_z$	1.25×2.5	[cm^2]
Maximum magnetic field	$\max(B_r)$	100	[G]
Position of $\max(B_r)$	$z_{\max(B_r)}$	0.75	[cm]
Anode voltage	U_d	200	[V]
Initial electron temperature	$\mathrm{T_{e,0}}$	10.0	[V]
Initial ion temperature	$T_{i,0}$	0.5	[V]
Initial plasma density	n_0	$5{\times}10^{16}$	[m^{-3}]
Maximum Ionisation	S_0	$5.23{\times}10^{23}$	[m^{-3}s^{-1}]
Center of S_{iz} profile	z_M	0.625	[cm]
Width of S_{iz} profile	L_S	0.75	[cm]
Simulation Parameter			
Permittivity scaling	α	1	-
Cell size	$\Delta x = \Delta y$	5×10^{-5}	[m]
Time step	Δt	5×10^{-12}	[s]
Electron sub-cycling	$\frac{\Delta t_i}{\Delta t}$	11	-
Initial number of particles per cell	N/NG	25	[part/cell]

Model 1 for the radial losses: sheath model

In the first approach, we set the potential drop at the walls by the use of a sheath model, such as the one described in Section 2.7, or in Chapters 5 and 6. The ions would be absorbed by the radial boundary, as well as the electrons of energy higher than the sheath potential. Electrons with smaller energy are reflected spectacularly. This model is more physical, and it would allow local charge imbalance. However, as there is no electric field self-consistently computed in the radial direction, the plasma cannot react to such imbalances. Hence, we chose not to use it.

Model 2 for the radial losses: flux equality

The second approach directly imposes the flux equality by absorbing at every time step the same number of electrons as ions. The electrons crossing the radial boundaries are sorted by their energy in the radial direction, and the electrons absorbed are the most energetic ones. The others are reflected specularly. Due to the small number of ions crossing the boundary, and for performance issues, we choose to impose the flux equality averaged over the domain of one CPU. As 360 CPU domains are used to decompose the whole simulation domain, this allows a partial locality of the flux equality.

While the sheath can be supposed infinitely thin, the ion flux to the wall usually depends on the pre-sheaths, which display an ambipolar electric field that accelerates the ions to the ion sound speed at the sheath edge. Since the development and validation of a pre-sheath electric field model in the radial model required more resources than available, there is no such pre-sheath model in the results presented in this chapter. Consequently, the ion flux to the wall is a thermal flux, which is much smaller than the flux created by a pre-sheath. Hence, using a realistic radial length of the order of $L_R = 2\,\mathrm{cm}$, the particle losses are underestimated.

One solution could be to reduce the radial length, so that the particle flux are closer to physical losses. Indeed, we can compensate the reduced ion flux (due to the reduced ion velocity) by increasing the density of the macro-particles. Assuming the macro-particles uniformly distributed over the third R direction, reducing L_R increases the radial density of macro-particles, hence the macro-particle flux.

The results given in the next sections are obtained by modeling the radial losses in the whole simulation domain. We choose to do so in order not to introduce a discontinuity in the radial boundary condition, as well as to increase the impact of the radial losses on the simulation results.

7.2 Results of the axial-azimuthal PIC simulations

In this sections, we present the results of the 2D PIC simulations using the test-case of Boeuf [8], described in Section 7.1.3; the parameters used for the simulations are given in Table 7.1. In this test-case, the ionization is fixed, consequently the simulation converges quickly towards a steady state, as the mean parameters stop evolving in approximately 8 µs.

We run three different cases: the first is the usual case, without the effects of the radial direction. It is expected to return the same results as obtained in Boeuf and Garrigues [8]. The two other cases model the influence of the radial direction. Two values of the radial length are used: $L_R = 4\,\text{cm}$ and $2\,\text{cm}$.

7.2.1 Simulation results: an overview

Figure 7.4 shows the axial and azimuthal distribution of the azimuthal electric field E_θ and the electron density n_e at steady state at $t = 10\,\mu\text{s}$ in the case where no radial losses are modeled. We see in both E_θ and n_e the ECDI, which wavelength is approximately $\lambda_\theta = 0.08\,\text{cm}$ at $z = 0.5\,\text{cm}$. The results observed are similar to those presented by Boeuf and Garrigues [8], but in order to validate the results, an exhaustive comparison has been conducted between seven independently developed PIC codes on this specific case. A good agreement has been obtained as shown in Charoy et al. [91].

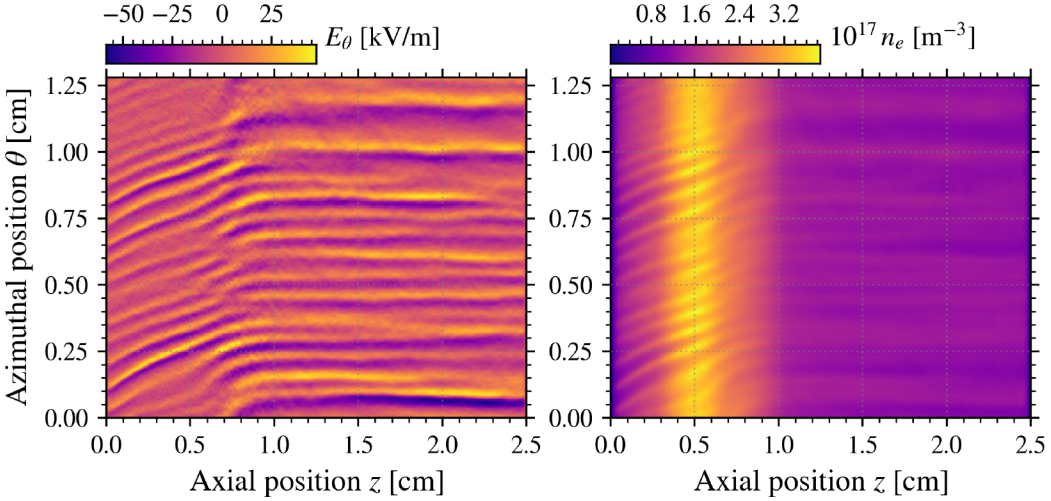

FIGURE 7.4 – Axial-azimuthal distributions of (left) the azimuthal electric field E_θ and (right) the electron density n_e at $t = 10\,\mu\text{s}$. The short scale azimuthal oscillation is the ECDI.

7.2.2 Simulation results: temporal evolution

Figure 7.5 presents the temporal evolution of the mean plasma density, the total temperature, and radial temperature. Both the electron density and the total temperature rise from the initial condition and reach the stationary state at $t = 8\,\mu s$. We see that when the radial direction is modeled the density, the mean electron temperature, and the radial electron temperature are reduced, as expected when increasing the losses when the ionization source term is constant.

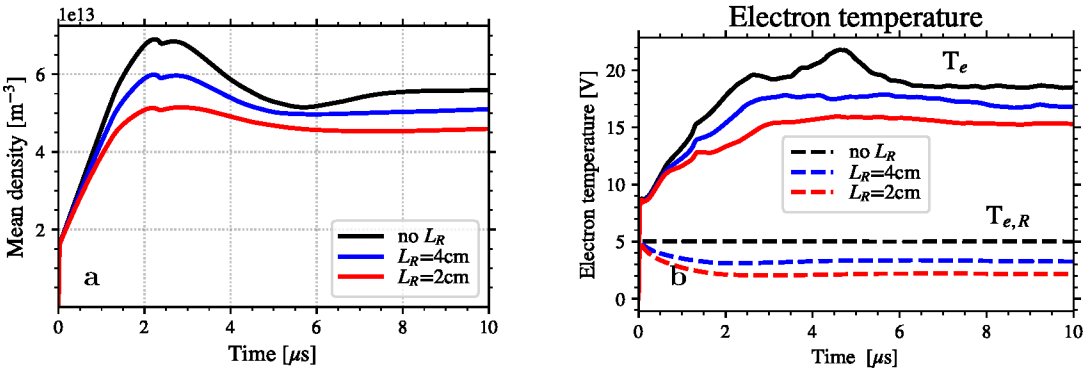

FIGURE 7.5 – Temporal evolution of (**a**) the mean plasma density, and (**b**) the mean (solid line) total electron temperature T_e and (dashed line) the radial temperature $T_{e,R}$ in the axial-azimuthal simulations, obtained with the three different radial models.

We see on Fig. 7.5.**b** that the radial temperature remains constant when the radial direction is not modeled. This is due to the fact that the collisions are not modeled in the simulations, so that there is no momentum and energy transfer from the axial and azimuthal directions to the radial direction. However, we know from the radial-azimuthal simulations that there is a transfer of energy between the axial direction and the radial direction, resulting in a plasma more isotropic than observed here. This aspect is discussed latter in Section 7.5.1. With the radial losses, the radial temperature decreases from the initial temperature $T_e = 5\,V$ to $T_{eR} \simeq 2.2$ and $3.3\,V$ for $L_R = 2$ and $4\,cm$, respectively. The total temperature T_e shows a similar decrease with the increase of the radial losses.

7.2.3 Simulation results: averaged axial profiles

Figures 7.6 and 7.7 show the axial profile at steady-state of several plasma quantities. The variables are averaged in the azimuthal direction and in time between $t = 8$ and $t = 10\,\mu s$. The results obtained with the three different radial models are overlaid. Fig. 7.6.**a** shows the axial electric field E_z. The differences in E_z are small, but we can still observe that the amplitude of E_z is reduced with the increased radial losses. The electron density n_e shown in Fig. 7.6.**b** is almost not affected, except for $z > 1\,cm$, where the electron losses at the wall can be seen.

Figure 7.7 shows the axial profiles of the electron axial density current and the electron temperatures. The electron temperatures are reduced by the radial losses in each direction $(T_{e,\theta}, T_{e,R}, T_{e,Z})$. The radial temperature $T_{e,R}$ is reduced uniformly everywhere, but the two other temperatures are mostly affected upstream, at approximately $z = 0.8\,cm$. Surprisingly, to a first approximation we could think that the radial losses should not reduce the axial and azimuthal temperatures. Indeed, if we suppose that the distribution function has separated variables

$$f(\mathbf{v}_e) = f_r(v_{e,r}) f_\theta(v_{e,\theta}) f_z(v_{e,z}),$$

then the absorption of electrons with high radial energy should not modify the distribution function in the other directions. However, the loss of energetic particles is an energy loss in the three directions, so that it will affect the power balance.

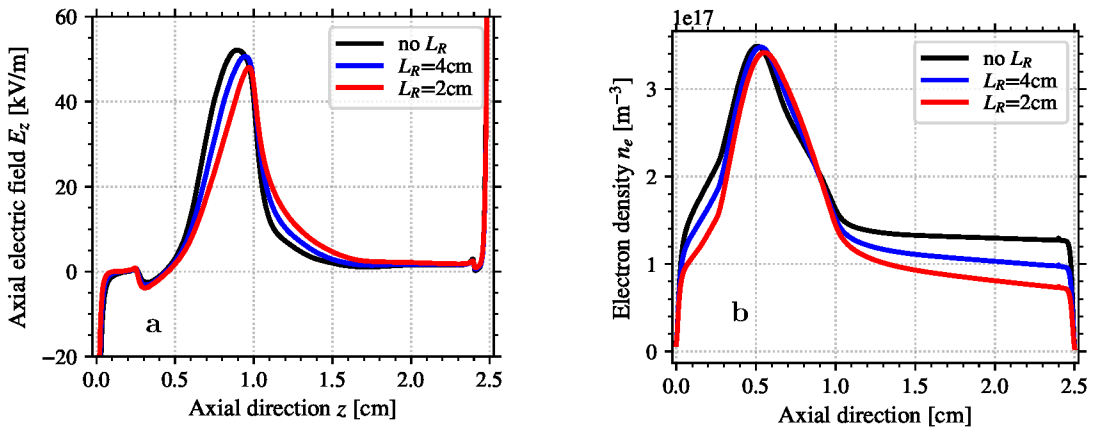

FIGURE 7.6 – Averaged axial profiles at steady state of (**a**) the axial electric field E_z, (**b**) the mean plasma density obtained with the three different radial models. The variables are averaged over the azimuthal direction and in time between $t = 8$ and $10\,\mu$s.

In addition, the electron heating comes principally from the Joule heating $\mathbf{J}_e \cdot \mathbf{E}$. As the axial electric field E_z, seen in Fig. 7.6.**a**, is almost unaffected, the difference in the electron temperature can also originate from the differences in the axial electron current. The axial electron density current $J_{e,z}$ is shown in Fig. 7.7.**b**. We see that $J_{e,z}$ decreases between $z = 0.2$ and $z = 1\,$cm, because of the ionization source term. We can also observe the sharp sign change at $z = 2.4\,$cm, in agreement with the cathode electron injection location. In addition, $J_{e,z}$ is significantly reduced in the whole domain by the radial losses, as there is approximately a factor of two between the case without radial losses and the case $L_R = 2\,$cm.

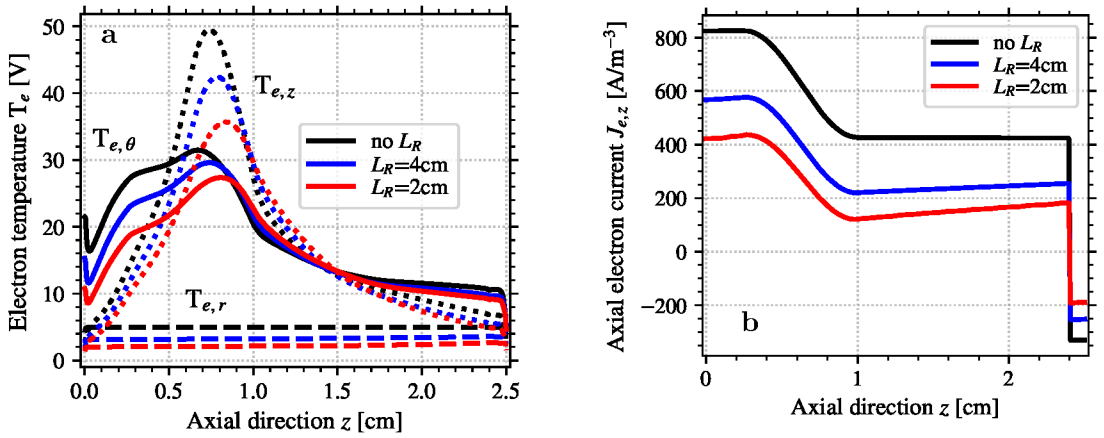

FIGURE 7.7 – Averaged axial profile at steady state of (**a**) the electron temperature, and (**b**) the axial electron current density $J_{e,z}$, obtained with the three different radial models. The variables are averaged over the azimuthal direction and in time between $t = 8$ and $10\,\mu$s.

We observe a factor of two on $J_{e,z}$ between the case $L_R = 2\,$cm and the case without losses. As we have seen in Fig. 7.6.**b** that the electron density is almost unaffected, this means that the electron axial velocity is reduced by the radial losses. Figure 7.8 shows the norm of the average electron velocity

$$v_{e,z} = |\frac{J_e}{en_e}|$$

We can see that the electron mobility is significantly affected by the radial losses. However, since the simulation is collisionless, the electron cross-field transport in the axial direction is only

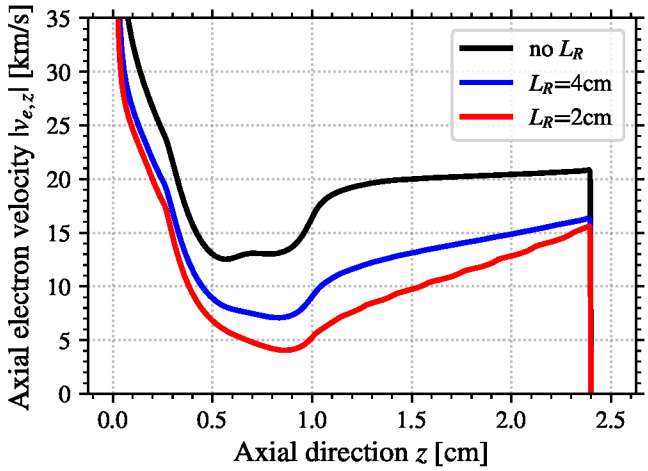

FIGURE 7.8 – Axial profile of the norm of the axial electron velocity measured in the PIC simulations for the three cases of radial losses.

due to the azimuthal instability. It is confirmed by Figure 7.9, that shows on the left the average standard deviation of the azimuthal electric field, and on the right the correlation term R_{ei}. We recall from Section 2.8 that

$$R_{ei} = -e < \delta n_e \delta E_\theta >_\theta, \tag{7.3}$$

with δn_e, and δE_θ the fluctuations of the electron density and azimuthal electric field, respectively. Moreover, we have from Eq. (1.9)

$$\mu_e = \frac{< \delta n_e \delta E_\theta >_\theta}{n_0 E_z} \frac{1}{B_r}$$

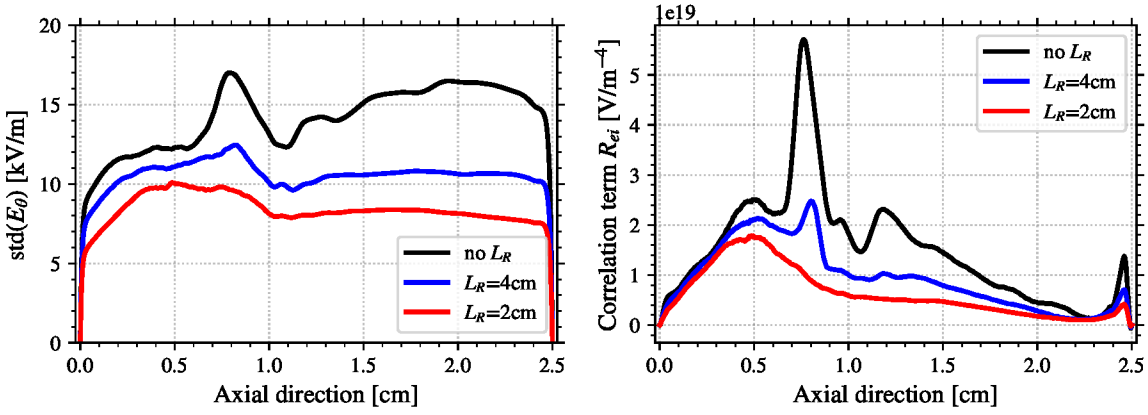

FIGURE 7.9 – Axial profiles of the characteristics of the instability, (left) average of the standard deviation of the azimuthal electric field, (right) electron-ion friction force calculated by the correlation between n_e and T_e.

We observe in Fig. 7.9 that the amplitude of the instabilities, as well as the correlation term, are significantly affected by the electron radial losses. This explain the reduction of the axial electron current, but also the reduction on the Joule heating, which reduces the electron axial and azimuthal temperatures.

To summarize the results presented in this section, we used a simple algorithm to model the radial particle losses in the 2D axial-azimuthal PIC simulation. We observe almost no impact on

the axial electric field E_z, and a slight diminution of the mean electron density n_e (up to 20% in total, but mostly in the near-plume region).

The electron temperature is also reduced, not only in the radial direction, where the radial losses have a direct impact, but also on the azimuthal and axial temperatures. This is consistent with the large reduction of the axial electron mobility, which lower the Joule heating. The reduction of the cross-field electron transport comes from the diminished amplitude of the azimuthal instability. In the next section, we analyze in more details the instability in order to explain the impact of the radial losses on the amplitude of the instability. In Section 7.5.1, we will discuss the radial heating of the electrons.

7.3 Characteristics of the azimuthal instability

We have observed in the previous section that the radial loss model did not modify significantly the plasma characteristics (densities, axial electric field), but it had a significant impact on the electron cross-field transport. Since the simulations are collisionless, the origin of the variation of the electron axial mobility comes from the azimuthal instability, which amplitude decreases with the radial losses as seen in Fig. 7.9. In this section, we investigate the possible mechanism responsible of the evolution of the oscillation characteristics. Several phenomena can have an impact, direct or indirect, on the azimuthal instability:

1. The radial loss algorithm used could induce numerical noise which affects the instability,
2. The electron temperature is decreased; if the amplitude of the instability saturates due to ion-wave trapping, then the amplitude would be lower, as shown in Eq. (3.4),
3. The growth rate is proportional to the azimuthal electron drift velocity, as seen in Eq. (3.16). If the growth rate is affected, then the wave amplitude at steady state could be reduced,
4. The radial losses could directly reduce the amplitude of the density oscillation.

Using the results of the 2D PIC simulation, we will discuss the four points in the next sections.

7.3.1 Overview of the azimuthal instability

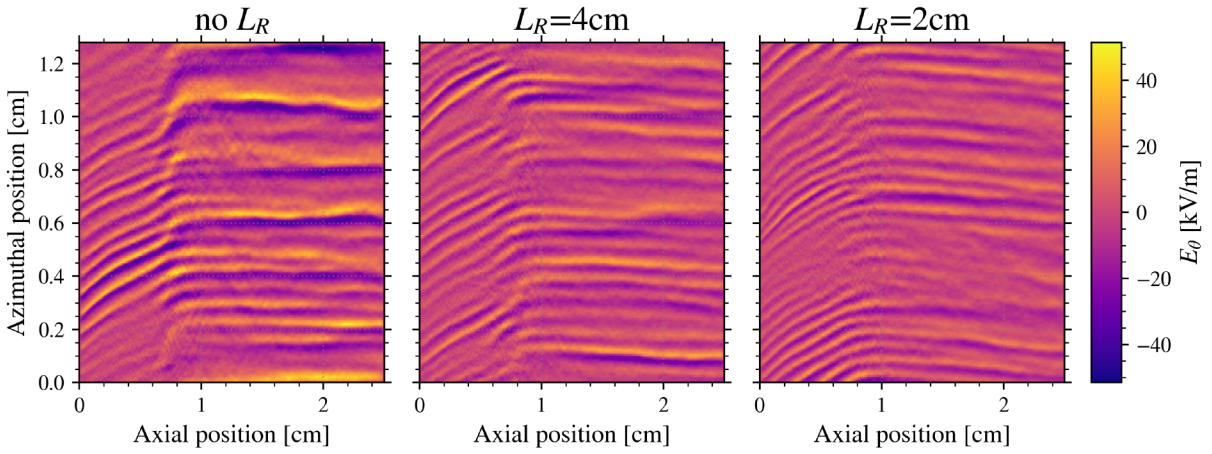

FIGURE 7.10 – Axial and azimuthal distribution of the azimuthal electric field E_θ obtained at $t = 10\,\mu s$ for the three cases with parameters given in Table 6.1 and three values of L_R. The same color limits are used for each figure.

We recall that three cases have been simulated: the nominal case without radial losses and two other cases with the radial losses modeled with $L_R = 2\,cm$ or $L_R = 4\,cm$. Figure 7.10 shows the azimuthal electric field at $t = 10\,\mu s$ for the three cases. The azimuthal instability is present

in all the simulation domain for the three cases. We note that using $L_R = 2$ or 4 cm the radial losses do not induce unphysical instabilities, such as observed in Section 2.5 with the modeling of the axial convection in radial-azimuthal simulations when adding radial losses. Therefore, we believe that there is no numerical noise or artifacts that affects the instability. This conclusion is confirmed by the spectra analysis of Section 7.4.1. From the characteristics of the instability seen in Fig. 7.10, two zones can be identified:

— The upstream region, $z < 8$ mm, where the instability presents a short wavelength, and is oblique.

— The downstream region, $z > 1$ cm, where the wavelength of the instability is larger and is almost perfectly azimuthal.

The radial losses seem to reduce the wavelength of the instability in both regions, but the main impact is in the downstream region.

We have seen in Chapter 3 that the instability wavelength is of the order of the Debye length λ_{De} and its frequency is of the order of the ion plasma frequency ω_{pi}. In contrast with Chapter 3, the two parameters now vary in the simulation domain. Figure 7.11 shows the axial evolution of the ion plasma frequency and the Debye length for the three cases. The Debye length is calculated using the azimuthal temperature $T_{e\theta}$.

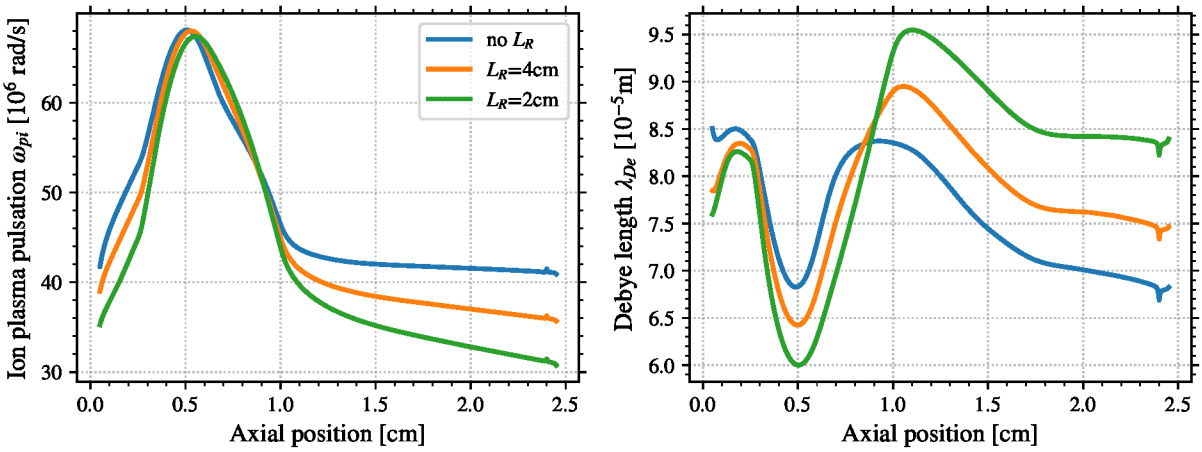

FIGURE 7.11 – Axial evolution of (left) the ion plasma frequency ω_{pi} and (right) the Debye length λ_{De} for the three cases averaged azimuthally and in time between $t = 6\,\mu$s and $t = 10\,\mu$s.

We see in Fig. 7.11 that ω_{pi} reaches a maximum at $z = 0.5$ cm, and decreases by almost a factor of two towards both the anode and the cathode. We observe that ω_{pi} is not significantly affected by the radial losses in the upstream region, but decreases with the increase of the losses in the downstream region. On the other hand, the Debye length λ_{De} presents a more complex behavior, as it reaches a local minimum at $z = 0.5$ cm and a local maximum at $z \simeq 1$ cm. The amplitude of the evolution of λ_{De} is smaller compared to ω_{pi}, as it changes in the axial direction by approximately 20% without the radial, and up to 40% with $L_R = 2$ cm. In addition, we see in Fig. 7.11 that the radial losses change λ_{De} in both regions, but not with the same trend. In the upstream region, the increase of radial losses decreases λ_{De}, while it increases λ_{De} in the downstream region.

7.3.2 Ion-wave trapping saturation

The test-case used here and proposed by Boeuf and Garrigues [8] allows the simulation to reach a steady-state. The authors state that the amplitude of the instability is consistent with an ion-wave trapping saturation. Therefore, we use the criterion developed in Section 3.1.5 and given by Eq. (3.7) to determine whether or not the modification of the wave amplitude is related to the ion-wave trapping. We recall the criterion used between the thermal and the wave energy densities

$$432\epsilon_{\text{wave}} = \epsilon_{\text{th}}, \tag{7.4}$$

with $\epsilon_{\text{th}} = \frac{3}{2} e n_e \text{T}_\text{e}$ and $\epsilon_{\text{wave}} = \frac{\epsilon_0}{2}\sigma^2_{E_\theta}$. Figure 7.12 shows the axial profile of the ration between $432\epsilon_{\text{wave}}$ and ϵ_{th}, averaged azimuthally and in time between $t = 6\,\mu\text{s}$ and $t = 10\,\mu\text{s}$ for the three cases of radial losses.

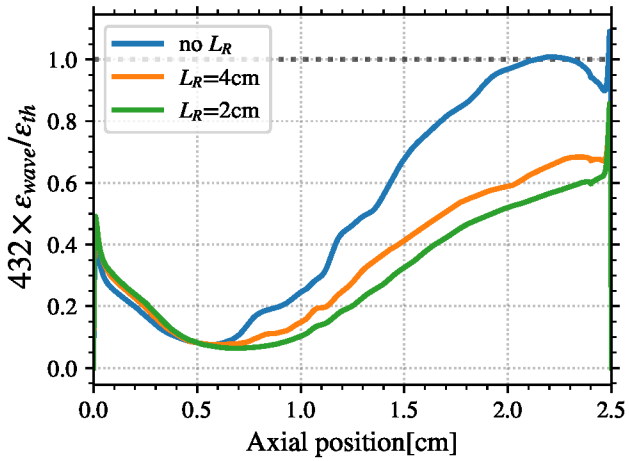

FIGURE 7.12 – Axial evolution of the ratio between $432\epsilon_{\text{wave}}$ and ϵ_{th} to characterize the ion-wave trapping, averaged azimuthally and between $t = 6\,\mu\text{s}$ and $t = 10\,\mu\text{s}$ for the three radial losses cases.

We see that the results observed for the case without radial losses do reach the saturation criterion, but only close to the cathode for $z > 2\,\text{cm}$. Nevertheless, for both cases with the radial losses modeled, the amplitude of the wave is smaller. Hence, it seems that the wave amplitude is reduced by the radial losses such that the ion-wave trapping is not the dominant saturation mechanism anymore.

7.3.3 Electron azimuthal drift velocity

We showed in Chapter 3 that the instability growth rate is proportional to the electron azimuthal drift. In the radial-azimuthal simulation, the drift was only due to the $\mathbf{E} \times \mathbf{B}$ drift

$$u_{E\times B} = -\frac{E_z}{B_r} \tag{7.5}$$

However, we saw in Figs. 7.6 and 7.7 that the electron density and the temperature $\text{T}_{e,z}$ present a large gradient. Therefore, the diamagnetic drift

$$u_{\text{Dia}} = \frac{\nabla_z(n_e \text{T}_{e,z})}{n_e B_r}$$

can also affect the electron drift velocity. Figure 7.13 shows the axial profile of the azimuthal electron mean velocity $u_{e,\theta}$ at steady-state ($t = 14\,\mu\text{s}$) for the case without radial losses (no L_R).

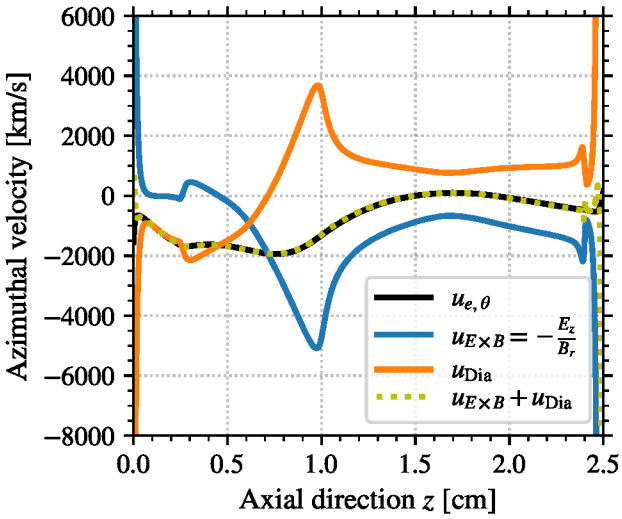

FIGURE 7.13 – Axial profile of (black solid line) the electron azimuthal velocity measured in the simulation, (blue solid line) the $\mathbf{E} \times \mathbf{B}$ drift velocity, (solid orange line) the diamagnetic velocity, and (dashed line) the sum of the $\mathbf{E} \times \mathbf{B}$ and diamagnetic velocities averaged azimuthally and between $t = 6\,\mu\mathrm{s}$ and $t = 10\,\mu\mathrm{s}$ for the case without radial losses (no L_R).

We can see that the $E \times B$ drift is not the only contribution to the electron azimuthal velocity, in contrast to the radial-azimuthal simulations. Instead, we have

$$u_{e,\theta} = u_{E\times B} + u_{\mathrm{Dia}}$$

everywhere in the simulation domain. We see that u_{Dia} is of the same order of magnitude as $u_{E\times B}$, but of opposite sign downstream. Figure 7.14 shows the values of $u_{e,\theta}, u_{E\times B}$, and u_{Dia} for the three cases. We can see that the magnitude of $u_{e,\theta}$ decreases when the radial losses are present. However, both the amplitude of u_{Dia} and $u_{E\times B}$ decreases.

Despite seeing previously in Section 7.2 that the radial losses do not modify significantly the axial electric field and the electron density, the electron azimuthal drift velocity does decrease with the radial losses. At the maximum, the difference represents a 20% variation, but on average the difference is below 10%. Therefore, the hypothesis of decreased growth rate to explain the reduction of the amplitude of the wave seems reasonable.

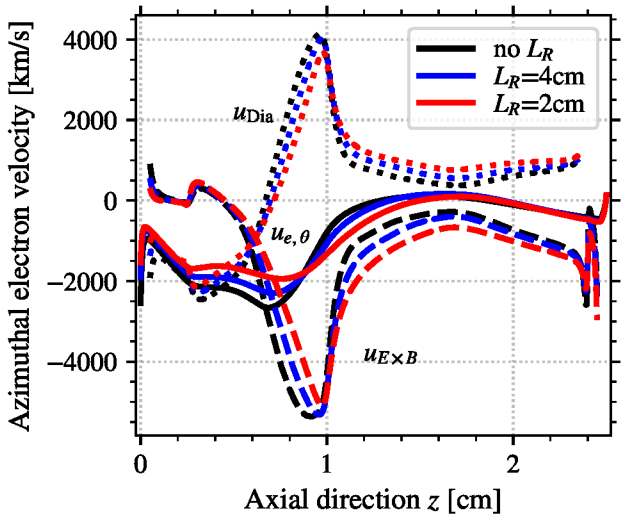

FIGURE 7.14 – Axial profile of the electron azimuthal velocity, the $\mathbf{E} \times \mathbf{B}$ drift velocity and the diamagnetic velocity averaged azimuthally and between $t = 6\,\mu s$ and $t = 10\,\mu s$ for the three different radial models. The sheaths (close to the axial boundaries) are removed for clarity.

7.3.4 Characteristics of the radial losses

The last hypothesis on the reduction of the wave amplitude is the direct impact of the radial losses. We recall that the electron flux equals the ion flux at each time step:

$$\Gamma_{R,e} = \Gamma_{R,i}. \tag{7.6}$$

The ion flux to the wall is a thermal flux

$$\Gamma_{R,i} \propto \bar{v}_{i,r}$$

with $\bar{v}_{i,r}$ proportional to the radial thermal velocity. However, we have seen that the radial temperature of the particles is constant. Assuming the ions distributed uniformly along the radial direction, the particle flux to the wall is proportional to the particle density

$$\Gamma_R \propto n_i. \tag{7.7}$$

Hence, the particle losses presents the azimuthal fluctuation of the wave

$$\Gamma_R(\theta) = \Gamma_0 + \delta\Gamma_R(\theta) \propto (n_{i,0} + \delta_{n_i})\bar{v}_{i,r},$$

with Γ_0 the mean particle loss, and $\delta\Gamma_R(\theta)$ the fluctuation of the losses due to the wave. Figure 7.15 shows the azimuthal-axial distribution of (left) the radial flux measured in the PIC simulation, and (right) the electron density, at $t = 10\,\mu s$ for the case $L_R = 2\,cm$. We assume the quasi-neutrality, hence $n_i = n_e$.

We see in Fig. 7.15 that the radial flux presents the same spatial characteristics as those of the electron density, as expected from Eq. (7.7). This means that the loss of particle is greater at the maxima of the density oscillations. Under this condition, the amplitude of the oscillation will be directly reduced as

$$\left.\frac{\partial \delta n_e}{\partial t}\right|_{\Gamma_R} = \gamma_R \delta n_e$$

with $\gamma_R < 0$ the damping rate of the instability due to the radial losses, which depends on the ion radial velocity $\bar{v}_{i,r}$. To summarize, we have shown that this direct impact of the radial losses on

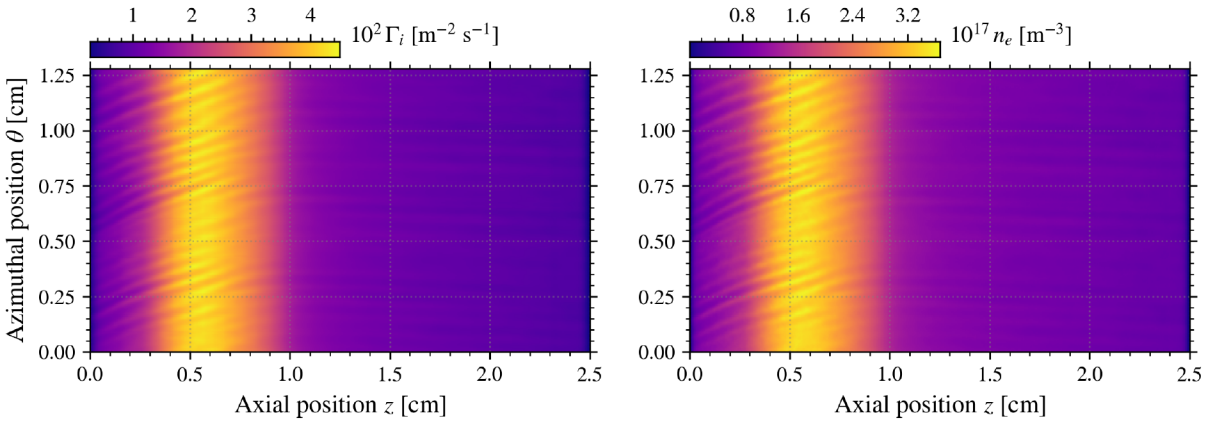

FIGURE 7.15 – Axial-azimuthal distribution of the (left) ion flux at the wall and (right) the electron density, for the case $L_R = 2\,\text{cm}$ at $t = 10\,\mu\text{s}$.

the amplitude of the density fluctuation could result in a reduction of the instability amplitude, hence the wave energy W.

The presence of a damping rate γ_R, combined with the reduction of the azimuthal drift velocity $u_{e,\theta}$ that is proportional to the instability growth rate, can explain the reduction of the wave amplitude at the steady-state. Indeed, the wave equation that takes into account the growth rate and the wave convection is [145]

$$\frac{\partial W}{\partial t} + \nabla \cdot (\mathbf{u}_i W) = 2\gamma_{\text{eff}} W \tag{7.8}$$

with γ_{eff} the effective growth rate, and $\mathbf{u}_i = u_{i,z}\mathbf{e}_z$ the ion mean velocity. As the radial losses do not affect significantly the axial electric field, $\mathbf{u}_i$ is the same for the three cases. Consequently, at steady state we have $\frac{\partial W}{\partial t} = 0$, so that if γ_{eff} is reduced because of γ_R, the wave energy W is reduced as well.

7.4 Spectral analyses of the waves

To better grasp the evolution of the instability with the radial losses, we proceed to a quantitative analysis of the instability by Fourier Transform. The spectral analyses are performed at $z_u = 0.55\,\text{cm}$ for the upstream region, and $z_d = 1.5\,\text{cm}$ for the downstream region. To give a better understanding of the wave observed, Figure 7.16 shows the temporal evolution of the azimuthal electric field E_θ at the positions z_u and z_d when no radial losses are modeled (no L_R).

In the upstream region, we see a monochromatic wave with a modulation of its amplitude. The downstream region is more complex, as there seems to be a combination of waves. We perform a 2D Fast Fourier Transform (FFT) on the spatio-temporal azimuthal electric field to obtain the dispersion relation of the wave observed. Figure 7.17 shows the 2D FFT obtained in (**a**) the upstream region and (**b**) the downstream region. We also display the 1 dimension (1D) FFT obtained by summing the 2D FFT in one direction. Concerning the upstream region, we see that the waves follow one well-defined curve, which corresponds to the Ion Acoustic Wave (IAW) Dispersion Relation (DR) Eq. (3.16) using the local Debye length and ion plasma frequency. The maximum of the wave is located at $k_\theta = 8.5\,\text{rad/mm}$ and $\omega = 35\,\text{rad.MHz}$.

The 2D FFT in the downstream region is presented in Fig. 7.17.**b**. In contrast to the upstream region, we can see that the waves do not follow one well-defined curve. The wave characteristics of the upstream region can still be seen, but a larger and slower wave is overlaid to it. The maximum of the wave is located at $k_\theta = 3\,\text{rad/mm}$ and $\omega = 20\,\text{rad.MHz}$. However, this new

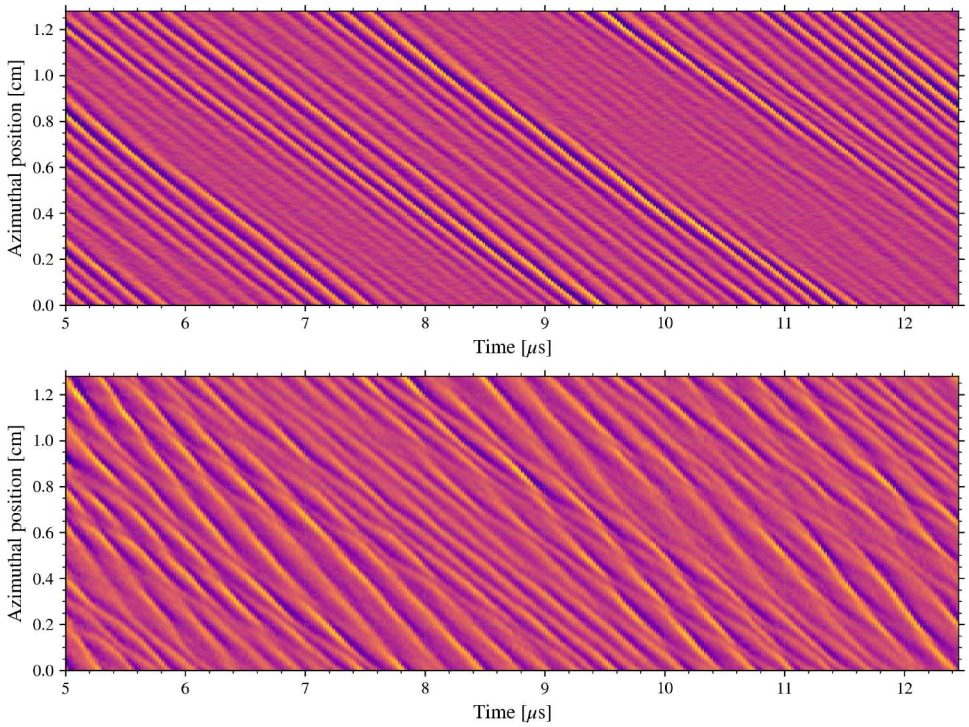

FIGURE 7.16 – Spatio-temporal evolution of the azimuthal electric field at (top) $z = z_u$ and (bottom) $z = z_d$ when no radial losses are modeled (no L_R). The beginning of the simulation ($t < 5\,\mu s$) is not shown.

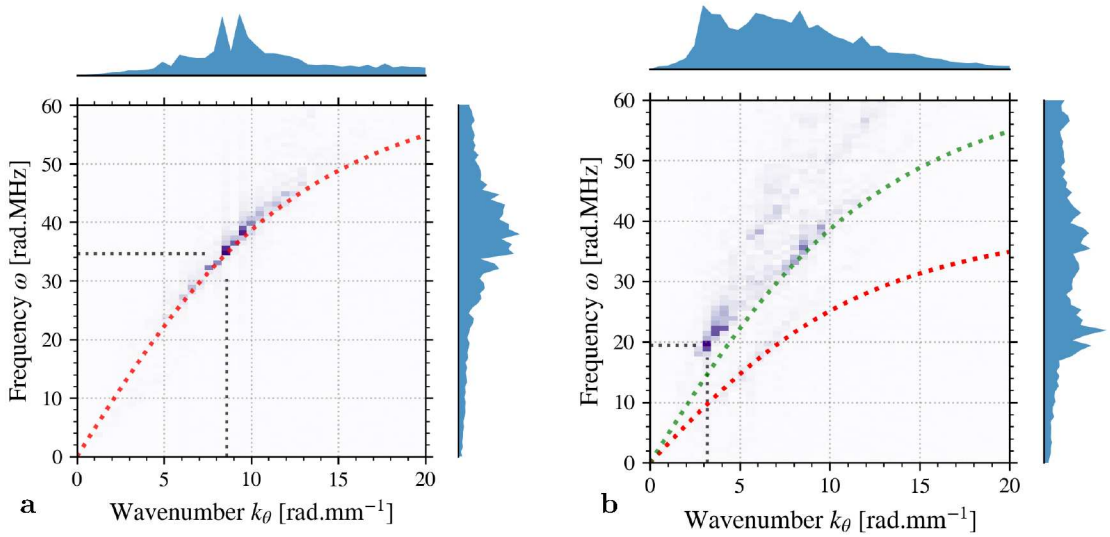

FIGURE 7.17 – 2D and 1D FFT of the azimuthal electric field in (**a**) the upstream region $z = z_u$, and (**b**) the downstream region at $z = z_d$, without radial losses. The black dotted lines highlight the position of the maximum of the 2D FFT. The red dotted line corresponds the IAW dispersion relation of Eq. (3.16) at $z = z_u$, and the green dotted line the IAW dispersion relation of Eq. (3.16) at $z = z_d$.

wave seems to follow the same dispersion relation as in the upstream region (green), instead of the DR using the local plasma parameters (red). This could mean that the wave originates in the upstream region, and is convected to the downstream region without changing the wave DR.

7.4.1 Impact of the radial losses on the FFT

Figures 7.18 and 7.19 show the 2D FFT obtained with the radial losses (for L_R=2 and 4 cm) in the upstream and downstream regions, respectively. In the upstream region, seen in Fig. 7.18, the results are similar to the case without radial losses, as if the radial losses do not modify the nature of the wave. This supports the qualitative analysis of Section 7.3.1 that concluded that the algorithm used does not induce any numerical noise that could create artificial instabilities.

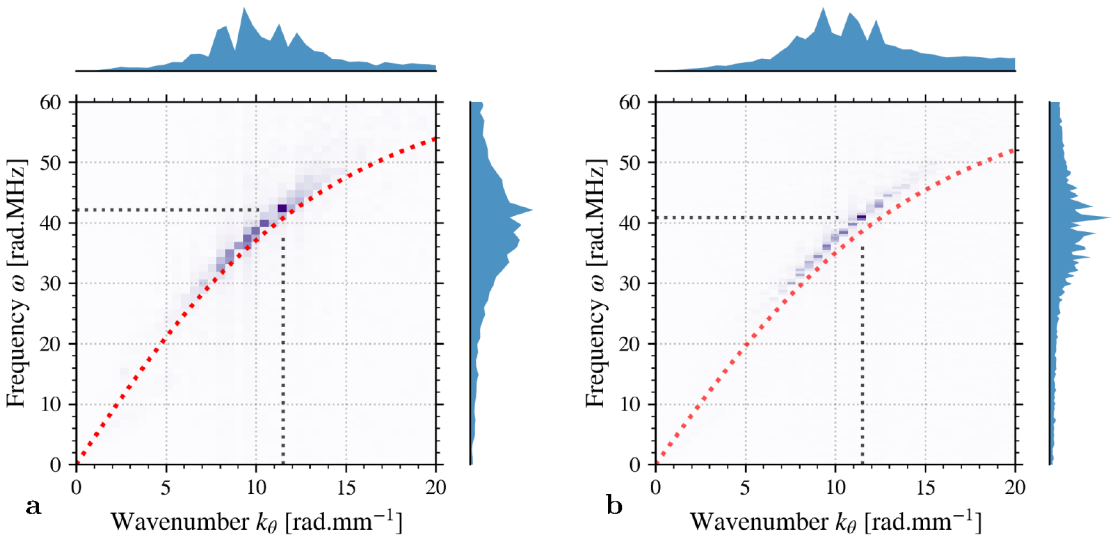

FIGURE 7.18 – 2D and 1D FFT of the azimuthal electric field in the upstream region $z = z_u$ with (**a**) $L_R = 4$ cm, and (**b**) $L_R = 2$ cm. The black dotted lines highlight the position of the maximum of the 2D FFT. The red dotted line corresponds the IAW dispersion relation of Eq. (3.16) at $z = z_u$.

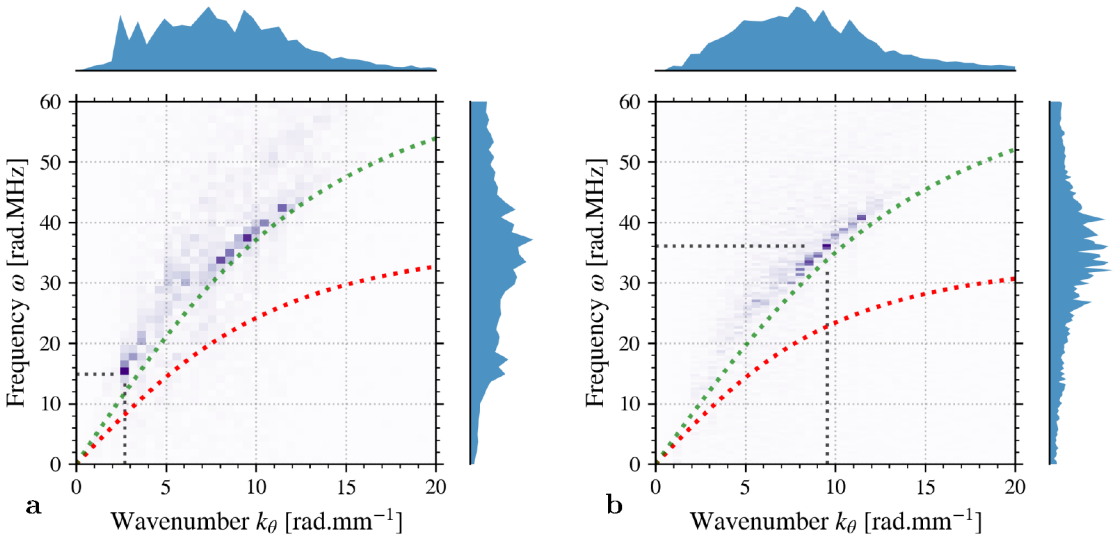

FIGURE 7.19 – 2D and 1D FFT of the azimuthal electric field in the downstream region $z = z_d$ with (**a**) $L_R = 4$ cm, and (**b**) $L_R = 2$ cm. The black dotted lines highlight the position of the maximum of the 2D FFT. The red dotted line corresponds the IAW dispersion relation of Eq. (3.16) at $z = z_u$, and the green dotted line the IAW dispersion relation of Eq. (3.16) at $z = z_d$.

However, in the downstream region, shown in Fig. 7.19, we do observe a difference due to the radial losses. For $L_R = 4$ cm, the low frequency-large wavelength wave already observed in

the case without losses is present. Moreover, the waves remain slightly scattered in regard to the theoretical IAW DR. However, these two observations are less visible than without the radial losses.

On the other hand, for $L_R = 2\,\text{cm}$, both the low frequency wave and the scattering of the wave disappear. Only the waves observed in the upstream region remains. The evolution of the waves can also be seen in Figure 7.20, where the 1D spectra obtained in the downstream region for the three cases are overlaid. To compare the three cases, the wavenumber and the frequency are normalized by the Debye length λ_{De} and the ion plasma frequency ω_{pi}, respectively. Since we saw in Figs. 7.17 and 7.19 that the wave dispersion relation is better characterized by the upstream region, we use the values of λ_{De} and ω_{pi} measured at $z = z_u$.

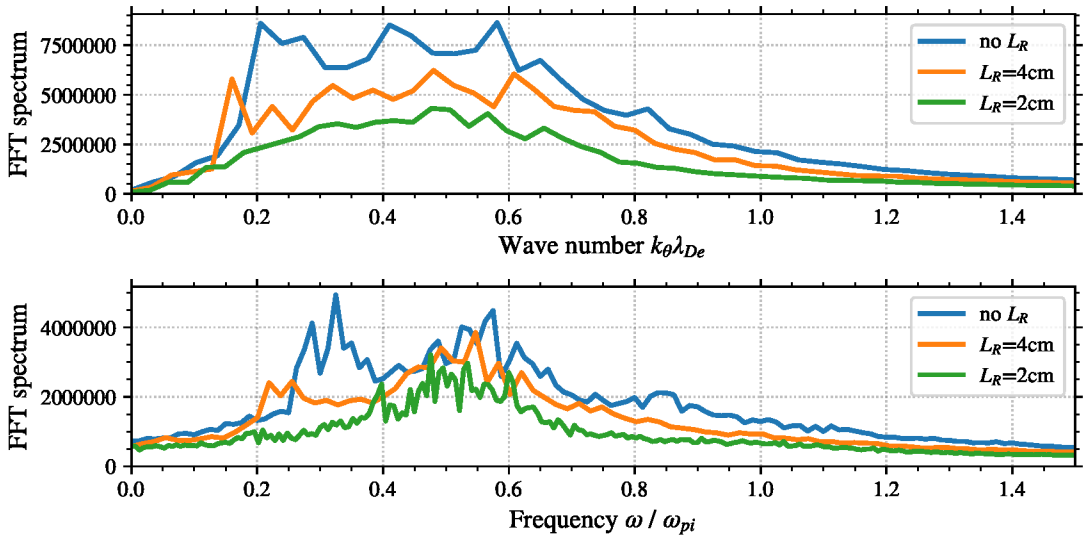

FIGURE 7.20 – Comparison of the frequency spectrum of the three axial-azimuthal simulations in the downstream region at $z = z_d$. On top, the spatial frequency spectra normalized by the Debye length λ_{De}; bellow, the temporal frequency spectra normalized by the ion plasma frequency ω_{pi}. The values of λ_{De} and ω_{pi} used are obtained in the upstream region at $z = z_u$, as the waves are better characterized by the upstream region.

On the wavenumber spectrum, we see that the amplitudes of the waves are reduced by the radial losses, as previously observed in Fig. 7.10. We can also confirm that the difference on wavelength between the three cases comes from the evolution of the Debye length, as the three spectra are approximately centered around the same wavenumber.

On the other hand, the temporal frequency spectra clearly show two maxima. The first one can be seen around $\omega = 0.5\omega_{pi}$ for the three cases. The second is observed at lower frequencies: for the case without losses, it is clearly seen at $\omega \simeq 0.3\omega_{pi}$; for the case $L_R = 4\,\text{cm}$, the second maximum is closer to $\omega \simeq 0.25\omega_{pi}$; for the third case $L_R = 2\,\text{cm}$, the second maximum disappears.

7.4.2 Axial evolution of the frequency spectra

To end the analysis of the instability characteristics, we present in Fig. 7.21 the axial evolution of the 1D FFT for the two extreme cases: without radial losses and with $L_R = 2\,\text{cm}$. We can see in Fig. 7.21 that in the case without radial losses, the low frequency oscillation appears abruptly, close to $z = 0.75\,\text{cm}$ which corresponds to the maximum of the magnetic field. Conversely, it does not show up for $L_R = 2\,\text{cm}$ in the frequency spectra.

The low frequency oscillations seems to originate from a non-linear phenomenon, such as an inverse cascade [44]. We have seen in Section 7.3 that the effective growth rate is reduced by the radial losses, due to the reduction of $u_{e,\theta}$ and the presence of γ_R. However, the convection of the wave by the ions is not affected by the radial losses [145]. Consequently, we believe that due

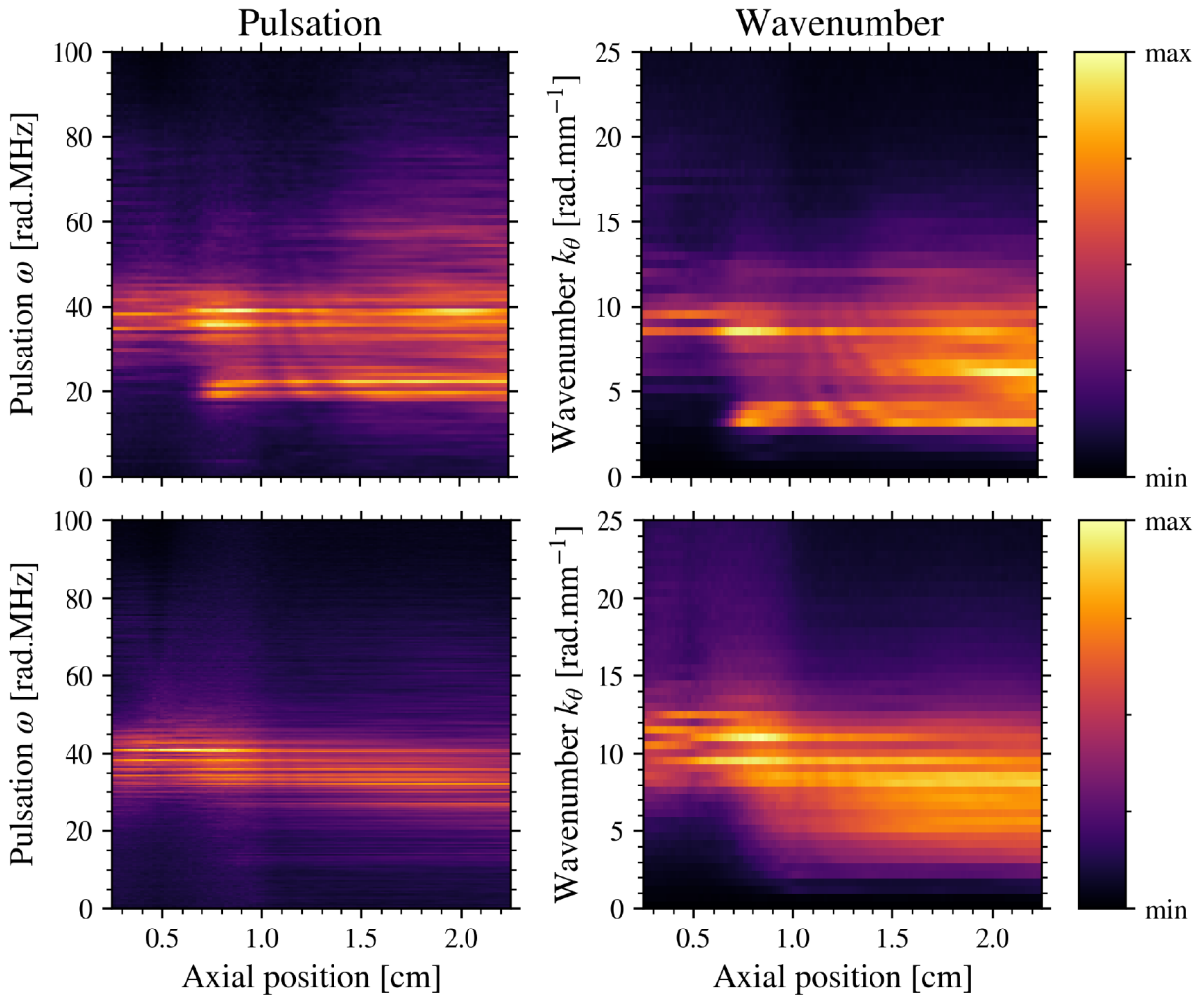

FIGURE 7.21 – Axial evolution of the 1D FT on (left) the frequency and (right) the wavenumber for (top) no radial losses, and (bottom) $L_r = 2\,\text{cm}$.

to the radial losses, the wave amplitude is smaller, and therefore does not reach the non-linear regime responsible of the low frequency and large wavelength waves.

7.5 Conclusion on the 2D PIC axial-azimuthal simulations

In this chapter, we have investigated the impact of the radial direction in a 2D PIC simulation of the axial-azimuthal domain. We proposed an algorithm in order to introduce in a 2D ($\mathbf{Z} - \theta$) simulation the effects of the radial direction. More precisely, we modeled the losses of particles, corresponding to fully absorbing walls without secondary electron emission. The model imposes a pseudo-local flux neutrality at the wall, reproducing the effect of a floating sheath. To test this model, we considered the simulation conditions of the pure 2D axial-azimuthal case proposed by Boeuf and Garrigues [8]. It uses a forced ionization source term, which allows to obtain a steady state of the discharge.

The model of radial losses has successfully shown its ability to reduce the plasma density and electron temperature. We were able to obtain a steady-state for three cases: one without radial losses (no L_R), and two with losses using a radial length of $L_R = 4\,\text{cm}$ or $L_R = 2\,\text{cm}$. We observed that the radial losses reduce the electron density slightly and that the axial electric field is almost unaffected. On the other hand, the electron temperature is significantly reduced and not only in the radial direction but in the three directions. The reduction of the electron temperature is correlated with a substantial decrease of the electron axial mobility.

Since the simulations are collisionless, the electron mobility comes from the azimuthal instability. We observed that the amplitude of the instability, thus the induced electron axial mobility, is reduced by the radial losses. Several hypotheses that could explain the decrease of the wave amplitude have been discussed. The most probable reasons are the decrease of the electron azimuthal drift, hence the reduction of the growth rate, and the fact that the radial losses absorb the particles preferentially at the maxima of the oscillations.

When radial losses are considered, the reduced wave amplitude is related to a decrease of the ion-wave trapping, which seems to be one of the dominant mechanisms of saturation when the radial losses are not modeled. In addition, the characteristics of the wave (frequency, wavelength) are modified. More precisely, in the upstream region, close to the maximum of the magnetic field, the waves are not affected. On the other hand, in the downstream region, a low-frequency and large wavelength oscillation is present when no radial losses are modeled (no L_R). The amplitude of this large wave is reduced for $L_R = 4\,\text{cm}$, and disappears for $L_R = 2\,\text{cm}$. We believe that this large wavelength oscillation comes from a nonlinear inverse cascade mechanism, most certainly related to the ion-wave trapping. As the wave amplitude is smaller, the nonlinear stage of the wave is not reached when the radial losses are modeled.

Lastly, we observed that the electrons are less isotropic than seen in the radial-azimuthal simulation. However, the plasma-wall interaction is governed by the radial temperature. Hence, a better understanding of the energy transfer between the different directions is important. To open the discussion on future work, we present in the following section some additional results we obtained on the radial heating observed in both the axial-azimuthal and the radial-azimuthal simulations.

7.5.1 Study of the radial electron heating

We have seen in Figs. 7.5 and 7.7 that the radial electron temperature is constant in both time and space, leading to a large anisotropy. This could be due to the lack of collisions in the 2D ($\mathbf{Z} - \theta$) case proposed by Boeuf. Thus, we investigate thereafter the impact of the neutrals on the electron anisotropy by modeling the collisions with the Monte Carlo Collision (MCC) algorithm.

2D axial-azimuthal simulation with collisions

To model the neutral density in the reference test-case of Section 7.2, we inject at the anode a constant xenon flow of rate $\dot{m} = 5\text{mg/s}$ at a temperature of $T_g = 640\,\text{K}$. Using a typical surface area, this corresponds to a neutral density at the anode of $n_g = 1.0 \times 10^{19}\ \text{m}^{-3}$ and a mean velocity of $u_g = 200\,\text{m/s}$. The evolution of the neutral density is modeled using the system of 1D fluid equations, and considers azimuthal uniformity:

$$\begin{cases} \partial_t n_g + \partial_z(n_g u_g) = -S_{iz} \\ \partial_t(n_g u_g) + \partial_z(n_g u_g^2) = -\partial_z p_g - S_{iz} u_g \\ \partial_t E + \partial_z(E u_g) = -\partial_z(p_g u_g) \end{cases} \tag{7.9}$$

with u_g, p_g the neutral axial velocity and the pressure, respectively, S_{iz} is the imposed ionization source term, and E the total energy per volume unit

$$E = \frac{p_g}{\gamma - 1} + \frac{1}{2} n_g u_g^2, \tag{7.10}$$

with $\gamma = 5/3$. This Euler system is solved using the HLLC Riemann solver, which has been validated on the shock tube test case [146]. The neutral temperature is kept constant by adding an artificial source term in the third equation of Eq. (7.9)

$$S_3 = -\frac{1}{\tau}\left(\frac{p_g}{\gamma - 1} - \frac{n_g R T_0}{\gamma - 1}\right) \tag{7.11}$$

with T_0 the desired temperature, and τ the relaxation time to reach T_0. We chose τ small enough so that T_n does not vary much, while preserving the Courant-Friedrich-Levy condition. In practice, we use $\tau = 10\,\text{ps}$. Finally, the neutral density is used in the MCC algorithm to model the electron-neutral and ion-neutral scattering and momentum transfer, but the creation of particles remains imposed by the same ionization profile S_{iz} as in Section 7.2. Figure 7.22 shows the neutral density and velocity obtained at steady-state.

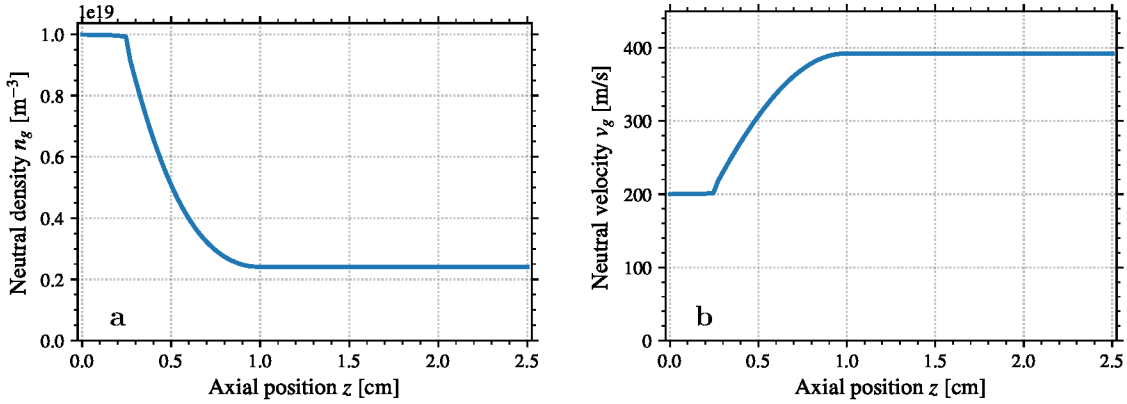

FIGURE 7.22 – Axial profile at steady-state ($t = 10\,\mu\text{s}$) of (**a**) the neutral density and (**b**) the neutral axial velocity, for the simulation test-case with the electron-neutral scattering.

We see in Fig. 7.22 that the neutral density is depleted between the anode and the cathode because of the ionization. The neutral density gradient and the ionization accelerates the neutrals in the axial direction by a factor of two, which reduces even more the neutral density. Thus, the impact of the neutral collisions will be more significant close to the anode.

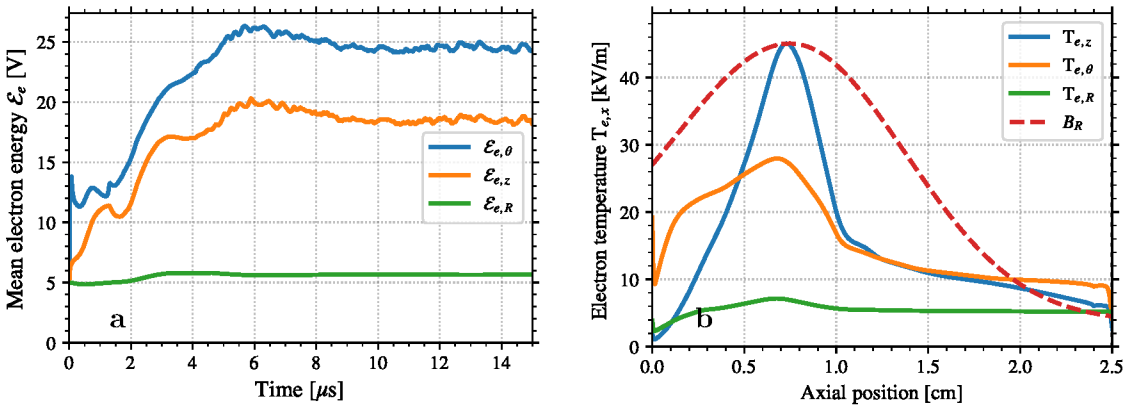

FIGURE 7.23 – (**a**) temporal evolution of the electron kinetic energy in the three directions and (**b**) axial profile of the electron temperature at steady state obtained for the simulation with the electron-neutral scattering.

Figure 7.23 shows the temporal evolution of the mean electron kinetic energy decomposed in the three directions on the left, and on the right it shows the axial profile of the electron temperatures, also decomposed in the three directions. [1] We see that there is a small transfer of energy between the radial direction and the other directions. In particular, close to the anode where the gas density is high, the radial and axial temperatures decrease below the initial temperature $\text{T}_{\text{e},inj} = 5\,\text{V}$. In contrast, at the maximum of the magnetic field where the axial and azimuthal electron temperatures are the highest, the radial electron temperature increases to $\text{T}_{\text{e}R} = 7\,\text{V}$. However, the anisotropy stays significant, compared to the observation of the

1. The kinetic energy is the sum of the temperature and the kinetic energy of the drift velocity

radial-azimuthal simulations presented in Chapter 4. Therefore, the neutral density is not the main reason for the electron heating.

Radial Joule electron heating in the radial-azimuthal simulation

The large anisotropy observed in Figures 7.5 and 7.23, compared to the results of Chapters 3 and 4 does not come from the electron-neutral scattering. Thus in this section, we investigate the electron energy gain due to Joule heating in the radial-azimuthal simulation described previously in Chapter 3. The Joule heating is

$$\mathbf{P}_{\mathrm{J}} = \mathbf{J}_e \cdot \mathbf{E}, \tag{7.12}$$

with $\mathbf{J}_e$ the electron density current and $\mathbf{E}$ the electric field. Figure 7.24 shows the radial profiles of the electron (and ion) current density $< J_{e,R} >$ and the radial electric field $< E_R >$, averaged in the azimuthal direction. We observe that the ion and electron current densities are equal, and they increase linearly with the radial position, in agreement with the use of a uniform artificial injection of particles (see Section 2.3 for more details).

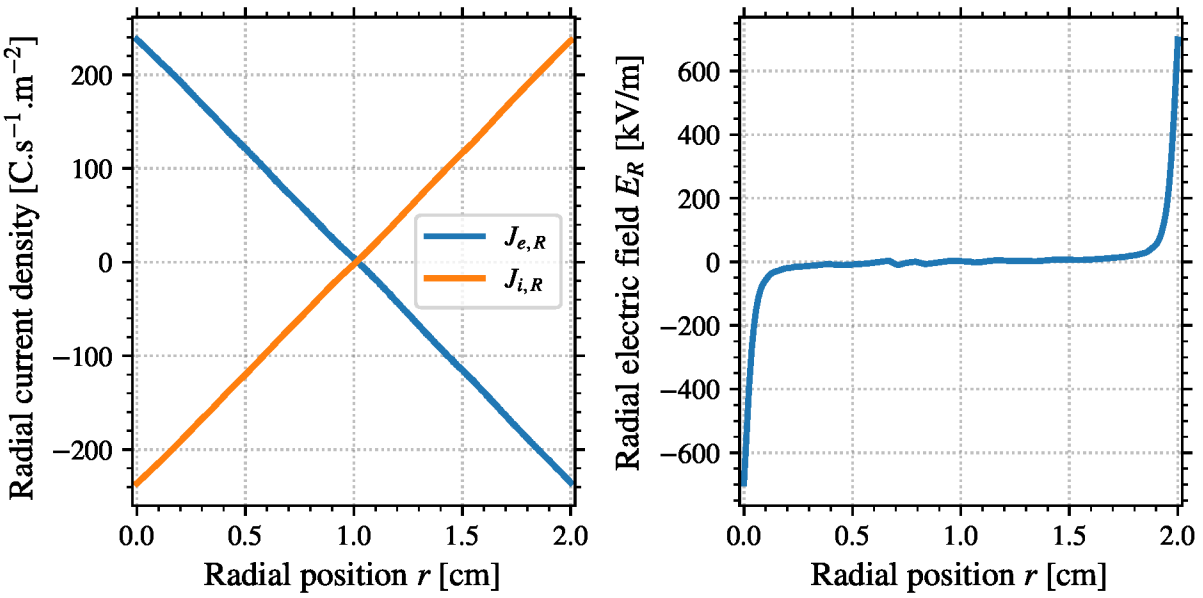

FIGURE 7.24 – Radial profiles averaged in the azimuthal direction of (left) the electron and ion current densities and (right) radial electric field in the radial-azimuthal PIC simulation presented in Chapter 4.

The radial electric field E_r shown in Fig. 7.24 is very small in the center of the system, and increases drastically in the sheath close to the walls. Consequently, from the product $< J_{e,R} >< E_R >$ we could expect the radial Joule electron heating to be small in the center of the discharge, and negative in the sheath. Figure 7.25 shows the mean Joule heating in the radial direction $P_{\mathrm{J,R}} =< J_{e,R} E_R >$ measured in the PIC radial-azimuthal simulation, and the product of the mean quantities $< J_{e,R} >< E_R >$.

We see in Figure 7.25 that, unexpectedly, the mean Joule heating $P_{\mathrm{J,R}}$ is not zero in the center of the simulation. This means that there is an energy transfer to the radial direction of the electrons due to the correlation between the fluctuations of $\mathbf{J}_e$ and $\mathbf{E}$. Consequently, for this energy transfer to be self-consistently observed in a simulation, the radial direction needs to be resolved.

A similar radial heating has been observed by Héron and Adam [38]. The authors observed no heating when the instability was only perpendicular to the magnetic field, as it is in a 1D or a 2D axial-azimuthal simulation. However, when the direction parallel to the magnetic field is resolved, the electrons are heated. However, the physical mechanism remains unclear. In Janhunen et al.

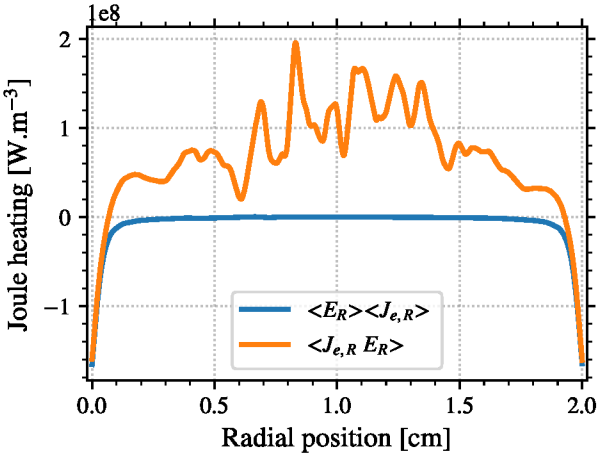

FIGURE 7.25 – Electron radial power gain averaged in the azimuthal direction in the 2D radial-azimuthal PIC simulation (conditions of Chapter 4).

[147], the authors observe a similar radial heating of the electrons, but due to the presence of a Modified Two Stream Instability (MTSI). As discussed in the previous chapters, we have not observed the MTSI in our simulations, meaning that it has to be due to another mechanism.

To conclude on this last Section 7.5.1, we observed that in the axial-azimuthal simulation the radial electron energy is too low compared to the radial-azimuthal results, even in the presence of electron-neutral scattering. We noted that in the radial-azimuthal simulation, where the radial electric field is self-consistently computed, the mean radial electron Joule heating is significant in the plasma bulk. This radial heating seems to be due to the instability, that presents radial structures. Consequently, this joule heating is absent of the 2D axial-azimuthal simulations. Therefore, a better understanding of the radial heating of the electrons is necessary, so that low-dimensional fluid and PIC simulations can realistically model the plasma-wall interactions. The electron distribution function measured in experiments or observed in a 3 dimensions (3D) PIC simulation would be beneficial to give to the community insights on the coupling and the relative importance of the radial, axial and azimuthal directions.

Chapter 8

Conclusion

8.1 Summary of the thesis

The Hall Effect Thruster (HET) is governed by two phenomena that are ill understood: the electron cross-field mobility – due to the azimuthal Electron Cyclotron Drift Instability (ECDI) and the electron collisions – and the wall interaction that is affected by the Secondary Electron Emission. The use of modeling for the future design of the HET requires a better understanding of both phenomena. As they are of kinetic nature, we used a Particle-In-Cell (PIC) simulation model, *LPPic* , that is presented in Chapter 2. Since full 3D realistic PIC simulations are still out of reach due to the excessive computational load, we used in this work bi-dimensional simulation domains to study both the radial-azimuthal and the axial-azimuthal planes of the HET.

8.1.1 Growth and saturation of the azimuthal instability

The radial-azimuthal simulation domain has first been used in Chapter 3 to provide more insights on the ECDI, and its interaction with the wall. The instability presents two phases: the first corresponds to the linear growth of the instability ; the second phase corresponds to the quasi-steady phase, during which the amplitude of the instability saturates.

We implemented a solver for the general Dispersion Relation (DR), that uses the Electron Velocity Distribution Function (EVDF) and the Ion Velocity Distribution Function (IVDF) measured in the PIC simulations to compute the growth rate and the frequency for a given wavevector. We observed a good agreement between the characteristics (wavenumber and frequency) observed in the PIC simulation and the theoretical DR of the ECDI. During the linear phase, the wave presents the cyclotron resonances, characteristic of the ECDI. Conversely, during the saturated phase the resonances broaden, and the ECDI DR can be approximated by the Ion Accoustic Wave (IAW).

We showed that the modulation of the wave amplitude during the saturated phase is certainly due to the ions, as the main saturation mechanism of the instability is the ion-wave trapping. However, due to the large xenon ion mass, the ion-wave trapping takes some time before being effective, resulting in the oscillation observed.

This hypothesis is strengthened by the resolution of the dispersion relation, when the ion temperature is taken into account. Indeed, we observe the same temporal oscillation of the maximum of the growth rate. However, the results of the General DR solver, using the IVDF, yields a growth rate that oscillates less than observed on the amplitude of the wave.

Lastly, we observed that in our simulation the instability does not present any radial modulation. Conversely, the ratio between the ion density fluctuation δn_i and the mean value n_i is constant along the radial direction. This corresponds to a wavevector strictly perpendicular to the magnetic field, in disagreement with the expected impact of the wall. Instead, it seems that the walls are totally screened from the instability.

8.1.2 Impact of the wall characteristics on the plasma-wall interaction

Using the 2D PIC simulation code in the radial-azimuthal domain, we presented in Chapter 4 a parametric study over the characteristics of the dielectric walls. We uncoupled and studied separately the two main aspects of the dielectric wall: the physical insulating layer between the plasma and the grounded electrode ; and the electron induced Secondary Electron Emission (SEE).

The dielectric layer has been modeled by solving the Poisson equation inside the layer, between the plasma and the grounded electrodes. The impact of the insulating layer alone has been observed to have only a small impact on the discharge. The azimuthal instability in the electric field is observed to be larger at the vicinity of the wall with the dielectric modeled, compared to the case with only the grounded wall. However, this difference disappears quickly after one Debye length. In addition, no impact of the dielectric is observed on the fluctuation of the ion density. Lastly, its impact on the electron mobility is not significant.

The impact of the SEE has been studied with a parametric study over the emissivity of the wall. We covered a large ensemble of parameters, from low emissive material (such as Graphite) to very high emissive material (as Alumina Al_2O_3). We observed that the increase of SEE is associated with a decrease of the mean electron temperature, which in turn decreases the amplitude of the instability, and the axial electron mobility. However, the SEE induces a so-called near-wall mobility, which compensates the total electron mobility.

Three regimes of emission have been observed depending on the wall emissivity. For a low emissivity, the sheath follows the usual positive sheath behavior. With a high emissivity, the sheath enters a Space-Charge Limited (SCL) regime, during which a potential well appears close to the wall. The potential well reflects the secondary electrons emitted back towards the wall, so that the effective total emission rate is strictly bellow one. The transition between the two regimes passes through a third unstable regime, during which the sheath oscillates between the two stable regimes. The nature of this so-called Relaxation Sheath Oscillation (RSO), and issues related to the value of the SEE rate are discussed in the next section.

Lastly, we combined both aspects of the dielectric wall together. We chose to use the SEE parameters that led to the oscillating regime when using only the grounded wall. These parameters are close to the one measured for the Boron-Nitride (BN) ceramic. The overall electron mobility and the plasma parameters were not significantly affected by the dielectric layer, compared to the case with only the grounded wall. However, we observed that the RSO was no more synchronous over the two walls, but instead it presented differences between the two opposing walls and along the azimuthal direction of the same wall. This could explain why such oscillations have not yet been observed experimentally, since the experimental measurement average this localized behavior.

8.1.3 Non-isothermal sheath model

We have observed with the parametric study that the rate of emission measured in the simulation is overestimated by the usual sheath models. Moreover, the sheath characteristics, like the potential drop, also differs from the theory. It appears that the discrepancy is due to the isothermal hypothesis used so far in the sheath models. Indeed, the PIC simulation presents a decreases of the electron temperature from the center of the channel to the wall.

This decrease of temperature is not due to the SEE, as the same results have been observed with a simplified 1D argon discharge without SEE, that is presented in Chapter 5. Instead, it comes from the absorption at the wall of the high energy tail of the electrons distribution function. As the gas pressure is low, the tail of the EVDF cannot be replenished by collisions fast enough compared to the losses at the wall. Hence, the EVDF follows a 2-temperature profile, which presents an evolution through a potential drop of the density and temperature similar to the polytropic state law. We observed with a parametric study that the polytropic index for the electron evolution through the sheath depends on the neutral pressure.

We have developed a stationary fluid model with polytropic electrons for the same conditions as the simplified 1D PIC simulation. Given the polytropic index measured in the PIC simulations, the fluid model gives results very close to those of the PIC simulations when the ionization source term is imposed (no heating), and a acceptable agreement with a self-consistent ionization and a Inductively Coupled Radio-Frequency (ICP RF) heating.

The sheath model with polytropic electrons has been extended to the case with Secondary Electron Emission (SEE) in Chapter 6. We observed in the PIC simulations that the polytropic state law could be used even in the presence of large rate of secondary electron emission. In addition, the polytropic index γ does not evolve significantly with the emissivity of the wall, so that we used a constant value $\gamma = 1.36$ over the range of parameters studied. Due to the reduction of the electron temperature at the wall with the polytropic state law, the modified sheath model allowed us to obtain the SEE rate and the plasma potential drop at the wall with a good agreement with the PIC simulation results.

Interestingly, the sheath model with polytropic electrons and SEE presents over a domain of electron temperature three coexisting solutions: one with a low emissivity, another corresponding to the Space Charge Limited (SCL) sheath, and a third in between. These three solutions induce an hysteresis evolution of the sheath with the electron temperature. Indeed, starting from a low electron temperature and rising, the sheath remains in the usual sheath regime until a maximum electron temperature value, at which it switches abruptly to the SCL regime. Reciprocally, starting from the SCL regime and decreasing the electron temperature, the sheath remains over a large domain of temperature in the SCL regime until the a minimum electron temperature value. This evolution is also observed in the PIC simulations, during the intermediate regime which presents quasi-periodic oscillations between the two regimes.

8.1.4 Modeling the radial dimension in a 2D axial-azimuthal PIC simulation

Lastly, we studied in Chapter 7 the axial-azimuthal simulation domain in order to challenge the conclusion obtained in the radial-azimuthal simulation domain. Indeed, the radial-azimuthal domain does not include the ionization region, nor the convection of the wave. We also proposed a model to include the impact of the wall in the radial direction in the 2D axial-azimuthal simulation.

We have chosen to present in this manuscript an axial-azimuthal simulation which follows the model of Boeuf and Garrigues [8] with an imposed constant ionization, so that the breathing mode is not present. We observed that under this condition, the electron drift was reduced by the diamagnetic drift as strong electron density and temperature gradients are present, in contrast to the radial-azimuthal simulation. The azimuthal instability also rises in this condition, but the wave convection becomes a significant phenomenon for the wave amplitude saturation, and the ion-wave trapping is less developed.

The radial loss model proposed considers a simple fully absorbing surface with an infinitely fine sheath located at a certain length $L_R = 2$ or $4\,\mathrm{cm}$. The ions crossing the surface are removed from the simulation, and part of the electrons are reflected in order to obtain a neutral loss. The presheaths are not modeled. We observed as expected that the radial losses reduce the particle density and the electron temperature, and do not induce any detectable numerical artifact.

Including the radial particle losses in the simulation is shown to reduce the amplitude of the instability, hence the anomalous electron axial mobility. Several phenomena could explain the reduction of the wave amplitude, such as the reduction of the azimuthal electron drift, the decrease of the electron temperature, or the absorption of the particle at the maximum of the oscillation that reduces the wave amplitude. As the wave amplitude is smaller than without the radial boundary modeled, it seems to remain in the linear phase, with less ion wave trapping and no inverse cascade.

To conclude on my doctoral project, I have used highly resolved kinetic simulations to better understand the plasma-wall interaction and the electron axial transport, two phenomena governing the behavior of Hall thrusters. The electron transport is enhanced by instabilities, whose amplitude depends on the relative importance of the axial convection of the wave and the growth rate. We have seen that the growth rate during the saturated quasi-steady-state is highly affected by particle-wave interactions, and that the quasi-linear relation dispersion solved with the measured distribution functions only returned rough estimations of the instability characteristics in the radial-azimuthal simulations. To better model the plasma-wall interaction, we developed a polytropic sheath model that better include the non-local nature of the electrons at low pressure. This new model can be used not only to model HETs, even in the presence of secondary electron emission, but also for other low-pressure plasmas.

8.2 Perspectives

The work of this thesis was focused on the better understanding of the fundamental physical phenomena involved in the Hall Effect Thrusters. There are several perspectives on this work. The first one concerns physics and theoretical work, the second is related to the simulation and modeling, and the third concerns the experimental insights required to validate the simulations and the theories. These three aspects are intertwined, and should be used together over three main issues highlighted by the work conducted during my thesis, namely the interaction of the instability with the wall; the non-linear stage of the instability with a focus on the particle-wave interaction; and the reliability of the simulation of the HETs. To finish with, a discussion on the improvement of the HET modeling is proposed.

8.2.1 Interaction of the instability with the wall

We observed in the radial-azimuthal PIC simulation no radial mode of the wave, so it seems that the walls are screened from the azimuthal instability by the sheath. Similar, but non-identical, screening was observed in Janhunen et al. [65], where the authors observed a radial mode larger than the radial length. In contrast, Taccogna et al. [44] observed short scale radial oscillations in a similar geometry. A comparison of the 2D PIC simulations obtained by different international groups in the radial-azimuthal domain is currently being conducted, and a better understanding of the discrepancy between the different results should be achieved in a short period of time.

Experimental investigation of the radial modulation of the instability would also be useful to validate the simulation results. Electrostatic probes cannot resolve yet the scale of the instability [148], and they may affect the discharge. The measurement could however be achieved by collective light scattering [40] resolved in the radial direction, for instance by orienting the primary laser beams in the axial direction.

In addition, we observed that modeling the radial particle losses in the axial-azimuthal simulation reduced the wave amplitude. The origin of the decrease of the instability is unclear, as it could be due to a reduction of the growth rate (function of the azimuthal drift velocity and electron temperature that are affected by the wall), or to a direct damping of the instability due to the particle loss in phase with the wave amplitude. In the parametric study of the wall emissivity presented in Chapter 4, we also observed an impact of the wall on the amplitude of the wave. However, in the configuration studied, the wave amplitude was governed by the saturation due to ion-wave trapping, in contrast to the axial-azimuthal simulation for which the wave convection is dominant. The damping effect of the walls on the wave could be investigated with a radial-azimuthal PIC simulation, for instance by varying the radial length of the channel or the emissivity of the material, but only if the effect of convection modeled is larger than the ion-wave trapping, so that the wave amplitude would not be governed by it.

8.2.2 Particle-wave interaction during the non-linear saturated stage

We have observed that the azimuthal instability affects the ion and the electron distribution functions, that have a counter reaction on the instability by modifying the dispersion relation. It also seems that it is responsible for the isotropization and the radial heating of the electrons, that impacts the plasma-wall interaction. The non-linear stage of the instability is unclear, and could require an in-depth mathematical and theoretical investigation of the different phenomena observed in the simulation, such as the resonances broadening, particle-wave coupling, the turbulent and inverse cascade, and the saturation mechanisms.

The saturation of the ExB instability could be investigated by simulations with a simplified geometry. Indeed, the 2D axial-azimuthal simulation used in Chapter 7 presents multiple gradients that increases the complexity of the physics observed. However, it is expected that the results of a 1D purely azimuthal simulation would be affected by the presence of the other directions. A simplified simulation, for instance without gradient, would allow a simplified understanding of the physics observed, and enable more efficient parametric studies.

We observed that depending of the 2D geometry used (radial-azimuthal or the axial-azimuthal domains), different phenomena are present. We proposed during this thesis to include in both domains the effect of the missing direction (the axial convection and the radial boundaries, respectively). However, in order to validate the results, a proper 3D simulation of the ExB configuration bounded by walls is necessary, in order to determine how the two directions are coupled with the instability.

Lastly, more insights from experimental measurements are required to validate or not the results of the simulation and theoretical investigations. The measurements of the electron and ion velocity distribution functions in the azimuthal direction would be a significant contribution to the understanding of the particle-wave interaction present in the HETs. However, the geometry and the usual parameter range of the HET increases the complexity of such measurements. More interactions with experimental and numerical works on other ExB devices, such as Magnetrons, that present similar behaviors could be beneficial to the HET community.

8.2.3 Improving precision and reliability simulations of the HET

We have seen that the kinetic phenomena in the HET are important in the behavior of the discharge. We derived from the kinetic simulations a polytropic sheath model that allows us to include some of the kinetic effects in a fluid model that reproduce the PIC simulation results. This model could be used in HET fluid simulations to better model the plasma-wall interaction. The value of the polytropic index could be self-consistently obtained with a Monte Carlo algorithm coupled to the fluid simulation, or an uncertainty quantification study could be conducted on its value to quantify the required accuracy of this polytropic index to obtain a good agreement with PIC results in a given range of conditions typical of HETs.

In addition to the low dimensional fluid simulations, that allow to obtain quickly rough estimations, kinetic simulations have to be improved. First, the theory of the PIC simulation is sparse, and many guidelines followed by the community are based on past experiences and not on a theoretical background. The impact of dynamically adaptive time step and mesh refinement should be studied, and reliable merging and splitting algorithms should be developed.

On top of that, the validation and the verification of the simulation codes need to be improved. The international work on the axial-azimuthal benchmark [91] is a first step in the improvement of the reliability of PIC modeling of magnetized plasmas. However, the reference case of the Benchmark uses an imposed the ionization, instead of a self-consistently computed source term. Hence, the simplified geometry of the magnetized column of Lucken et al. [95] could be a choice of interest for the low pressure magnetized plasma community. In addition, as discussed previously a detailed comparison of the results obtained in the radial-azimuthal simulation domain is currently being conducted, and a similar effort is lead by the community for the purely 1D azimuthal PIC simulation.

8.2.4 Improving HET modeling, design and developments

As presented in the introduction of this thesis, the long term objective of this work is to improve the design of the future Hall effect thrusters. The "light" fluid models that are currently used in the development process use crude estimations of the plasma-wall interaction and the anomalous electron mobility. On the other hand, "heavy" kinetic simulation that can model accurately such phenomena are too costly to be used during the industrial development.

In this thesis, we proposed a new model for the plasma-wall interaction that can improve the accuracy of fluid models. The new model could reproduce accurately the PIC simulation results given the value of the polytropic index obtained from the PIC results. The value of the polytropic index could be estimated without the PIC simulation, by using a simple Monte Carlo simulation or experimentally by measuring the radial evolution of the electron density with the electron temperature or the plasma potential.

Conversely, the issue of the electron cross-field transport is less understood compared to the plasma-wall interaction. As a matter of fact, if there is a general agreement on its origin, the saturation mechanism remains difficult to evaluate. More insights from the simulations have been given is this thesis, but we also showed its complexity. Indeed, the general dispersion relation solver that uses the velocity distribution functions measured in the PIC simulation could not described accurately the observed instability, as particle-wave interactions and non-linear mechanisms are important during the saturated stage. Recently, a proposition to model the electron transport following a data-driven approach using a machine-learning model trained on experimental data has been presented [45]. Unfortunately, the current data set is sparse which limits the applicability of the model. More experimental measurements, as well as measurements of better accuracy are required in order to improve the modeling of HETs [149].

One reason for the lack of usable data is the wide variety of thrusters used in experiments, so that the measurement of one of them cannot be combined to that of another. In addition, most thrusters are confidential due to the close relation between research and industry, so that few of the required information to reproduce experiment are available. The Radio Frequency plasma community had a similar problem, that has been solved by proposing a Reference Cell at the Gaseous Electrical Conference in 1989[150]. Five years later, 66 experimental measurements and 17 numerical models of this unique Reference Cell have been published. A similar reference thruster should be used the improve the model accuracy, and allow a more efficient thruster design.

Another reason is the limited range of parameters achievable experimentally. Indeed, a thruster is designed to be used at a nominal power, mass flow rate and magnetic field topology, that depends on its geometry. Consequently, the numerical models are fitted over a small range of parameters, which reduces the versatility of such models. The PPS®X00 Laboratory Model, developed during my thesis, will allow us to investigate a wider range of geometry, wall material, and magnetic field topology. It will enable a better verification of the numerical models used, and pave the way to improve the design of future low-power thrusters. It could be interesting to have a similar Laboratory Model for the design of higher power thrusters.

Annexe A

Scalability tests

In this annexe, we give more information on the scalability tests conducted. We conducted both a weak and a strong scalability tests. We recall that the strong scalability keeps the load constant while increasing the computational performance, here the number of CPU. The weak scalability keeps the load to the number of CPU ratio constant. However, it does not correspond to the need we had, which is to find the optimal number of CPU for a given task. Beside, the results of the weak scalability were less clear to analyze. Hence, we discarded them.

The parameters of the strong scalability test used are given in Table A.1. They are close to the parameter used in production, presented in Table 4.1. The smaller test-case uses the same settings, except for the domain which is divided by a factor of 4. The dielectric boundary conditions are not modeled (no Secondary Electron Emission (SEE), no dielectric layer). The Inputs, set-up, and Outputs are not taken into account in the study of the performances. However, the usual diagnostics (mean density, fluxes, temperature, at boundaries and in the plasma) are computed. The performances are averaged over the 1000 first time steps of the simulations. Hence, the load is well balanced between the CPU.

An example of the relative importance of each module of the simulation over a time step is given in Table A.3. Each module is called 1000 times, except for the outputs function, that writes the diagnostics to the disk, which is called only once. Its duration is divided by the number of time steps, in order to compare it to the other modules. To give an order of magnitude, taking $t = 10.08\,\mathrm{s}$ for one time-step corresponds to an average of $8.2\,\mathrm{ns}$ per particle.

TABLE A.1 – Operating and numerical parameters used in the strong scalability large test-case.

Physical Parameter	notation	Value	Unit
Gas		Xenon	-
Domain dimensions	$L_x \times L_y$	1.0×1.023	[cm^2]
Radial magnetic field	B_0	200	[G]
Axial electric field	E_0	2×10^4	[Vm^{-1}]
Mean plasma density	n_0	1×10^{17}	[m^{-3}]
Initial electron temperature	$T_{e,0}$	1.0	[V]
Initial ion temperature	$T_{i,0}$	0.05	[V]
Neutral gas pressure	P_n	0.1	[mTorr]
Neutral gas temperature	T_n	300	[K]
Neutral gas density	n_g	3.22×10^{18}	[m^{-3}]
Simulation Parameter			
Time step	Δt	4×10^{-13}	[s]
Cell size	$\Delta x = \Delta y = \Delta z$	5×10^{-7}	[m]
Number of particles per cell	N/NG	150	[part/cell]
Number of particles	N	2×614099924	[particles]
Number of time steps	N_t	1000	–

TABLE A.2 – Modified parameter for the strong-scalability small test-case. The other parameters are given in Table A.1.

Physical Parameter	notation	Value	Unit
Domain dimensions	$L_x \times L_y$	1.0×1.023	[cm^2]
Simulation Parameter			
Cell size	$\Delta x = \Delta y = \Delta z$	1×10^{-6}	[m]

TABLE A.3 – Performances of the large test-case (parameters of Table A.1) when using 96 CPUs, average over 1000 time steps.

Module	Duration one time-step [s]	Percentage
Total	10.08	100
Diagnostics particle to mesh	6.03	59.9
Particle motion	2.88	28.6
Monte Carlo Collision	0.729	7.31
Outputs	0.287	2.84
Poisson solver	0.075	0.75

Annexe B

Calculation of the SEE rate with and without saturation

The calculation of $\bar{\sigma}_{\mathrm{Maxw}}$ in Eq. (4.11) was done neglecting the saturation of σ at $\sigma_{\max}$. The exact value of $\bar{\sigma}_{\mathrm{Maxw}}$ is proposed here including the saturation. Eq. (4.10) give, using the Maxwellian hypothesis

$$\bar{\sigma}_{\mathrm{Maxw}}(\mathrm{T_e}) = \sigma_0 + (1-\sigma_0)\frac{2\mathrm{T_e}}{\epsilon^*} + \frac{\int_{\epsilon_{\max}}^{+\infty}(\sigma_{\max} - \sigma(\epsilon) f_M(\epsilon) d\epsilon}{1/4 n_e \bar{v}} \tag{B.1}$$

with $\epsilon_{\max} = \frac{\sigma_{\max}-\sigma_0}{1-\sigma_0}\epsilon^*$ is the minimum energy for which $\bar{\sigma} = \sigma_{\max}$. We obtain

$$\begin{aligned}
\bar{\sigma}_{\mathrm{Maxw}}(\mathrm{T_e}) =& \sigma_0 + (1-\sigma_0)\frac{2\mathrm{T_e}}{\epsilon^*} && \text{(B.2)}\\
&+ (\sigma_{\max}-\sigma_0)(\epsilon_{\max}+1)\exp(-\epsilon_{\max}) && \text{(B.3)}\\
&+ (\sigma_0-1)(\epsilon_{\max}^2 + 2\epsilon_{\max} + 2)\frac{\mathrm{T_e}}{\epsilon^*}\exp(-\epsilon_{\max}) && \text{(B.4)}
\end{aligned}$$

Figure B.1 shows the evolution of the SEE rate $\bar{\sigma}_{\mathrm{Maxw}}$ as a function of the electron temperature $\mathrm{T_e}$ normalized by the crossover energy ϵ^*. On the left of Fig. B.1, we can see the comparison between the calculation neglecting the saturation Eq. (4.11) and the calculation without neglecting it Eq. (B.2). We can see that the two values are close up to $\frac{\mathrm{T_e}}{\epsilon^*} \sim 1$, where the two values start to diverge from each other. The right panel of Fig. B.1 shows the evolution of the relative error as a function of $\frac{\mathrm{T_e}}{\epsilon^*}$. We can see that at $\frac{\mathrm{T_e}}{\epsilon^*} \sim 1$, the error only equals 2%.

On the other hand, the SEE rate $\bar{\sigma}$ crosses the threshold value of $\bar{\sigma}_{\mathrm{cr}} \simeq 1$ at $\mathrm{T_e}/\epsilon^* = 0.5$. We know that the a theoretical SEE rate above $\bar{\sigma}_{\mathrm{cr}}$, the a potential well is present so that electrons are reflected to the wall, and therefore the effective SEE rate is close to $\bar{\sigma}_{\mathrm{cr}}$. Hence, the error between Eq. (B.2) and Eq. (4.11) can always be neglected.

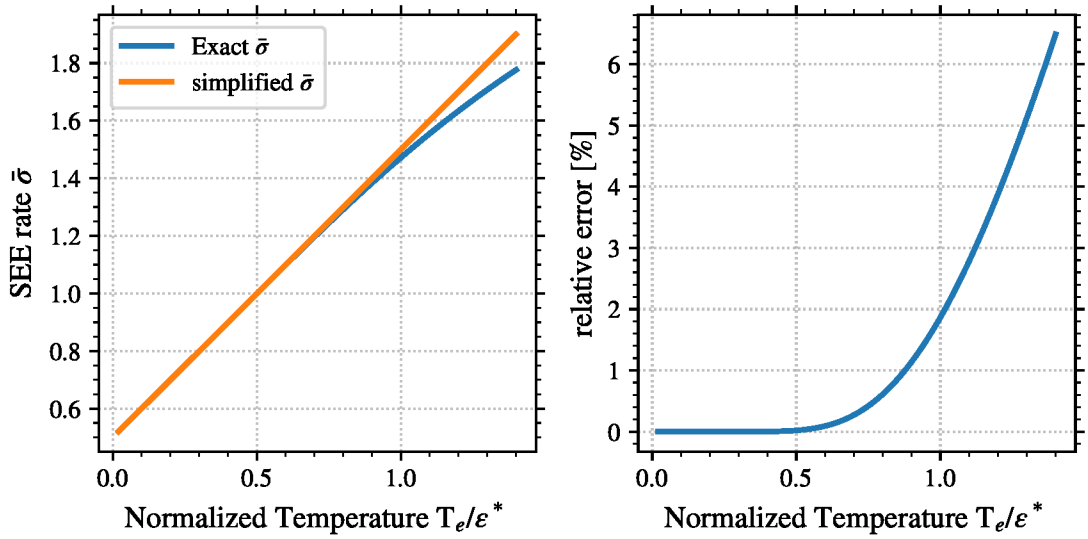

FIGURE B.1 – Evolution of the SEE rate from a Maxwellian distribution function without and with the saturation at $\sigma_{\max}$.

Bibliography

[1] u/ucarion. R/space - I made a delta-v subway map of the Solar System. www.reddit.com/r/space/comments/29cxi6/i_made_a_deltav_subway_map_of_the_solar_system/, Retrieved in 2019.

[2] A. Phelps. Phelps database. www.lxcat.net, retrieved on November 16 2016.

[3] Cross sections extracted program MAGBOLTZ. www.lxcat.net, version 7.1 june 2016.

[4] T. Lafleur, S. D. Baalrud, and P. Chabert. Theory for the anomalous electron transport in Hall effect thrusters. I. Insights from particle-in-cell simulations, *Physics of Plasmas*, 23 (5):053502, 2016.

[5] V. Croes. *Modélisation bidimensionnelle de la décharge plasma dans un propulseur de Hall*. PhD thesis, Université Paris-Saclay, 2017.

[6] S. Barral, K. Makowski, Z. Peradzyński, N. Gascon, and M. Dudeck. Wall material effects in stationary plasma thrusters. II. Near-wall and in-wall conductivity, *Physics of Plasmas*, 10(10):4137–4152, 2003.

[7] Y. Raitses, A. Smirnov, D. Staack, and N. J. Fisch. Measurements of secondary electron emission effects in the Hall thruster discharge, *Physics of Plasmas*, 13(1):014502, 2006.

[8] J. P. Boeuf and L. Garrigues. E × B electron drift instability in Hall thrusters : Particle-in-cell simulations vs. theory, *Physics of Plasmas*, 25(6):061204, 2018.

[9] C. Boniface, J. Charbonnier, L. Lefebvre, V. Leroi, and T. Lienart. An Overview of electric propulsion activities at CNES. In *IEPC*, Geaorgia Institute of Technology, Atlanta, Geaorgia, USA, 2017.

[10] O. Duchemin, J. Rabin, L. Balika, M. Diome, J.-M. Lonchard, and X. Cavelan. Development Status of the PPS©5000 Hall Thruster Unit. In *IEPC-2017-415*, Georgia Institute of Technology, Atlanta, Georgia, USA, 2017.

[11] J. Vaudolon, V. Vial, N. Cornu, and I. Habbassi. PPS-X00 Hall Thruster Development at Safran. In *IAC*, Bremen, Germany, 2018.

[12] K. A. Zona. NASA - Liquid Hydrogen–the Fuel of Choice for Space Exploration. www.nasa.gov/topics/technology/hydrogen/hydrogen_fuel_of_choice.html, 2019.

[13] C. Charles. Plasmas for spacecraft propulsion, *Journal of Physics D: Applied Physics*, 42 (16):163001, 2009.

[14] S. Mazouffre. Electric propulsion for satellites and spacecraft : Established technologies and novel approaches, *Plasma Sources Science and Technology*, 25(3):033002, 2016.

[15] D. Lev, R. M. Myers, K. M. Lemmer, J. Kolbeck, H. Koizumi, and K. Polzin. The technological and commercial expansion of electric propulsion, *Acta Astronautica*, 2019.

[16] S. Samukawa, M. Hori, S. Rauf, K. Tachibana, P. Bruggeman, G. Kroesen, J. C. Whitehead, A. B. Murphy, A. F. Gutsol, S. Starikovskaia, U. Kortshagen, J.-P. Boeuf, T. J. Sommerer, M. J. Kushner, U. Czarnetzki, and N. Mason. The 2012 Plasma Roadmap, *Journal of Physics D: Applied Physics*, 45(25):253001, 2012.

[17] P. Lascombes. Electric Propulsion For Small Satellites Orbit Control And Deorbiting : The Example Of A Hall Effect Thruster. In *15th International Conference on Space Operations*, Marseille, France, 2018. American Institute of Aeronautics and Astronautics.

[18] V. Croes, T. Lafleur, Z. Bonaventura, A. Bourdon, and P. Chabert. 2D particle-in-cell simulations of the electron drift instability and associated anomalous electron transport in Hall-effect thrusters, *Plasma Sources Science and Technology*, 26(3):034001, 2017.

[19] V. Croes, A. Tavant, R. Lucken, R. Martorelli, T. Lafleur, A. Bourdon, and P. Chabert. The effect of alternative propellants on the electron drift instability in Hall-effect thrusters : Insight from 2D particle-in-cell simulations, *Physics of Plasmas*, 25(6):063522, 2018.

[20] I. Adamovich, S. D. Baalrud, A. Bogaerts, P. J. Bruggeman, M. Cappelli, V. Colombo, U. Czarnetzki, U. Ebert, J. G. Eden, P. Favia, D. B. Graves, S. Hamaguchi, G. Hieftje, M. Hori, I. D. Kaganovich, U. Kortshagen, M. J. Kushner, N. J. Mason, S. Mazouffre, S. M. Thagard, H.-R. Metelmann, A. Mizuno, E. Moreau, A. B. Murphy, B. A. Niemira, G. S. Oehrlein, Z. L. Petrovic, L. C. Pitchford, Y.-K. Pu, S. Rauf, O. Sakai, S. Samukawa, S. Starikovskaia, J. Tennyson, K. Terashima, M. M. Turner, M. C. M. van de Sanden, and A. Vardelle. The 2017 Plasma Roadmap : Low temperature plasma science and technology, *Journal of Physics D: Applied Physics*, 50(32):323001, 2017.

[21] Earth Fact Sheet. `https://nssdc.gsfc.nasa.gov/planetary/factsheet/earthfact.html`.

[22] D. Gawron, S. Mazouffre, N. Sadeghi, and A. Héron. Influence of magnetic field and discharge voltage on the acceleration layer features in a Hall effect thruster, *Plasma Sources Science and Technology*, 17(2):025001, 2008.

[23] L. Dubois, F. Gaboriau, L. Liard, C. Boniface, and J. P. Boeuf. ID-HALL, a new double stage Hall thruster design. II. Experimental characterization of the inductive ionization source, *Physics of Plasmas*, 25(9):093504, 2018.

[24] J.-P. Boeuf. Tutorial : Physics and modeling of Hall thrusters, *Journal of Applied Physics*, 121(1):011101, 2017.

[25] E. Y. Choueiri. Plasma oscillations in Hall thrusters, *Physics of Plasmas*, 8(4):1411, 2001.

[26] J. P. Boeuf and L. Garrigues. Low frequency oscillations in a stationary plasma thruster, *Journal of Applied Physics*, 84(7):3541–3554, 1998.

[27] S. Barral and E. Ahedo. Low-frequency model of breathing oscillations in Hall discharges, *Physical Review E*, 79(4), 2009.

[28] K. Hara, M. J. Sekerak, I. D. Boyd, and A. D. Gallimore. Perturbation analysis of ionization oscillations in Hall effect thrusters, *Physics of Plasmas*, 21(12):122103, 2014.

[29] C. L. Ellison, Y. Raitses, and N. J. Fisch. Cross-field electron transport induced by a rotating spoke in a cylindrical Hall thruster, *Physics of Plasmas*, 19(1):013503, 2012.

[30] M. S. McDonald and A. D. Gallimore. Rotating Spoke Instabilities in Hall Thrusters, *IEEE Transactions on Plasma Science*, 39(11):2952–2953, 2011.

[31] G. S. Janes. Anomalous Electron Diffusion and Ion Acceleration in a Low-Density Plasma, *Physics of Fluids*, 9(6):1115, 1966.

[32] J. Carlsson, I. Kaganovich, A. Powis, Y. Raitses, I. Romadanov, and A. Smolyakov. Particle-in-cell simulations of anomalous transport in a Penning discharge, *Physics of Plasmas*, 25 (6):061201, 2018.

[33] S. Barral, K. Makowski, Z. Peradzyński, and M. Dudeck. Transit-time instability in Hall thrusters, *Physics of Plasmas*, 12(7):073504, 2005.

[34] J. Vaudolon. *Electric Field Determination and Magnetic Topology Optimization in Hall Thrusters*. PhD thesis, Université d'Orléans, 2015.

[35] J. C. Adam, A. Héron, and G. Laval. Study of stationary plasma thrusters using two-dimensional fully kinetic simulations, *Physics of Plasmas*, 11(1):295–305, 2004.

[36] A. Ducrocq, J. C. Adam, A. Héron, and G. Laval. High-frequency electron drift instability in the cross-field configuration of Hall thrusters, *Physics of Plasmas*, 13(10):102111, 2006.

[37] J. C. Adam, J. P. Boeuf, N. Dubuit, M. Dudeck, L. Garrigues, D. Gresillon, A. Heron, G. J. M. Hagelaar, V. Kulaev, N. Lemoine, S. Mazouffre, J. Perez Luna, V. Pisarev, and S. Tsikata. Physics, simulation and diagnostics of Hall effect thrusters, *Plasma Physics and Controlled Fusion*, 50(12):124041, 2008.

[38] A. Héron and J. C. Adam. Anomalous conductivity in Hall thrusters : Effects of the non-linear coupling of the electron-cyclotron drift instability with secondary electron emission of the walls*Physics of Plasmas*, 20(8) :082313, 2013.

[39] S. Tsikata, N. Lemoine, V. Pisarev, and D. M. Grésillon. Dispersion relations of electron density fluctuations in a Hall thruster plasma, observed by collective light scattering, *Physics of Plasmas*, 16(3):033506, 2009.

[40] S. Tsikata. *Small-Scale Electron Density Fluctuations in the Hall Thruster, Investigated by Collective Light Scattering*. PhD thesis, Ecole Polytechnique, 2009.

[41] S. Tsikata, C. Honoré, and D. Grésillon. Collective Thomson scattering for studying plasma instabilities in electric thrusters, *Journal of Instrumentation*, 8(10):C10012–C10012, 2013.

[42] F. F. Chen. *Plasma Physics*. Number Vol. 1 in Introduction to Plasma Physics and Controlled Fusion. Springer US, New York, 2 edition, 2006.

[43] N. B. Meezan, W. A. Hargus, and M. A. Cappelli. Anomalous electron mobility in a coaxial Hall discharge plasma, *Physical Review E*, 63(2), 2001.

[44] F. Taccogna, P. Minelli, Z. Asadi, and G. Bogopolsky. Numerical studies of the ExB electron drift instability in Hall thrusters, *Plasma Sources Science and Technology*, 2019.

[45] B. Jorns. Predictive, data-driven model for the anomalous electron collision frequency in a Hall effect thruster, *Plasma Sources Science and Technology*, 27(10):104007, 2018.

[46] A. I. Morozov. Wall conduction in a highly magnetized plasma, *Journal of Applied Mechanics and Technical Physics*, 9(3):249–251, 1972.

[47] A. I. Morozov and V. V. Savel'ev. Theory of the near-wall conductivity, *Plasma Physics Reports*, 27(7):570–575, 2001.

[48] N. Gascon, M. Dudeck, and S. Barral. Wall material effects in stationary plasma thrusters. I. Parametric studies of an SPT-100, *Physics of Plasmas*, 10(10):4123–4136, 2003.

[49] M. Villemant. *Modélisation et caractérisation expérimentale de l'influence de l'émission électronique sur le fonctionnement des propulseurs à courant de Hall*. PhD thesis, Institut Supérieur de l'Aéronautique et de l'Espace (ISAE), 2018.

[50] K. Ohya and T. Ishitani. Monte Carlo study of secondary electron emission from SiO2 induced by focused gallium ion beams, *Applied Surface Science*, 237(1-4):602–606, 2004.

[51] Y. Raitses, D. Staack, A. Smirnov, and N. J. Fisch. Space charge saturated sheath regime and electron temperature saturation in Hall thrusters, *Physics of Plasmas*, 12(7):073507, 2005.

[52] D. Sydorenko, A. Smolyakov, I. Kaganovich, and Y. Raitses. Effects of non-Maxwellian electron velocity distribution function on two-stream instability in low-pressure discharges, *Physics of Plasmas*, 14(1):013508, 2007.

[53] F. Taccogna and L. Garrigues. Latest progress in Hall thrusters plasma modelling, *Reviews of Modern Plasma Physics*, 3(1), 2019.

[54] F. Taccogna and P. Minelli. Three-dimensional particle-in-cell model of Hall thruster : The discharge channel, *Physics of Plasmas*, 25(6):061208, 2018.

[55] G. Fubiani, J. P. Boeuf, and L. Garrigues. 3D Particle-in-Cell simulation of the ExB electron drift instability inHall thrusters : Effect of the dielectric surfaces on the anomalous transport. In *LW1.00066*, Portland, OR (USA), Nov. 5-9, 2018.

[56] M. A. Lieberman and A. J. Lichtenberg. *Principles of Plasma Discharges and Materials Processing : Lieberman/Plasma 2e.* John Wiley & Sons, Inc., Hoboken, NJ, USA, 2005.

[57] L. Landau. On the vibrations of the electronic plasma, *Journal of Physics*, X(1):25–34, 1945.

[58] J. H. Malmberg and C. B. Wharton. Collisionless Damping of Electrostatic Plasma Waves, *Physical Review Letters*, 13(6):184–186, 1964.

[59] D. S. Filippychev. Modeling beam instability in plasma, *Computational Mathematics and Modeling*, 1(1):71–74, 1990.

[60] P. Cagas, A. Hakim, and B. Srinivasan. Boundary Conditions for Continuum Simulations of Wall-bounded Kinetic Plasmas*arXiv :1906.07056 [physics]*, 2019.

[61] R. W. Boswell and I. J. Morey. Self-consistent simulation of a parallel-plate rf discharge, *Applied Physics Letters*, 52(1):21–23, 1988.

[62] Y. Raitses, I. D. Kaganovich, A. Khrabrov, D. Sydorenko, N. J. Fisch, and A. Smolyakov. Effect of Secondary Electron Emission on Electron Cross-Field Current in $E \\times B$ Discharges, *IEEE Transactions on Plasma Science*, 39(4):995–1006, 2011.

[63] D. Sydorenko. *Particle-in-Cell Simulations of Electron Dynamics in Low Pressure Discharges with Magnetic Fields.* PhD thesis, University of Saskatchewan, 2006.

[64] H. Ueda, Y. Omura, H. Matsumoto, and T. Okuzawa. A study of the numerical heating in electrostatic particle simulations*Computer physics communications*, 79(2) :249–259, 1994.

[65] S. Janhunen, A. Smolyakov, D. Sydorenko, M. Jimenez, I. Kaganovich, and Y. Raitses. Evolution of the electron cyclotron drift instability in two-dimensions, *Physics of Plasmas*, 25(8):082308, 2018.

[66] V. Vahedi, M. A. Lieberman, G. DiPeso, T. D. Rognlien, and D. Hewett. Analytic model of power deposition in inductively coupled plasma sources, *Journal of Applied Physics*, 78 (3):1446–1458, 1995.

[67] LXCat project. `www.lxcat.net`, 2019.

[68] S. Pancheshnyi, S. Biagi, M. Bordage, G. Hagelaar, W. Morgan, A. Phelps, and L. Pitchford. The LXCat project : Electron scattering cross sections and swarm parameters for low temperature plasma modeling, *Chemical Physics*, 398:148–153, 2012.

[69] C. K. Birdsall. Particle-in-cell charged-particle simulations, plus Monte Carlo collisions with neutral atoms, PIC-MCC, *IEEE Transactions on Plasma Science*, 19(2):65–85, 1991.

[70] M. M. Turner, A. Derzsi, Z. Donkó, D. Eremin, S. J. Kelly, T. Lafleur, and T. Mussenbrock. Simulation benchmarks for low-pressure plasmas : Capacitive discharges, *Physics of Plasmas*, 20(1):013507, 2013.

[71] M. M. Turner. Kinetic properties of particle-in-cell simulations compromised by Monte Carlo collisions, *Physics of Plasmas*, 13(3):033506, 2006.

[72] J. Boris. Relativistic plasma simulation-optimization of a hybrid code. In *Fourth Conference on Numerical Simulations of Plasmas*, 1970.

[73] A. Domínguez-Vázquez, F. Taccogna, and E. Ahedo. Particle modeling of radial electron dynamics in a controlled discharge of a Hall thruster, *Plasma Sources Science and Technology*, 27(6):064006, 2018.

[74] M. Keidar and I. D. Boyd. On the magnetic mirror effect in Hall thrusters, *Applied Physics Letters*, 87(12):121501, 2005.

[75] D. Yu, H. Liu, Y. Cao, and H. Fu. The Effect of Magnetic Mirror on Near Wall Conductivity in Hall Thrusters, *Contributions to Plasma Physics*, 48(8):543–554, 2008.

[76] O. C. Ibe. 9 - Brownian Motion. In O. C. Ibe, editor, *Markov Processes for Stochastic Modeling (Second Edition)*, pages 263–293. Elsevier, Oxford, 2013.

[77] M. Furman and M. Pivi. Probabilistic model for the simulation of secondary electron emission, *Physical Review Special Topics - Accelerators and Beams*, 5(12), 2002.

[78] J. Pierron, C. Inguimbert, M. Belhaj, T. Gineste, J. Puech, and M. Raine. Electron emission yield for low energy electrons : Monte Carlo simulation and experimental comparison for Al, Ag, and Si, *Journal of Applied Physics*, 121(21):215107, 2017.

[79] J. Vaughan. A new formula for secondary emission yield, *IEEE Transactions on Electron Devices*, 36(9):1963–1967, 1989.

[80] D. Sydorenko, A. Smolyakov, I. Kaganovich, and Y. Raitses. Modification of electron velocity distribution in bounded plasmas by secondary electron emission, *IEEE Transactions on Plasma Science*, 34(3):815–824, 2006.

[81] G. D. Hobbs and J. A. Wesson. Heat flow through a Langmuir sheath in the presence of electron emission, *Plasma Physics*, 9(1):85–87, 1967.

[82] E. Ahedo and F. I. Parra. Partial trapping of secondary-electron emission in a Hall thruster plasma, *Physics of Plasmas*, 12(7):073503, 2005.

[83] E. Ahedo. Presheath/sheath model with secondary electron emission from two parallel walls, *Physics of Plasmas*, 9(10):4340–4347, 2002.

[84] D. M. Goebel and I. Katz. *Fundamentals of Electric Propulsion : Ion and Hall Thrusters*. JPL Space Science and Technology Series. Jet Propulsion Laboratory, California Institute of Technology, 2008.

[85] T. Lafleur, S. D. Baalrud, and P. Chabert. Theory for the anomalous electron transport in Hall effect thrusters. II. Kinetic model, *Physics of Plasmas*, 23(5):053503, 2016.

[86] P. Coche and L. Garrigues. A two-dimensional (azimuthal-axial) particle-in-cell model of a Hall thruster, *Physics of Plasmas*, 21(2):023503, 2014.

[87] T. Lafleur, R. Martorelli, P. Chabert, and A. Bourdon. Anomalous electron transport in Hall-effect thrusters : Comparison between quasi-linear kinetic theory and particle-in-cell simulations, *Physics of Plasmas*, 25(6):061202, 2018.

[88] R. D. Falgout and U. M. Yang. Hypre : A Library of High Performance Preconditioners. In G. Goos, J. Hartmanis, J. van Leeuwen, P. M. A. Sloot, A. G. Hoekstra, C. J. K. Tan, and J. J. Dongarra, editors, *Computational Science — ICCS 2002*, volume 2331, pages 632–641. Springer Berlin Heidelberg, Berlin, Heidelberg, 2002.

[89] G. M. Amdahl. Validity of the single processor approach to achieving large scale computing capabilities. In *Proceedings of the April 18-20, 1967, Spring Joint Computer Conference on - AFIPS '67 (Spring)*, page 483, Atlantic City, New Jersey, 1967. ACM Press.

[90] M. M. Turner. Verification of particle-in-cell simulations with Monte Carlo collisions, *Plasma Sources Science and Technology*, 25(5):054007, 2016.

[91] T. Charoy, J.-P. Boeuf, A. Bourdon, J. Carlsson, P. Chabert, B. Cuenot, D. Eremin, L. Garrigues, K. Hara, I. Kaganovich, T. Powis, A. Smolyakov, D. Sydorenko, A. Tavant, O. Vermorel, and W. Villafana. 2D axial-azimuthal Particle-In-Cell benchmark for low-temperature partially magnetized plasmas*accepted manuscript in Plasma Sources Sceince and Technology*, 2019.

[92] A. Tavant, V. Croes, R. Lucken, T. Lafleur, A. Bourdon, and P. Chabert. The effects of secondary electron emission on plasma sheath characteristics and electron transport in an E x B discharge via kinetic simulations, *Plasma Sources Science and Technology*, 27(12): 124001, 2018.

[93] A. Tavant, R. Lucken, A. Bourdon, and P. Chabert. Non-isothermal sheath model for low pressure plasmas, *Plasma Sources Science and Technology*, 28(7):075007, 2019.

[94] R. Lucken, V. Croes, T. Lafleur, J.-L. Raimbault, A. Bourdon, and P. Chabert. Edge-to-center plasma density ratios in two-dimensional plasma discharges, *Plasma Sources Science and Technology*, 27(3):035004, 2018.

[95] R. Lucken, A. Bourdon, M. A. Lieberman, and P. Chabert. Instability-enhanced transport in low temperature magnetized plasma, *Physics of Plasmas*, 26(7):070702, 2019.

[96] C. Honore, S. Tsikata, D. Gresillon, A. Heron, J. Cavalier, and N. Lemoine. Hall Thruster small scale plasma fluctuations : Qualifying 2D PIC Simulations against Collective Scattering Experimental Data. In *Proceedings of the 32nd International Electric Propulsion Conference*, 2011.

[97] J. Cavalier. *Modèles cinétiques et caractérisation expérimentale des fluctuations électrostatiques dans un propulseur à effet Hall*. PhD thesis, Université de Lorraine, 2013.

[98] J. Cavalier, N. Lemoine, G. Bonhomme, S. Tsikata, C. Honoré, and D. Grésillon. Hall thruster plasma fluctuations identified as the E×B electron drift instability : Modeling and fitting on experimental data, *Physics of Plasmas*, 20(8):082107, 2013.

[99] K. Hara. An overview of discharge plasma modeling for Hall effect thrusters, *Plasma Sources Science and Technology*, 28(4):044001, 2019.

[100] V. N. Tsytovich. *An Introduction to the Theory of Plasma Turbulence*. Pergamon Press, 1972.

[101] G. Belmont, R. Grappin, F. Mottez, F. Pantellini, and G. Pelletier. *Collisionless Plasmas in Astrophysics*. Wiley-VCH Verlag GmbH & Co. KGaA, Weinheim, Germany, 2013.

[102] T. Lafleur, S. D. Baalrud, and P. Chabert. Characteristics and transport effects of the electron drift instability in Hall-effect thrusters, *Plasma Sources Science and Technology*, 26(2):024008, 2017.

[103] J. Weiland and H. Wilhelmsson. Coherent non-linear interaction of waves in plasmas1977.

[104] B. D. Fried and S. D. Conte. The Plasma Dispersion Function*Academic Press, New York and London*, page 424, 1961.

[105] H.-S. Xie. Generalized plasma dispersion function : One-solve-all treatment, visualizations, and application to Landau damping, *Physics of Plasmas*, 20(9):092125, 2013.

[106] S. Janhunen, A. Smolyakov, O. Chapurin, D. Sydorenko, I. Kaganovich, and Y. Raitses. Nonlinear structures and anomalous transport in partially magnetized ExB plasmas, *Physics of Plasmas*, 25(1):011608, 2018.

[107] T. Lafleur and P. Chabert. The role of instability-enhanced friction on 'anomalous' electron and ion transport in Hall-effect thrusters, *Plasma Sources Science and Technology*, 27(1): 015003, 2017.

[108] L. F. Ziebell, R. Gaelzer, and F. J. R. Simões. Dispersion relation for electrostatic waves in plasmas with isotropic and anisotropic Kappa distributions for electrons and ions, *Journal of Plasma Physics*, 83(5), 2017.

[109] K. Rönnmark. WHAMP- Waves in Homogeneous, Anisotropic Multicomponent Plasmas*KGI Report*, 179, 1982.

[110] J. A. C. Weideman. Computing the Hilbert Transform on the Real Line*Mathematics of computation*, 64(210) :745–762, 1995.

[111] S. Fortune. Polynomial root finding using iterated Eigenvalue computation. In *Proceedings of the 2001 International Symposium on Symbolic and Algebraic Computation - ISSAC '01*, pages 121–128, London, Ontario, Canada, 2001. ACM Press.

[112] K. I. M. McKinnon. Convergence of the Nelder–Mead Simplex Method to a Nonstationary Point, *SIAM Journal on Optimization*, 9(1):148–158, 1998.

[113] M. J. D. Powell. An efficient method for finding the minimum of a function of several variables without calculating derivatives*The Computer Journal*, 7(2) :155–162, 1964.

[114] E. E. Salpeter. Electron Density Fluctuations in a Plasma, *Physical Review*, 120(5):1528–1535, 1960.

[115] P. Chabert. What is the size of a floating sheath ?, *Plasma Sources Science and Technology*, 23(6):065042, 2014.

[116] I. B. Bernstein and T. Holstein. Electron Energy Distributions in Stationary Discharges, *Physical Review*, 94(6):1475–1482, 1954.

[117] V. A. Godyak and R. B. Piejak. Paradoxical spatial distribution of the electron temperature in a low pressure rf discharge, *Applied Physics Letters*, 63(23):3137–3139, 1993.

[118] S. Mouchtouris and G. Kokkoris. A hybrid model for low pressure inductively coupled plasmas combining a fluid model for electrons with a plasma-potential-dependent energy distribution and a fluid-Monte Carlo model for ions, *Plasma Sources Science and Technology*, 25(2):025007, 2016.

[119] V. A. Godyak, R. B. Piejak, and B. M. Alexandrovich. Electron energy distribution function measurements and plasma parameters in inductively coupled argon plasma, *Plasma Sources Science and Technology*, 11(4):525–543, 2002.

[120] A. Meige and R. W. Boswell. Electron energy distribution functions in low-pressure inductively coupled bounded plasmas, *Physics of Plasmas*, 13(9):092104, 2006.

[121] I. Kaganovich, M. Mišina, S. V. Berezhnoi, and R. Gijbels. Electron Boltzmann kinetic equation averaged over fast electron bouncing and pitch-angle scattering for fast modeling of electron cyclotron resonance discharge, *Physical Review E*, 61(2):1875–1889, 2000.

[122] I. D. Kaganovich, Y. Raitses, D. Sydorenko, and A. Smolyakov. Kinetic effects in a Hall thruster discharge, *Physics of Plasmas*, 14(5):057104, 2007.

[123] P. Chabert and N. Braithwaite. *Physics of Radio-Frequency Plasmas*. Cambridge University Press, 2011.

[124] T. Lafleur, C. Charles, and R. W. Boswell. Electron temperature characterization and power balance in a low magnetic field helicon mode, *Journal of Physics D: Applied Physics*, 44(18):185204, 2011.

[125] Y. Zhang, C. Charles, and R. Boswell. A Polytropic Model for Space and Laboratory Plasmas Described by Bi-Maxwellian Electron Distributions, *The Astrophysical Journal*, 829(1):10, 2016.

[126] S. Kuhn, K.-U. Riemann, N. Jelić, D. D. Tskhakaya, D. Tskhakaya, and M. Stanojević. Link between fluid and kinetic parameters near the plasma boundary, *Physics of Plasmas*, 13(1):013503, 2006.

[127] N. Jelić, K.-U. Riemann, T. Gyergyek, S. Kuhn, M. Stanojević, and J. Duhovnik. Fluid and kinetic parameters near the plasma-sheath boundary for finite Debye lengths, *Physics of Plasmas*, 14(10):103506, 2007.

[128] P. L. Bhatnagar, E. P. Gross, and M. Krook. A Model for Collision Processes in Gases. I. Small Amplitude Processes in Charged and Neutral One-Component Systems, *Physical Review*, 94(3):511–525, 1954.

[129] K.-U. Riemann, J. Seebacher, D. D. T. Sr, and S. Kuhn. The plasma–sheath matching problem, *Plasma Physics and Controlled Fusion*, 47(11):1949, 2005.

[130] K. U. Riemann. The Bohm criterion and sheath formation, *Journal of Physics D: Applied Physics*, 24(4):493–518, 1991.

[131] V. Demidov, C. DeJoseph, and A. Kudryavtsev. Anomalously High Near-Wall Sheath Potential Drop in a Plasma with Nonlocal Fast Electrons, *Physical Review Letters*, 95(21), 2005.

[132] M. M. Turner. Collisionless electron heating in an inductively coupled discharge, *Physical Review Letters*, 71(12):1844–1847, 1993.

[133] M. J. Kushner. Monte-Carlo simulation of electron properties in rf parallel plate capacitively coupled discharges, *Journal of Applied Physics*, 54(9):4958–4965, 1983.

[134] P. Y. Lai, T. Y. Lin, Y. R. Lin-Liu, and S. H. Chen. Numerical thermalization in particle-in-cell simulations with Monte-Carlo collisions, *Physics of Plasmas*, 21(12):122111, 2014.

[135] J. M. Dawson. Thermal Relaxation in a One-Species, One-Dimensional Plasma, *Physics of Fluids*, 7(3):419, 1964.

[136] D. Montgomery. Thermal Relaxation in One- and Two-Dimensional Plasma Models, *Physics of Fluids*, 13(5):1405, 1970.

[137] A. Smirnov, Y. Raitses, and N. J. Fisch. Electron cross-field transport in a low power cylindrical Hall thruster, *Physics of Plasmas*, 11(11):4922–4933, 2004.

[138] S. Barral, J. Miedzik, and E. Ahedo. A Model for the Active Control of Low Frequency Oscillations in Hall Thrusters. In *44th AIAA/ASME/SAE/ASEE Joint Propulsion Conference &amp ; Exhibit*, Hartford, CT, 2008. American Institute of Aeronautics and Astronautics.

[139] J. P. Verboncoeur, M. V. Alves, V. Vahedi, and C. K. Birdsall. Simultaneous Potential and circuit solution for 1D bounded plasma Particle simulation codes*Journal of Computational Physics*, 104 :321–323, 1993.

[140] L. Wei, L. Han, Y. Ding, D. Yu, and C. Zhang. Stabilizing low-frequency oscillation with two-stage filter in Hall thrusters, *Review of Scientific Instruments*, 88(7):073502, 2017.

[141] C. Shon, H. Lee, and J. Lee. Method to increase the simulation speed of particle-in-cell (PIC) code, *Computer Physics Communications*, 141(3):322–329, 2001.

[142] J. Teunissen and U. Ebert. Controlling the weights of simulation particles : Adaptive particle management using k-d trees, *Journal of Computational Physics*, 259:318–330, 2014.

[143] M. Vranic, T. Grismayer, J. Martins, R. Fonseca, and L. Silva. Particle merging algorithm for PIC codes, *Computer Physics Communications*, 191:65–73, 2015.

[144] J. Adam, A. Gourdin Serveniere, and A. Langdon. Electron sub-cycling in particle simulation of plasma, *Journal of Computational Physics*, 47(2):229–244, 1982.

[145] R. Martorelli, T. Lafleur, A. Bourdon, and P. Chabert. Comparison between ad-hoc and instability-induced electron anomalous transport in a 1D fluid simulation of Hall-effect thruster, *Physics of Plasmas*, 26(8):083502, 2019.

[146] D. Tordeux. *Modélisation de la dynamique des neutres dans un code PIC d'un plasma froid magnétisé : application à la propulsion électrique*. Master Thesis, Master 2 de Physique des Plasmas et de la Fusion, Palaiseau, 2018.

[147] S. Janhunen, A. Smolyakov, D. Sydorenko, M. Jimenez, I. Kaganovich, and Y. Raitses. Evolution of the electron cyclotron drift instability in two-dimensionspage 13, 2018.

[148] Z. Brown, A. and B. Jorns. Propagation and Evolution of the Electron Cyclotron Drift Instability in a Hall Thruster : Fitting Experimental Data and Analytical Models. In *Bulletin of the American Physical Society*, volume Volume 63, Number 11. American Physical Society, 2018.

[149] I. G. Mikellides and A. Lopez Ortega. Challenges in the development and verification of first-principles models in Hall-effect thruster simulations that are based on anomalous resistivity and generalized Ohm's law, *Plasma Sources Science and Technology*, 28(1): 014003, 2019.

[150] J. Olthoff and K. Greenberg. The Gaseous Electronics Conference RF Reference Cell - An Introduction, *Journal of Research of the National Institute of Standards and Technology*, 100(4):327, 1995.

Titre: Interaction plasma-paroi et tranport des électrons dans les moteurs à effet Hall.

Mots clés: Propulsion électrique, simulation PIC, modèle de gaine polytropique, instabilité de dérive cyclotronique

Résumé: Les moteurs électriques pour satellites, qui accélèrent les ions d'un plasma, sont primordiaux pour le succès des missions spatiales (GPS, météo, communication, etc.). Le moteur à effet Hall fait partie des technologies les plus performantes et utilisées. Cependant, sa conception et son optimisation sont longs et coûteux, car des processus clefs sont encore mal compris, en particulier, le transport des électrons et l'interaction plasma-paroi. Afin d'étudier ces deux phénomènes, nous utilisons une simulation cinétique bidimensionnelle.
Grace aux résultats de simulation 2D, nous avons mis en évidence que les électrons sont non-locaux, car ils sont absorbés plus vite aux parois qu'ils ne sont thermalisés par les collisions. En conséquence, nous avons développé un modèle de gaine avec une loi d'état polytropique pour les électrons, qui décrit plus précisément l'interaction plasma-surface. Ce modèle peut être utilisé en présence, ou non, d'émission électronique secondaire. Lorsque l'émission secondaire est présente, le modèle de gaine présente jusqu'à trois solutions, ce qui explique les oscillations de gaines observées dans les simulations.
L'instabilité azimutale observée, responsable du transport des électrons, est comparée aux relations de dispersions de l'instabilité acoustique ionique et l'instabilité cyclotronique de dérive électronique. Nous montrons que la phase de croissance linéaire est bien comprise, mais que l'état stationnaire dépend de l'interaction onde-particule et de phénomènes non-linéaires qui ne sont pas pris en compte dans les relations de dispersion.

Title: Plasma-wall interaction and electron transport in Hall Effect Thrusters

Keywords: Electric propulsion, PIC simulation, non-isothermal sheath model, cyclotron drift instability

Abstract: Electric propulsion systems that accelerate plasma ions are important for the success of spatial missions (GPS, weather forecast, communication, etc.). The Hall effect thruster is one of the most used and efficient technology. However, its conception and optimization is slow and costly, as key processes are still poorly understood, in particular the electron transport and the plasma-wall interaction. In order to study both phenomena, we use a bi-dimensional kinetic simulation.
We showed with 2D PIC simulation results that electrons are non-local, as they are absorbed more quickly at the wall compared to the collision frequency. Consequently, we derived a non-isothermal sheath model using a polytropic state law for the electrons that describes more accurately the plasma-wall interaction. The model can be used with and without secondary electron emission. With electron emission, the sheath model can present up to three solutions, explaining the oscillations observed in the simulations.
The azimuthal instability observed, responsible for the electron transport, is compared to the dispersion relation of the ion acoustic wave and the electron cyclotron drift instability. We show that, while the first linear stage of the instability is well understood, the saturated quasi-steady-state is affected by particle-wave interactions and non-linear mechanisms that are not included in the dispersion relation.

Université Paris-Saclay
Espace Technologique / Immeuble Discovery
Route de l'Orme aux Merisiers RD 128 / 91190 Saint-Aubin, France